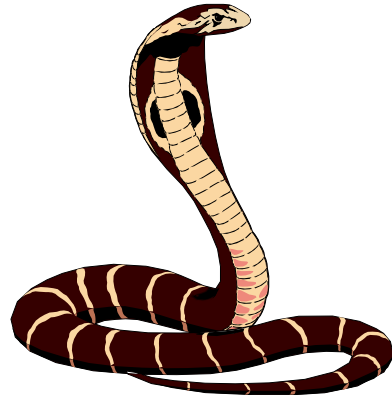


DATA ANALYSIS AND BACKGROUND
STUDIES FOR THE COBRA
NEUTRINOLESS DOUBLE-BETA DECAY
EXPERIMENT



Christopher J. Reeve
University of Sussex, Brighton, UK

A thesis submitted to the University of Sussex
Physics and Astronomy Department
as partial fulfilment of the requirements for a degree of
Doctor of Philosophy.

June, 2009

Abstract

Neutrinos are the lightest known particles, with masses of at least a million times smaller than the electron. Although they were originally thought to be massless, recent oscillation experiments have been able to prove the existence of their finite mass but only put lower constraints on their masses. The COBRA experiment is a new approach to make use of the expected rare process called neutrinoless double-beta decay. If successful, the experiment will be able to provide the key information to a real measurement of the neutrino mass. It will require a measurement of a decay half-life that could be up to 10^{28} years. Such a measurement is extremely difficult to make because of the natural radioactivity of all materials that form part of the experiment.

This thesis is an analysis of data taken with detectors of the COBRA experiment, with a view to improving its performance and identifying backgrounds in the apparatus so that measures can be taken for their removal. Among the results, this research has identified the source of electronic disturbances, most notably micro-discharges in the high voltage cables. It has revealed that radon is currently the dominant background. The existence of a dead layer on the detectors was confirmed and even constrained. A new limit for the internal contamination of the detectors was found. An investigation into the four-fold forbidden beta decay of ^{113}Cd was performed, and limits were calculated on a number of decay modes of neutrinoless double-beta decay.

Declaration

I hereby declare that this thesis has not been submitted and will not be submitted, in whole or in part, to another University for the award of any other degree.

Signature:

Acknowledgements

I would like to thank my first supervisor, Prof. Kai Zuber, for his time and enthusiasm with which he introduced the COBRA experiment to me, and the many ways of looking at the data. His suggestions at structuring the contents of my thesis were also very helpful. Many thanks go to my second supervisor, Prof. Philip Harris, for helping me prioritise and set regular targets when writing up my thesis. His tips for how to organise my ideas were particularly helpful.

The greatest thanks must go to Dr. Jaime Dawson and Dr. Jeanne Wilson who were both postdoctoral researchers at the University of Sussex and were always there to discuss any questions I had with my research. On the many trips working under the mountain in Italy, despite the tight schedules and long working days, they were always full of energy and a pleasure to work with. I think we made a good team. Even after they became busy with new jobs elsewhere, I am particularly grateful for their continued support and kindness to read and give valuable feedback on my thesis.

Of the Dortmund crew I'd like to thank Henning for introducing me to Poison, Daniel for teaching me the ropes of looking after the experiment and lengthy discussions on the phone, Thanks also to Oliver and Tobias for your support.

Thanks to Matthias Junker, Matthias Laubenstein, Daniel Bemmerer and Oleg for their assistance at LNGS. Particular thanks to Matthias Junker for providing me with affordable accommodation and Daniel and Oleg for driving me around when I didn't have a car. Also many thanks to the kind people at the Chemistry and Electronics labs at LNGS for going out of their way to assist me in various tasks.

Huge thanks to my family for their moral support. Finally, and by no means least, I'd like to thank my dearest friend Kaily for all her patience, hospitality, and keeping my spirits up through difficult times. Thank you all very much!

I should also thank STFC (formerly PPARC) for funding me for three years to work on COBRA. I should thank LyX with which I wrote this thesis and would highly recommend. It made my writing experience much more enjoyable. Other software that I relied on for this thesis was Inkscape with which I drew most diagrams and JabRef which was very useful for managing my references.

Preface

The work for this thesis has been carried out between January 2005 and December 2008. My involvement with the COBRA experiment included many trips to the underground laboratory in Italy, LNGS, where I frequently worked together with postdoctoral researchers and other PhD students, and also by myself. This work included installing the apparatus in clean-room conditions, running tests on each detector and electronic components to optimise their performance, extensive calibrations, and improvising solutions for when electronic components sometimes broke. Creativity was also often required, for example, in redesigning the lead shielding and constructing a system, with limited available resources, to allow the source feed-throughs to be accessed from outside the neutron shield. A good understanding for grounding the experiment to avoid ground loops was also gained.

Back at the University of Sussex, where I was based, I was wholly responsible for monitoring the LNGS data as it was collected. In addition, performing calibrations that are necessary in order to achieve accurate energy measurements with our detectors would have to be regularly arranged and the apparatus remotely prepared. I also took part in the planning of upgrades to the experiment and helping with related projects [DRR⁺⁰⁸, DDK⁺⁰⁸] and with bench-top tests [DMR⁺⁰⁸]. By replicating the LNGS set-up at Sussex I was able to locate the source of spurious events that dominated the LNGS data. This hands-on experience was vital for gaining a better understanding of the data, which is the focus of my thesis.

Most of my effort was aimed at developing analysis tools for the data with the purpose of simplifying a complex analysis procedure. In addition, using these tools I was able to investigate the data to gain a better understanding of the detectors and the radioactive backgrounds. The knowledge obtained from these studies will be central to designing a larger scale setup.

Throughout my studies I worked closely alongside Dr. J. Dawson and Dr. J. Wilson at Sussex as well as Dr. D. Müenstermann from Germany. Details of collaboration members are given on page 175. Occasionally there was some overlap in our research, however, all work contained in this thesis is my own, unless specifically stated within the text. This includes plots, photos and analysis. A summary of overlapping work is now described.

J. Dawson was mostly responsible for the research and project management in the COBRA laboratory at Sussex. Using J. Dawson's set-up I was able to show that electrical discharges were occurring in the unshielded high voltage cables that were preventing us from taking useful

data at LNGS. J. Dawson then went on to develop electronics that could be used to reject these discharge events (the HV-veto) and D. Müenstermann made an effective shield for the cables. D. Müenstermann was responsible for most of the hardware design and is referenced frequently in the introductory chapters of this thesis.

J. Dawson also took part in the analysis of the ^{113}Cd beta spectrum. All data preparation and an initial analysis was performed by myself. While I was busy writing my thesis, J. Dawson improved the analysis and compiled the results to be published [DRW⁺09]. Thus, the results presented in Section 5.1 are based on this paper.

J. Wilson and B. Morgan developed Venom (page 44) with which many simulations were produced for this thesis. J. Wilson also developed a tool to work with my analysis software for calculating neutrinoless double-beta decay half-lives and wrote detailed documentation on how the tool worked. Thus, Section 5.2, that describes the fitting method and presents the results is based on the documentation.

Contents

Acknowledgements	ii
Preface	iii
List of Figures	xii
List of Tables	xiii
Introduction	xiv
1 A Neutrinoless Double-Beta Decay Experiment	1
1.1 Theory	1
1.1.1 Two-neutrino double-beta decay	1
1.1.2 Neutrinoless double-beta decay	2
1.2 General Considerations	5
1.3 Experimental Methods	6
1.3.1 Germanium detector experiments	6
1.3.2 Other DBD experimental approaches	7
1.3.3 Non DBD approaches	9
1.3.3.1 Cosmological	9
1.3.3.2 Single beta decay endpoint	9
1.4 The COBRA Concept	10
1.5 Experimental Backgrounds	13
1.5.1 Radiation type and their impact	13
1.5.2 Radiation sources	15
2 The COBRA Setup	19
2.1 Development Stages	20
2.2 64-Array Experimental Setup	22
2.2.1 Introduction	22
2.2.2 The detectors	22
2.2.2.1 How the detectors work	22
2.2.2.2 How the detectors are used	26

2.2.2.3	How the detectors are made	26
2.2.3	Detector holders	27
2.2.4	Kapton cables	27
2.2.5	Detector contacts	27
2.2.6	Nest	28
2.2.7	Source feed-throughs	28
2.2.8	Shielding—passive	28
2.2.8.1	Copper and lead	29
2.2.8.2	Faraday cage	29
2.2.8.3	Neutron shield	29
2.2.9	Shielding—active	32
2.2.9.1	High voltage discharge veto	32
2.2.9.2	Muon veto	32
2.2.9.3	Other sensors	32
2.2.10	Electronics	33
2.2.10.1	Preamplifiers	34
2.2.10.2	The ADCs	34
2.2.10.3	DAQ software	36
2.2.11	Data structure and management	36
2.2.11.1	A description of recorded data	36
2.2.11.2	File sizes	37
2.2.11.3	Organisation of data	38
2.2.11.4	Calibrations	38
2.3	ACID—Analysis Code	39
2.3.1	General discussion	39
2.3.2	Key requirements	39
2.3.3	Framework and analysis techniques	40
2.3.3.1	The programs	40
2.3.3.2	Data structure	41
2.3.3.3	Structure properties	42
2.3.3.4	Flags	43
2.3.3.5	Navigation	44
2.4	Venom	44
3	Data Selection and Performance	46
3.1	Data Taking Periods	46
3.2	Calibrations	47
3.2.1	Calibration method	49
3.2.1.1	Calibration tool	49
3.2.1.2	Calibrations with ^{57}Co and ^{228}Th sources	50
3.2.1.3	Combining calibrations	51
3.2.1.4	Calibrations over time	52

3.2.2	Resolutions	52
3.2.2.1	Doppler broadening	53
3.2.2.2	Resolution results	54
3.2.2.3	Average resolution	54
3.3	Quality Control	55
3.3.1	General considerations and theory	55
3.3.1.1	The Poisson equation	55
3.3.1.2	Time differences	56
3.3.1.3	Probability of coincident events	56
3.3.1.4	Fitting a Poisson distribution	57
3.3.2	Energy spectra	61
3.3.3	Using the Poisson distribution	62
3.3.4	Waterfall plots	64
3.3.5	Time-difference plots	65
3.3.6	Correlation plots	67
3.4	Electronic Background and Stability	68
3.4.1	Possible causes of disturbances	68
3.4.2	Bursts	69
3.4.2.1	Direct observations	69
3.4.2.2	Characterisation of bursts in the data	70
3.4.3	Micro-discharge	73
3.4.3.1	Early observations	73
3.4.3.2	Studies of un-shielded HV cables	73
3.4.3.3	Studies of shielded HV cables	76
3.5	Data Cleaning Technique	81
3.5.1	File size cut and dead time	82
3.5.2	Threshold cut	82
3.5.2.1	Motivation for a new approach	82
3.5.2.2	Human involvement and general comments	83
3.5.2.3	Method	84
3.5.2.4	Suggested improvements	86
3.6	Summary of Usable Data	87
4	Radioactive Background Study	90
4.1	External Backgrounds	90
4.1.1	Paint contribution	91
4.1.2	Radon evidence	93
4.1.2.1	Cathode signals	94
4.1.2.2	Alpha-alpha timing coincidences	100
4.1.3	Beta-alpha timing coincidence	104
4.1.4	Count rate consistency checks	112
4.1.5	Completing the spectrum	115

4.1.5.1	Dead layer constraints	115
4.1.5.2	Single detector studies	117
4.1.5.3	Indications of remaining backgrounds	118
4.2	Internal Backgrounds	123
4.2.1	Search for Bismuth-214	123
4.2.1.1	Expected random background and choice of lower threshold . . .	124
4.2.1.2	Bismuth contamination limit	125
4.2.2	Alpha-alpha limits	127
5	General Analysis	132
5.1	Investigation of the ^{113}Cd Shoulder	132
5.1.1	Introduction	132
5.1.2	Background model	134
5.1.3	Sources of systematic errors	136
5.1.3.1	Cadmium content and crystal mass	136
5.1.3.2	Crystal dead layer	136
5.1.3.3	Efficiency	137
5.1.3.4	Energy calibration	137
5.1.4	Fit method	137
5.1.5	Results	138
5.1.6	Discussion	141
5.2	Neutrinoless DBD Limits	143
5.2.1	Background parameterisation	143
5.2.2	Calculating the half-life	143
5.2.3	Results	144
Summary and Suggestions		147
A	Additional Figures and Tables	151
B	Users Guide for ACID1.7	158
B.1	Introduction	158
B.2	sfalist2root	158
B.2.1	Compiling	159
B.2.2	Required files	159
B.2.2.1	list_group_name	159
B.2.2.2	group_stats.dat	159
B.2.3	Executing	160
B.2.3.1	example	160
B.2.3.2	options	160
B.3	joingroups	161
B.4	sfaplot	161
B.4.1	Getting started	161

B.4.2 Tutorial	162
B.4.2.1 A first look at the data	163
B.4.2.2 Identifying talking detectors	164
B.4.2.3 Investigating and removing correlated events	164
B.4.2.4 Investigating count rates	166
B.4.2.5 Locating the noise thresholds	167
B.4.2.6 Plotting and combining energy spectra	168
B.4.2.7 Suggested organisation	169
C Data-taking Log	171
Collaboration Members	175
Nomenclature	178
Publications	179
Bibliography	180

List of Figures

1.1	Atomic mass parabola for an even number of nucleons.	2
1.2	Neutrino accompanied and neutrinoless double-beta decay.	3
1.3	Distribution of beta radiation energy for 2ν and 0ν DBDs.	5
1.4	Sum spectrum of HM data.	8
1.5	Single beta spectrum near the end point.	9
1.6	A drawing of the 64-array prototype.	10
1.7	Better signal to background for small detectors.	12
1.8	Comparison of 0ν DBD ^{130}Te signal to 0ν DBD ^{116}Cd background.	18
2.1	The Gran Sasso mountain LNGS laboratory plan.	19
2.2	Photo of first prototype detector array and data.	20
2.3	Front view diagrams of detector nest and shielding.	23
2.4	Photos of the detectors and holder.	24
2.5	Schematic of a Frisch-grid gas detector and a CPG CZT detector.	25
2.6	A picture of the experiment before all of the cables were attached.	30
2.7	Side cross-sectional view of nest, copper and lead.	30
2.8	Collection of photos.	31
2.9	Schematic of the main electronics used in the experiment.	33
2.10	Measurement of the ADC timing resolution.	35
2.11	Format of a data file.	37
2.12	Example of <i>run</i> file sizes.	38
2.13	Simulation of muon passing through a detector array.	45
3.1	Representation of a noisy signal.	48
3.2	Typical calibration spectrum using a ^{22}Na radioactive source.	49
3.3	Calibration spectra of ^{57}Co and ^{228}Th	51
3.4	Calibration slopes for working detectors.	52
3.5	Calculation of an average resolution equation.	54
3.6	Simulated Poisson distributions fitted with Poisson function.	58
3.7	Distributions of fitted means and their uncertainties.	59
3.8	Distributions of $\text{Prob}(\chi^2)$	60
3.9	Energy spectrum with corresponding life-time plot.	62

3.10 A Poisson distribution and energy spectrum with noisy runs removed.	63
3.11 Waterfall plot	64
3.12 Time-difference plots to search for electronic pickup.	66
3.13 A correlation plot.	67
3.14 A photograph of a burst.	70
3.15 Waterfall plots of detector 13 show a closer look at bursts.	71
3.16 Time-difference plots for bursts.	72
3.17 Energy distributions of burst events.	72
3.18 Energy spectra before and after the HV cable was shielded.	74
3.19 Distribution of event time separations.	74
3.20 Timing correlation plot of Figure 3.19b.	75
3.21 Correlation plots from data with unshielded HV-cables.	76
3.22 Waterfall plots of the HV-veto.	77
3.23 Distribution of event separations with shielded HV cable.	78
3.24 Most noticeable correlations between the HV-veto and detector signals.	79
3.25 Technique for highlighting ‘talking’ detectors.	80
3.26 Correlation plots between detectors 2, 14 and 15.	81
3.27 Example waterfall plot from group sfa20_20070425.	83
3.28 Total live-time for datasets L1a-c as a function of energy with a maximum of 10.8 kg days.	89
4.1 Comparison of simulated paint contaminants with the data.	92
4.2 Comparison of simulated 609 keV gamma peak heights to background.	93
4.3 Comparison of simulated radon and paint background with the data.	94
4.4 Comparison of a sum spectrum with and without the HV-veto cut.	95
4.5 Correlation plot of the right-hand HV-veto and detector 8.	97
4.6 A zoom in on the alpha correlation.	98
4.7 Anode and cathode signals of a pixellated CZT detector.	99
4.8 Correlation of detectors 7 and 8.	100
4.9 Timing coincidence correlation plot for the $^{222}\text{Rn} \sim ^{214}\text{Pb}$ decays.	102
4.10 Histogram of event separation for the $^{222}\text{Rn} \sim ^{214}\text{Pb}$ decay cut.	102
4.11 Timing coincidence correlation plot for the $^{218}\text{Po} \sim ^{210}\text{Pb}$ decays.	103
4.12 Timing coincidence correlation plot for the $^{214}\text{Bi} \sim ^{210}\text{Pb}$ decays.	105
4.13 Alpha measurements of an Americium-241 by a CZT detector.	105
4.14 Energy spectra of the first and second $^{214}\text{Bi} \sim ^{210}\text{Pb}$ decays.	106
4.15 Comparison of the sum spectrum with Po-214 alpha spectrum.	108
4.16 Decay curves for the $^{214}\text{Bi} \sim ^{210}\text{Bi}$ search.	110
4.17 Count rates per week for 5–8 MeV and 2–5 MeV.	111
4.18 Alpha energy spectra from the ^{214}Po decay for each detector.	113
4.19 A comparison of the total number of events per day observed in Figure 4.18.	114
4.20 The count rate below 6 MeV is compared with paint and detector mass.	114
4.21 Comparison of energy spectrum before and after the move.	115

4.22 Comparison of various simulations with the data.	116
4.23 Energy spectra showing the high energy events of each working detector.	117
4.24 Energy spectrum showing smaller peaks at high energy.	118
4.25 Gaussian fit on an exponential background for the ^{190}Pt alpha peak.	120
4.26 Bismuth-214 beta spectrum in comparison to detector lower energy thresholds. .	124
4.27 Energy spectrum of the ^{214}Po events compared a simulation of internal decays. .	126
4.28 Timing coincidence correlation for the $^{222}\text{Rn} \curvearrowright ^{214}\text{Pb}$ search.	129
4.29 Timing coincidence correlation for the $^{224}\text{Ra} \curvearrowright ^{216}\text{Po}$ search.	129
4.30 Event separation distribution plots for the ^{222}Rn and ^{224}Ra search.	130
4.31 Timing coincidence correlation for the $^{220}\text{Rn} \curvearrowright ^{212}\text{Pb}$ search.	130
5.1 Summed live-time and summed energy plot of datasets L1a-b.	133
5.2 The ^{222}Rn simulation is scaled to the energy spectrum of the detectors.	134
5.3 ^{113}Cd spectra and fit with c_1 , c_2 and c_3 fixed.	139
5.4 Histogram of the determined half-lives for all 11 detectors.	141
5.5 Example of ^{113}Cd spectrum and fits.	142
5.6 Combined spectrum DBD half-life fit for ^{116}Cd and ^{130}Te to g.s.	145
A.1 Detector numbering schemes.	151
A.2 SRIM simulation of alpha ranges in CZT.	152
A.3 Event rate of a selection of ^{214}Po decays.	152
B.1 Waterfall plot shows first eight hours of data.	163
B.2 Numerical approximation of previous spectra compared to new data.	164
B.3 Correlation plots used to investigate features in the data.	165
B.4 Waterfall of tagged events.	165
B.5 Event rate distribution of flagged events.	167

List of Tables

1.1	DBD isotopes in CZT detectors and their transitions.	11
2.1	Example of bias towards some bins with non-integer re-binning.	35
2.2	Data structures used to access the data with <code>sfaplot</code>	41
3.1	Data taken during research for this thesis.	47
3.2	Detector resolutions for datasets L1a-c.	53
3.3	Template for energy cuts.	85
3.4	Summary for datasets L1a-c.	88
4.1	Radioactive contamination measurements of detector and passivation materials.	91
4.2	Alpha emitters in the radon-220 chain.	101
4.3	Most likely beta spectrum end points and de-excitation γ 's from the ^{214}Bi decay.	104
4.4	Possible alpha emitters for the 3170 keV peak.	119
4.5	Possible alpha emitters for the 6370 keV peak.	122
4.6	Summary of internal contamination results of the CZT crystals.	131
5.1	Table of background and ^{113}Cd counts and systematic uncertainty.	135
5.2	Table of systematics	136
5.3	Measurements by other authors of spectral shape parameters for Equation (5.3).	138
5.4	Table of ^{113}Cd fit results.	140
5.5	Summary of fits for $\beta^- \beta^-$ decays.	146
5.6	Summary of fits for $\beta^+ \beta^+$ decays.	146
A.1	Uranium-238 Decay Chain.	153
A.2	Thorium-232 Decay Chain.	154
A.3	Q-values of naturally occurring alpha emitters.	155
A.4	Alpha energies from naturally occurring isotopes.	156
A.5	Alpha emitters in the Uranium-233 chain.	157
A.6	Physical properties of CdZnTe and CdTe [Kie05].	157

Introduction

This introduction is an attempt to explain the motivation for an experiment, COBRA, on which I have been working, in a form that can be understood by anyone with an interest in physics. I shall begin by asking: what are neutrinos and how do we know they exist? I will explain briefly why we believe they have mass and how the COBRA experiment intends to measure their mass. I shall conclude by providing an outline of the contents of this thesis.

The existence of neutrinos was postulated in the 1930s by Pauli [Wol30] when measurements of beta radiation (energetic electrons) released by nuclear decays were usually found to have less energy than expected. At this time, Albert Einstein [Ein05] had presented his famous equation relating energy with mass, $E = mc^2$, which told us that the difference in mass of two atoms, when one atom decays to another, is equivalent to the energy released to the product particles of the decay. In beta decay, the sum of the masses and kinetic energies of the product did not add up and showed that energy was somehow escaping the experimental setup.

Where was the energy going? A logical explanation is that the energy was escaping as radiation in the form of a very small particle that the experiment could not detect. Hence the neutrino, which means ‘little neutral one’, became the accepted name. Neutral—because already all the charge had been accounted for.

It was not until 1953 that the first observations of neutrino signals were published by Cowan and Reines [RC53], where the experiment involved surrounding a nuclear reactor of an electrical power station with 300 litres of liquid scintillator. The scintillator produces flashes of light whenever there is an interaction with a neutrino. The experiment took advantage of the huge neutrino flux (the rate of particles passing through a given area) coming from the reactor, and confirmed just how small the cross section of neutrinos are, that is, their probability to interact with matter. Indeed, it is often quoted that it would take the distance of several *light years* of the heavy metal, lead, to stop just one neutrino!

It was originally assumed by many scientists that the neutrino was massless. That is, it has no rest mass—just like a photon of light. Such a particle must travel at the speed of light to exist. But theories had been suggested indicating ways of testing whether they have a mass or not. This of course must be done indirectly because you can’t weigh them since they would pass through your scales and you can’t measure their speed because by observing them, you would stop them! By this time, it was already known that there are in fact more than one kind of neutrino. They come in three *flavours*, one for each member of a family of three particles of similar properties, namely the *electron*, *muon* and *tauon*. In addition to these three flavours of

neutrino, each neutrino was expected to have an anti-particle, just like for the electron there is a positron that is identical except for having an opposite charge. One theory predicts a further two kinds of *sterile* neutrino for each flavour that we can never expect to observe, giving a total number of 12.

The theories proving whether or not neutrinos have a mass rely on the fact that a particle with a finite mass can't travel at the speed of light, otherwise, as Einstein also demonstrated, they would require an infinite energy. Moreover, only particles travelling at less than the speed of light can undergo changes 'mid-flight'. It transpires that calculations predict that if neutrinos have mass, that one flavour of neutrino can turn into a neutrino of a different flavour. This is called neutrino oscillation, because the probability of observing this change oscillates with the distance from a neutrino source.

A number of large scale experiments were built that could test this oscillation theory. The Homestake experiment [CDD⁺⁹⁸] that used 615 metric tons of tetrachloroethylene (common dry-cleaning fluid) to capture electron neutrinos from the sun was the first to observe a lack of interactions. This deficit was confirmed by Super-Kamiokande [FHI⁺⁹⁸] using 50 000 tons of ultra-pure water contained in a tank surrounded by photomultipliers as their detector. In 2001, the Sudbury Neutrino Observatory (SNO) [AAA⁺⁰¹] provided solid confirmation that neutrinos oscillate, proving that neutrinos do have mass.

However exciting, the oscillation experiments will never be able to provide actual measurements of their masses. But they are able to provide likely upper and lower limits on their masses (mass eigenstates), being somewhere between 10–50 meV [Zub06] for the electron neutrino, which corresponds to between about 10 and 50 million times lighter than an electron, or about 10^{-38} kg. The upper boundary is particularly important as it sets a limit on how sensitive an experiment must be in order to make an actual mass measurement and provides a lot of motivation for projects where an actual measurement is only currently just out of reach.

This is where the COBRA experiment fits in. There are now a number of experiments trying to reach the 'fruit' of the first neutrino mass measurement, and each has a slightly or very different approach. The COBRA approach, which is the brain child of K. Zuber, uses an array of 1 cm^3 CdZnTe semi-conducting detectors to search for a predicted rare nuclear decay that could occur inside the detectors if neutrinos have mass. The decay is called neutrinoless double-beta decay and is introduced properly in Chapter 1. The important point is that the rate of this nuclear decay, if it is found to exist, can be used to calculate mass of the neutrino. Furthermore, it will also reveal much more about the nature of the neutrino. For example, it would throw out the idea that there are six sterile neutrinos that we can never detect, and demonstrate that the observed neutrinos and anti-neutrinos of the same flavour are in fact the same particle, leaving us with just three types of neutrino.

The burning question is, "so what"? Why should we be so interested in neutrinos, let alone their mass? To really appreciate their importance you have to appreciate science for what it is: trying to piece together the unknown. One could perceive some practical applications, such as spying on another country's nuclear programme, but the more fascinating applications are in our understanding of the universe. Until recently, neutrinos were thought to play a large role in

explaining the large amounts of *dark matter* that is unaccounted for in the universe. They still are believed to play an important role in big bang theories for the creation of the universe, such as why there is much more matter than anti-matter in the universe today.



The COBRA experiment is still in a research and development stage, but is already taking useful data. The experiment is located in a large underground laboratory (LNGS) underneath the Gran Sasso mountain in Italy, which is approximately 3000 metres high. The reason for it being underground is to protect it from cosmic radiation and radioactive isotopes that are produced by this radiation. This type of experiment is often called “low-level”, not so much because they are located underground, but because they must be located in ultra low radioactive conditions that are not achievable on the Earth’s surface.

At the same time as keeping up with my various tasks, described in the Preface, I developed many analysis tools to help deal with the increasing complexity of the experiment. This work is presented in Chapter 2, together with a description of the experimental apparatus. Chapter 3 then demonstrates some of the main problems encountered in the data and the methods by which they were dealt with.

In Chapter 4 a study of the radioactive backgrounds is presented. This includes a comparison to simulations, the identification of various peaks in the data and a method devised to use successive alpha decays to calculate that the internal uranium and thorium impurity of the detectors is more than three orders of magnitude below than previously measured. Finally in Chapter 5, a general physics analysis is performed, which includes an analysis of the beta spectrum of ^{113}Cd , and the best limits of neutrinoless double-beta decay ever acquired with CdZnTe.

Although this thesis is just a small step towards an actual measurement of the neutrino mass, already interesting physics has been investigated. The knowledge gained from the background analysis will enable better judgements to be made when building the next experimental set-up, which could ultimately be the first to make a definite measurement of neutrinoless double-beta decay.

Chapter 1

A Neutrinoless Double-Beta Decay Experiment

This chapter introduces the key ideas and equations behind neutrinoless double-beta decay and the fundamental requirements that any double-beta decay (DBD) experiment must achieve in order to observe the decays. The chapter thus motivates the design of the COBRA experiment and the fundamental ideas behind the design are outlined.

1.1 Theory

Neutrinoless DBD should be possible if a number of conditions are satisfied. Foremost, an atom must be able to decay through the process of two-neutrino DBD. Next, the neutrino is required to have a mass and to be a Majorana particle. These conditions are now described and the key equation relating the half-life of neutrinoless DBD to the effective neutrino mass is presented.

1.1.1 Two-neutrino double-beta decay

Double-beta decay, which is the simultaneous emission of two electrons from a nucleus, was first proposed in 1935 by Maria Goeppert-Mayer [GM35], who recognised the problem demonstrated in Figure 1.1 and presented calculations for the probability of the decay. The figure shows the mass on the y-axis (arbitrary scale) for different atoms with an even number of nucleons (protons or neutrons). On the x-axis, the proton number, Z , is given with the most stable atom at Z_0 . The atoms form two parabolas, which can only occur with an even number of nucleons. The upper parabola, marked with circles and labelled O-O, has odd numbers of neutrons and protons. The spots that form the lower parabola labelled E-E represent atoms with even numbers of protons and neutrons. This dependence of atomic mass on the proton-neutron ratio is represented by the last term of the Semi-Empirical Mass Formula.

The atom labelled (c) is the only fully stable atom in the figure because it has the lowest mass, and thus the highest binding energy, for the number of nucleons in the atom. Atom (b) is not

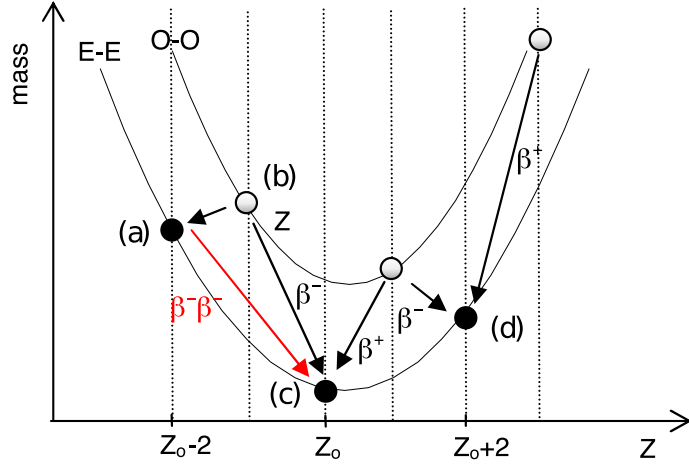


Figure 1.1: Atomic mass parabola for an even number of nucleons.

stable and would decay via beta radiation with a neutron turning into a proton, and an electron (beta radiation) and an anti-neutrino. Symbolically this can be written as, $n \rightarrow p + e^- + \bar{\nu}_e$. Atom (a), in order to decay to atom (c) must go through two beta decays. This can't occur in separate stages because by doing so would require extra energy to create the intermediate state (b). Thus (a) is a meta-stable state that can only decay with the suppressed process of the simultaneous emission of two beta particles. The process for two-neutrino (2ν) DBD is often symbolically written,

$$(Z, A) \rightarrow (Z + 2, A) + 2e^- + 2\bar{\nu}_e, \quad [2\nu\beta^-\beta^-] \quad (1.1)$$

where the brackets represent atoms of proton number Z and mass number A. This process—where two neutrinos are also released—has already been observed (*e.g.* [EMNV91]).

1.1.2 Neutrinoless double-beta decay

Neutrinoless ((0ν)) DBD was proposed by G. Racah [Rac37] in 1937 and is identical to the above process (Equation (1.1)) except that no neutrinos are emitted. It can be symbolically represented as,

$$(Z, A) \rightarrow (Z + 2, A) + 2e^-. \quad [0\nu\beta^-\beta^-] \quad (1.2)$$

Note that this would violate lepton number conservation by two units—a rule included in the *Standard Model* that requires the number of leptons (*e.g.* electrons and neutrinos) existing before and after an interaction to remain constant, with an anti-lepton counteracting the existence of a lepton. This rule however is based purely on observation and has no theoretical backing.

The suggestion of neutrinoless DBD came very soon after Ettore Majorana published a paper [Maj37] proposing that the neutrino, which is a fermion¹, could be its own anti-particle. This

¹A fermion is defined as a $1/2$ integer spin particle.

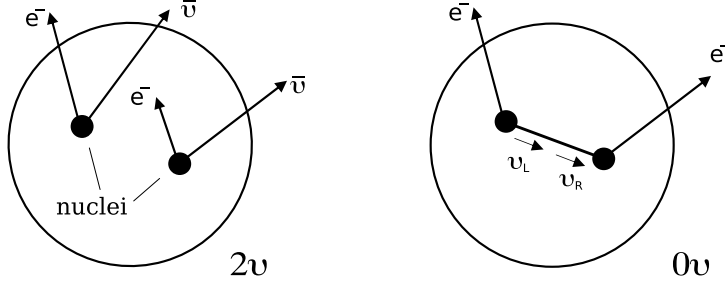


Figure 1.2: Neutrino accompanied (left) and neutrinoless (right) double-beta decay.

idea is in conflict with the neutrino being a Dirac particle like all other fermions in the Standard Model. As was mentioned in the introduction, if the neutrino is a Dirac particle this would lead to there being four different neutrino states for each flavour: ν_L , ν_R , $\bar{\nu}_L$, $\bar{\nu}_R$, where the bars indicate anti-particles and subscripts denote helicity, the direction of the neutrino's spin relative to its velocity. Only left-handed neutrinos and right-handed anti-neutrinos have ever been observed, because, as the theory states, the ν_R and $\bar{\nu}_L$ are sterile and cannot interact through the W^\pm or Z^0 bosons. A Majorana particle has only two states, ν_L and ν_R , where for example, ν_R neutrinos are created in β^- -decays and ν_L neutrinos are created in β^+ -decays, there is no distinction between a neutrino and anti-neutrino ($\nu_R \equiv \bar{\nu}_R$, $\nu_L \equiv \bar{\nu}_L$). Note that this also implies that neutrinos can't have a magnetic moment [KKS95].

Quantum mechanics tells us, that if neutrinos have mass, then a left-handed neutrino is a slight admixture of a right-handed neutrino and *vice versa*. The dependence on mass can be appreciated in consideration of this relativity thought experiment: Because a neutrino with finite mass must travel at less than the speed of light, then it follows that it is possible to be in a frame of reference where one is going faster than the neutrino. Thus a neutrino, which appears to have a spin in 'the same direction' as its velocity (ν_R) in one frame of reference, would appear to have a spin in the opposite direction to its velocity (ν_L) from another frame of reference, travelling faster than the neutrino. With the helicity of a massive neutrino not fixed, the admixture of the neutrino states provides the possibility that an 'anti-neutrino' (ν_L) is observed as a 'neutrino' (ν_R).

Neutrinoless DBD can then be thought of as the decay of a neutron within an atom, producing an electron and an anti-neutrino that is then absorbed as a neutrino by another neutron in the atom:

$$\begin{aligned} (Z, A) &\rightarrow (Z+1, A) + e^- + \bar{\nu}_e, \\ (Z+1, A) + \nu_e &\rightarrow (Z+2, A) + e^-. \end{aligned} \tag{1.3}$$

The only particles that escape the nucleus are two electrons. This is also demonstrated in Figure 1.2, where, on the left, two-neutrino DBD is shown and, on the right, neutrinoless DBD is illustrated.

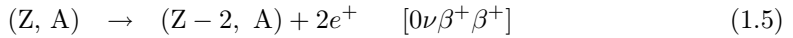
The extent of the mixing between the ν_L and ν_R states, and thus the probability of a neutrino

noless DBD to occur, is dependent on the neutrino mass, and the half-life of the decay [Zub06] has been shown to take the form,

$$\left(T_{1/2}^{0\nu}\right)^{-1} = G^{0\nu} |M^{0\nu}|^2 \left(\frac{\langle m_{\nu_e} \rangle}{m_e}\right)^2, \quad (1.4)$$

where m_e is the electron mass, $\langle m_{\nu_e} \rangle$ is the *effective* neutrino mass, $G^{0\nu}$ is the phase space—a number that can be precisely calculated. $|M^{0\nu}|$ is the nuclear matrix element of the transition and is less easy to calculate. Calculations must be performed separately for each DBD isotope studied, and depending on the theoretical model used, values may vary by factors of 2–4 [Pov, Vas].

There are 35 known isotopes that are expected to decay via neutrinoless DBD because they show the configuration necessary for the decay that was indicated in Figure 1.1. This includes isotopes that decay through other possible neutrinoless modes involving the emission of positrons (e^+) or through electron capture (EC),



These transitions are also of interest, particularly when the *signature* of the decay is striking. For the example, where two positrons are emitted, they annihilate with electrons and produce two pairs of 511 keV gammas in opposite directions. These decays are, however, typically more suppressed (have longer half-lives) so the most favourite isotopes to use for the search are usually those with the shortest half-life as they will provide a stronger signal to detect.

The decay rate of neutrinoless DBDs are proportional to Q^5 , with Q being the energy released in the decay. It is therefore an advantage to study isotopes with a large Q-value. Another important advantage of a high Q-value arises from the following:

Whereas the energy of the beta radiation from 2ν DBDs is distributed over a large energy range, for the energy released in the decays is shared between the beta radiation and the neutrinos, in the case of 0ν DBDs all of the energy goes to the beta radiation. This is demonstrated in Figure 1.3, where the signature of 0ν DBDs can be seen as a peak located at the Q-value of the decay. Because there is typically more background radiation with lower energies (this is observed throughout this thesis) a 0ν DBD signal with a larger energy will be easier to observe.

The scale, as well as the relative scales of the distributions in Figure 1.3, are arbitrary. The actual number of neutrinoless decays is much lower than the two neutrino decays. This provides a potential problem because 2ν decays are intrinsic to the same isotopes that can decay through 0ν DBD. The tail (the right side) of the 2ν DBD spectrum continues up to the Q-value (minus the neutrino mass) and so there is a small possibility that 2ν decays can be mistaken for 0ν decays. The only way to minimise this background is to use detectors with exceptionally good energy resolution. The width of the 0ν DBD peak in Figure 1.3 represents a distortion of the true signal due to the resolution of a detector.

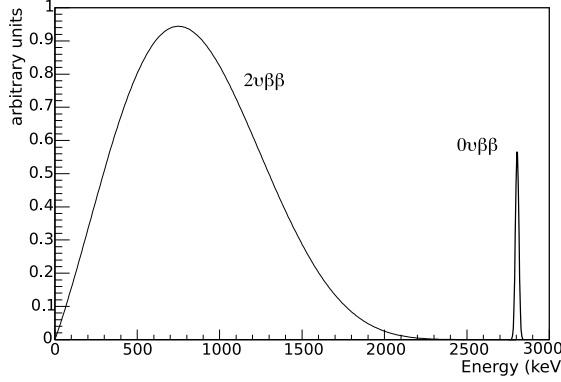


Figure 1.3: Distribution of beta radiation energy for 2ν and 0ν DBDs. The diagram is a schematic to show how the total beta energies form a continuous spectrum for 2ν decays, and a peak at the Q-value of the decay when no neutrinos are emitted.

1.2 General Considerations

This section looks at the minimum physical requirements of a neutrinoless DBD experiment in order to make a successful observation. The difficulties that experiments face arise from the exceptionally long half-lives of the decays. Oscillation experiments are able to provide measurements of the difference of neutrino flavour masses-squared, $\Delta m^2 = m_i^2 - m_j^2$, where m_i and m_j are the masses of two neutrino mass eigenstates [Zub06]. Depending on the order of neutrino flavour masses (see neutrino mass hierarchy, *e.g.* [PP04, Jul05]) oscillation results require the electron neutrino mass to be either < 5 meV, between 10 meV and 50 meV, or > 50 meV. With the likely scenario that predicts an electron neutrino mass of the order of 50 meV, half-lives in the region of 10^{26} – 10^{27} can be expected by applying Equation (1.4) [Zub06]. Even compared to the age of the universe ($\sim 10^{10}$ years) this is a long time.

A ‘rule of thumb’ is that a good handful of matter contains approximately Avogadro’s number ($\sim 10^{24}$) of atoms, so with just a thousand handfuls of DBD source atoms you already have one atom for each year of the atoms’ half-lives. It is then likely that one of these atoms will decay within a year. If we take as an example an average isotope containing ~ 100 nucleons, then this implies we require about 100 kg of source atoms to observe one decay per year. It is quantities of this order that all DBD experiments must satisfy, regardless of their approach.

The precise number can be easily calculated for a specific isotope with

$$T_{1/2}^{0\nu} = \ln 2 \cdot \frac{aN_AM}{M_{CZT}N_{\beta\beta}} \cdot t, \quad (1.8)$$

where M is the used mass, a is the fraction (or abundance) of the isotopes of interest², M_{CZT} is the molar mass of CZT, $N_{\beta\beta}$ is the number of observed decays, N_A is Avogadro’s number and t is the measuring time. This equation can of course also be used in the way it is presented, for calculating the half-life of DBDs from the number of observed decays, $N_{\beta\beta}$.

Although it was demonstrated that the quantity of isotopes required are realistically achievable

²It is unlikely that a pure sample of the isotope of interest is possible to study.

in terms of mass, being able to identify the decays is altogether different. The main problem arises from that within this quantity of material containing the isotopes of interest, contamination of other radioactive isotopes is unavoidable. Some radiation from these isotopes are bound to imitate neutrinoless DBD signals. Furthermore, it is also possible that radiation can enter from outside an experiment. Consequently, DBD experiments are in a constant battle to try to reduce the background of false events. When the number of background events overwhelm the signal, instead of applying Equation (1.8), an upper limit on the half-life must be made. There are many ways of calculating this, but it essentially depends on the experimental quantities according to [Zub06]

$$T_{1/2}^{0\nu} \propto a\epsilon \sqrt{\frac{M t}{\Delta E B}}, \quad (1.9)$$

where the parameters a , M , and t are the same as above, and ϵ is the detection efficiency, ΔE is the resolution of the detector and B is the background index, which is the rate of background events per unit of energy.

The challenge is thus three-fold. An experiment needs to,

1. Increase the signal strength.
2. Reduce the background.
3. Discriminate between background and signal events.

Increasing the signal strength involves using as many DBD source atoms as possible, as has been discussed. It is therefore an advantage to choose an isotope with a large *natural abundance*, which is the naturally occurring fraction of the isotope within deposits of the element in nature. It is possible to enrich the levels of a particular isotope but this is currently an extremely expensive process. Reducing the background involves careful material selection and effective shielding from outside radiation sources. Discriminating between signal and background events can be achieved in various ways that can be unique for different experiments, however, good energy resolution is critical to all experiment techniques.

1.3 Experimental Methods

The number of double-beta decay experiments is too large to summarise here. However, a comparison to a few of the most important past and present experiments and their approaches is presented.

1.3.1 Germanium detector experiments

Currently the world's best limit on a neutrinoless DBD half-life is held by germanium semiconductor detectors. Namely, by the Heidelberg-Moscow experiment (HM), closely followed by the International Germanium Experiment (IGEX). Germanium has a DBD isotope, ^{76}Ge , with a Q-value of 2039 keV. The advantages of using these detectors are similar to that of CZT (see

Section 1.4), in that due to their production process they are highly radioactively clean and they have exceptionally good energy resolution (about 0.2% FWHM at the Q-value [ACK⁺07]).

One disadvantage of germanium detectors is that they have a very small (semiconductor) band gap so that they must be operated at liquid nitrogen temperatures (77 K or -196°C). Although experimental setups and the background level in both experiments were similar, IGEX reported that their dominant background was from cosmogenics activation³, whereas HM concluded that radioactive uranium daughter radionuclides on the copper surfaces of the containers that encapsulated the detectors was their dominant background source.

Initially, neither experiment reported to have observed evidence of neutrinoless DBD, so based on their backgrounds⁴, half-lives ($T_{1/2}^{0\nu}$) of $>1.9 \times 10^{25}$ yr and $>1.6 \times 10^{25}$ yr for HM and IGEX [ABC⁺00] were calculated, which corresponds to a neutrino mass of $\lesssim 0.35$ eV. However, a subgroup of the HM collaboration later claimed that they had identified a peak in the signal region. This caused a lot of controversy because it suggested a neutrino mass of between 0.2–0.6 eV, which is larger than most people expected and would imply the neutrino masses of the different flavours are effectively the same (degenerate). Furthermore, many researchers were unhappy with the way the group had presented their results and found them less than convincing. Particularly, it was felt that there was no satisfactory explanation of neighbouring peaks in the data.

Using pulse shape analysis, for example, by looking at how fast signals from the detectors took to reach maximum amplitude, discrimination between single and multiple site energy depositions within a detector could be made, and was used to reject many events that were less likely produced by DBDs. A sum energy spectrum of the signal region after the pulse shape selection was made is given in Figure 1.4 and shows a convincing peak in the signal region. This replaces an original plot in [KK03], which was less convincing.

There are two main experiments using germanium that intend to verify or disprove the above claim, namely GERDA and Majorana⁵. Majorana is following the traditional approach of shielding their detectors against external radiation with copper and lead, and GERDA⁶ will operate their detectors in a bath of liquid argon that acts both to keep the detectors cold and as a shield. Both experiments ultimately hope to measure half-lives of up to some 10^{27} years. However, even if both experiments confirm HM’s observation, at least one more DBD experiment would be required to observe a DBD signal at a different Q-value to help eliminate the possibility that the observed peak is not an unknown background.

1.3.2 Other DBD experimental approaches

The experiment CUORICINO⁷ holds the next longest half-life measurement on ^{130}Te ($Q = 3530$ keV) at $T_{1/2}^{0\nu} > 2 \times 10^{24}$ yr [AAAI⁺05]. CUORICINO uses an array of TeO_2 crystals cooled to 8 mK and detects slight increases in temperature as a result of energy depositions within a crystal due to an internal DBD decay. Their FWHM energy resolution is an impressive 0.3% at

³See page 16 for a description of cosmogenics activation.

⁴The HM background in the signal region was 0.12 counts/kg/keV/yr [Zub06].

⁵<http://majorana.npl.washington.edu/>

⁶<http://www.mpi-hd.mpg.de/gerda>

⁷<http://crio.mib.infn.it/wig/Cuoricinopage>

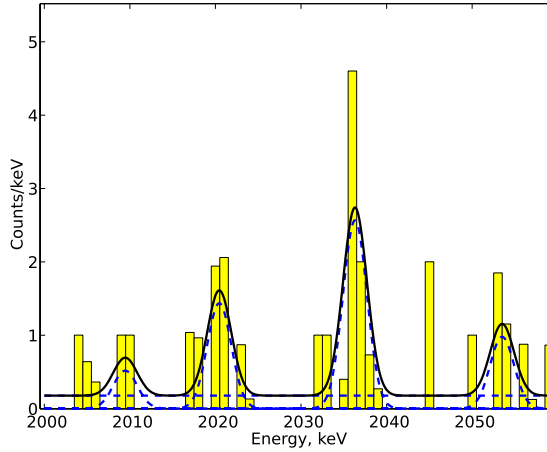


Figure 1.4: Sum spectrum (for detectors 2, 3, 4 and 5 between 1995–2003) of HM data after pulse shape discrimination has been made. A peak in the signal region of 2039 keV is the most prominent. The left-most and right-most peaks are claimed to be gammas from the decay of ^{214}Bi but the peak at 2030 keV is not identified. Taken from [KK05].

the Q-value. Their current dominant background is from surface contamination of their detectors [EV02], which they hope to control in the ultimate proposal, CUORE, which would involve scaling up CUORICINO from 41 kg to \sim 750 kg with 988 detectors, and be competitive with the germanium experiments.

NEMO 3⁸ is an experiment that uses techniques perfected in high energy particle physics experiments. It consists of a large number of thin foils containing various DBD sources arranged in a cylindrical form of 2.5 m high and 3.1 m diameter. Energetic particles are tracked as they pass through and ionise gas between the foils and the type of particle can be identified by their trajectory within a 25 G magnetic field. Finally, the energy of the particles are recorded when they hit plastic scintillators, which emit flashes of light that are observed with photomultiplier tubes. In short, it is a very complex set-up that enables DBD events to be identified by their spiralling tracks. A major drawback however is that the energy measurements have only 14–18% resolution (FWHM at 1 MeV) [SR08] which limits their ability to discriminate between 0ν and 2ν DBDs. Currently their dominant backgrounds are unwanted radionuclides on the foils containing the DBD sources, where, for example, single beta decays to an excited state can mimic DBDs if the gamma passes some of its energy to a second electron through Compton scattering, but itself escapes detection [AAB⁺05]. The collaboration is currently performing research towards a new proposal, SuperNEMO, which intends to deal with both the energy resolution and radioactive background issues.

Other planned experiments include EXO, which will use large quantities of ^{136}Xe as its DBD source, MOON, which will study ^{100}Mo , and CAMEO is proposing to use $^{116}\text{CdWO}_4$ scintillating crystals within the BOREXINO neutrino detector [EV02].

⁸<http://nemo.in2p3.fr>

1.3.3 Non DBD approaches

It is worth mentioning a couple of other approaches to measure the mass of neutrinos.

1.3.3.1 Cosmological

Although it is now believed that neutrinos contribute less than 5% of all cosmic matter [Teg05], this is already enough to influence the pull of gravity in the universe. Where the gravitational pull of dark matter has for a long time been known to be responsible for drawing galaxies together to form clusters, dark energy, which consists of 70% of cosmic matter and includes neutrinos, travels at too great velocities to cluster on small scales. This results in a retarding effect on the rate of clustering. Cosmologists are able, based on estimates of the number of neutrinos in the universe, to calculate the mass of the sum of the different types of neutrino. There are a number of recent sub-eV estimates for the neutrino mass, with [SSM06] reporting an upper limit on the sum of the neutrino masses at $< 0.17 \text{ eV}$ (95% C.L.). The author, [Teg05], discusses ways of improving the cosmological limits to the 30 meV scale. However, it should be noted that several assumptions [EL06] are involved in deriving these limits.

1.3.3.2 Single beta decay endpoint

Another, and perhaps most direct method to measure the neutrino mass is to simply look at the end point of a single beta-emission spectrum. A typical radionuclide to study is tritium (${}^3\text{H}$) largely because of its low Q-value of 18.6 keV. Because energy must go towards creating a massive neutrino, the end of the beta spectrum must fall short of the Q-value. This is demonstrated in Figure 1.5, where the dotted line represents a beta spectrum with a zero neutrino mass and the solid line represents a beta spectrum for massive neutrinos. In this example a neutrino mass of 1 eV is used, so the solid line falls short by 1 eV, where no energy goes to the kinetic energy of the neutrinos.

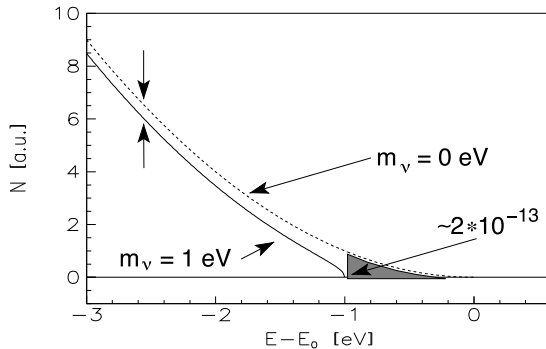


Figure 1.5: A sketch of the single beta spectrum near the end point. The dotted line is the beta spectrum for massless neutrinos and the solid line is the beta spectrum for a neutrino with a 1 eV mass. The fraction 2×10^{-13} corresponds to the fraction of the shaded area compared to the total number of beta decays. Taken from [Bon06].

For a neutrino mass of 50 meV a fractional difference in energy compared to the end point of the beta spectrum is of the order of 10^{-6} . This is too small for modern science to discriminate between. Such experiments rely on that the end of the beta spectrum has been calculated to be slightly distorted, as shown in Figure 1.5, and they attempt to measure this distortion.

KATRIN is the largest of such experiments to investigate the tritium end point and aims to be able to reach levels of 0.2 eV [Bon06]. This is below the neutrino mass claim of the Heidelberg-Moscow experiment. There are no plans to attempt to build a more sensitive tritium experiment than KATRIN.

1.4 The COBRA Concept

COBRA (Cadmium-telluride **0** neutrino double-**Beta** Research Apparatus) is the brain-child of Kai Zuber and involves using an array of Cadmium-Zinc-Telluride (CZT) semi-conductor detectors. All three elements of the detectors contain DBD isotopes, although zinc is only included in small quantities ($\sim 5\%$) as it is required to improve the performance of the detectors. Like germanium DBD experiments, COBRA has the advantage that the CZT detectors act both as the source and the detector, which improves the efficiency of detecting the full Q-value of internal DBD decays. Because CZT detectors are produced in a similar way to germanium detectors they are also expected to be very *clean* in terms of radioactive impurities. Unlike germanium, however, CZT detectors operate best at room temperature, which is a technical advantage in that no dirty cryostats need to be used and scaling up a prototype experiment is made much easier. A drawing of the current prototype (the 64-array) is shown in Figure 1.6 and demonstrates how the detectors (cubes) can be arranged in arrays in special holders and then stacked on top of each other.

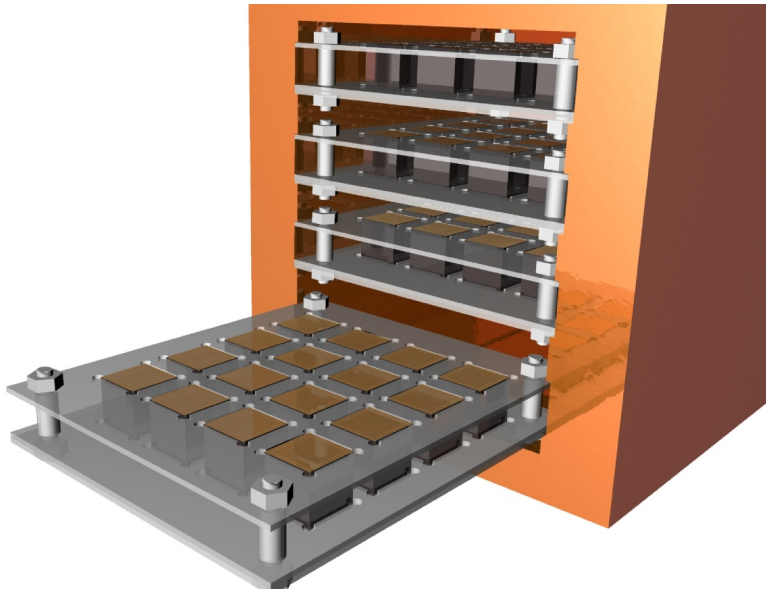


Figure 1.6: A drawing of the 64-array prototype. Taken from [Mue07].

The isotopes in CZT detectors that decay via double-beta decay are shown in Table 1.1. The favourite isotopes to search for are ^{116}Cd and ^{130}Te because of their high Q-values of 2805 keV and 2529 keV and reasonable natural abundances of 7.5% and 33.8% respectively. The Q-value of ^{116}Cd is conveniently above the most energetic gamma (2614 keV) of the naturally occurring uranium and thorium radioactive decay chains.

Transition	Decay mode	Q-value (keV)	nat. ab. (%)
$^{64}_{30}\text{Zn} \rightarrow ^{64}_{28}\text{Ni}$	β^+ -EC, EC-EC	1096	48.6
$^{70}_{30}\text{Zn} \rightarrow ^{70}_{32}\text{Ge}$	$\beta^- \beta^-$	1001	0.6
$^{106}_{48}\text{Cd} \rightarrow ^{106}_{46}\text{Pd}$	$\beta^+ \beta^+, \beta^+$ -EC, EC-EC	2771	1.25
$^{108}_{48}\text{Cd} \rightarrow ^{108}_{46}\text{Pd}$	EC-EC	231	0.89
$^{114}_{48}\text{Cd} \rightarrow ^{114}_{50}\text{Sn}$	$\beta^- \beta^-$	534	28.72
$^{116}_{48}\text{Cd} \rightarrow ^{116}_{50}\text{Sn}$	$\beta^- \beta^-$	2805	7.47
$^{120}_{52}\text{Te} \rightarrow ^{120}_{50}\text{Sn}$	β^+ -EC, EC-EC	1722	0.096
$^{128}_{52}\text{Te} \rightarrow ^{116}_{54}\text{Xe}$	$\beta^- \beta^-$	868	31.69
$^{130}_{52}\text{Te} \rightarrow ^{130}_{54}\text{Xe}$	$\beta^- \beta^-$	2529	33.80

Table 1.1: DBD isotopes in CZT detectors and their transitions [KMZ03]. Decay modes are also shown, which can involve the emission of two electrons ($\beta^- \beta^-$), two positrons ($\beta^+ \beta^+$), electron capture (EC) or a combination of positron and electron capture. The energy released in the decays (Q-value) and natural abundance (nat. ab.) of the isotopes are also shown.

Typical sizes for CZT detectors are just $\sim 1\text{ cm}^3$ and weigh about 6 g. To achieve the required mass an array of 64 000 detectors is envisaged. The size of the detectors is limited by the current technology in growing the crystals (or *boules*) from which the detectors are cut, where fractures that occur in the boules must be avoided. However, COBRA uses the small size of the detectors to its advantage by being more sensitive to internal beta radiation than gamma radiation and being able to further suppress the gamma background by rejecting multiple *coincidences*. This is explained now in slightly more detail.

Although simulations [Ree04, Kie05] have shown that the efficiency of observing the full energy of the electrons in a 1 cm^3 detector from the 0ν DBDs of ^{130}Te and ^{116}Cd is reduced to 65% and 61% respectively, this must be compared with the efficiency of observing a similar energy gamma. The probability of observing the full energy of a 2614 keV gamma inside a detector is just $\sim 0.4\%$. This is illustrated in Figure 1.7 which shows how the actual number of events (blue) is reduced in size due to the small dimensions of the detectors, but overall, the relative size of the signal peak to background peak (signal to background ratio) can be seen to increase (magenta). Furthermore, any gammas that escape a detector, due to their large range, are likely to pass through neighbouring detectors in the array and also deposit some energy. This is called a *coincidence*. Such events⁹ can be discarded because multiple depositions that occur at the same time are most likely to be produced by a single nuclear decay that involves gamma radiation.

⁹The use of the word *event* in this thesis is used to represent any signal recorded by the experiment. The most

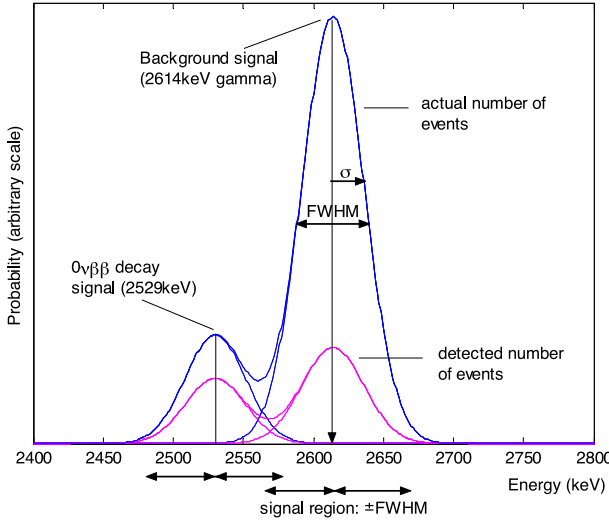


Figure 1.7: Drawing demonstrates a better signal to background is observed for small detectors [Ree04]. The blue curves represent the true number of background and signal events and the magenta curves represent the detected number of events at their full energy. The background peak is reduced by a larger fraction than the signal peak due to the large range of the gamma radiation and small detector size.

The overlapping peaks in Figure 1.7 also demonstrate how the resolution of a detector is important for distinguishing between signal and background events. CZT detectors have good resolutions of down to 2% FWHM¹⁰ at 662 keV [LAL03] and even better at larger energies. Still finer resolutions are expected with ongoing research, with already techniques claiming to improve resolutions to less than 1% [RS07]. CZT detectors are commercially available and are used in medical and industrial imaging, as well as space science and high energy particle physics, and are used for their exceptional efficiency at detecting x-rays [Lee04]. Due to the detector's wide range of applications, despite their current high price tag with costs varying between \$500–\$10 000 [Zub08] according to their quality, their price is expected to drop.

A summary of the advantages of using CZT detectors for DBD searches are,

- ▷ High DBD Q-values.
- ▷ Room temperature detectors.
- ▷ Coincidences between detectors help reduce background.
- ▷ Good energy resolution.
- ▷ Radioactively clean production technique.
- ▷ Commercially available.

important information recorded in an event is the time, energy and location(s)—that is, in which detector(s) the event was observed.

¹⁰Resolutions are typically quoted by the full-width-half-maximum (FWHM) of a Gaussian function which is fitted to a peak. The FWHM is related to the standard deviation σ of a Gaussian by, $\text{FWHM} \equiv 2\sqrt{2\ln 2} \cdot \sigma \approx 2.35 \sigma$.

Some disadvantages are the current price of detectors and the complexity of the electronics and cabling close to the detectors, which must also be radioactively clean. A more detailed discussion on some technical issues is made with a description of the apparatus for the current prototype in Chapter 2.

1.5 Experimental Backgrounds

Backgrounds are any events that produce similar signals to neutrinoless DBDs and so should be limited as much as possible. They form two broad categories, namely electronic and radiative. Electronic backgrounds are an engineering problem and are discussed in detail in Chapter 3, where investigations into rejecting these backgrounds are made. This section summarises the most prominent radiation backgrounds to the COBRA experiment and their origins. Motivation is thus made for shielding the apparatus, which involves locating the experiment deep underground and surrounding the detectors with lead and copper, as well as selecting only materials that are less likely to have been exposed to strong sources of radiation.

1.5.1 Radiation type and their impact

The current most prominent backgrounds to the COBRA experiment are alpha, beta and gamma radiation, with greater protection against neutrons and muons expected to be required in the future.

- Alphas Alpha radiation is fast-moving ${}^4\text{He}$ ions that are emitted by heavy unstable isotopes and have energies typically between 2–9 MeV. Alphas lose their energy very quickly when they pass through solids, mainly through the process of ionization. Their penetration depths are within a few microns in a solid up to several cm in air—depending on their energy. Thus the full energy of alphas would be seen in the case of an alpha source inside a CZT detector and external sources are easy to shield against. Alphas are released with well defined energies, but the precise energies they receive are usually slightly less than the Q-value of the decay as the atom that is created is often left in an excited state. The atom immediately de-excites, producing x-rays of \sim 100 keV that can be stopped by a few cm of copper. Occasionally, alphas can interact with the nucleus of a light atom, with the nucleons of the alpha particle being absorbed and a neutron being rejected. These are known as (α, n) interactions and can lead to a significant neutron source if the number of alpha decays near the apparatus is large. In addition, isotopes that decay via alpha emission are also subject to spontaneous fission, and also a source of neutrons [Heu95]. Neutrons are difficult to shield against and have a large impact (see below).
- Betas Beta radiation is energetic electrons (or positrons) that are released by a nucleus as β^- radiation when a neutron decays into a proton, and β^+ radiation when a proton turns into a neutron. As mentioned previously, the Q-value of the decay is shared with neutrinos so the beta energies can vary from nothing to several MeV. Betas also lose

their energy by ionising the material they pass through and have ranges of a few mm in a metal. In addition to sharing their energy with neutrinos, the nucleus is also often left in an excited state and releases its energy in the form of high-energy gammas. In the case of β^+ radiation, when the positrons have lost their kinetic energy they annihilate with an electron and produce two 511 keV gammas in opposite directions.

- Gammas Gamma radiation, released from the excited nucleus following beta decays can have energies up to 11 MeV [Lun], although most naturally occurring isotopes produce gammas energies with less than 2.6 MeV. Several cm of lead are required to stop most gammas. Attenuation of the gammas usually occurs before they are finally absorbed by a material, and involves many interactions via the *photoelectric* and *Compton* effects and through *pair production*. See [Kno79a] or [Leo87] for a thorough description of these processes.
- Muons Energies of the above particles as well as other heavier particles (mainly protons) that hit the Earth from outer space (see *cosmic radiation* in the next sub-section) have been recorded in excess of 10^{20} eV [Sim83]. Most of these particles decay or lose their energy before they reach the Earth's surface. However, muons are particularly penetrating and are created in the Earth's atmosphere mostly as the decay products of charged mesons [FP00] that in turn are created through the bombardment of primary cosmic radiation. These energetic muons lose their energy at roughly a constant rate of ~ 2 MeV per g/cm². With the density of CZT detectors at 5.9 g/cm³, such a muon would deposit about 12 MeV in 1 cm of CZT. No effective shield can be built to protect the experiment from these particles and it is for this reason that the COBRA experiment must be located deep underground. Even so, the muon flux, which is ~ 1 cm⁻² min⁻¹ at sea level is reduced to a still observable ~ 0.96 m⁻² hour⁻¹ [Mue01] at the LNGS underground facility by 3600 m.w.e.¹¹ of rock above the laboratory. For this reason an *active* shield must be installed to help reject potential collisions with the detectors from the analysis.
- Neutrons ^{113}Cd , which makes up about 5.5% of currently used CZT detectors, has a very large cross-section for thermal neutrons of ~ 21 kbarn [Mun03]. The reaction, $^{113}\text{Cd}(n,\gamma)^{114}\text{Cd}$, can produce gammas with energies up to 9 MeV [Mue01], and so to avoid partial energy depositions that can fall in the DBD signal regions any exposure to neutrons must be avoided. One source of neutrons has already been identified above, as from either spontaneous fission of a heavy alpha emitting isotope or through an interaction with alpha particles. Additionally, energetic cosmic radiation, namely muons underground, can sometimes disintegrate nucleons that they hit—a process called spallation. This also leads to a source of neutrons. Thermal neutrons behave like a gas [Rot96] because they bounce mostly elastically off atomic nuclei. Since they do not interact with electrons through the Coulomb force they are able to find their way through most materials from where they were created, *e.g.* in the surrounding rock, and possibly pass

¹¹Meters water equivalent and is the equivalent depth of water that would offer the same protection. Rock being denser offers greater protection.

by a CZT detector that will likely capture it. Thus surrounding the experiment in a material like ^{113}Cd that is also effective at capturing neutrons is essential. ^{10}B is another isotope with a large cross-section ($\sim 4\text{ kbarn}$) and is used in the experiment by boxing the apparatus in borated polyethylene. The above cross-sections are only valid for thermal neutrons of $\sim 2.2\text{ km/s}$ ($\sim 25\text{ meV}$). The cross sections of fast neutrons are much reduced and so these must be slowed down before the boron is an effective shield. This was investigated in a Diploma thesis [Oeh04] for the COBRA experiment, in which it is shown that the current shielding reduces the neutron background by more than five orders of magnitude and a further two orders of magnitude if the neutrons are first slowed down with paraffin wax bricks. The neutron flux in the near by LNGS experimental Hall A (Figure 2.1b) has been measured to be roughly 10^{-6} cm/s for thermal neutrons and less than $3 \times 10^{-6}\text{ cm/s}$ for neutrons with greater than 50 meV [BBd⁺⁸⁹], and if we assume a 100% capture efficiency of a CZT detector and no shielding the rate corresponds to a total background of $\sim 50\text{ counts/kg/day}$. This alone (even without shielding) is not great enough to be observable above other backgrounds so for the analysis in this thesis the neutron background can be ignored.

1.5.2 Radiation sources

This section summarises the isotopes that are expected to be observable by the COBRA experiment and categorises them by their origin.

Primordial Radioactive isotopes that have been around since the Earth was formed are those with very long half-lives. The most abundant of these, and hence most likely to contaminate the experiment, are ^{238}U (uranium), ^{232}Th (thorium) and ^{40}K (potassium) [Heu95], which have half-lives of $4.5 \times 10^9\text{ years}$, $1.4 \times 10^{10}\text{ years}$ and $1.3 \times 10^9\text{ years}$ respectively. ^{87}Rb (rubidium) is also naturally abundant but with a Q-value of just 280 keV should not affect the DBD searches. ^{238}U and ^{232}Th on the other hand both decay via alpha radiation with energies greater than 4 MeV , and most importantly both decay via a chain of unstable isotopes releasing high energy α , β , and γ radiation. The most prominent of the isotopes in the chains are given in Tables A.1 and A.2 on pages 153 and 154. Half-lives of the listed daughter radionuclides vary from $0.3\text{ }\mu\text{s}$ to $2 \times 10^5\text{ yr}$. Because of this huge range, and because the isotopes have different chemical properties, the number of observable isotopes in the chains can become out of equilibrium. For example, more decays might be observed from a mother radionuclide in a sample than from the daughter nuclides. A good example of this is with ^{222}Rn (radon) that is part of the ^{238}U chain. Being a noble gas it is able to leach out of a material (such as in rock or concrete) it was created in and exist in the air for a few days before decaying to the metalloid ^{218}Po (polonium) through the emission of a 5.5 MeV alpha (see Section 4.1.2 for more detail). Radon is thus a common problem for low background experiments, because not only can it accumulate in the air surrounding the detectors, the daughter nuclides that are created are also radioactive and can attach themselves to detector surfaces increasing the level of radioactivity close to the detectors—even

after the radon source has been removed.

Anthropogenic Man-made radioactivity, namely fallout from nuclear power stations and nuclear weapons testing, although some exist naturally, are slowly on the increase. Still, current levels are usually well below the activity of the natural sources mentioned above, with 1 Bq/m³ activity of ⁸⁵Kr in the air in the Western hemisphere [Heu95] compared to recent measurements of \sim 40 Bq/m³ of ²²²Rn in the air at COBRA's current location. Accidents have occurred, such as the Chernobyl disaster in 1986 where large amounts of ¹³⁷Cs was released into the atmosphere, and radioactive sources sometimes contaminate recycled materials [Lub98]. The abundance of isotopes such as ³H, ¹⁴C and ⁹⁰Sr have also increased because of human activity. However, all these isotopes have low Q-values and can not affect the main signal regions. ²³⁵U, which is used as a fuel for nuclear power and in weapons has a similar chain of daughter nuclides as the ²³⁸U and ²³²Th chains, and the signature of the high energy alphas and gammas should be easily distinguishable to the COBRA experiment if contamination exists.

Cosmogenic Radiation from cosmic rays has already been mentioned in connection with why it is necessary to place the experiment deep underground. Radiation entering the Earth's atmosphere consists mainly of protons (90%), with alpha particles and then other heavier particles the runners up. All of these particles bombard the upper atmosphere and the end product of particles is a reduced flux at sea level consisting mainly of muons, neutrons, electrons, protons and pions with the following approximate relative proportions 1420:480:340:13:1 respectively [Heu95]. Go deep underground and this ratio changes again with muons and neutrons being the only remaining significant backgrounds.

The main impact of cosmic radiation on low-level experiments occurs when materials used in the experiments have been exposed to this radiation on the surface. The bombardment of these particles on matter leads to interactions such as (n, γ) or the complete disintegration of nuclei, and produces radionuclides that can exist long after the materials have been taken underground. Such radioactive materials created by cosmic radiation are known as cosmogenics. These are a particular problem if they are created inside the CZT detectors themselves. Predicting which radionuclides can be created is a complicated and ongoing task. Some research has been done to calculate the cross-sections of radionuclide production in CdTe through proton induced reactions [PCP⁺96], which is useful for space applications of the detectors where proton radiation is highest. Their approach involved firing 1.7 GeV protons at their sample and then identifying the created radionuclides from their gamma energies with a germanium detector. Cross-sections of neutrons and protons at this energy are likely to be similar and so can be used as a guide as to the isotopes we might expect from interactions from similar energy neutrons on the Earth's surface. The only radionuclides identified by [PCP⁺96] that have half-lives greater than 90 days are ^{110m}Ag (250 d), ⁸⁸Y (107 d), ^{121m}Te (119 d), and ^{123m}Te (154 d), where the half-lives are given in brackets. The first two isotopes have Q-values of 2892 keV and 3623 keV respectively, which are greater

than main DBD signal regions.

- Intrinsic Double-beta decay involving the emission of two neutrinos are background events that cannot be avoided because they are produced by the same isotopes that can decay via neutrinoless DBD. The two neutrino beta spectrum, which was sketched in Figure 1.3, effectively slightly overlaps the signal region due to the finite energy resolution of the detectors. The approximate fraction, F , of 2ν events observed in the signal region has been calculated to be

$$F \approx \frac{7Q\delta^6}{m_e}, \quad \delta = \frac{\Delta E}{Q}, \quad (1.10)$$

where Q is the Q-value of the decay, m_e is the mass of the electron and ΔE is the FWHM resolution. The number 7 depends on the FWHM, which is $\sim 5\%$ for the 2805 keV DBD signal region of ^{116}Cd . It is about 5 for 10% resolution and 8.5 for 1% resolution [EV02]. The fraction of 2ν events compared to 0ν event can thus be estimated by multiplying Equation 1.10 by the ratio of the decay rates, $\Gamma^{2\nu}/\Gamma^{0\nu} \equiv T_{1/2}^{0\nu}/T_{1/2}^{2\nu}$. For a 1% resolution and the half-life of the 2ν DBD of ^{116}Cd measured at 2.7×10^{19} yr [BBD⁺07], using a value of 10^{27} yr for the half-life of 0ν DBD, results in a background to signal ratio of just $\sim 10^{-3}$. This number increases dramatically for larger resolutions due to the power of 6 in Equation 1.10.

The 2ν DBD signal of ^{116}Cd also overlaps other 0ν DBD isotopes in CZT that have lower Q-values. For example, ^{130}Te has a Q-value of 2529 keV and a half-life of the 0ν DBD is probably greater than 10^{26} years. In Figure 1.8 we compare the current best limit on this decay, which is 3.0×10^{24} years [AAA08], to the 2ν DBD decay rate of ^{116}Cd . We assume a resolution of 2% FWHM and model the ^{116}Cd beta spectral shape, $F(E)$, according to the equation [TY95]

$$F(E) = (E^4 + 10E^3 + 40E^2 + 60E + 30) \times E(Q - E)^5, \quad (1.11)$$

where Q is the Q-value of the decay. Already the 2ν DBD decay rate can be seen to dominate the signal region of ^{130}Te . Thus if the ^{130}Te signal is two orders of magnitude lower it will be effectively impossible to measure. Consequently, for isotopes with smaller Q-values than 2805 keV, searches to excited states, electron capture and β^+ emission, which have more unique signatures, will be of particular interest to the COBRA experiment.

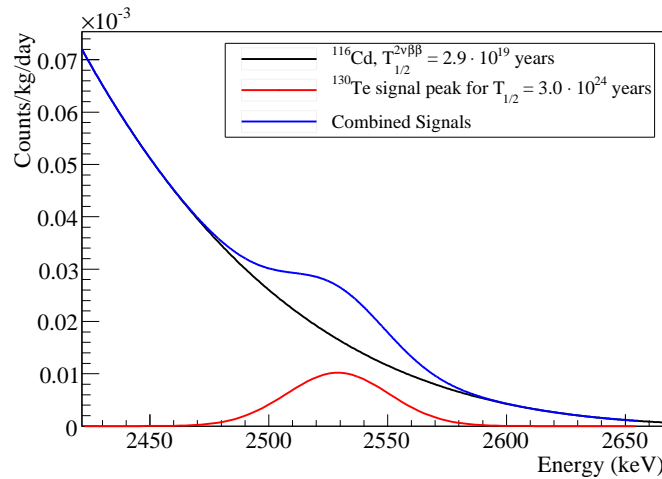


Figure 1.8: A comparison of the two neutrino DBD decay rate of ^{116}Cd to the current best limit on the neutrinoless DBD rate of ^{130}Te . The figure is generated with a ROOT macro written by collaborator T. Köttig and assumes a FWHM resolution of 2%.

Chapter 2

The COBRA Setup

Details of the COBRA apparatus are now presented, followed by a description of the data and the analysis tools that were developed for this thesis. The experiment is located in Italy, 130 km North-East of Rome in Gran Sasso National Laboratory (Laboratori Nazionali del Gran Sasso or LNGS). The laboratory is built approximately halfway through a 10.4 km tunnel that passes underneath the Gran Sasso mountain, which is part of the Apennine mountain range. The highest mountain peak (Figure 2.1a) is 2912 m above sea level and sits just to the side of the laboratory. The quantity of rock above the laboratory is about 1400 m, which corresponds to 3600 m.w.e. of shielding against most cosmic rays. The muon flux in the laboratory is about $0.96 \text{ m}^{-2} \text{ hour}^{-1}$.

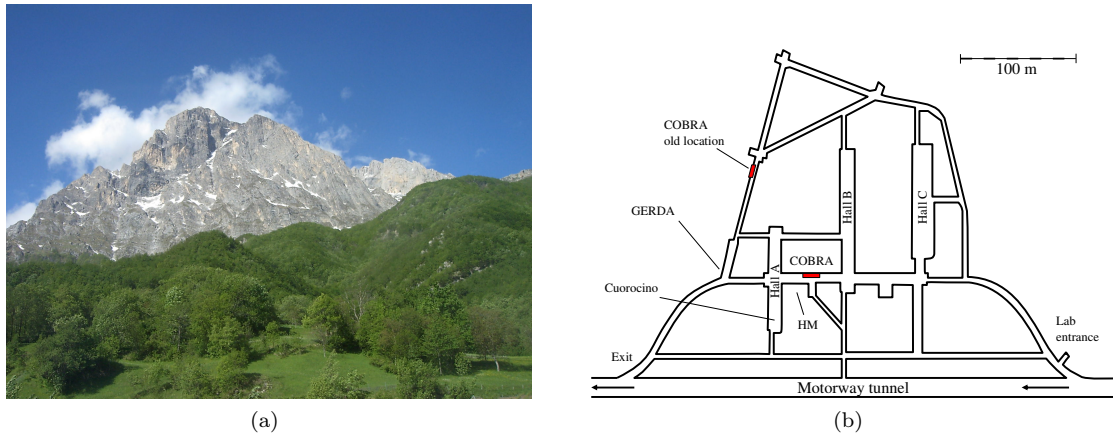


Figure 2.1: The Gran Sasso (great stone) mountain (a) and LNGS laboratory plan (b) shows the early and current location of the COBRA experiment. Locations of the mentioned DBD experiments that are/were located at LNGS are also shown. Map adapted from [LNG].

2.1 Development Stages

Early development stages of the COBRA experiment are described in detail in [Kie05, Mue07, Oeh04]. A brief summary of these stages is presented here. Development work for the COBRA experiment started at the University of Dortmund where a background rate of about 20 counts/keV/kg/day was observed in the 2.8 MeV signal region when the detectors were not shielded [Mue07]. The detectors were then installed at LNGS at the location labelled “COBRA old location” in Figure 2.1b, and with the addition of copper and lead shielding similar to the 64-array described in Section 2.2 the background was reduced by two orders of magnitude. This prototype consisted of an array of four co-planar grid CZT detectors, also similar to those used in the 64-array. The detectors each require three contacts to be made, which was achieved with RG-176 coaxial cables bonded to the detectors using conducting silver-filled epoxy. The detectors were held in a Pertinax holder embedded in a copper brick (see Figure 2.2a).

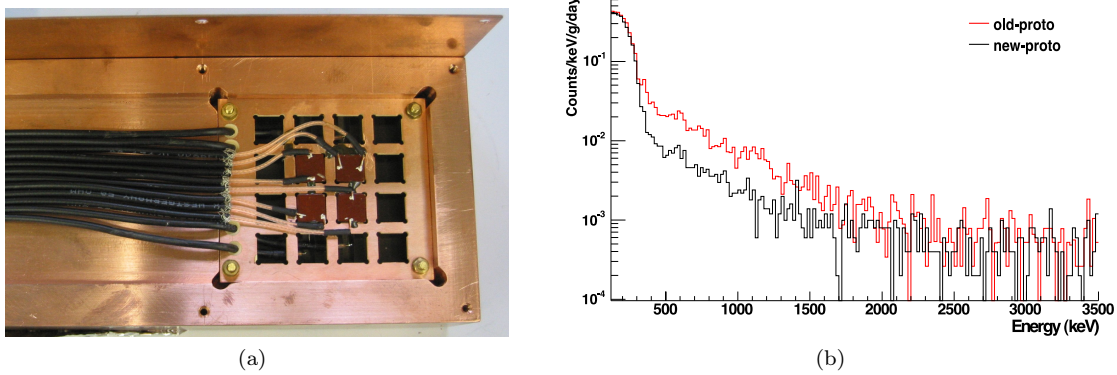


Figure 2.2: Photo of first prototype detector array and data. The photo, taken from [Kie05], shows four 1 cm^3 co-planar CZT detectors held in a copper brick with large cables, silver epoxy glue and Pertinax detector holder. The graph (b) shows an energy spectrum from this old prototype (courtesy of H. Kiel), together with an energy spectrum (analysed for this thesis) from a new prototype using Kapton cables, a Delrin detector holder and a copper-based conductive glue.

The main concerns with this setup was that the cables, Pertinax holder, and silver used in the epoxy were all known to be slightly radioactive. An improvement was then made in December 2004 to replace the cables with thin Kapton foils on which printed copper traces carry the signals from the detectors. The Pertinax holder was also replaced with Delrin and bonding to the detectors was achieved with a solvent based glue mixed with copper powder. Energy spectra taken before (red) and after these changes (black) are shown in Figure 2.2b. The figure shows the number of events observed for each keV of energy per gram of CZT per day (counts/keV/g/day). The region between 350–1500 keV shows a large reduction in the background, however in the signal regions, 2530 keV and 2805 keV, no significant drop in the background was observed.

Identifying what are the next most dominant backgrounds was the motivation behind Chap-

ter 4. The red colour of the detectors in Figure 2.2a is paint that coats the detectors to prevent the surfaces of the detectors reacting with damp air that would eventually affect the performance of the detectors. Measurements of samples of this paint were found to have significant levels of uranium and thorium (Chapter 4 page 91), and preliminary simulations indicated that this was the next dominant background in the signal regions [Wil05]. These simulations did not include a dead layer, which is a thin layer of the detectors close to the surface that is likely not to be sensitive to radiation deposits. The findings in Chapter 4 differ slightly to the results in [Wil05] in that radiation from radon gas and its daughter nuclides was found to dominate the background spectrum.

Despite the known radioactivity of the paint, plans went ahead to install an array of 64 similar detectors to test the feasibility of using a large quantity of CZT detectors in a low background experiment. It was found that improvements had to be made to the contacting technique and Kapton cables, which is explained in more detail shortly. Testing how effective coincidence events¹ are at rejecting backgrounds or identifying unique signatures of rare events is also a goal of the 64-array. Some research towards this, performed on data prepared for this thesis, was carried out by J. Wilson and D. Müenstermann and described in [Mue07]. This research, however, is currently hampered by technical problems reported in Chapter 3.

Following a request to the manufacturer of the detectors, four detectors were prepared with a clear passivation coating. These detectors are still being tested at the time of writing but early indications show a large drop in the background rate.

With any technical problems ironed out and confirmation that the best low-background materials have been found, the next development stage of the experiment could see an expansion to an array of 64 000 detectors. However, it may be found that coincidence rejection between detectors is not sufficient to discard all remaining backgrounds, so a number of parallel areas of research continue. These include operating the detectors in a scintillating liquid, which would help discard external backgrounds, and internal backgrounds that involve gamma rays. The possible use of pixellated detectors that would enable three dimensional tracking of electrons inside the detector volume would also help discriminate between radiation types. The possibility of using slabs of CZT would make the experiment more compact and the reduced surface area to detector volume would be a great advantage because surfaces can easily become contaminated with radionuclides.

¹A coincident event is when more than one energy deposition is observed in different detectors at the same time.

2.2 64-Array Experimental Setup

This section describes the apparatus used for the 64-array.

2.2.1 Introduction

The design of the 64-array is to set up an array of 64 co-planar CZT detectors using the same materials as the modified 4-array, described above. The detectors are arranged in four layers of 4×4 arrays. The detector *nest* consists of machined copper bricks that form a box in which the detector holders can be slid. This was demonstrated in Figure 1.6 on page 10, and a cross-section front view of the nest is shown in Figure 2.3a.

The shield that protects the detectors from outside radiation is made up of tightly stacked copper and lead bricks. The lead is an effective shield against gamma radiation. However, lead contains some radionuclides that emit x-rays, so to stop these an innermost layer of highly pure copper is used. This is demonstrated in Figure 2.3b. Also shown in the figure is the copper Faraday cage that shields against radio-waves and a borated polyethylene shield to keep out neutrons. The whole apparatus sits on rubber shock absorbers (Figure 2.8c) and sand to dampen high frequency vibrations from vehicles or machinery outside the cabin (Figure 2.8d) in which the experiment is housed.

The setup described here is located between Halls A and B (Figure 2.1b) at LNGS. The 64-array was first installed at the “old location” during March 2006, where the setup differed slightly in that there were no shock absorbers and the neutron shield sat directly on concrete. In addition, this initial setup also included paraffin bricks that surrounded the polyethylene. These served to slow down neutrons so that they can be more effectively captured by the borated polyethylene (see [Oeh04]). However, space was limited in the new location and because the neutron background is not currently believed to be observable above other backgrounds the paraffin bricks were not re-installed after the move.

To date, only the first layer of detectors have been installed because the contacting technique was found to be insufficiently reliable. A couple of months of data was taken with the first layer in the old location and several months of data from the new location. The precise installation and running dates are given in the beginning of Chapter 3.

2.2.2 The detectors

A brief description of how the detectors work, are used, and how they are produced is now presented.

2.2.2.1 How the detectors work

The basic principal behind how CZT detectors work, is that a large potential difference is applied across the semi-conducting crystal to produce a uniform electric field of about 1500 V/cm. When a nuclear decay inside a detector occurs and produces radiation, or radiation enters from outside

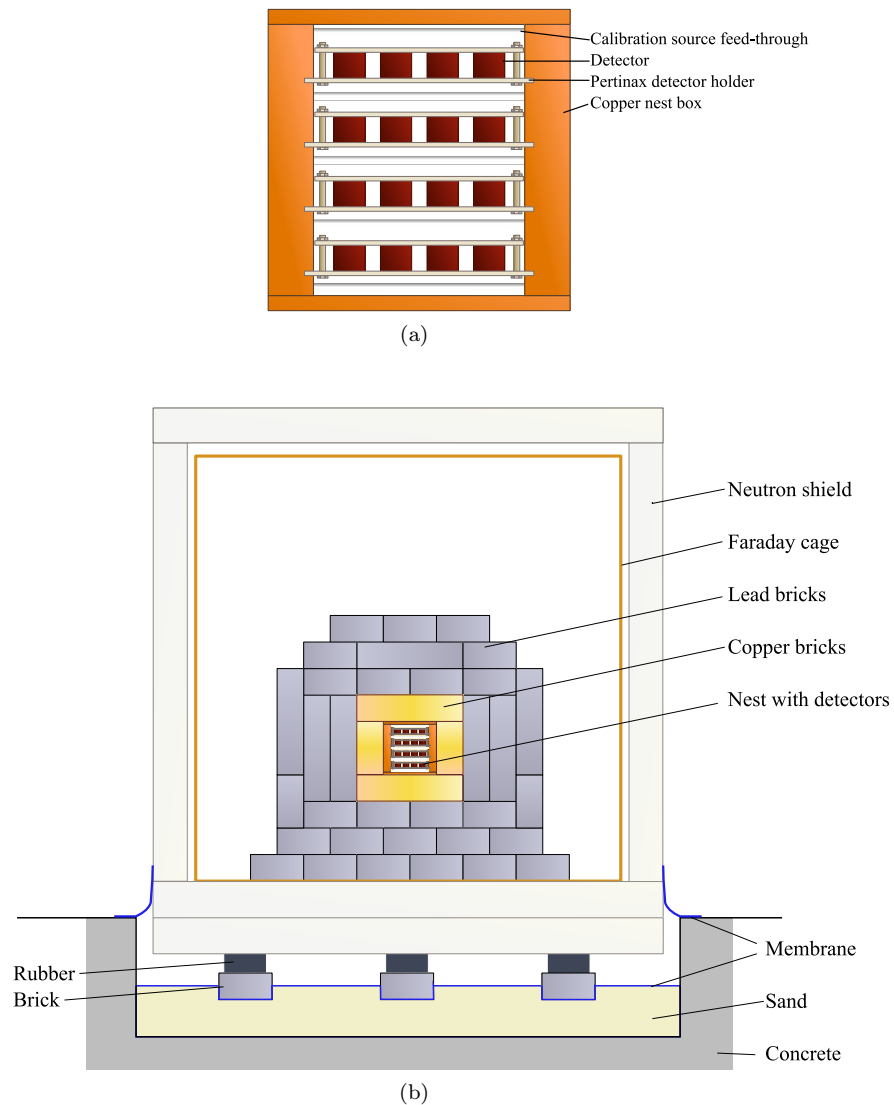


Figure 2.3: Front view cross-section diagrams of detector nest (a) and shielding (b).

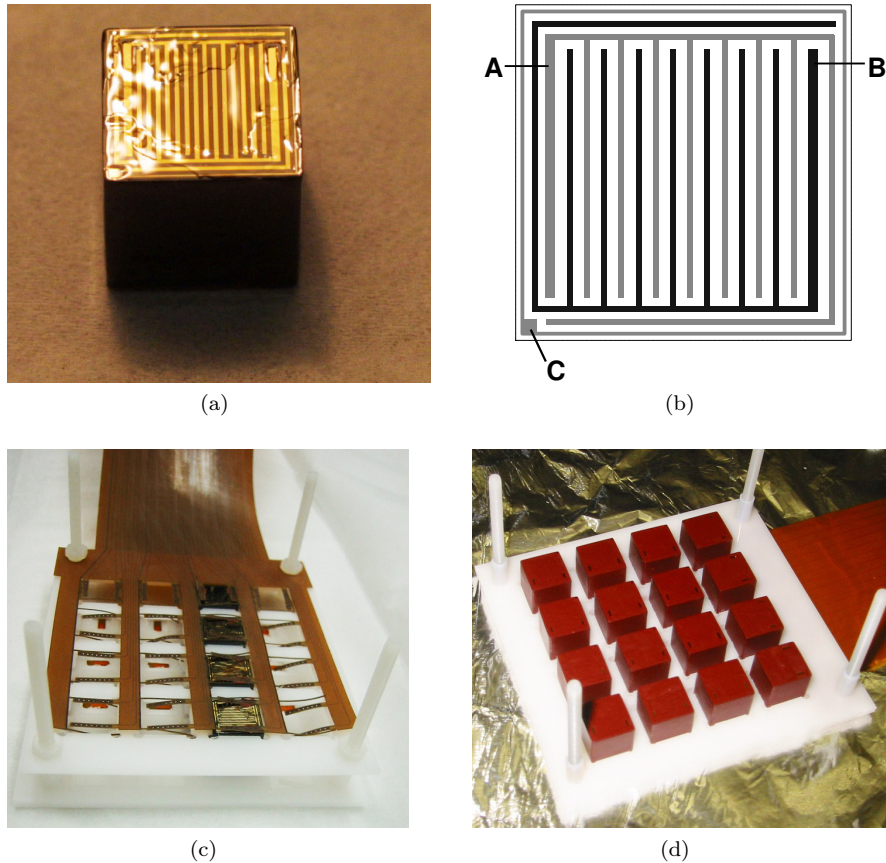


Figure 2.4: Photos of the detectors and holder. (a) A photo of CZT detectors similar to those used in the 64-array but with clear passivation lacquer. (b) A diagram of the anode grids that can be seen in (a), with A, B and C marking the contact points. (c) Four detectors with a clear lacquer sitting in a Delrin holder. The vertical nylon bolts have not yet been cut. The brown Kapton cable that carries the signals along copper traces is also shown. (d) The 16 detectors that form the first layer of the 64-array are shown in a partially constructed Delrin holder. Photos (a), (c) and (d) are from the COBRA archive.

into the detector volume, interactions with the radiation provide electrons enough energy to jump the band gap from the valence to the conduction band, which at room temperature is 1.56 eV [SD98]. The electrons then quickly move to the anode and the holes created in the valence band move towards the cathode². The total charge of the liberated electrons and holes is proportional to the energy deposited by the radiation inside the detectors.

However, the mobility of the holes in CZT is so poor that most or all of the holes never reach the cathode, depending on where they were created inside the detector. Consequently, if the total charge pulse across the detector were measured, different readings would be found depending on where the interaction with the radiation occurred. To solve this problem, two main types of CZT detectors have been developed, namely CPG (co-planar grid) and pixellated detectors.

Pixellated detectors divide the anode contact into segments. Charge pulses are collected between each segment and the single cathode contact. Electrons (mostly) only induce a signal on the segment directly below where they were liberated. The footprint of the holes, due to their poor mobility, is spread over a larger area so the induced signal from holes on a single pixel is much reduced. Thus the charge pulse size between the anode and a pixel is mostly independent of the interaction depth. A small depth dependence remains, but this can be compensated with post-processing (see [Blo07]).

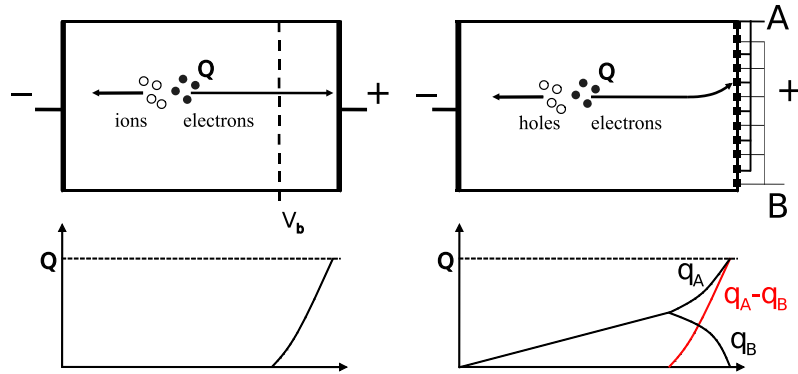


Figure 2.5: Schematic of a Frisch-grid gas detector (top left) and a CPG CZT detector (top right). In both cases the liberated electrons travel towards the anode. With the gas detector the anode is blind to the electrons until they pass through the Frisch-grid, which is held at an intermediate potential. On passing through the grid a charge pulse is induced on the anode proportional in size to the distance travelled by the charge carriers between the grid and the anode. The induced charge is schematically shown underneath as a function of the distance travelled by the electrons. With the CPG detector, initially both grids observe an induced charge, which cancels out when subtracted from each other ($q_A - q_B$). When the electrons approach the anode and can differentiate between the two potentials of grids A and B the direction of motion of the charge carriers changes towards the greater potential, and a charge pulse is observed between the grids.

²The anode and cathodes are the electrical contacts at greater and lesser potential respectively. In this experiment the cathode is the gold plating on the bottom of the detectors and is held between -500 and -1500 V and the anode is held at ground.

CPG detectors, which are the type used in the 64-array, use a technique that is similar to Frisch-grid detectors: In CPG detectors [MHS⁺98] two integrated, but isolated grids form the anode contact are held at slightly different potentials (between 20–50 V, which is small compared to the potential difference across the detector volume). These grids can be seen in Figures 2.4a-b, where (a) shows the anode contact shining through a detector coated in the special clear lacquer and (b) shows a diagram of the anode. Diagrams comparing Frisch-grid gas detectors and CPG detectors are shown in Figure 2.5. While the free electrons created in a CPG detector travel towards the anode they are deflected towards the grid of highest potential. This deflection results in an induced signal between the two grids. By amplifying the signals separately for each grid with pre-amplifiers and taking the difference of the two signals, the resulting signal has a pulse height that is proportional to the number of electrons freed in the detector, which in turn is proportional to the energy deposited in the crystal. This proportionality is also largely independent of the location of an interaction within a detector.

2.2.2.2 How the detectors are used

The detectors are placed with their cathode contacts on the bottom. This contact is connected to a high-voltage supply with a typical voltage of about –1500 V. The precise voltage used varies between detectors according to how they perform when tested at different voltages. A larger voltage of –2500 V can sometimes produce better resolution but can lead to breakdown across the detector that causes sporadic ‘bursts’ of false³ events. Thus choosing a lower voltage between –750 and –1000 V is often necessary.

The anode grids are on the top of the detectors. One grid is held at ground and the other held at about –30 V. Again the precise voltage is determined by testing the detectors at different voltages. Breakdown is also possible between the grids and some detectors would only work (at a reduced energy resolution) at ~5 V (see Section 3.4.2.1).

The contact, C, in Figure 2.4b is for the *guard ring* that surrounds the anode grids. This is usually kept at ground to help isolate the grids from noise due to leakage current across the surface of the detectors between the anode and cathode. The guard rings are however not currently connected as this could increase the dead layer of the detectors. Points labeled A and B in Figure 2.4b are the contact points for the grids.

2.2.2.3 How the detectors are made

The detectors used in the 64-array are manufactured by eV PRODUCTS⁴ using a high temperature oven that vaporises the elements, Cd, Zn and Te and allows them to condense to form boules of crystalline CZT [SCNC02]. These boules can be large, for example with a 9 cm diameter and weighing 4 kg [SD98]. Defects in the crystalline structure limit the maximum detector sizes that can be cut from the boules where the defects must be avoided because they increase electron trapping that would spoil the resolution and efficiency of a detector. After cutting, the detectors are polished and anode and cathode contacts are applied. Gold is a key element used

³These false events are discussed in detail in the following chapter.

⁴www.evproducts.com

to make the contacts, however, (as became apparent in the analysis: see page 118) platinum is also used to make the contacts. Finally, five of the sides of the detectors are painted to prevent surface corrosion. The cathode contact and contact points A, B and C on Figure 2.4b are left unpainted. The precise methods used to produce the detectors for the 64-array are a trade secret of eV PRODUCTS.

2.2.3 Detector holders

A detector holder can be seen in Figures 2.4c-d and is made from Delrin⁵ and designed and produced at Dortmund University (for technical drawings see [Mue07]). Radiation measurements of the holders did not find any contaminants [Mue07]. The detector holders were thoroughly cleaned after milling by placing them in a sonic acetone bath for at least 5 minutes followed by at least 5 minutes in an isopropanol bath [Sch08].

2.2.4 Kapton cables

The Kapton cables, which are just visible in Figures 2.4c-d, are used to collect the anode signals as well as deliver the high voltage to the detectors. The cables were also produced at Dortmund and were made by printing copper traces onto a sheet of Kapton and then glueing another sheet of Kapton on top with epoxy resin. The Kapton sheets were then cut to shape using a laser. The low capacitance ($\sim 132 \text{ pF/m}$ [Mue07]) of the cables make them suitable to collect the anode signals and the high resistivity of Kapton and epoxy resin enables the cables to be used to supply the high-voltage. However, once installed it was found that micro-discharges occurred in the high voltage cables (see Section 3.4.3 on page 73) that were picked up by the unshielded signal cables. To avoid this the high voltage Kapton cables were covered in thin copper foil. Again technical drawings of these cables can be found in [Mue07].

It is likely that the high voltage cable will be replaced with cables that produce fewer discharges because close to the detectors the shielding is less effective so that it can still generate false events.

2.2.5 Detector contacts

It has already been mentioned that the detectors are bonded to the Kapton cables with a mixture of solvent based glue and copper powder. The advantages of using this mixture are:

- ▷ It has been tested and found to be radioactively clean.
- ▷ It can be easily be removed.
- ▷ The anode contacts are very delicate so using a glue is less likely to damage them than wire bonding or using needles.

The main problem with using this contact technique was that the conductive glue did not stick well to the shiny gold cathode surfaces and frequently lost contact. Even contacts to the anodes, where the glue could partly bond to the paint, sometimes failed. Consequently, new bonding techniques are currently being tested.

⁵Delrin is the brand name for Polyoxymethylene plastic.

2.2.6 Nest

The detector nest, previously shown in Figure 2.3a, is a box made entirely from copper with three thin bricks making up the walls and two plates are attached to the top and bottom with nylon bolts. Two small bricks form a door to the nest with a thin gap between the bricks just wide enough to allow the Kapton cables through. Also see [Mue07, Appendix C] for technical drawings.

Copper was chosen to be placed close to the detectors because the element not only contains no long-lived isotopes, but the manufacturing process involves routinely purifying the copper through electrolytical dissolution. The redox potential of copper for the reaction $\text{Cu} \rightleftharpoons \text{Cu}^{2+} + 2\text{e}^-$ in an acid solution is 377 mV, which is much higher than the naturally occurring radio nuclides of potassium, uranium and thorium, and most of their daughters. Consequently these isotopes are effectively all removed from copper [Heu95] by the end of the manufacturing process.

Cleaning of the surface of the copper after machining was performed in a number of stages. First the nest components were placed in ultra sonic baths with acetone and isopropanol as above. Then the components were placed in a solution of 5% citric acid and distilled water for several hours before rinsing with distilled water. This cleaning process is important to remove radionuclides, such as the daughter products of radon, that can stick to surfaces.

2.2.7 Source feed-throughs

The source feed-throughs, also drawn in Figure 2.3a and pictured in Figure 2.6b on page 30, are tubes made from Teflon. They enable radioactive sources attached to the end of a flexible wire to be inserted from the outside of the apparatus close to the detectors. There are five feedthroughs so calibrations can be made from both the top and bottom of the detectors.

2.2.8 Shielding—passive

Shielding can be categorised as either passive or active, where the former consists mainly of a selection of materials to stop radiation, and the latter consists mainly of the monitoring of sensors. Already mentioned, the 3600 m.w.e. of rock above the experiment forms the outermost protection against background radiation. The sand and rubber shock absorbers on which the experiment rests can also be categorised as passive shielding against vibrations. A picture of one of the rubber feet is shown Figure 2.8c on page 31.

The COBRA cabin in which the experiment is housed (pictured in Figure 2.8d) also acts like a shield by protecting the experiment from dust that can contain high levels of naturally occurring radionuclides. Offices and storage space are located in the upper cabin and the apparatus in a room in the lower cabin. The experiment room is divided into two areas with polythene curtains. The area closest to the door contains most of the electronics. While stepping into this area outdoor shoes are replaced with plastic socks to avoid carrying in dirt. A sticky mat covers the floor to catch any dust and fibres falling from clothing. Behind the polythene curtains is where access to the detectors is gained. Before entering this area protective overalls and hoods are worn to prevent dust and hair escaping into this area. All areas are regularly cleaned meticulously. An

overpressure is created in the cleanest area to help keep dust out. This is achieved by drawing air from outside through a clean-room filter. The filter is shown in Figure 2.8b.

2.2.8.1 Copper and lead

The innermost shield that has the largest impact at reducing the background levels are the copper and lead bricks that surround the copper nest. Most bricks have dimensions of $20 \times 10 \times 5$ cm with a small number of half-bricks with dimensions $10 \times 10 \times 5$ cm. The copper and lead shielding in Figure 2.3b (page 23) was drawn with roughly the correct proportions and configuration of bricks, based on photographs taken during installation. The only key difference is that the left-hand side of the actual installation had to be modified to allow special bricks to be fitted that enable the source feed-throughs to ‘snake’ their way through the shielding to the nest. As can be seen in Figure 2.3b, care was taken to stagger the bricks to ensure there were no direct cracks through the shield to the nest.

The ultra pure copper bricks that sit closest to the nest to stop x-rays coming from the lead bricks were also cleaned with the same standard as described above, which included a citric acid bath. In addition, during the installation after the move of the experiment within LNGS, the copper bricks were first wiped down with acetone and then with ethanol to remove lead-oxide dust that can fall on the bricks during dismantling.

The lead bricks come in three standards. The innermost bricks that sit next to the copper bricks are made from particularly low-background lead having been salvaged from an old sunken ship [Zub08], so most cosmogenics in it have already decayed. The next layer of lead, which looks identical, has been more recently produced. An outer layer of lead bricks are of similar quality but are painted so they could not be cleaned as harshly. The lead ‘castle’ is shown in Figure 2.6.

Figure 2.7 shows a side cross-sectional view of the experiment and demonstrates how special V-shaped bricks enable the Kapton cable to pass through the shield without there being a direct line of sight into the nest.

2.2.8.2 Faraday cage

The Faraday cage, shown in Figure 2.8a, protects the unshielded signal cables from picking up radio signals either from radios used by the firemen in the laboratory or other electronics such as lighting and electric motors. A small hole is cut in the side of the shield to allow the signal, high voltage and other power cables through the cage. It is possibly due to this hole that the Faraday cage was found not to be completely effective at keeping out radio waves. A small test that was performed is described in Section 3.4.

2.2.8.3 Neutron shield

The neutron shield has already been mentioned in this chapter (page 22) and in Section 1.5.1 on page 13. It can be seen partially constructed behind and underneath the Faraday cage in Figure 2.8a. The shield is made from 7 cm thick borated polyethylene, where ^{10}Bo is very effective

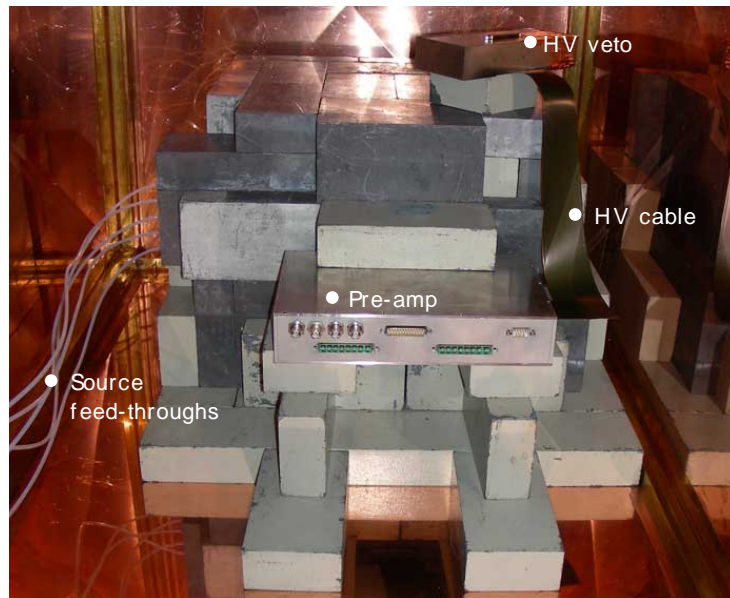


Figure 2.6: A picture of the experiment before all of the cables were attached.

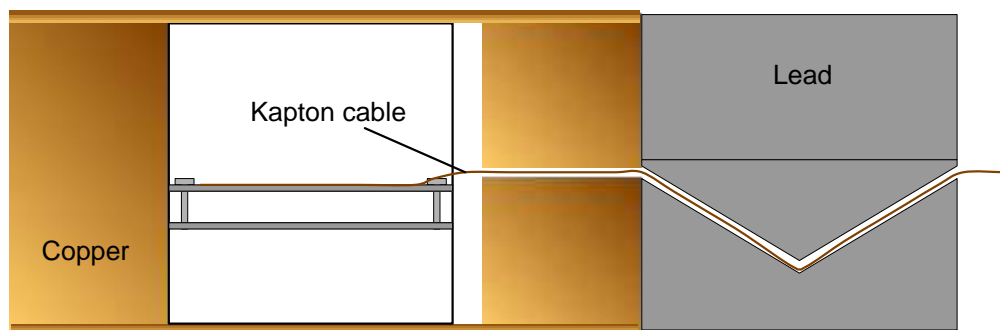


Figure 2.7: Side cross-sectional view of nest, copper and lead. Taken from [Mue07].

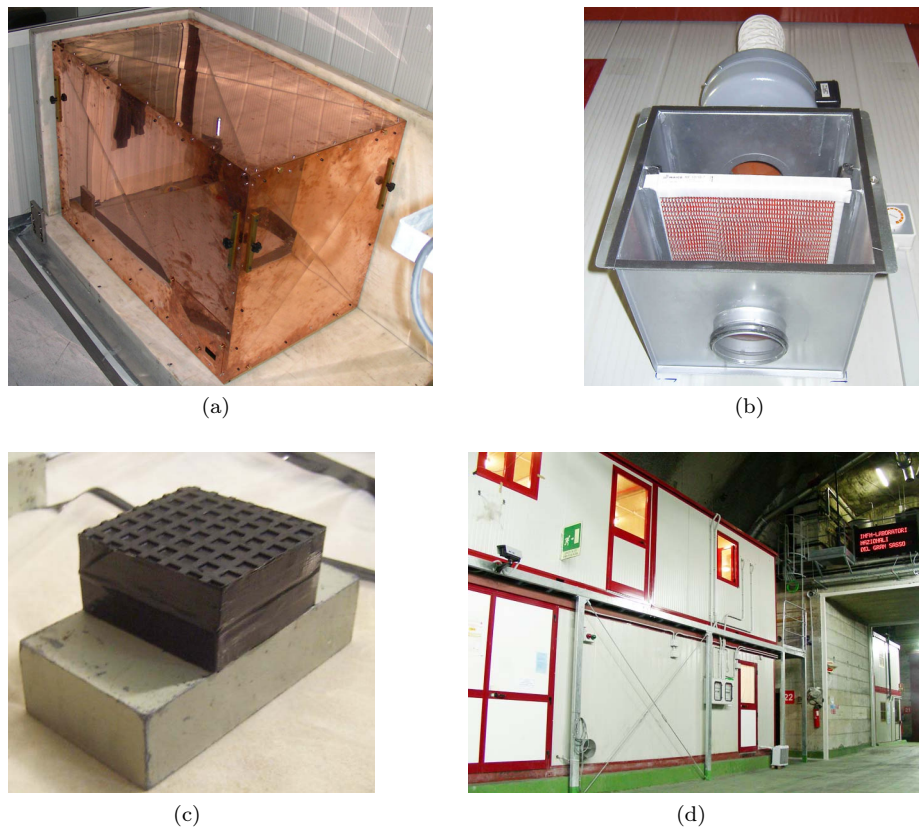


Figure 2.8: Collection of photos show (a) the Faraday cage, (b) the cabin air filter, (c) one of the shock absorbers on which the whole apparatus rests and (d) a picture of the cabins used for the experiment in the current location between halls A and B. Photos (a) and (d) were taken by O. Schultz.

at capturing thermal neutrons with its cross-section of $\sim 4 \text{ kbarn}$. The reaction $^{10}\text{B}(\text{n},\alpha)^7\text{Li}$ also frequently releases 478 keV de-excitation gammas [AZG06] but they are easily stopped by the lead shield.

2.2.9 Shielding—active

The active vetoes or ‘shields’ are now described. A *veto* is a method of rejecting background events based on the simultaneous measurement of a separate instrument.

2.2.9.1 High voltage discharge veto

The high voltage (HV) veto is currently the most critical to the COBRA experiment. Micro-discharges that occur in the HV Kapton cables can be picked up by the unshielded signal cables but are discarded with a veto. The possible cause and the impact of the micro-discharges is discussed Section 3.4. The HV-veto involves a quick fix, to help discriminate between real events and those caused by pickup from discharges in the high-voltage lines. This was achieved by connecting spare signal ports, designed for recording events from the anode, to the high voltage lines via a high voltage safe capacitor. This is demonstrated in Figure 2.9 on the next page. As it turned out, the method led to the discovery described in Chapter 4 that the veto was also sensitive to alpha radiation on the cathode surface.

2.2.9.2 Muon veto

A muon veto has not yet been installed but will be required in the future. As discussed in Section 1.5.1, the muon background is about $\sim 0.96 \text{ m}^{-2} \text{ hour}^{-1}$. This corresponds to only about one interaction per 1 cm^3 detector per year, which is well below the current background rate. When the muon background is significant the experiment will be covered with scintillators and any events coincident with a flash of light from a scintillator would be rejected.

2.2.9.3 Other sensors

Other sensors being tested are a mains spike detector, vibration sensor, humidity monitor and two thermometers. The mains spike and vibration detectors were designed to report true/false responses when they detect a disturbance above a certain threshold. However, more careful testing of the devices is necessary before it can be determined how useful they are. Due to the difficulties in adjusting thresholds the devices were often left unconnected. For this reason they are not used in the analysis for this thesis.

The humidity monitor, a Humeril⁶ HTM1505, is located in the Faraday cage and has reported readings between 30–40% relative humidity (RH). The humidity, H_{rel} , which is reported through TTL logic can be calibrated with the following equation [Daw06],

$$H_{rel} = \frac{1}{30.21[\text{V}]} \times \left(\frac{A + 113[\text{Ch}]}{3303[\text{Ch}/\text{V}]} \times 1000 - 814[\text{V}] \right). \quad (2.1)$$

⁶www.humirel.com

where A is the reported number in channels (Ch). The temperature probes are AD22100 sensors manufactured by Analog Devices⁷ and also use TTL logic and are calibrated in degrees Celsius with the equation

$$T = \frac{1}{0.0225 \text{ [V/}^\circ\text{C]}} \times \left(\frac{A + 113 \text{ [Ch]}}{3303 \text{ [Ch/V]}} - 1.375 \text{ [V]} \right). \quad (2.2)$$

One probe is located on the lead castle and another on the VME crate.

2.2.10 Electronics

A schematic of the basic electronic setup used in the COBRA experiment is shown in Figure 2.9. The diagram shows a detector held at -1500 V on the cathode, and the anode grids at -30 V and 0 V . The charge pulses from the detector are amplified to a voltage signal with the preamplifier. At this point the signal shape is saw-toothed with a rise time of $\sim 100 \text{ ns}$ and fall time of several μs . To help discard any disturbances on the signal lines the shaper acts as a narrow band filter that only allows signals through of a similar scale as the rise time of real events. The resulting signal has a Gaussian form that is more suited for the ADC to measure. The ADC (Analogue to Digital Converter) measures the height of the Gaussian signal, which is reported to a VMEbus and processed on a computer by the DAQ (data acquisition) software before being saved to a hard drive.

Also shown in Figure 2.9 is the HV-veto, which currently involves monitoring the cathode signals via a high voltage safe capacitor C . For each additional detector anode signal there is a separate preamplifier, shaper and ADC port. The cathode signals are combined in groups of eight.

The electronics used by the COBRA experiment is also covered in [Mue07] and [Kie05]. For the context of this research it is worth noting a number of details.

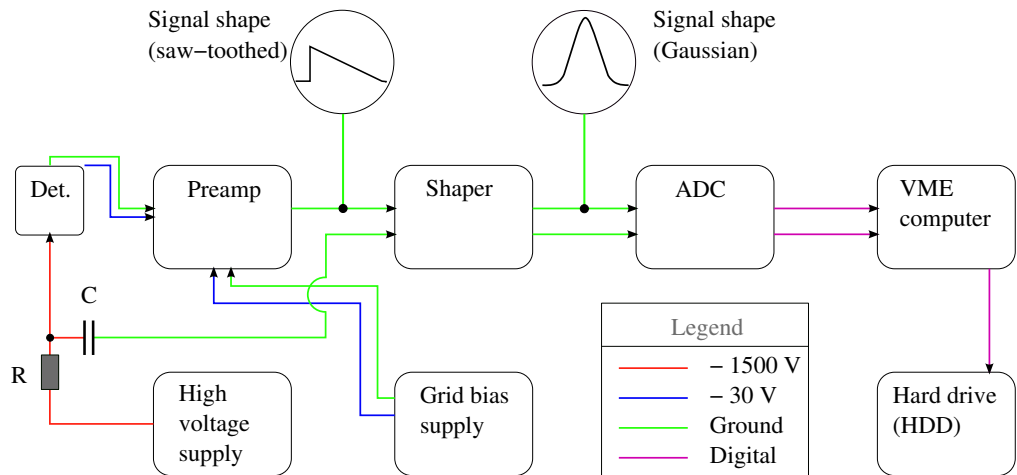


Figure 2.9: Schematic of the main electronics used in the experiment.

⁷ www.analog.com

2.2.10.1 Preamplifiers

The preamplifiers use OP-amps to measure the charge pulses from the detectors. The output signal from the OP-amps is a voltage pulse. It is at this point that the preamplifier subtracts the two anode signals. The level of subtraction, or balance, is controlled electronically with a potentiometer. Optimisation of the potentiometers (one for each detector) is vital before data-taking because it has a great impact on the resolution of the output signal. The optimised setting varies with the leakage current across the grids and the grid bias potential. Even a slight dependence in the optimum potentiometer setting has been observed with the high voltage setting. For this reason, ideally, each possible combination of high voltage, grid bias and potentiometer settings should be tested to find which provides the best resolution.

2.2.10.2 The ADCs

After shaping, the voltage signals are converted to a numerical readout via peak sensing ADCs custom built in Dortmund. These are controlled by a VME crate and computer. The requirements of the ADCs are to provide high resolution voltage measurements with accurate time stamps and short dead-time⁸, as well as being easily scalable to accommodate upgrades to the experiment. For the current status of the experiment this is mostly achieved, and is a great improvement on previous setups.

There are four ADC ports per ADC module where each module occupies one slot of the VME crate. Each ADC has a remotely adjustable amplifier and *trigger threshold*⁹ that is set as low as possible and above the *noise level*¹⁰. In order to make an accurate reading of a signal pulse height the ADCs use a peak-and-hold technique where the highest voltage reached in about a $50\ \mu\text{s}$ period is held until it is reset. A reset is made only when an event occurs above a trigger threshold¹¹. When an ADC is triggered all ADCs in the same module are also triggered, which enables coincident signals to be recorded. A ribbon cable connected to each ADC module also allows all modules in the crate to be triggered at the same time. Coincident signals between models can be matched later in the analysis since they have the same time stamp.

Timing is done at 1 ms precision using the system Unix time¹² and at a precision of $8\ \mu\text{s}$ with a separate timer that cycles every 9.6 hours [Kie05]. The smallest time difference that can be recorded with the ADCs is $120\ \mu\text{s}$, which is the time required for the triggers to be propagated, a reading to be made, and the held voltage to drop back to zero. This is demonstrated in Figure 2.10, which shows a histogram of event separation in time (dots). Each dot is $8\ \mu\text{s}$ apart. The vertical dashed line marks the shortest time that the ADCs can accurately measure. Just

⁸The time after processing a reading during which time the ADC is blind to further activity.

⁹The trigger threshold is the voltage that a signal pulse must reach in order to be recorded.

¹⁰The noise level is the voltage that most electronic disturbances on the signal lines will not pass. This is not strictly speaking a level as it drops approximately exponentially in frequency with greater voltage and so is relative to the signal frequency.

¹¹This is an important point to note, because it means that recorded sub-threshold measurements are the largest signals observed by the ADC following the previous trigger and are not necessarily correlated to events recorded above the trigger thresholds. Consequently, using sub-threshold events as a veto is not possible because it would lead to a loss of good data.

¹²The number of seconds elapsed since midnight UTC of January 1, 1970, not counting leap seconds [Wik].

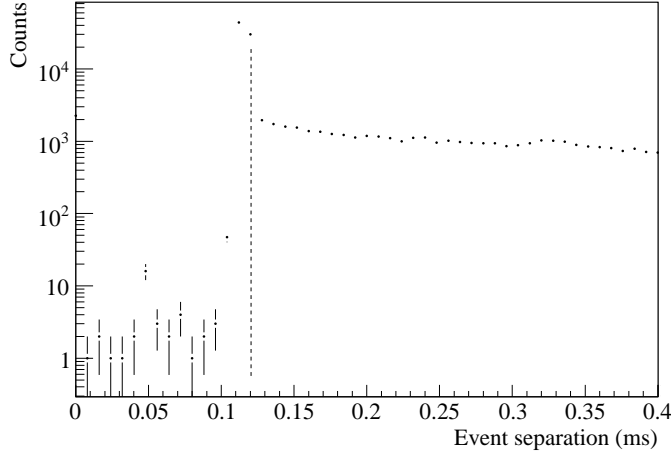


Figure 2.10: Measurement of the ADC timing resolution. A histogram (dots) of the time separation between events is created for datasets L1a-c. The vertical (dashed) line marks the minimum timing measurement.

below $120\,\mu\text{s}$, the two dots showing particularly high count rates arise from noisy periods where the ADC is forced to record multiple events with the same minimum time stamp, in order to avoid the ADC buffers over-filling. Such noisy periods are rejected in the cleaning process described in this thesis. The small number of events at shorter time separations are also believed to result from the ADCs struggling to keep up with a noisy period.

The ADCs are 14-bit and so have $2^{14} = 16\,384$ channels. If an amplification is chosen such that the 16 384th channel corresponds to 12 MeV, which is greater than the largest energy we expect to see from a nuclear decay, then the resolution of the ADC is approximately 0.732 keV. This is sufficient for the current detectors, which have resolutions of about 20–50 keV; however, because the ADC resolution is just below 1 keV, which is the unit of energy that energy spectra are often presented, an interference effect can be observed as ‘whiskers’ on the spectra.

n	$\times 0.732$	bin	n	$\times 0.732$	bin
1	0.732	0	5	3.660	3
2	1.464	1	6	4.392	4
3	2.196	2	7	5.124	5
4	2.928	2	8	5.856	5

Table 2.1: Example of bias towards some bins with non-integer re-binning.

This is a simple numerical effect of taking the already binned data (0.732 keV ADC bins in this example) and re-binning by a non-integer number. The effect is illustrated in Table 2.1, which shows that the first ADC channel has an energy of 0.732 keV and when rounded to the lowest integer falls in the zeroth bin of a histogram. The second channel has an energy of 1.464 keV and falls in the first bin. Bins 2 and 5, however, have twice as many entries as do approximately every second bin. If the effect poses a problem to the analysis it can be overcome in two ways: One

way is to re-bin the data in units of the resolving time, which is not practical when combining datasets with different resolving times. The other way is to remove the ADC binning by adding a random number between -0.5 and $+0.5$ keV to the energy of each event. This is the method used in this analysis.

2.2.10.3 DAQ software

The DAQ software was written by H. Kiel in C and updated by J. Wilson. It is installed on the VME computer that is called *cobra3*. This computer is mounted on a control computer called *cobra2* from which client commands are sent to the DAQ software [Wil06]. Both computers run Linux operating systems.

2.2.11 Data structure and management

2.2.11.1 A description of recorded data

The DAQ records all information in ASCII format to the location on disk from which the application is started, typically `/data/COBRA` on *cobra3*. A new file is created on the hour and named according to the format `daq_YYYY_MM_DD_HH_MM_SS.dat` where `YYYY` is the year and `MM` the month *etc.* and the time is given in UTC¹³. If the DAQ is instructed to write to disk mid-hour the file name will be named accordingly and is closed and a new file created at the turn of the following hour with the `MM` and `SS` values always set to 00 (*i.e.* the first data file is less than an hour long). A full hour's worth of data is usually referred to here as a *run*.

Each data file is laid out as demonstrated in Figure 2.11. In this example the triggers are propagated to all ADC modules and written out consecutively. When triggers are not propagated only readings from the ADC module that triggered are written to file. Such features of the DAQ data format are important to note when designing a script to read the ASCII files.

Coincident signals that are part of the same event can be identified by having the same time stamp and Unix time. However, it should be noted that some events that should have had identical time stamps occasionally differed by about 10 units¹⁴. This corresponds to $10 \times 8 \times 10^{-6} = 80\ \mu\text{s}$, which is still acceptable since the shortest times between two real events that the ADCs can measure is $120\ \mu\text{s}$.

As a temporary modification to the setup, ADC module 6 is used by the HV-veto to record discharge events observed on the high voltage cathode cables. In order to minimise the size of the data files, only discharge events that are coincident to an anode signal are written to file. However, in order to have an accurate record of the dead time it is necessary to count the number of HV discharge events that have caused the ADCs to trigger. This number is recorded in the data files at the end of each line of module 6, as indicated in Figure 2.11.

The *footer* of a data file, labeled **SETTINGS**, was introduced to the DAQ code out of necessity to keep track of changes made to the apparatus for the analysis of the data. The parameters are written to disk just before closing a data file when the DAQ is stopped or on the turn of each

¹³Coordinated Universal Time, used for British winter time.

¹⁴This is a known bug of the ADC.

The diagram illustrates the structure of a data file. At the top, it shows the header information: 'run name' (STARTdaq_2007_06_21_22_00_00.dat/1182463200) and 'start time in Unix time (seconds)' (1182463200). Below this, several event lines are shown, each starting with a timestamp (e.g., 1 1 3729121363 1182463202.095997). The data is annotated with brackets indicating field widths and types. For example, 'energies (channels)' is indicated by a bracket under the numbers 389, 56, 104, etc. Other annotations include 'TTL veto number', 'temperature 1', 'temperature 2', 'humidity reading', 'flowmeter reading', 'ADC module number', 'time stamp (8E-6 seconds)', and 'Unix time (seconds)'. A section at the bottom contains constant run settings: 'END3600' (run length), 'SETTINGS' (with sub-fields for 'det', 'on', 'HV', 'GB(16)', 'Amp', and 'Thr'), and a final group of settings labeled 'collective run settings printed at end of file'.

```

run name
start time in Unix time (seconds)

STARTdaq_2007_06_21_22_00_00.dat/1182463200
1 1 3729121363 1182463202.095997 389 71 104 348 65535 6207 5999 3952 13118
1 2 3729121363 1182463202.095997 56 257 92 79 65535 6207 5999 4128 13102
1 3 3729121363 1182463202.095997 104 63 93 137 65535 6207 5983 4256 13118
1 4 3729121363 1182463202.095997 159 56 91 70 65535 6207 5999 4352 13102
1 6 2 3729121363 1182463202.095997 627 856 0 767 65535 6207 5999 4416 13118 18
1 1 1 3729145031 1182463202.285981 441 77 113 373 65535 6207 5983 4368 13118
1 2 2 3729145031 1182463202.285981 60 258 209 90 65535 6207 5983 4432 13102
1 3 4 3729145031 1182463202.285981 97 51 71 141 65535 6207 5999 4480 13118
1 4 4 3729145031 1182463202.285981 158 66 92 77 65535 6207 5983 4512 13118
1 6 2 3729908496 1182463208.395981 624 851 0 770 65535 6207 5999 4528 13118 3

ADC module number
det no. with greatest energy
time stamp (8E-6 seconds)
Unix time (seconds)
energies (channels)
TTL veto number
temperature 1
temperature 2
humidity reading
flowmeter reading

.
.

END3600 — run length (seconds)
SETTINGS
det: 1, 2, 3, 4, 5, 6, 7, 8, 9, ...
on: 1, 1, 1, 1, 1, 1, 1, 1, ...
HV: -6, -1250, -1251, -6, -1248, -7, -997, -998, -997, ...
GB(16): 0, 20, 30, 0, 40, 0, 40, 30, 30, ...
Amp: 23, 23, 23, 23, 23, 23, 23, 23, ...
Thr: 21, 3, 4, 19, 2, 14, 3, 10, 4, ...


run name
start time in Unix time (seconds)

first event
second event
collective run settings printed at end of file

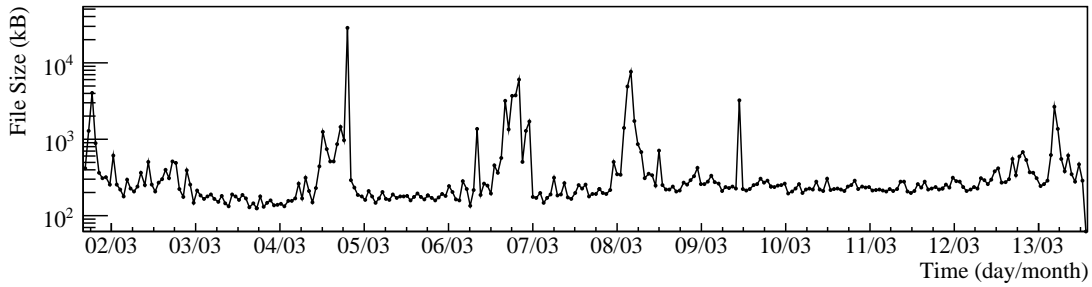
```

Figure 2.11: The data file format. In this example the triggers are propagated to all ADC modules and written out consecutively. Readings from module 5 are not reported since none of the ADCs in that module have been activated. Each line with the same time stamp and Unix time are one coincident event. All parameters that are constant during a run are recorded at the end of the file, where **det** refers to the detector number or ADC number, **on** refers to whether the ADC is activated, **HV** is the High Voltage in volts, **GB**, the Grid Bias in volts, **Amp** is the ADC amplification setting and **Thr** is the ADC trigger threshold setting.

hour. It is therefore possible that settings could have changed mid run without being recorded. This is only likely to occur with the trigger threshold setting, which is sometimes necessary to change. For the analysis this is fine if the threshold is increased, but at time of writing the DAQ should be stopped before thresholds are decreased.

2.2.11.2 File sizes

As can also be seen in Figure 2.11, the number of characters recorded per line to a data file is about 75. So per event, for 6 ADC modules about $75 \times 6 = 450$ bytes are recorded. This should amount to just 7kB per hour for 6 ADC modules but is rarely achieved in practice because of sporadic noisy periods that are recorded when the trigger thresholds are set as low as possible. Consequently, file sizes vary between 100kB and 10MB and can potentially use a GB within minutes. Figure 2.12 demonstrates how the files sizes varied between February and March 2007.

Figure 2.12: Example of *run* file sizes.

2.2.11.3 Organisation of data

The data recorded by the DAQ on *cobra3* is copied regularly to the computer *cobra2* in the directory `/data/COBRA/DIR_NAME`, where `DIR_NAME` is named according to the date that the pre-calibration is made with prefix describing the setup. *E.g.* `.../sfa20_20071108`, where “`sfa`” stands for Sixty Four Array, and `20` is the number of ADCs in use. The `README` in `cobra2:/data/COBRA/` is used to describe the contents of the folder, and in particular, refers to the files `LOG_DATA.TXT` and `LOG_HARDWARE.TXT`. The former file is used to summarise all of the data contained within the folder and should be the first place to look before compiling the data. The current contents of this file are provided in Appendix C. The latter file is used for any hardware changes that are made to the experiment that may be useful in the data analysis. Such changes should also be recorded in separate `README` files located in the data directories. `README` files can be created by running the client command, `client readme`, and copying the generated template from `/mnt/data/COBRA/new_README`¹⁵ to the data directory on *cobra2*.

2.2.11.4 Calibrations

Calibrations are performed with ^{22}Na , ^{232}Th and ^{57}Co radioactive sources (see Section 3.2) and are taken before and at the end of typically a two-week data taking period, but may be several weeks apart if no-one is available to perform the calibration. A new data directory is created on each calibration. Pre-calibration files are saved to a sub-directory called `PreCalib` and post-calibration files are saved in `PostCalib`. In the event that the DAQ is stopped suddenly, for example if there is a power cut, a pre- or post-calibration may not be taken. In addition, if no changes are made to the apparatus after a post-calibration, the calibration is also used as a pre-calibration for the following period of data. Comments are added both to the `README` in the data directory and to `LOG_DATA.TXT` to specify which calibration should be used for which set of data. It is also useful for the analysis to provide a copy of the common calibration in each data folder.

In special situations such as a calibration drift being clearly visible, the data files are split in two with additional comments specifying clearly when the calibrations were made and to which data they belong. Splitting the data in a folder can create confusion if a backup or local copy of

¹⁵The `/data` directory on *cobra3* is mounted on *cobra2* under `/mnt/data`

the data has already been made, but is usually worth while for the analysis of the data. With the development of analysis tools it is common to have to go back to recompile the data from the raw data files many times. Thus in order to minimise the work involved with the compilation, keeping like data together is essential in order to avoid repeating past analysis. If a proper database is set up in the future it should make book-keeping simpler by linking each run to its calibration files.

See Section 3.2 for a discussion on the analysis of calibrations.

2.3 ACID—Analysis Code

Analyser for COBRA's Interesting Data

2.3.1 General discussion

In order to analyse the data for this thesis much work was done developing tools to make the analysis easier. The analysis code had to serve two purposes: physics analysis, and identifying problems with the electronics. The latter requirement contributed most to the complexity of the software since it was required to be both flexible and interactive. However, despite demands for flexibility, simplicity was always a key aim in the software development, which is important to anyone new to the code.

The analysis code, ACID, is still being developed, but the most important functions have been written and amount to many thousands of lines of code. It is hoped, that if the code does not survive further major upgrades to the experiment, that the experience gained can at least contribute to future analysis methods. It would be useful for the simulation package (see Section 2.4 below), which is written in C++, to link more closely with the analysis tools. Currently the simulation package does not support time, which would greatly benefit understanding the backgrounds for timing searches (Section 4.2) as well as handling the varying data thresholds (Section 3.5.2) that had to be introduced.

ACID code is written in C with a little C++, and makes use of the analysis tool kit ROOT¹⁶, developed at CERN. The following sub-sections look at the basic techniques of the analysis code, then in Chapter 3 some of the main functions are mentioned with examples of their use. A tutorial to using ACID is given in Appendix B.

2.3.2 Key requirements

The key requirements of the analysis tool kit are as follows:

- | | |
|-------|---|
| Speed | Despite being a low background experiment, due to the inevitable inclusion of noise resulting in large data files, all parts of the code that are CPU intensive must be pre-compiled. |
|-------|---|

¹⁶See <http://root.cern.ch/>

- Interactive Due to the above requirement it is essential that the pre-compiled functions are interactive enough that they can be used for refined requirements without recompiling. For example, as many input parameters as possible should be allowed and their output should be accessible by other functions. The use of interpreted code is most useful for handling the compiled functions.
- Modular The analysis should be broken down into manageable chunks and run largely independently. Too large chunks—and the functions become cumbersome and difficult to maintain. Too small (and interlocking) chunks—can cause undesired behaviour of one function with the development of another, and require more maintenance.
- Memory Due to the fast response of computer RAM (rapid access memory) compared to the response of a hard disk drive, there are obvious advantages in speed in loading all of the data to RAM for analysis. However, due to the potentially large data files to be analysed, loading everything to RAM is not practical. ROOT’s binary files offer a good solution to this using compressing algorithms based on the same technology as `gzip` and indexing that greatly enhances access speeds [ROO].
- Documentation Even for those familiar with the code, due to the inevitable large number of options and variables associated with each function, instructions on how to use each function and its limitations should be easily accessible.

2.3.3 Framework and analysis techniques

2.3.3.1 The programs

The steps involved in analysing the data are shared between a collection of programs. The discussion here assumes a reasonable knowledge of C or C++ and of ROOT. The programs are listed below.

`sfalist2root`: This is a pre-compiled application that takes as its input a list of calibration and resolution equations for each detector and a list of data files to be analysed. It stores the data in calibrated form together with all important information (explained in the following subsections) in a compressed format in a single ROOT binary file. The application uses code from `list2root`, developed by H. Kiel for the previous 4-array COBRA setup, but unlike the original code does not perform any analysis itself. The main developments were to introduce arrays for each `leaf` of an event so that the analysis of any number of detectors could more easily be handled. Two more `trees` were also added to the data file and many more `leaves` to aid the analysis. These included ADC trigger threshold settings and navigational aids to provide easy access to settings without duplication.

`joininggroups`: Also a pre-compiled application, this is used for combining different datasets.

`sfaplot`: This provides easy access to the data in the ROOT files and includes many functions for the analysis of the data and amounts to about 4000 lines of carefully written code.

All main functions begin with `ss` for quick listing of the functions on pressing the TAB key. A few basic functions such as `SSload` and `SSsavechanges` are expected to be used by anyone using the analysis software. A number of functions for common tasks such as plotting energy spectra, the energy of every event against time, the number of events within an energy window, and creating histograms of the time between events, are also provided for general use. Then there are dozens of functions either in the beta or experimental stage or for small tasks such as undoing changes to the data. Examples of the output of the main functions are given in Section 3.3.

`calibrate`: This tool was developed by J. Dawson as a standard calibration method to be used by COBRA and uses the peak searching and background subtraction technologies of ROOT. To enable a better fit of the calibration peaks two Gaussian functions are fitted on either side of a peak and an average resolution is returned. The tool was extended by myself—to further automate calibrations and export the results into a suitable format.

A more detailed introduction to using the analysis tools is provided in Appendix B and examples of their use can be found throughout Chapter 3 together with a discussion of difficulties encountered and why certain analysis methods were called for. For the discussion of Chapter 3 it is probably still worth describing the approach, or framework, on which the functions depend.

Event structure	Run structure	Group structure	Properties
Energy* time timer time status*	high voltage setting* ADC amplification setting* ADC threshold setting* lower data threshold*	upper threshold* lower threshold* calibration equation* resolution equation*	Flags
veto flag*	detector on/off status* flag*	detector on/off status* flag*	Navig
run number group number	start time first event time number of events group number	start time first run number number of events number of runs group name	

Table 2.2: Data structures used to access the data with `sfaplot`. Entries marked with an asterisk are vectors with an entry for each detector, except the *status* entry which is also a vector but holds readings of the temperatures of the lead castle and the VME crate, the humidity inside the Faraday cage and the flow-meter reading of nitrogen entering the Faraday cage. See Section 2.3.3.3 on the next page for more information on the structure entries.

2.3.3.2 Data structure

A central reference point when writing a new function for ACID are the C structures that are used to access the data and are represented in Table 2.2. As the table demonstrates, the data is divided and stored in three categories of *events*, *runs*, and *groups*.

An *event structure*, which holds information associated to individual events, is itself a kind of array, stored in binary format on disk. Information from only one event is loaded to RAM at a time. The only exception to this is the *flag*, which has to be loaded to RAM because it must be modified, and consequently is the main parameter limiting the size of a ROOT file that can be analysed. The *run* and *group* structures occupy only a small amount of memory and are also loaded to RAM.

The *run* structure stores all of the information that is common to a data file. To keep the analysis simple, only complete¹⁷ data files are included in the ROOT file so each *run* is equivalent to exactly 3600 seconds of data taking. A *group* is usually defined by a set of *runs* with the same calibration. On disk, a *group* can be identified by a folder containing a set of *runs* (or data files). The name of the folder is the same as the *group name* stored within the *group structure*.

Note, the *event structure* stores all events in a dataset, which can comprise of thousands of *runs* and many *groups*. The *run* and *group structures* likewise store their information separately for the whole dataset. Each structure holds navigation pointers and knows to which *run* or *group* it belongs. The decision to store the data in this format was made early on and appeared most practical, providing easy access to event information for simple functions. However, if the code were to be translated to C++ it would probably be possible to store the data in a nested way such that the *groups* contain the *runs* which provide access to the *events*. It could be investigated whether this would simplify more complicated functions by allowing a “*group Class*” to be able to automatically check whether a particular region of data is suitable for analysis.

Entries in the structures fall into the three categories, *properties*, *flags* and *navigation* and are now described.

2.3.3.3 Structure properties

Event Structure The main properties of the *event structure* are the energy and time of each event. The *status* entry holds information that is required to be monitored and can vary on a smaller time-scale than an hour. Currently these are set as the temperatures of the lead castle and the VME crate, the humidity inside the Faraday cage and the flow-meter reading of the nitrogen entering the Faraday cage. These can easily be changed if required.

Run structure The properties of the *run structure* are all the parameters that can be requested by the DAQ. The grid bias voltage is not included here since at the time of writing the grid bias supply does not provide feedback. The difference between the “ADC threshold setting” and the “lower data threshold” should be noted. The former is the trigger threshold that can have a number between 0 and 127 reported by the ADCs and must be converted to energy for use in the analysis (refer back to Section 2.2.10.2 on page 34). The latter is a variable that must be calculated during data cleaning and is essentially an estimate of the noise threshold in keV.

Group structure From the *group structure*, the calibration equation is most frequently used in the analysis for translating the ADC threshold number to its value in channels and then keV,

¹⁷A complete data file is exactly an hour long. An incomplete data file is one where, for example, the DAQ has been stopped before a whole hour has expired.

which can be compared to the data. The resolution equation is frequently used during the analysis in coincident searches. The upper threshold is the largest energy that the ADCs can record and is calculated by passing the largest channel number (2^{14}) through the calibration equations. The lower threshold is by default set to zero but can be set to a chosen channel number when converting the raw data to a ROOT file with `sfalist2root`. This tells the program not to include any data below the required channel number from a specified detector when there is no energy deposition above the trigger thresholds on any other detectors. Using this feature can speed up analysis by reducing the ROOT file size by discarding uncorrelated noise events. Uncorrelated noise events can of course be discarded from the ROOT files at any time during the analysis.

2.3.3.4 Flags

The flags are used to mark the data if it is not suitable for analysis. Flags are also useful for selecting events or periods of data for independent analysis.

Event structure The `veto` entry is an integer, and when converted to a binary number each 0 and 1 can represent a veto or state of separate instruments. Currently connected are the vibration and mains spike detectors, but it is also used by the ADC to report errors and referred to as a TTL number in the DAQ manual [Wil06]. The entry, `flag`, is normally just set to 0 or 1 and is only used in the analysis. Initially set to 0, the idea is that any function can run through the data marking individual events (setting the flags to 1) that can then be plotted or highlighted by analysing the data again with another function. This approach to analysing the data greatly reduces the complexity of functions compared to trying to solve multi stage problems all in one go. The disadvantage to running many times over the data is analysis speed, but the typical time to process a 70 MB file of 100 hours of data and produce a spectrum takes about 10 seconds (using a modern laptop with 2.4 GHz processor and 2 GB RAM), which is quite acceptable.

Sometimes more complex tasks are required that need more than a two-state flag. One modification that is being introduced is the ability to accept different flag numbers where 0 specifies that the data is good and anything non zero can either be discarded or plotted, or, only plotted if the flag is set to a specific value. A number is often chosen from the ASCII character map, such as ‘b’ (for background) that has the ASCII number 98. Using such flags to mark different identified backgrounds, correlated events, or identified electronic noise, enables the tagged events to be more easily compared with each other.

Another method that would avoid overwriting flags and aid correlation checks between backgrounds would be to compress and decompress binary numbers. This method was successfully used when an event flag was required for each detector in the analysis. The small processing time required to convert an integer to and from a binary number was found to be worthwhile, because the alternative of filling a large array with the size of the number of detectors times the number of entries requires a large amount of RAM. This can easily lead to memory shortages, requiring the use of a slower access hard disk drive.

Individual events are normally only flagged for removal when they can be clearly tagged as being coincident with a veto event or identified background. It can be tempting also to use the

event flag for the removal of periods of data. For example, marking all events within a 10 second period to be rejected. Doing so greatly increases the complexity of keeping track of the live-time. A method of keeping track of such cuts was experimentally developed and involved saving the start and end times of each cut and a function for merging separate cuts together. However, a decision between collaboration members was made that periods of data would only be rejected on a hourly, or *run* to *run* basis. The advantage of this method is that it is more simple to keep track of the live-time, but a potential disadvantage is that noise that slightly overlaps a run boundary could be missed.

Run structure The detector on/off status in the *run structure* is set to 1 (on) or 0 (off) to specify whether an ADC was active or not. This allows detectors to be turned off between calibrations (if they cause problems) without having to start a new *group*, thus reducing work but keeping analysis simple. The separate *flag* is provided for the user to discard whole runs that are identified as being defective in the analysis. Both flags are used when calculating the used live-time. Modifications to the flags are easily saved enabling *flag* to be also used for plotting selections of data without losing cuts already made.

Group structure The *group structure* has similar flags as the *run structure* with a slight difference in use of the “detector on/off status” flag in that it is set by the user. Having compiled the data once, the user may decide that despite an ADC being on, none of the data is suitable for use. Turning the detector off by hand in the *group structure* prevents the data from being used, even if the “detector on/off status” is set to *on* in the *run structure*. The user should also enter the changes into an input file of `sfalist2root` that sets the flag again if the data must be recompiled.

2.3.3.5 Navigation

Navigation is required for accessing information of one structure from another. It is also used for jumping about the *event structure* to increase processing speed. There are two approaches to writing a function:

1. Loop over the whole *event* tree while checking the flag status of each event, including *run* and *group* flags.
2. Loop over all *groups* and all *runs* within each *group* and all *events* within each *run* while checking the relevant flags on each loop.

Depending on the purpose of the function one method will require fewer lines of code than the other.

2.4 Venom

Venom is a simulation package for the COBRA experiment that was developed by B. Morgan and J. Wilson and replaces the previous simulation package, *Poison*, developed by H. Kiel. Both

simulation packages use the Geant4 toolkit¹⁸ that was designed primarily for simulating the high energy particle experiments at CERN¹⁹. The toolkit also works well for low background experiments and allows ‘particles’ to be created and tracked within specified materials.

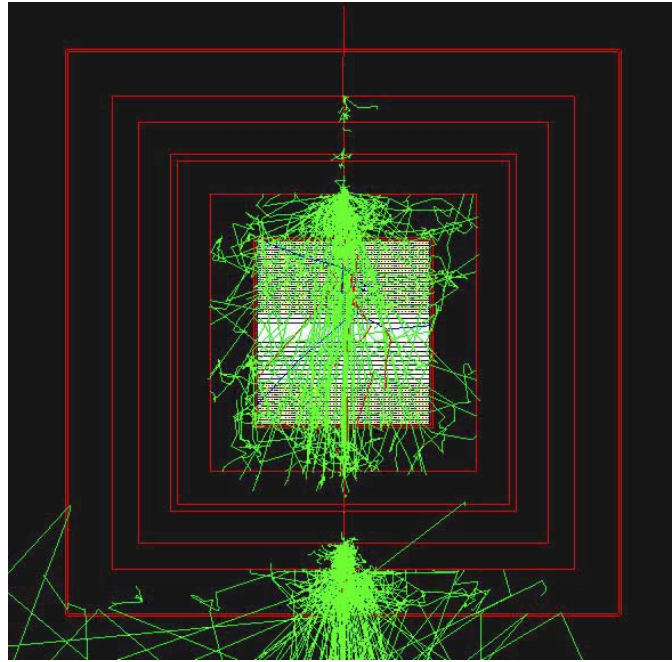


Figure 2.13: Simulation using *Venom* of a muon passing through an array of detectors and giving rise to showers of secondary particles. Picture taken from COBRA photo archive.

Venom can be used to simulate particles either in simple arrays of detectors or in a model of the current 64-array prototype. Figure 2.13 demonstrates a muon passing through a large array of detectors (central area) surrounded by copper and lead shielding, producing showers of secondary particles. The green lines show the paths taken by gammas. A few traces (blue) of nuclear fragments can also be seen. Simulations are particularly useful for calculating the efficiency of detecting radiation from known radiation sources. In Chapter 4 simulations are used to generate energy spectra from known backgrounds that can be compared to real data.

Different *event generators* are used depending on which background is being simulated. Single radioactive decays were simulated by Geant4’s **GRDM** package. However, because the radioactive decay chains are not fully implemented in the package the event generator, **chaingen**, was developed by B. Morgan and J. Wilson. This generator uses code from the **GRDM** package but correctly includes all of the main ^{238}U and ^{232}Th chain branching fractions and allows the user to change the fractional intensities of the decays in the chain to represent a decay chain that is out of equilibrium. Double beta decays can also be simulated with **decay0** [PTZ00] or another custom decay generator, **DBGen**, originally written by H. Kiel.

¹⁸www.geant4.org

¹⁹www.cern.ch

Chapter 3

Data Selection and Performance

Before the data can be used for signal and background searches, selections must first be made in order that data of the same quality can be analysed and that any electronic noise is removed. Various methods are used to achieve this and are demonstrated in this chapter. Based on the experience of these tests a method to automate data preparation is developed and demonstrated. Automation is key to the successful running of the experiment because for larger arrays of detectors it will be impossible to monitor and prepare the data without an equally scalable work-force.

3.1 Data Taking Periods

Data analysed for this thesis is considered in different parts as shown in Table 3.1 on the following page. Each part, called a *dataset*, is made up of a collection of *groups*, which in turn are made up of hour-long *runs*. Definitions of *runs* and *groups* were made in Section 2.3.3. The selection of *groups* that form a *dataset* are made for discussion purposes enabling periods of data that were taken under different conditions to be easily compared.

The main datasets analysed in this thesis are L1a-c with an occasional comparison with other datasets. Other data taken at LNGS during research for this thesis are also summarised.

A report comparing datasets CAM and VME1 was made by myself [Ree06a] to confirm that the CAMAC and VME data acquisition systems were consistent, which they were. For that set-up an array of 4 red-painted detectors were used. Later a comparison of VME2 with VME1 was made [Ree06b] to check if the background levels dropped when replacing the Pertinax holder with Delrin and the thin Kapton cables were also used for the first time. Only a small drop in the background was observed indicating that there were other more prominent backgrounds.

Layer 1 of the 64-array (red-painted detectors) was installed on the bottom of the nest in the beginning of March 2006 (L1u), but due to pick-up from the HV-cable most data was not useful for physics analysis. The DAQ was stopped and started many times while various tests were performed to solve the nature of the problem. Later in the year, four colourless detectors were also installed on the top rung of the nest and some useful data was taken (CL1) and showed a significant drop in the background.

Name	Description	Period day/month/year	Live-time hours days	
CAM	CAMAC DAQ - Pertinax holder, 4-array	10/02/05→17/03/05	602	25.1
VME1	First use of VME DAQ, 4-array			
VME2	Delrin holder and Kapton cables	29/04/05→22/02/06	5494	229
L1u	Layer 1 (16-array) - unshielded	26/03/06→05/12/06	-	-
L1a	Pre-move - Shielded HV-cable & veto	22/01/07→10/04/07	1094	45.6
L1b	Post-move	25/04/07→23/07/07	1878	78.2
L1c	New pre-amps & N-flushing	30/07/07→26/09/07	1039	43.3
L1d	New number scheme	21/10/07→17/03/08	2461	102
CL1	Colourless detector data - Unshielded Kapton cables	10/08/06→23/09/06	1018	42.4
CL2	Colourless detector data - Shielded cables & N-flushing	21/03/08		

Table 3.1: Data taken during research for this thesis.

By December 2006 a shielded high voltage (HV) Kapton cable and veto had been made and were installed just before Christmas. No shielded HV cable was made for the colourless detectors and they were therefore removed. Due to a technical reason¹ useful data taking did not start till 22 January 2007. Datasets L1a-c cover data from this point onwards and most detectors ran with very few problems.

In October 2007, an attempt to install the remaining detectors of the 64-array with a new contact technique developed in Dortmund was only partially successful and the 48 detectors were removed again in order to improve the contacting technique. The contacting technique required a new numbering scheme to be used for the detectors (see page 151). This scheme was not reversed for dataset L1d and because there was no time to modify the analysis tools to compare data with different numbering schemes a cut-off date for data analysed for this thesis was set at before this date.

3.2 Calibrations

Calibrations, as has been mentioned previously, are made every two weeks if possible, but due to practical and financial limitations calibrations were not usually taken more often than once

¹The problem was, that in order to save disk space and reduce dead time, the ADC module used for the HV-veto was modified so that it could not self trigger and would only be read out when an unmodified ADC module triggered. This had the undesired effect that the modified module would not reset properly before a real event, and led to sub-threshold events being falsely recorded with a greater energy. A work-around was implemented in the DAQ software by J. Wilson that enabled unmodified ADCs to be used by rejecting HV signals that were not coincident with a detector signal. This keeps data files to a manageable size.

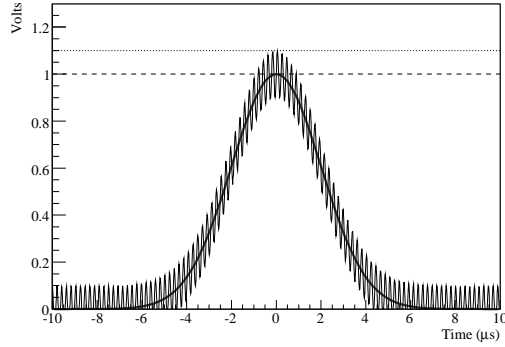


Figure 3.1: Representation of a noisy signal. Note, a sinusoidal signal is used only for demonstration purposes. Noise, for example, from leakage currents through the detectors, looked random and some frequencies were able to pass through the shapers.

a month. Need for frequent calibrations result from calibration drifts. Precise calibrations are required for gamma peaks in the data to be identified and limits on DBD signals to be accurately made.

There can be more than one cause for a calibration drift. A common cause is a change in amplification that can arise from a change in temperature of the electronics, particularly in an amplifier. Another cause of drift could arise from changes in the active volume of a detector. For example if the high voltage is not sufficient and drops, not all electrons generated by an event close to the cathode may reach the anode.

A third cause of calibration shift can arise from the way the ADCs measure the pulse height of an event making the calibration sensitive to the noise level of a detector. This is demonstrated in Figure 3.1. The solid, Gaussian curve represents a signal before entering an ADC with no noise. A sinusoidal oscillation is added to represent a noisy signal. The dashed line shows the actual pulse height of the event and the dotted line shows the height of the noisy peak as measured by the ADCs giving an offset to all measurements. A calibration made with such noise is only valid for as long as the noise level remains constant.

Comparisons of pre- and post-calibrations in this section show that slight calibration drifts do occur but appear to be small for most detectors. Better understanding can be made by prolonged measurement of a calibration source. However, carrying out tests is made difficult by the time also required to take *low level data*² as well as the remoteness of the experiment. On a number of occasions calibrations were made (remotely) over several days, but it was found not to be a sufficient time to reach conclusions as to the dominant causes of calibration shifts. Slight shifts in calibration were sometimes observed but were rare and would occur only on a small number of detectors. Two temperature sensors exist, one inside the Faraday cage and another on the VME crate. However, although calibration shifts were often observed shortly after calibration when the temperature of the cabin would also return to equilibrium (having usually increased in

²Low level data refers to data taken with no calibration source, that is in normal data taking mode.

temperature due to the body heat of someone working in the cabin), no correlation of temperature and calibration shift has yet been observed.

3.2.1 Calibration method

COBRA currently has use of three calibration sources. ^{22}Na and ^{57}Co which COBRA owns itself, and ^{228}Th , to which access is limited and hence is used less often. The radioactive sources are attached to thin cables and are fed in through Teflon tubes (as was demonstrated in Figure 2.6b) close to the detectors. Gammas pass through the metal casing of the source and between 1–3 cm of air to the detectors where some gammas deposit their full energy. A histogram of the number of events observed by each ADC channel number is saved and the peaks that accumulate in the histogram corresponds to the energy of the gammas released by the radioactive source.

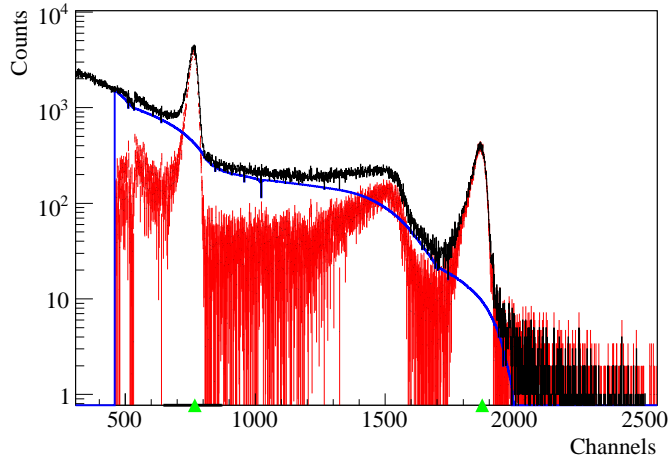


Figure 3.2: Typical calibration spectrum using a ^{22}Na radioactive source (black). The background of the gamma peaks (blue) is predicted and subtracted (red). The peaks are then fitted and marked (green). The energy of the peaks are 511 keV and 1274.5 keV.

An example of a typical calibration spectrum shown (in black) in Figure 3.2 uses the ^{22}Na (sodium) calibration source. The sodium source decays via positron emission ($^{22}\text{Na} \rightarrow {}^{22}\text{Mg} + \beta^+ + \gamma$) with a de-excitation gamma energy of 1274 keV and can be seen at about 1870 channels. The positrons annihilate with an electron, when they have lost their kinetic energy, and produce 511 keV gammas in opposite directions that correspond to the rest mass of the electrons and positrons. One of these annihilation gammas is observed by the detectors and produces the lower energy peak at 750 channels.

3.2.1.1 Calibration tool

Calibrating 64 or more detectors can take a lot of time if done ‘by hand’, so creating a tool to automatically locate and fit the peaks was developed by J. Dawson [Daw]. The tool first locates the peaks and predicts the background (blue line) before subtracting the background

(red spectrum) and then fitting the peaks. Because the peaks are slightly asymmetric, which is characteristic of CZT detectors³, the peak shape is approximated by two Gaussian halves with different standard deviations. The average of the Gaussian means are then reported together with the average of the standard deviations.

To save more time I further automated the tool to loop through the detectors and write the results to file when the user confirms that the fit is successful. Entirely automating the process is made difficult by the fact that some detectors may have poor resolutions or very different calibrations. Other difficulties arise from poor statistics from some detectors (if the calibration source was not placed correctly), different noise levels, and the location of the trigger threshold that produces the sharp step that can be seen just over 500 keV.

If a calibration fails it is usually obvious, in which case the starting parameters for a fit can be modified to enable a successful calibration to be made. However, obtaining the correct resolution is more difficult and requires the background to be accurately subtracted. As in the example of Figure 3.2 the blue line can be seen to not precisely overlay the data (black). This will result in the background being slightly underestimated and in turn an underestimate of the resolution will be made.

Some improvements to the calibration technique might be:

- ▷ To record the unique starting parameters for the fit that can be later accessed and to save time on each successive calibration (these numbers would have to be updated whenever an amplifier or noise threshold changes).
- ▷ Rather than subtracting the background the estimate for the background could be scaled as an extra parameter when fitting the peak.
- ▷ The trigger threshold could also be recorded during calibration and the fit restricted above its value to avoid sub-threshold events affecting the fit.
- ▷ Information about the kind of radioactive source could also be used, such as known relative distances between photopeaks and their relative size.

3.2.1.2 Calibrations with ^{57}Co and ^{228}Th sources

Examples of ^{57}Co and ^{228}Th calibrations are shown in Figure 3.3 on the following page. The ^{57}Co peak is at 225 channels and corresponds to 122.1 keV. The peak below this is from noise threshold events that are recorded when a neighbouring detector is triggered. The accumulation of events at 350 channels is probably due to the intensity of the source leading to separate signals overlapping in time. The peaks labelled “double” and “single escape” in the ^{228}Th spectrum arise from the pair production of the 2614 keV gamma ($\gamma \rightarrow e^+ + e^-$) inside a detector. The positron quickly annihilates to create two 511 keV gammas. In the case of the single escape one of the 511 keV gammas escapes the detectors and with the double escape neither of the 511 keV gammas are detected [Kno79b, p297]. The peak labelled with two energies is a superposition of a 510.8 keV

³This slight asymmetry is mostly due to hole trapping that is not completely alleviated by the anode grids. To a lesser extent, electron trapping and electric field inhomogeneities might also play a part.

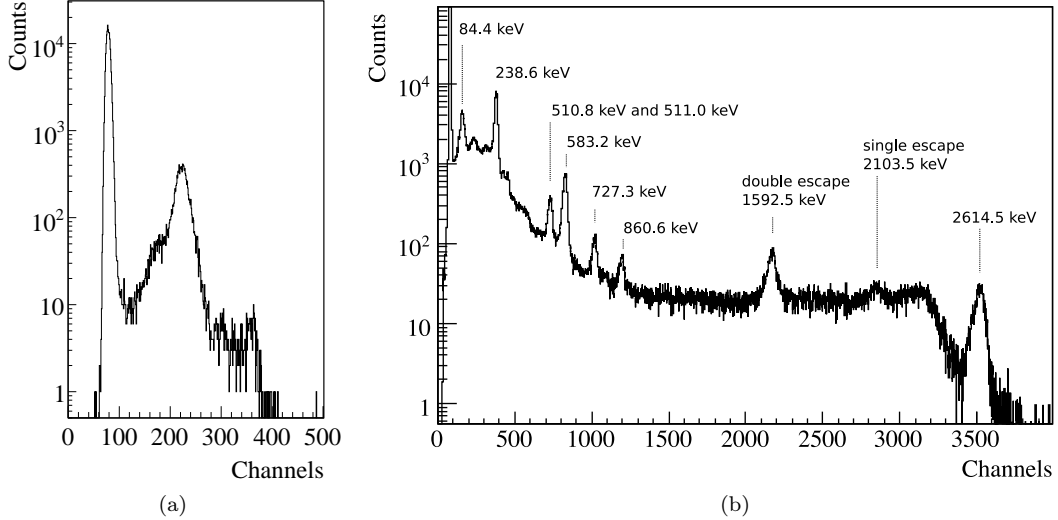


Figure 3.3: Calibration spectra of (a) ^{57}Co and (b) ^{228}Th . The energy of the ^{57}Co peak is 122.1 keV and the energy of the main gamma peaks of ^{228}Th are labelled.

gamma⁴ and a 511 keV gamma from a pair production and annihilation gamma created outside of the detectors. The Compton edge of the 2614 keV gamma is also clearly visible at 3200 channels.

3.2.1.3 Combining calibrations

Calibrations made before and after a period of undisturbed data-taking can usually both be used to provide a better estimate for the calibration. To calculate an equation relating channel numbers of an ADC to energy requires at least two calibration points at different energies. The method used for the data analysed in this thesis was to create a graph, with on the y-axis, the energy and its uncertainty in channels found with the fitting tool, and the known energy of the peaks on the x-axis. Channels were plotted on the y-axes to ensure the uncertainties in channels were included in the fit. A least-squares fit of a first order polynomial was then made to the data with the `Minuit` package in ROOT. The slope m and offset c of the fit was used to calculate the a function for the energy, E , of each channel number, Ch , with $E = Ch/m - c/m$.

Combining more calibration data, be it a post-calibration from the same source or a calibration from the ^{228}Th source, would be achieved by including the calibration points in the same graph described above. A new straight line would then be fitted to the data. This method is mentioned as it is suggested that it is more accurate than the alternative approach of calibrating each spectrum separately and calculating the average of the slopes and intercepts at the end. Another advantage of this method is that calibration points where the fit failed are easy to spot.

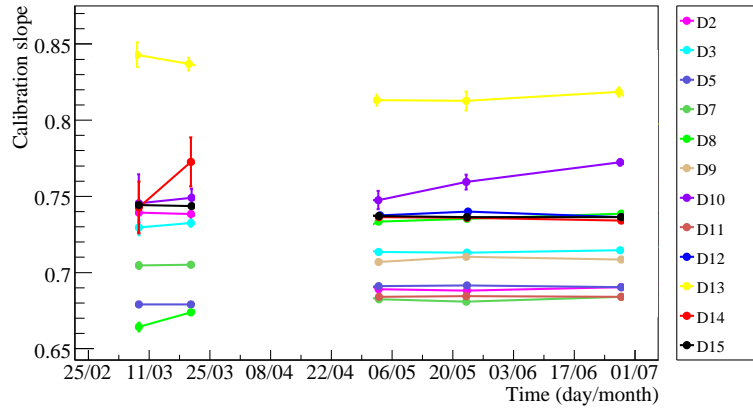


Figure 3.4: Calibration slopes as a function of time for working detectors.

3.2.1.4 Calibrations over time

Monitoring how calibration equations vary with time is a good way to learn about the reliability of the detectors. However, due to development work on the apparatus, amplification of the electronics were sometimes changed and new optimum voltages were used. Consequently these calibrations cannot be compared. In fact there are a very limited number of calibrations that can be compared for datasets L1a-c, where no maintenance work was performed in between. Figure 3.4 shows the slopes of some calibration equations and are linked together where no development work was carried out in-between. What is interesting to note is that often different detectors observe shifts in the calibration in opposing directions. This suggests that whatever causes the changes in calibration is not merely environmental, such as a change in temperature. The detectors that most consistently show calibration shifts, namely detectors 8, 10 and 13 have been noted to have problems with large leakage currents. Detectors 10 and 13 have had to be run at reduced high voltages of -697 V and -595 V and grid biases of just -5 V and -10 V respectively. The detectors that are not shown in Figure 3.4, namely 1, 4, 6, and 16 could not be operated. Of these detectors either one of the contacts to the detectors are believed to be broken, or in the case of detector 16, leakage current between the anodes and cathode was so bad that it could not be operated for any useful length of time.

3.2.2 Resolutions

Knowing the resolution of each detector is essential for an accurate limit on neutrinoless DBDs to be determined and is also required for other background searches. This section summarises the difficulties encountered when calculating the resolutions.

The first difficulty already mentioned arises from fitting a calibration spectrum as it requires an understanding of the underlying continuum that distorts the photopeaks. This continuum is an amalgamation of Compton spectra and is sensitive to the geometry of the set-up and particularly

⁴The 510.8 keV gamma is produced with a quarter of the efficiency of the 2614 keV gamma from the same daughter isotope, ^{208}Tl . See Table A.2.

Detector	Resolution equation (FWHM)	
	slope $\times 10^2$	const. (keV)
2	2.31 5	10.7 7
3	2.29 5	8.5 4
5	1.87 5	9.1 4
7	2.19 5	17.2 4
8	4.31 9	8.6 5
9	2.06 6	9.5 4
10	5.9 2	34 1
11	3.05 4	11.7 3
12	2.09 4	10.0 3
13	4.3 3	26 2
14	1.80 4	10.5 3
15	2.22 4	9.2 3

Table 3.2: Detector resolutions for datasets L1a-c. Uncertainties on the last digit are given in italics. Note the slopes should be multiplied by a factor of 10^{-2} .

the source location, which is different for each detector. In addition, depending on the setting of the pre-amp potentiometers⁵, the shape of a peak can be distorted, ‘squashed’ to the left or right. Moreover, in a complicated spectrum such as from the ^{228}Th source, with the current resolutions the main photopeaks often overlap. These problems are described in detail in an internal COBRA note [Daw05].

Another issue worth mentioning is the Doppler broadening effect.

3.2.2.1 Doppler broadening

Doppler broadening [Sie80] affects the width of peaks of annihilation gammas. When a positron annihilates with an electron, normally it must lose all kinetic energy before doing so. The total energy of the gammas released is thus equal to the combined mass of the electron and positron. However, it is possible that the positron encounters an electron with finite kinetic energy but the same velocity as itself. With no relative velocity, they can annihilate and produce two gammas of slightly greater or lesser energy than 511 keV, relative to the detector, with the shift in energy depending on whether the gamma travels in the same or in the opposite direction to the original electron and positron. This will normally produce a symmetric distortion (or broadening) of the 511 keV photo peak, and thus will not affect the calibration. It does, however, prevent annihilation peaks to be used to gain an accurate resolution calibration. Compensating for the distortion is difficult to do because it is sensitive to properties of the material in which the annihilation occurs. In our case annihilation can occur not only in the detector but any part of the supporting structure or the radioactive source itself. Incidentally, this effect has been used as a non-destructive method

⁵The potentiometers were introduced on page 34.

to investigate defects and levels of zinc in CZT detectors [AW05], a number that we need to know more accurately.

3.2.2.2 Resolution results

To minimise distortions to the peaks for the reasons mentioned above, only the largest energy photopeaks from the ^{57}Co , ^{22}Na and ^{228}Th calibrations are used and the fits were performed by J. Dawson. The parameters of the straight-line fits for the resolutions are given in Table 3.2, which relate the resolutions of the working detectors in Full Width Half Maximum of a Gaussian function ($\text{FWHM} \equiv 2\sqrt{2\ln 2} \cdot \sigma \approx 2.35 \cdot \sigma$) to the energy in keV. The resolutions as a fraction of energy are typically 3.9% and 2.6% for energies 662 keV and 2805 keV respectively.

3.2.2.3 Average resolution

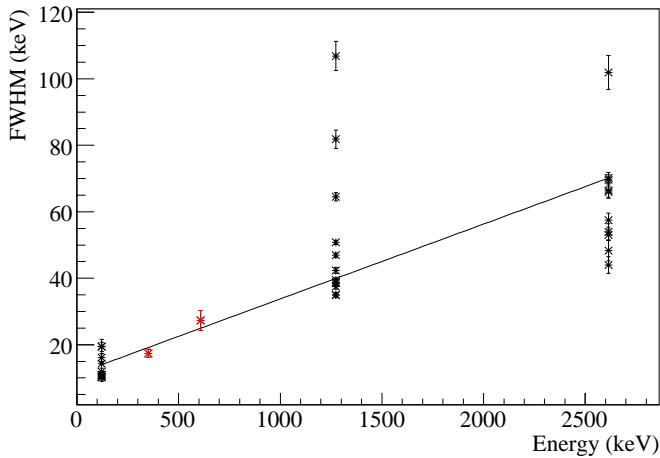


Figure 3.5: Calculation of an average resolution equation for the detectors includes the highest energy gammas from the ^{57}Co , ^{22}Na and ^{228}Th sources (black) and the 352 keV and 609 keV gammas (red) visible in a sum energy spectrum. The fit provides the relation given in Equation 3.1.

The average resolution is useful to calculate for when the data of all detectors are analysed together, which is often done in this thesis to improve statistics. Done precisely, it should be noted that a resolution equation representing all detectors should be calculated by weighting the resolution of individual detectors by the quantity of data they provide. For example, a detector with poor resolution may have been turned on for only a short period of time and so would have had less impact on the joint resolution. In addition, it should be noted that data composed from various resolutions produce non-Gaussian peaks. Moreover, if data is included where the calibration drifts, this will lead to a broadening of the peaks. An approximation to the combined resolution (using the same data that were used to calculate the individual resolutions in Table 3.2) is shown in Figure 3.5. Also included in the fit are the fitted resolutions of the two peaks at 352 keV and 609 keV (red) that are observable in the data (see Section 4.1.1) and the

average resolution was found to be:

$$\text{FWHM} = (2.25 \pm 0.02) \times 10^{-2} \cdot \text{Energy} + (11.2 \pm 0.2) \text{ keV}. \quad (3.1)$$

3.3 Quality Control

3.3.1 General considerations and theory

Like any experiment that is covering new ground, very little can be taken for granted as what to expect from the data. When an event is recorded in this experiment there might be evidence indicating that the event is no more than electronic noise. For example, if the event is seen to occur at the same time as a recorded disturbance. Without such evidence, on an event-to-event basis there is no way of telling if an event is real or not. If the researcher is not given any physical reason *not* to believe his or her data, then there is no motivation to build a *veto* system. This is a real problem for low count rate experiments, as the lower the rate, the greater importance is put on individual events. Given more than just one event, already the powerful tools of statistics can be used. For example, it might be possible to calculate what is the probability that two events occur within a specific time. If the probability is smaller than a chosen probability the pair of events might be removed. These are the techniques the COBRA experiment must use, and based on clues given by statistical probabilities, determine what data is usable and whether new techniques for vetoing false signals must be developed.

One key piece of information that we can use is that all nuclear decays occur randomly in time, with an average frequency determined by the half-life of the isotopes. From this, tests can be made to check that the number of events within a given period occur randomly and any period of data that is likely not to be random is removed, thus enabling the quality of the data for analysis to be improved.

3.3.1.1 The Poisson equation

It can be shown (see [Kno79a]) that data of random origin, when binned in counts per unit time, forms a Poisson distribution:

$$P_\nu(n) = \frac{\nu^n e^{-\nu}}{n!}, \quad (3.2)$$

where n is the number of counts in a bin and ν is the mean of the distribution and the average counts per unit time. So fitting a Poisson function to such a sample of data enables a goodness of fit to be calculated, which gives the probability that the data agrees with theory. Furthermore, any periods of data that fall outside, for example, 3 standard deviations from the mean of the distribution, should be rejected since periods of data with many more counts than the average number are more likely to contain noise.

The rate of events is dependent on the size of the window of energy that is analysed as well as the size of the unit of time. The larger the energy window and larger the time unit, the higher the rate. A more detailed study of fitting with a Poisson distribution is made in Section 3.3.1.4

and an example of fits to the data is given in Section 3.3.3.

3.3.1.2 Time differences

Another equation that can be derived from the random nature of the data is the distribution of the time between events and is also demonstrated in [Kno79a, p97]:

$$P_r(t) dt = r e^{-rt} dt \quad (3.3)$$

where $r = 1/\nu$ is the rate of events and t is time. The equation derives from the product of the probabilities of no events occurring in time t and 1 event occurring after this time within the infinitesimal time dt . It should however be noted, that this equation only holds true if all events contributing to the event rate r have a rate of decay⁶ much lower than r . This is true for most decays.

3.3.1.3 Probability of coincident events

This section looks at some equations required to calculate the expected number of chance (uncorrelated) events observed in a particular time window and is used to understand the significance of the number of counts observed in later background studies. It is sometimes necessary to know the number of expected chance events that are observable as a single event due to the timing resolution of the ADCs. These numbers can easily be calculated also using Equation (3.3). The number, N , of expected coincident events within a given period is given by the integral over Equation (3.3) within the required time window times the number of events, N_0 , that exist in the selection of data studied:

$$\begin{aligned} N &= N_0 \int_{t_1}^{t_2} r e^{-rt} dt \\ &= N_0 (e^{-rt_1} - e^{-rt_2}) \end{aligned} \quad (3.4)$$

where t_1 and t_2 are the initial and final times of the period of interest. This can also be given as a rate

$$R = r (e^{-rt_1} - e^{-rt_2}). \quad (3.5)$$

Also of interest is the number of coincidences between events over different energy regions in the same detector or different detectors. Different energy selections, A and B, lead to different event rates r_A and r_B . When noting that the rate, r , outside the brackets of Equation (3.5) relates to the number of events in selection A, and inside the brackets is the probability for a second event to occur in selection B, then it can be seen that the equation can be modified as

$$R = r_A (e^{-r_B t_1} - e^{-r_B t_2}). \quad (3.6)$$

⁶The rate of decay is related to the half-life of the decay via $r = \ln 2/T_{1/2}$.

The equation can be further generalised for any number of rates r_n as

$$R = r_0 \sum_{i=1,2,3\dots}^n (e^{-r_i t_1} - e^{-r_i t_2}) \quad (3.7)$$

where the selection for r_0 is coincident with an event from *any* selection but itself. Or, for the expected number of events with a coincidence in all selections the product is used:

$$R = r_0 \prod_{i=1,2,3\dots}^n (e^{-r_i t_1} - e^{-r_i t_2}). \quad (3.8)$$

A similar derivation for Equation (3.6) can be found in [Kno79a, p668], but for the approximation that rt is very small making the distribution of Equation (3.4) essentially flat. In this approximation the substitution $\exp(-rt) \approx 1 - rt$ can be used in Equation (3.6) thus simplifying it to

$$R \approx r_A r_B \Delta t, \quad (3.9)$$

where $\Delta t = t_2 - t_1$.

3.3.1.4 Fitting a Poisson distribution

Fitting a Poisson distribution to the data is done with ROOT's standard least-squares fitting algorithm using the `Minuit` library. However, strictly speaking, the least-squares method should not be used for low count statistics because it requires uncertainties that are *normally* distributed [SDH97]. In counting experiments when the number of counts are large, the uncertainty on the number of counts is given by the square root on the number of counts, n . Counts in the Poisson distributions may be as low as 24 in total with one or two counts in the tails of the distributions. The uncertainty on a bin with a few counts is Poissonian. Rather than implement a more advanced fitting technique as described in [SDH97], Monte Carlo tests are made to demonstrate that the least-squares fitting method is sufficient for the purposes of this analysis.

A typical mean of 2.5 counts per hour is used as an example and results of the test for the equivalent number (N) to 24 hours and 2400 hours of data taking are compared. First, a Poisson distribution is generated with a random number generator and the uncertainty $\sigma_n = \sqrt{n}$ is used on the contents of each bin. The distribution is then normalised and fitted with a Poisson function. Examples of such fits are given in Figure 3.6. The results of the fits are both in agreement with the simulated rate of 2.5 counts/hour and have reasonable values of χ^2 .

To check the success rate of the fits and the accuracy of the estimated uncertainty, 10 000 Poisson distribution samples were generated and their fit results histogrammed. Samples for 24 and 2400 random events, N , are shown in Figure 3.7 on page 59. The distribution of means (Figure 3.7a) for $N = 24$ demonstrates that for the small sample size, a Gaussian mean of 10 000 samples is 2.574 ± 0.005 counts/hour and is just 3% from the true value of 2.5 counts/hour. The standard deviation that was calculated to be 0.465 ± 0.004 counts/hour is similar to the average

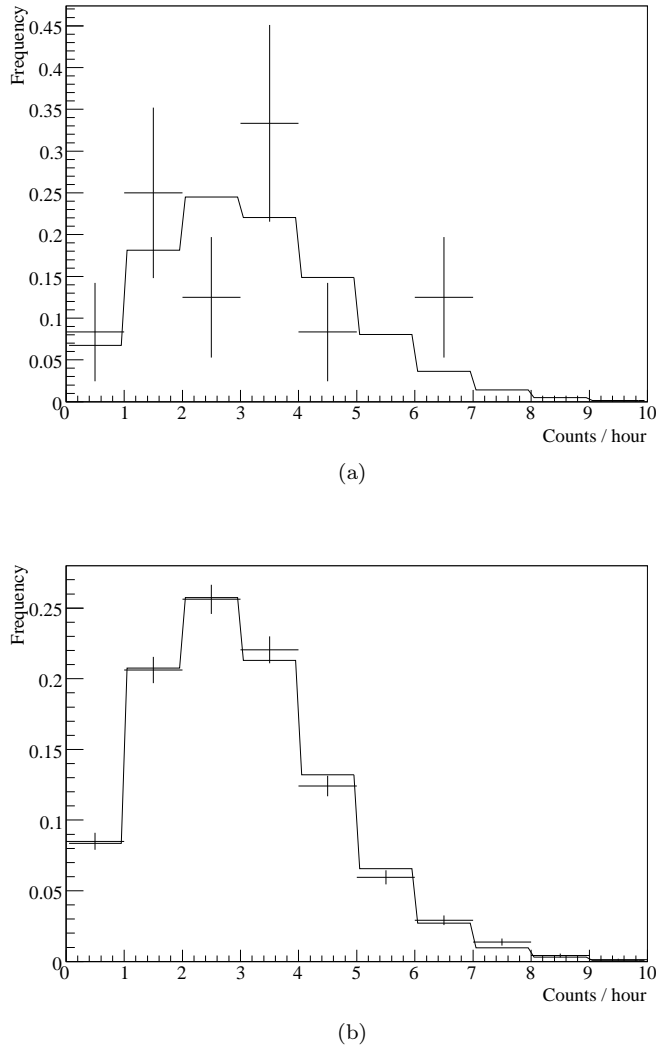


Figure 3.6: Simulated Poisson distributions fitted with a Poisson function. Poissonian randomly distributed events are generated (crosses) with a mean of 2.5 and histogrammed as shown. (a) 24 random events (N) are generated which is equivalent to 24 hours of data when counts are made per hour. The mean of the distribution was calculated with the fitting routine to be 2.70 ± 0.59 counts/hour which is in good agreement with the true value of 2.5. The probability of χ^2 was 0.22. (b) 2400 random events are generated and the mean is calculated to be 2.481 ± 0.033 counts/hour, again in agreement and with $\text{Prob}(\chi^2) = 0.55$.

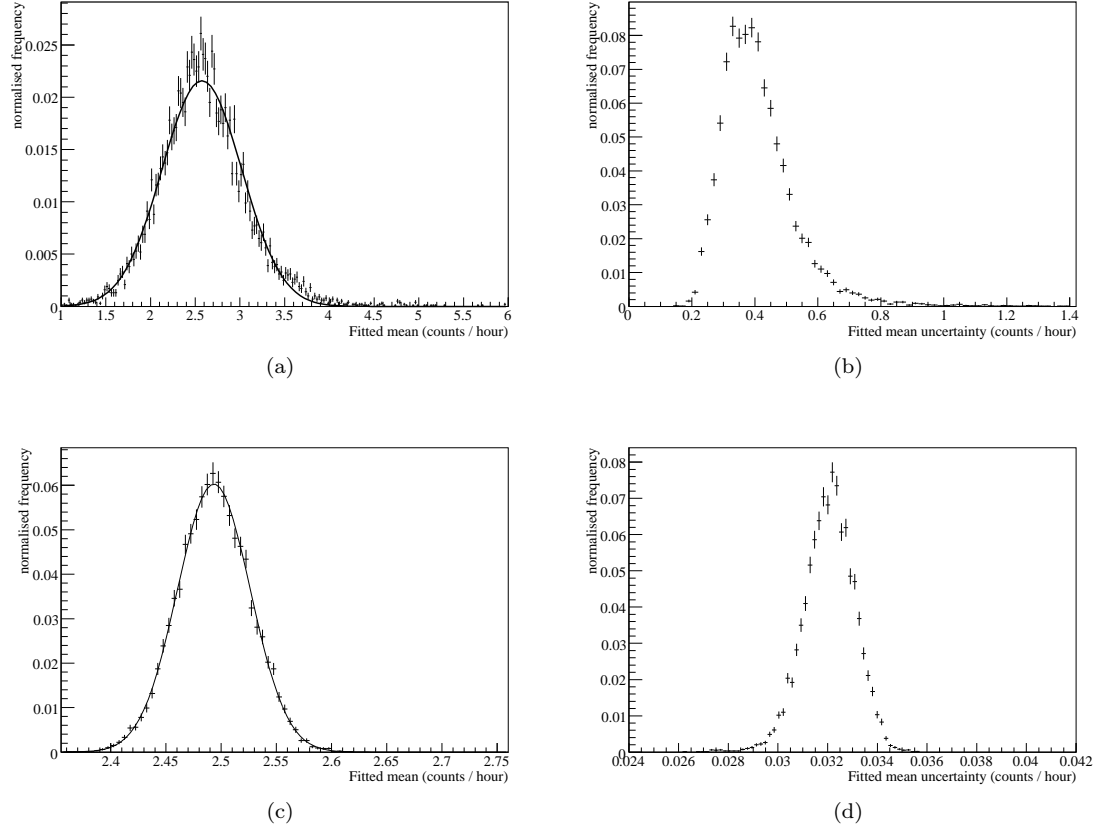


Figure 3.7: Distributions of fitted means (a,c) and their uncertainties (b,d) are generated by fitting 10 000 randomly generated Poisson samples as in Figure 3.6. A Gaussian function was fitted to the distribution of means and the mean and standard deviation of the fitted Gaussian function was noted. For the distribution of uncertainties a weighted average is made. With N denoting the number of events generated in a sample, the results are as follows: (a) $N = 24$, $\text{mean} = 2.574 \pm 0.005$, $\sigma = 0.465 \pm 0.004$, $\text{Prob}(\chi^2) = 1.2 \times 10^{-14}$. (b) $N = 24$, average uncertainty: 0.41. (c) $N = 2400$, $\text{mean} = 2.4936 \pm 0.0003$, $\sigma = (3.30 \pm 0.02) \times 10^{-2}$, $\text{Prob}(\chi^2) = 0.91$. (d) $N = 2400$, average uncertainty: 3.21×10^{-2} .

uncertainty of the Poisson fits (Figure 3.7b), which was calculated at 0.412 ± 0.002 counts/hour. However, they differ by more than their errors, suggesting that the fitting technique is at its limitation. The same can be said for the shape of Figure 3.7a, which should be normally distributed. But still the proportion of the distribution outside 3σ from the mean accounts for just 1.5% compared to the expected 0.27% of a Gaussian function.

Demonstrated in Figures 3.7c-d are the distributions of samples of 100 times the statistics with $N = 2400$, and it was found that the standard deviation of the distribution of means also drops by the same order of magnitude. In addition, the distribution of means also forms a better Gaussian distribution, demonstrating that if most bins of the Poisson distribution have large counts, that fitting with the standard least-squares method works well.

In attempt slightly to improve the fit for smaller count samples some modifications to the fitting technique were tested. One test made was to try to compensate for the non-Gaussian uncertainties of the sample bins. It was noted that bins with few counts have Poissonian uncertainties, and according to [Geh86, PRO] a better estimate of the uncertainties (compared to \sqrt{n}) can be approximated with the following formula:

$$\sigma_n = 1 + \sqrt{n + 0.75}. \quad (3.10)$$

It was hoped that the larger uncertainty given to the low count bins, as predicted by the equation, would improve the estimate of the position of the mean. However the opposite was observed with a slightly worse estimate of 2.574 ± 0.004 counts/hour. This of course has little importance compared to the uncertainty on each measurement, which was between 0.03–0.6 counts/hour, depending on the sample size (Figure 3.6). Equation 3.10 is however used later in the analysis.

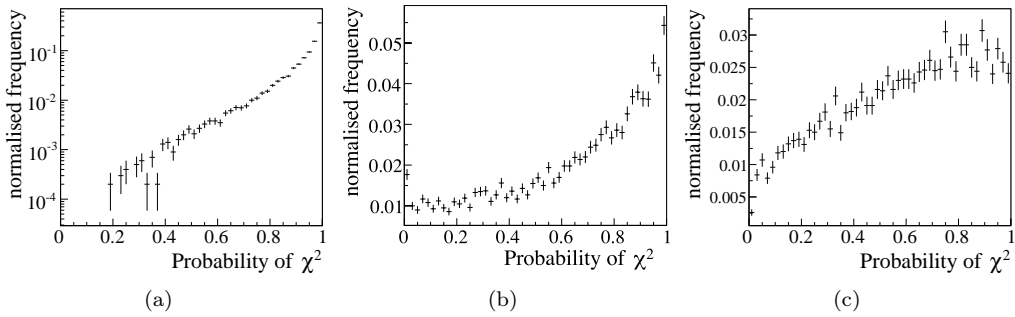


Figure 3.8: Distributions of $\text{Prob}(\chi^2)$ for variations to the fitting method for samples with, $N = 24$. (a) The uncertainty on each bin of the samples (such as in Figure 3.6) is estimated with Equation (3.10) and results in a distribution with mean value of 0.92. (b) The uncertainty is estimated with $\sigma_n = \sqrt{n}$ and has a mean of 0.64. (c) Again $\sigma_n = \sqrt{n}$ is used but with the addition of a scaling factor included in the fit and results in a mean of 0.58.

Where changes were most noticeable was with the distribution of the probability of χ^2 in Figure 3.8. Such a distribution should be flat, and any slope or non-uniformity is indicative of a

bias in the fit [Har06, Bar89]. Ensuring $\text{Prob}(\chi^2)$ is estimated correctly is useful when preparing the data since it is used as a method to decide whether some or all of the data should be rejected. It was found that the $\text{Prob}(\chi^2)$ distribution was less uniform when using Equation (3.10) than when using $\sigma_n = \sqrt{n}$, where means of the distributions, which are expected to be 0.5, were 0.92 and 0.64 respectively.

A further improvement was seen when including a scaling factor when fitting the Poisson distribution despite not being necessary for the fit. It was found that a marginally better estimate of the mean was made (again negligible compared to the standard deviation) and distribution of $\text{Prob}(\chi^2)$ was flatter with a mean of 0.58. When the sample statistics were increased to 2400 counts the means of the $\text{Prob}(\chi^2)$ distributions for Equation (3.10), \sqrt{n} and the scaling factor method came to 0.70, 0.58 and 0.51 respectively.

In conclusion, the fitting method used here has been found to be adequate with good estimates of the uncertainties on the fits. The estimate of $\text{Prob}(\chi^2)$ was found to be slightly biased towards the probability of 1 with the level of the bias dependent on the number of counts in the Poisson distribution. The $\text{Prob}(\chi^2)$ distribution is sufficiently spread out to enable the rejection of noisy data samples that have probabilities close to 0. An improvement in the flatness of the $\text{Prob}(\chi^2)$ distribution was found when including a scaling factor in the fit.

3.3.2 Energy spectra

Energy spectra are created with the ACID functions `SSplot_spec` and `SSplot_spec2`. Function `SSplot_spec` was coded first and plots the number of events per keV bin over a specified energy range. Bin size and normalisation can be changed from the input parameters of the function. The function was later replaced by `SSplot_spec2` when it was recognised that knowing in advance over what energy range the data could be plotted, was a big problem due to constantly changing noise thresholds on many of the detectors. This function, which is now most commonly used, instead of scaling the whole spectrum as one, handles each keV bin separately according to the bin's live-time. When noisy regions of the data exist less data is available to analyse, leading to bins with smaller statistics and larger errors. The errors are estimated again by the square root of the number of counts in the bin. To demonstrate this a cleaned⁷ sum spectrum of all working detectors is given in Figure 3.9 on the following page together with the measuring times.

Features in the energy spectra are discussed in detail throughout the analysis, but a couple of observations are worth making now. One is the sharp rise in counts below 320 keV. This is due to the beta spectrum of the four-fold forbidden non-unique decay of ^{113}Cd . Half-life calculations for the decay are made in Chapter 5. The two photopeaks at 352 keV and 609 keV, which form part of the ^{238}Th chain, are (later) identified to come mainly from ^{214}Bi atoms outside the detectors. The count rates fall roughly exponentially above 1 MeV to just below 12 MeV, above which no events are seen. The end of the spectrum is included to bring attention to the illusion that the count rates increase between 11 and 12 MeV. This effect comes about due to the decreasing measuring time at high energy and does not amount to an increase in count rates when the increasing space

⁷ Electronic disturbances have been removed.

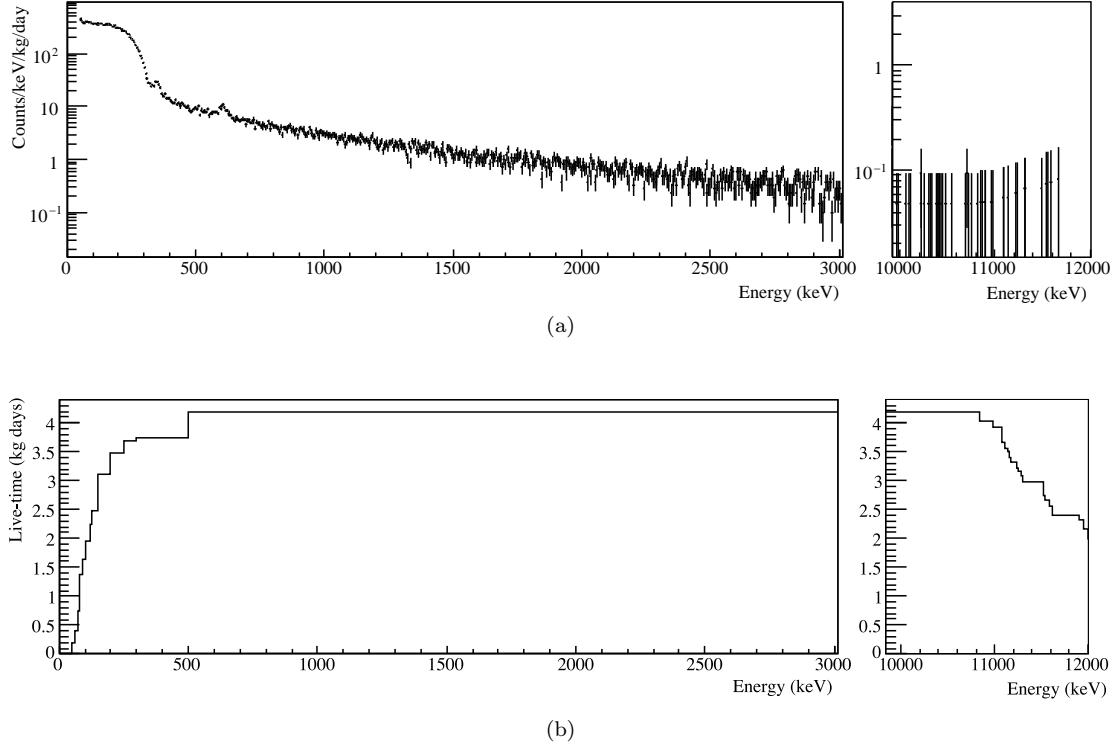


Figure 3.9: Energy spectrum with corresponding live-time plot. (a) A sum energy spectrum with standard cuts of the best detectors (2, 3, 5, 7, 8, 9, 11, 12 and 15) for the period 21 Jan to 10 July 2007. Bins are 5 keV in width and are always rescaled to give counts per keV. (b) The live-time plot shows how much measuring time was used for the corresponding energies of the energy spectrum (a) and is presented in units of kg days, which is the number of days the experiment would have to run with a 1 kg detector and accumulate the same statistics.

between filled bins is considered. The decreasing measuring times at high energy result from different upper energy thresholds due to slightly different amplification settings of the shapers. Amplifications can also be changed at the ADCs, but are held to the same factor for the set of data shown in the figure. The measuring time also decreases towards low energies and is due to different ADC trigger thresholds and noise thresholds.

3.3.3 Using the Poisson distribution

Poisson distributions are created from data using the ACID functions `SSplot_eph` or `SSplot_epp`. The first function is more generally used and counts the number of events in hourly increments, or multiples thereof. The latter function can be used for counting the number of events for any time increment and is most useful for spotting disturbances in the data on short time intervals. An example of a cut on excessive count rates is given in Figure 3.10.

A particularly noisy sample of data was chosen to demonstrate the tail (red crosses) that will

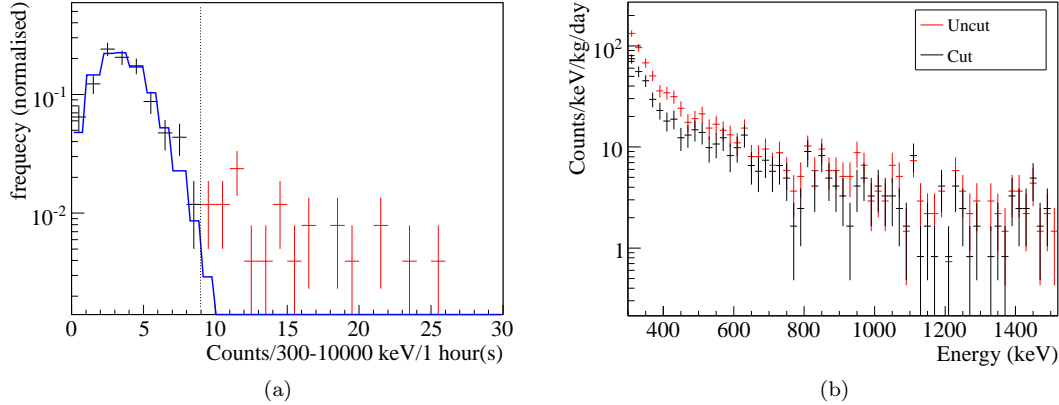


Figure 3.10: A Poisson distribution (a) demonstrating how noisy runs are removed and how the energy spectrum (b) is affected, with a sample of data taken from detector 13 between 2 and 14 Mar 2007. The Poisson distribution (crosses) was created by counting the frequency of the number of events per hour in the energy range 300–10 000 keV. Particularly noisy runs occur in the tail on the right of the distribution (red crosses). A fit of the first 8 bins returns a mean of 3.04 ± 0.12 counts/hour and $\text{Prob}(\chi^2)$ of 0.58.

develop to the right of the Poisson distribution as a result of the noise. A cut is made to the data to reject the most noisy *runs*, *i.e.*, those with more than 8 counts per hour. The method to decide at what point the cut is made, is first to fit a Poisson function to the data as described in Section 3.3.1.4 and then integrate the function to locate the position at which at least 99% of the distribution is included. The fit is then remade to obtain a better estimate of the mean and $\text{Prob}(\chi^2)$ for the fit. Before the cut is made the Poisson function fits the distribution with a $\text{Prob}(\chi^2)$ of 2.1×10^{-2} . After the cut, the fit is remade and has a $\text{Prob}(\chi^2)$ of 0.58 and a mean of 3.04 ± 0.12 counts/hour.

Despite rejecting less than 1% of the *runs* with the cut, the rejected data accounts for an extra 42% of events (a factor of 1.4). The effect of the cut is made clear when comparing the energy spectrum before and after the cut is made. This is demonstrated in Figure 3.10b.

Choosing the best place to cut on the Poisson distribution (*i.e.* what percentage of the distribution should be used) is bounded by two criteria. On one hand, sufficient noise must be rejected and on the other, the mean of the distribution, R_{cut} , should not be noticeably reduced below the true mean, R_{tru} , of the actual signal rate. Doing so would falsely reduce the count rate in a final energy spectrum and introduce systematic underestimates of DBD half-lives. By how much R_{cut} is shifted from R_{tru} can be calculated by integrating the product of the fitted Poisson distribution $P_\nu(n)$ with the count rate n ,

$$R_{cut} = \sum_{n=0}^{cut} P_\nu(n) \cdot n. \quad (3.11)$$

In the example of Figure 3.10 where 99.6% of the distribution is included and a mean $R_{cut} = 3.04 \pm 0.12$ counts/hour was found, this leads to a fractional change of rate, $(R_{cut} - R_{tru})/R_{cut}$,

of $(1.3 \pm 0.3)\%$.

Calculating the effect of cuts on the average count rate is made more complicated when more than one cut is made. Producing different Poisson distributions from the same dataset frequently uncovers more tails to the distributions that are non-statistical. It is thus tempting, for example, to repeat 10 such cuts with varying time windows. This, however, would lead to the mean count rate, R_{cut} , being shifted by at least 10%, which is not acceptable. As is presented in Section 3.5, the number of times the cleaning method is performed for this thesis is limited to once or twice for the same energy window, but is repeated many times for different energy ranges. This it was found has the potential to be more effective. However, tuning the technique is difficult and something that can only be done by direct visual inspection of the data.

3.3.4 Waterfall plots

In order to gain a clearer picture of what is disturbing the data and leading to the tails in the Poisson distributions presented in the last section, it is helpful to plot each event in a graph against its position in time. Such graphs are referred to in this thesis as *waterfall* plots and an example of the same period of data plotted in Figure 3.10 is presented in such a form in Figure 3.11. As was already mentioned, the data was chosen for its particularly noisy nature. The ACID function for this is `SSplot_waterfall`.

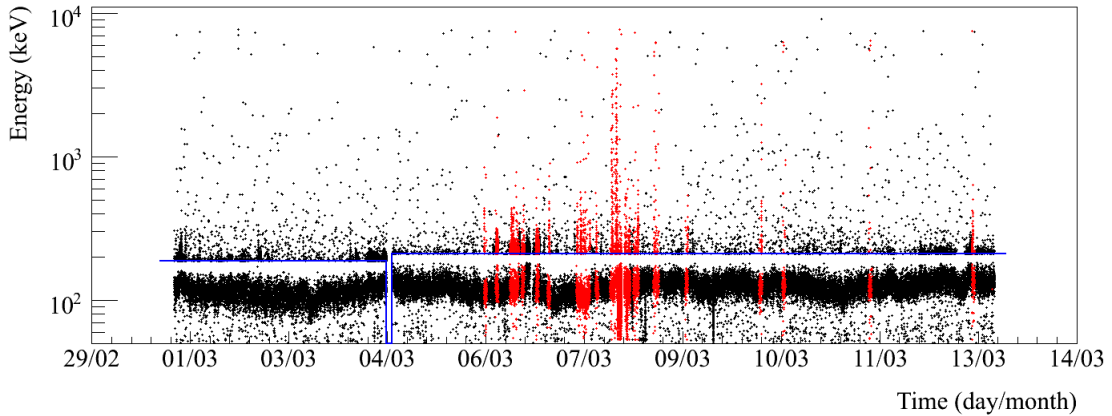


Figure 3.11: Waterfall plot

The main features in the waterfall plot are described below.

Trigger threshold The blue line on the waterfall plot marks the trigger threshold of the ADC. Knowing the location of the trigger threshold is essential for the cleaning process. In order to achieve this, first the DAQ software was modified (by J. Wilson) to report the ADC threshold number. A calibration equation relating the ADC threshold number to channel numbers was then found and using the calibration equation for channel number to energy the threshold in keV can then be calculated.

Sub-threshold events Events below the blue line are referred to as sub-threshold events. These are recorded whenever a neighbouring detector causes the DAQ to trigger and are effectively a sample of the noise threshold for that detector. However, as previously noted, the precise time of a recorded sub-threshold event is not known.

Highlighted events The highlighted (red) events are from *runs* flagged by the method described in the previous section. The highlighted ‘spikes’ are referred to as *bursts*, due to their nature that they occur for just brief moments. A closer inspection of these features is made in Section 3.4.2.

Gap in data Between 4 and 5 March a gap in the data is seen. In this case the DAQ was stopped temporarily to increase the trigger threshold on some detectors. A similar gap is also observed when *runs* are rejected when a file size is too large (see Section 3.5.1).

Real events The random scatter of events above the trigger threshold are the energies measured from radioactive decays.

3.3.5 Time-difference plots

Equation (3.3) was given in Section 3.3.1.2 and showed that the probability for an event to occur after a particular time, increases exponentially with shorter times. This is demonstrated with the ACID function, `SSplot_timediffs`. An example of such a plot is given in Figure 3.12. Detector 7, from datasets L1a-c is used for the example and is prepared first to remove any evidence of bursts. The tool is used to measure the time between events that have an energy within the window of 100 keV to 10.1 MeV and a histogram is created of the data. In Figure 3.12a, the histogram is then normalised and fitted with an exponential of the form $\exp(Slope \cdot t + Constant)$. The uncertainty on each bin is taken as the square root of its contents. The Prob(χ^2) of the fit is 0.90, which confirms that the data is statistically randomly distributed. The fit did not include time differences of less than 1 s because at shorter times some short-lived isotopes distort the distribution.

Figures 3.12b-c look at the distribution of event separations for shorter time differences. Most of the events that deviate from the random exponential form observed in both plots lie in the first bin. These are later shown to be predominantly fast β - α decays from ^{214}Bi contamination in the paint and on the detector surface. What these plots are particularly sensitive at revealing is highly repetitive signals, such as pick up from AC power supplies. The frequency of the mains supply at LNGS is 50 Hz, so pick up from such a signal (or multiples thereof), which corresponds to a period of 0.02 s, would be observable as a peak at the corresponding period on the time-difference plot. Figure 3.12c demonstrates that there is no pickup at this frequency. Indeed, no such pickup has ever been observed.

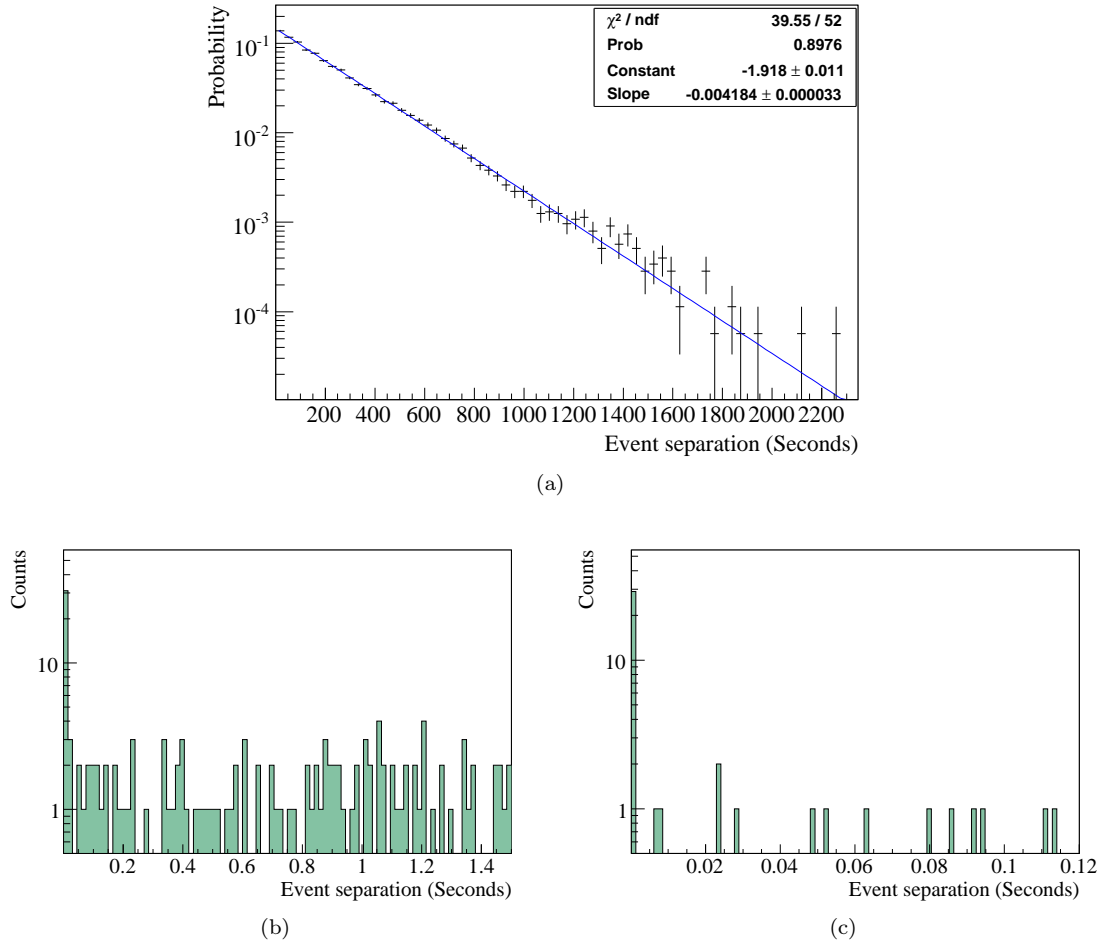


Figure 3.12: Time-difference plots to search for electronic pickup. (a) Events separated by more than one second are statistically random in time and form an exponential distribution. (b,c) A closer look at the short periods do not reveal any features that signify pickup of a high-frequency electronic signal. Interference with a 50 Hz signal would produce events with 0.02 s. No features were expected in (b) and the time range is just shown for completeness.

3.3.6 Correlation plots

Plotting the energy of one detector against the energy of another is particularly useful when investigating pickup of one detector's signal with another. These plots are often referred to as correlation plots in this thesis. The ACID function that is used to create them is `SSplot_correlations`. The function can also be used to compare the energies seen by a preceding or trailing event on the same or different detector. In the example in Figure 3.13, the energy observed by detectors 14 and 15 is compared for the same event.

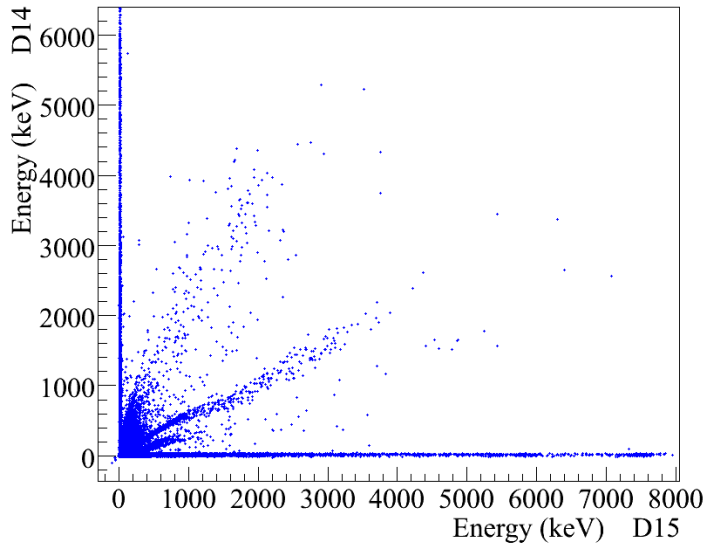


Figure 3.13: A correlation plot.

Most event energies are not correlated between the detectors and form the horizontal and vertical bands along the axes. For a small number of events we would expect to see an energy deposition on both detectors, for example, when a gamma passes through both detectors depositing energy. The large number of events that form diagonal bands in Figure 3.13 cannot be explained by real coincidences of signals because the natural coincident rate between other detectors is much lower. These might be picked up from the high voltage supply—exactly how is not yet understood. The effects are investigated further in Section 3.4.3. Most detectors do not show such dramatic correlations. However, no effective method has yet been developed to automatically identify exactly which detectors are suitable for *cross-detector coincidence analysis*⁸. For this thesis all coincident events, real and pickup, are removed.

⁸This refers to searches of multiple energy depositions in different detectors that have the signature of a rare signal, such as a neutrinoless DBD to excited states.

3.4 Electronic Background and Stability

This section attempts to summarise the features seen in the data for the periods stated in Table 3.1. Conclusions as to the cause of the features are limited because the detectors were not available for testing during their operation. It is hoped that these documented examples will prove useful as a starting point for future lab tests. Some attempt is made to characterise the features to provide some clues as to their origin.

3.4.1 Possible causes of disturbances

Leakage current Current leaking between detector anodes and cathodes (high voltage leakage current) or between the grids (grid bias leakage current) is believed to be the dominant problem of some detectors resulting in rapidly changing noise thresholds.

HV discharge Discharge from the high voltage lines became an evident problem when the experimental setup was expanded and pickup from the discharges was seen on neighbouring detectors. Discharges can occur to ground or within a dielectric itself. The latter, micro discharge [DV05, H⁺00, HO02], has been identified as a major problem.

Humidity To investigate why the performance of detectors was observed to vary with time, changes in humidity were investigated as a possible course by recording the humidity inside the Faraday cage with each event. No correlation with humidity has yet been shown.

Temperature Moisture levels on the detector surfaces, which could lead to greater surface leakage currents, could also be affected by changes in temperature. Again no correlation has yet been observed.

Power stability Questions were raised about the stability of the power supply for the experiment. Any spikes in the supply might be seen in the data. A veto was developed to flag any noisy periods of the power supply.

Radio pickup Evidence suggesting that the detectors or unshielded cables inside the Faraday cage could be sensitive to external electromagnetic waves was found with a small test involving two hand-held transceivers. When one transceiver was placed inside the Faraday cage it was still able to pick up a signal from a neighbouring transceiver. At the time no detailed investigation could be made into the level of pick-up from the detectors, however the test raised concern over how effective the Faraday cage was. The use of radio transmitters are restricted at LNGS but they are sometimes used by both security and firemen. In addition many high power electric motors are used in the laboratory and often electric welding is done, both of which can produce broadband interference.

Microphonics High frequency vibrations can also be a concern. When changes to the experiment were made it was sometimes noticed that banging on the Faraday cage, and even talking, was picked up on the detector signals lines. These affects were usually solved by improving grounding but could potentially be responsible for some of the features observed in the data.

Loose connections Poor connections on signal lines can lead to unnecessary radio frequency pickup as well as ground loops.

Piezoelectric effect Piezoelectricity has been reported in CdTe [ACD⁺96] and it is uncertain whether such effects could be observed in the data as a result of pressure applied to the COBRA detectors by their holders. For example, microphonics might be observed through piezoelectricity produced by detectors vibrating in their holders.

3.4.2 Bursts

The word *burst* has become the term used by the COBRA collaboration to describe the brief periods of electronic noise seen in the data shown in the waterfall plot example in Figure 3.11. Because the effect was not observed before the detectors were installed at LNGS, a record is provided of some of the observations made at LNGS and in the data that should prove useful for studying the behaviours under more controlled conditions.

3.4.2.1 Direct observations

During maintenance trips to LNGS to investigate such problems the signal lines were monitored with an oscilloscope. This required some patience because, as Figure 3.11 suggests, the effect comes and goes with often days between activity. The effect was eventually caught on camera as is demonstrated in Figure 3.14 on the next page, and shows the voltage on two signal lines against time, from detectors of the early 4-array prototype. The oscilloscope was set at 1 ms per division and a vertical scale of 2 mV and 20 mV per division on channel 1 and channel 2 respectively was used. Channel 1 shows a typical noise level for a detector. Channel 2 demonstrates a burst on a neighbouring detector as an erratic wobble of the base-line.

Later many more observations of this sort were made with the installation of the 64-array, and it became evident that the frequency and size of the disturbances were dependent on the high voltage or grid bias. A slight distinction was observable between high voltage and grid bias effects, with the high voltage effect being more ‘burst’ like and the grid bias effect was more continuous. The continuous noise would disappear when the grid bias was turned down, and such detectors would produce a reasonable calibration with between -5 V to -10 V , compared to -30 V to -40 V for correctly working detectors. This led to the suspicion that there is probably breakdown between the grids. An example of these detectors are 10, 11 and 13 from datasets L1a-c. The other noisy detectors showed a slight reduction in the burst rate when the high voltage was turned down, but the bursts could not be eliminated because the detectors require at least

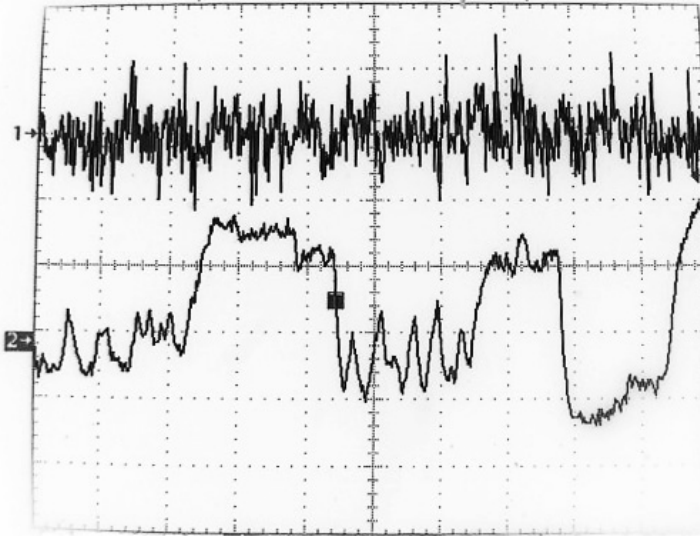


Figure 3.14: A photograph (negative) of a burst observed on an oscilloscope. The time scale (x-axis) is 1 ms per division. The amplitude on Channel 1 (upper signal) is set at 2 meV per division and channel 2 (lower signal) is set at 20 meV per division.

–5 kV to provide a reasonable resolution. An example of detectors with suspected breakdown across the bulk of the detector from datasets L1a-c are 8 and 13.

Detector 16 also showed the symptoms of leakage current on both the grid bias and high voltage settings and could not be operated continuously for more than approximately one day at a time. The remaining detectors from the first layer that are turned off, namely 1, 4 and 6 are suspected to have broken contacts.

3.4.2.2 Characterisation of bursts in the data

A closer look at the bursts in the data is now made to document their nature.

Figure 3.15 on the following page shows waterfall plots of brief periods of data from detector 13 from dataset L1b. Figure 3.15a shows a particularly energetic period of bursts and the burst marked with an arrow is amplified in Figure 3.15b. Figure 3.15c shows a slightly earlier period of data from the same detector to demonstrate a continuously noisy period.

The waterfall plots show some structure in the frequency of the bursts. To investigate this a time-difference plot is created for the noisy period of Figure 3.15c and is demonstrated in Figure 3.16 on page 72. The plots show that the burst events do not occur with a precise frequency, otherwise peak or bump-like features would be visible. However, the events can be seen *not* to drop exponentially (which would be a linear drop on the logarithmic scale). This shows that the burst events are not distributed randomly in time and are more likely to be closely spaced together.

The distribution of the energy of the burst events in Figure 3.15c is investigated in Figure 3.17.

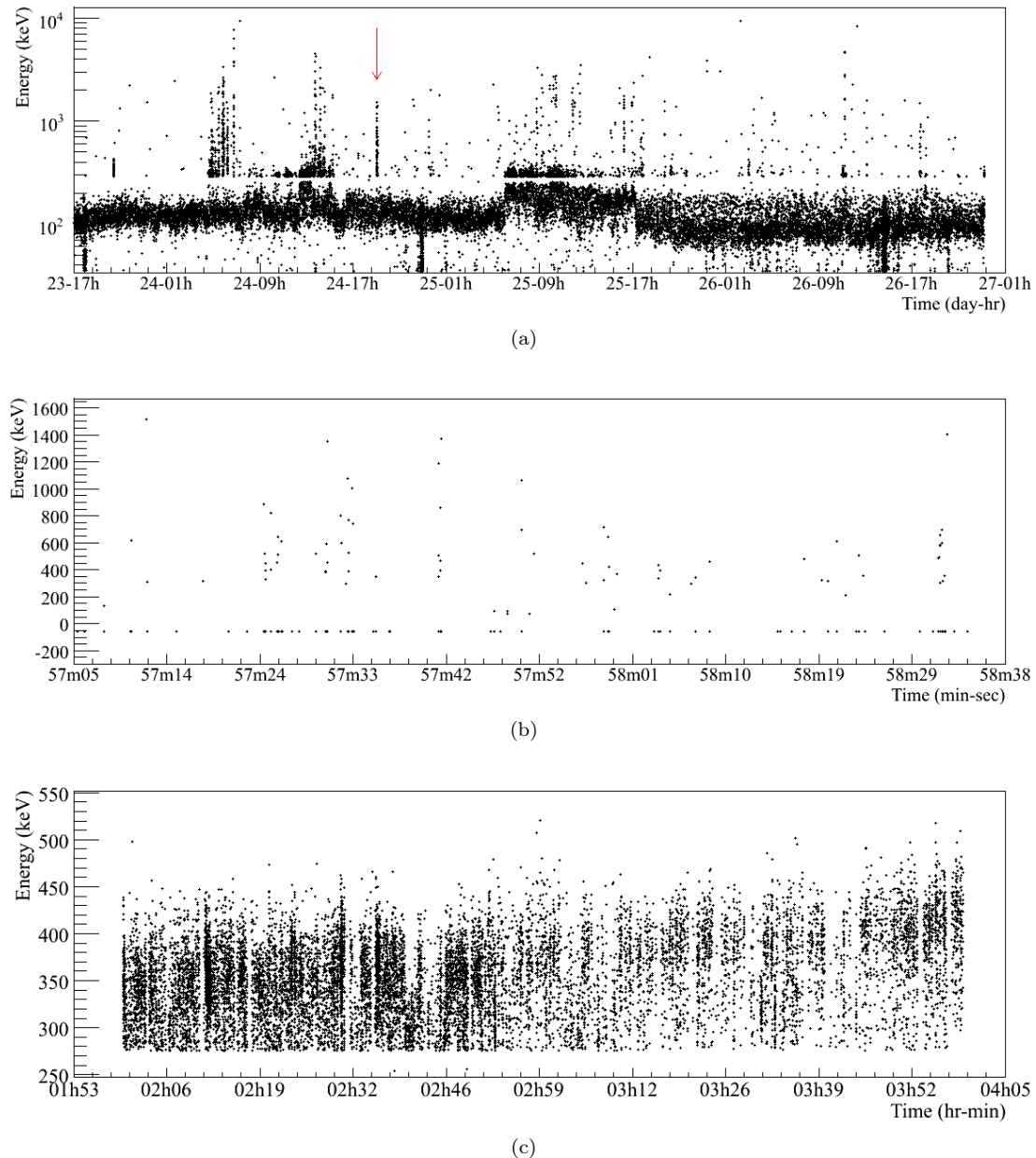


Figure 3.15: Waterfall plots of detector 13 show a closer look at bursts.

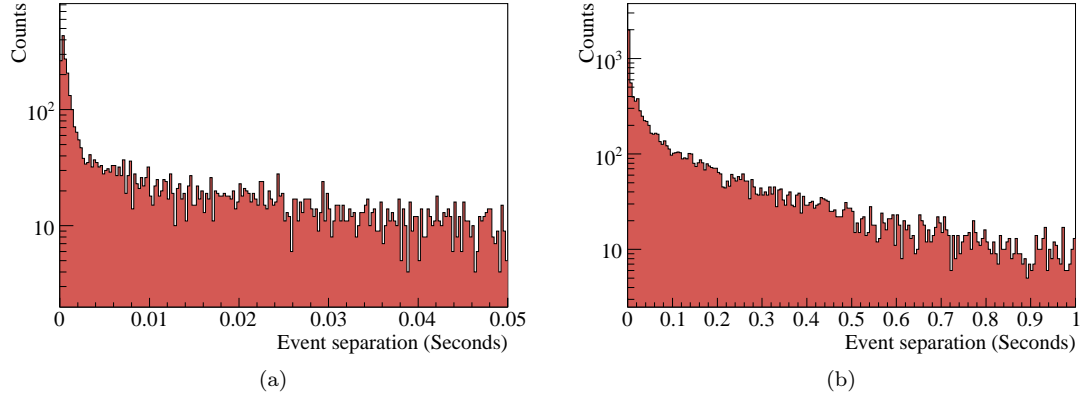


Figure 3.16: Time-difference plots for the events shown in Figure 3.15c.

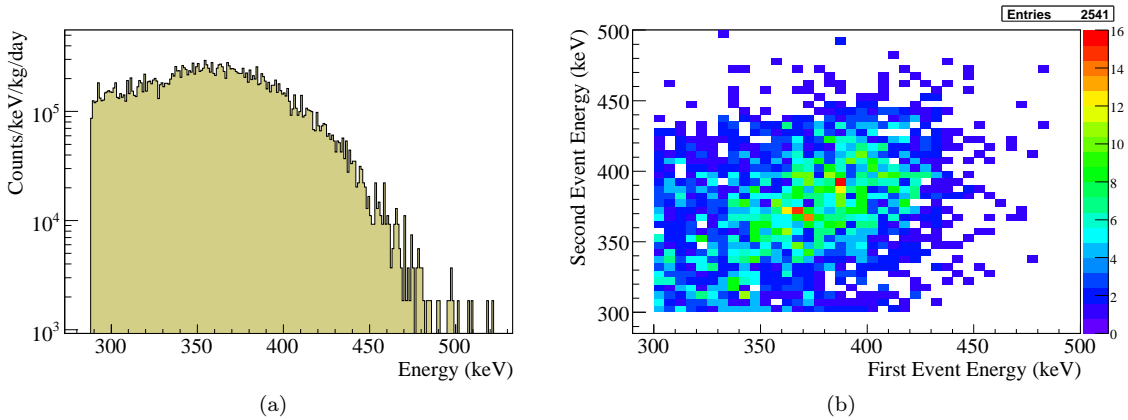


Figure 3.17: Energy distributions of burst events of in Figure 3.15c. (a) The energy distribution of the bursts. (b) A comparison of the energy of the first and second events of the same bursts. A cut is made to include only events that are separated by less than 10 ms.

It should be noted that the shape of the energy spectrum of Figure 3.17a is unique to this particular burst. Often a more exponential shape is observed. Figure 3.17b shows the energy of the first and second events of the burst with a cut made that only events with less than 10 ms are plotted. The number of counts in each pixel is represented by the colour strip. A slight elongation of the distribution of events is seen demonstrating there is a slightly greater chance that if the first event is energetic that the second event is too.

3.4.3 Micro-discharge

This section describes the phenomenon of *micro-discharge* that is observed on the high voltage lines, and characterises their effect on the data.

3.4.3.1 Early observations

Micro-discharge was first discovered at the first installation of layer 1 of the 64 array at LNGS, when a higher rate of events was seen than expected. A complex pattern of pickup was observed and it was found that when only the high voltage of one detector was turned on often more events were seen on a neighbouring detector, as opposed to the active detector. By testing a similar set-up at Sussex with two detectors it was found that pickup by the signal lines was also made when the high voltage (HV) cables were not attached to a detector. When different power supplies returned the same results, it became clear that the HV cables were responsible. J. Wilson found the phenomenon of micro-discharges reported by the SNO low-background experiment [H⁺00] and in engineering journals [DV05, HO02], which report effects consistent with what we observe. [H⁺00] states that “Studies have shown that this discharge effect occurs mainly at interfaces and in microscopic voids between dielectric surfaces”. These observations led to the development of shielded HV cables—the same Kapton cables covered in a thin layer of copper, which have proved partially successful. New thin cables with higher voltage ratings are also being tested.

3.4.3.2 Studies of un-shielded HV cables

Energy spectra Early spectra obtained from the first layer of the 64-array, dataset L1u, showed none of the usual features that were observed in the data from the 4-array. Figure 3.18 on the following page shows a spectrum from detector 2 for the period 27 July to 7 August 2006 in comparison to a sum spectrum from later data (datasets L1a-c) where the HV cables were shielded. The unshielded data shows roughly 300 times the rate of events as shielded data, and perhaps surprisingly, above 1 MeV the two spectra follow each other quite nicely. It should be noted, however, that the unshielded spectrum extends over 20 MeV.

Event time distributions Again to investigate the nature of the micro-discharge events, time-difference plots were created for the same unshielded data as in Figure 3.18 and is demonstrated in Figure 3.19. Figure 3.19a looks at the time between events that are separated by more than

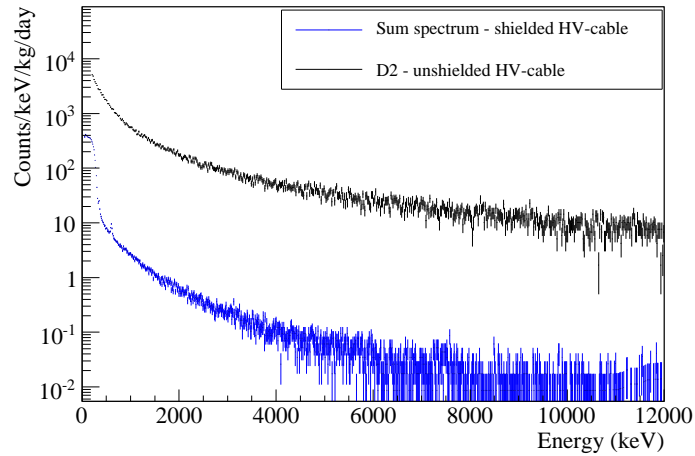


Figure 3.18: Energy spectra before and after the HV cable was shielded.

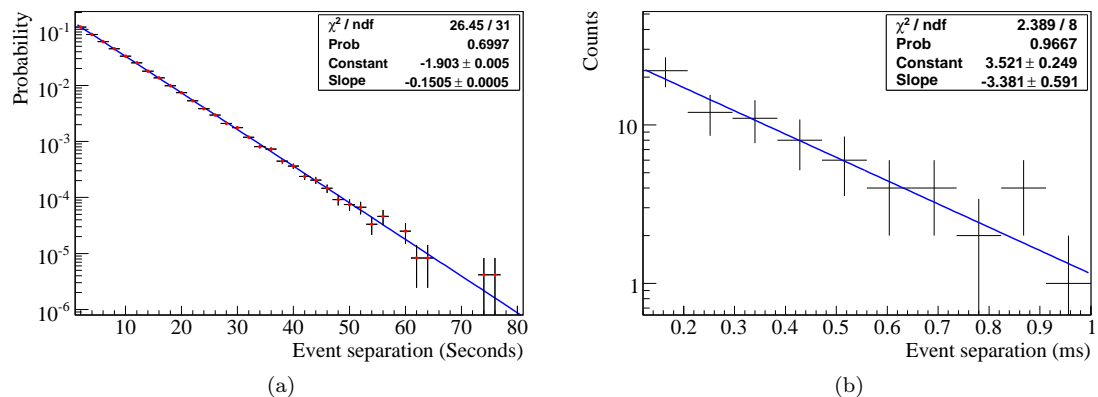


Figure 3.19: Distribution of event time separations with unshielded HV cable. (a) shows the range for the maximum observed intervals and (b) shows the range for the interval of interest for the ^{214}Bi search made in Section 4.1.3.

1s and have an energy greater than 200 keV. The histogram is normalised and an exponential of the form $\exp(-\text{Slope} \cdot E + \text{Constant})$ is fitted. The fit is good, with a $\text{Prob}(\chi^2)$ of 0.70, and demonstrates that the events are randomly distributed in time like ordinarily uncorrelated radioactive decays.

Figure 3.19b looks at the event separations for the same data but with a tighter energy window (for no special reason) of 0.5–10 MeV. In addition, the time window is restricted between 120–1000 μs . The significance of this time window is appreciated in Chapter 4 where it is used to identify ^{214}Bi contamination in the paint and from radon on the detector surface. The isotope, which is also part of the ^{238}U chain, when it decays via beta radiation is followed with a half-life of 164.3 μs by the alpha decay of ^{214}Po (see page 104). It therefore comes as a surprise that the decay constant of Figure 3.19b, which corresponds⁹ to a half-life of $205 \pm 36 \mu\text{s}$, is just one standard deviation larger than the half-life of the ^{214}Po decay. It is difficult to say whether this is a coincidence or is evidence that the micro-discharges are stimulated by radiation from nuclear decays. Short tests have already been made at Sussex to check if the micro-discharge rate changed when a gamma source was placed on the HV cable, but the observations were not conclusive. These results suggest that more careful or prolonged observations may be worthwhile.

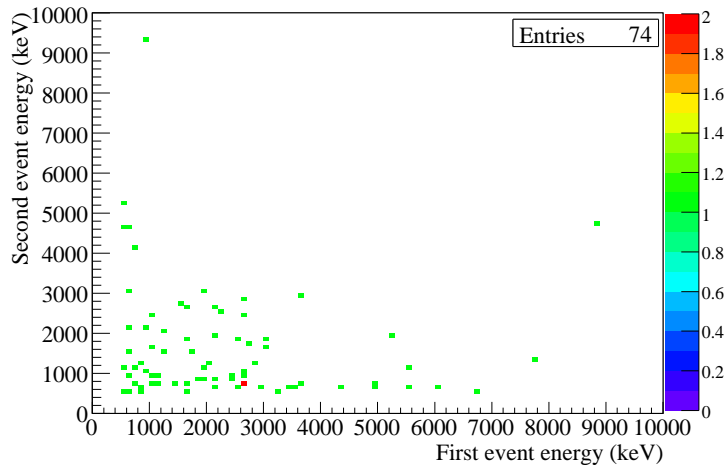


Figure 3.20: Timing correlation plot shows the first and second event energies of Figure 3.19b.

Timing correlations To further investigate the nature of the events that contribute to the half-life of Figure 3.19b the energies of the first and second events for the same selection of events are compared in Figure 3.20. Although the statistics are quite low, the majority of events can be seen to be randomly distributed. This reveals that the events that contribute to the decay curve of Figure 3.19b are not the same as those that are identified as being from ^{214}Bi on the detector surface in Chapter 4 (see Figure 4.12 on page 105 for comparison), because those decays showed a larger secondary energy.

⁹The decay constant, $\lambda = \ln 2/T_{1/2}$.

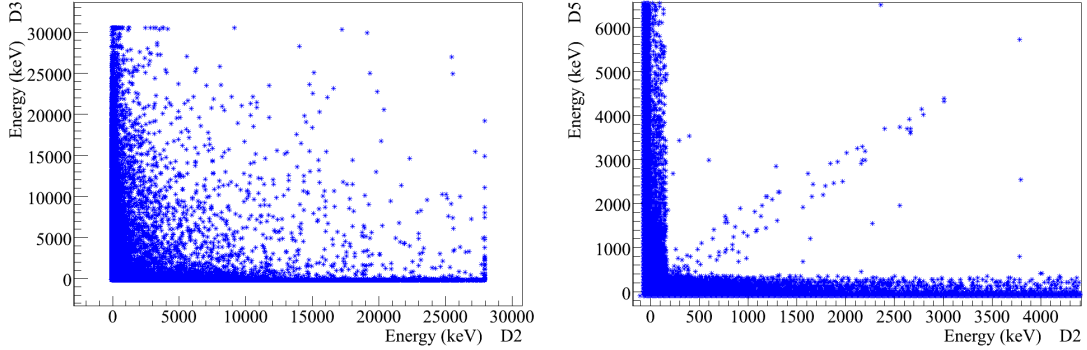


Figure 3.21: Correlation plots from data with unshielded HV-cables.

Cross-detector correlations Figure 3.21 demonstrates examples of the correlations that were observed between detectors before the HV cable shielding was implemented. Two main effects were observed. Figure 3.21a demonstrates the most common coincident events observed between some detectors that show no linear correlation of the energies. An explanation for this could be that the signal lines act like antennas and pick up the electromagnetic pulse from an electrical discharge at different strengths or phases, depending where the breakdown signal occurred.

Figure 3.21b demonstrates the other main effect. Some detectors show few coincident events but do show a linear correlation in energy. No pattern was identified relating the detectors that show correlated events to their position in the array. A possible explanation for these observations is that the high voltage lines in the HV Kapton cable overlapped certain signal lines from the signal Kapton cable on their passage between the detectors and the pre-amp. Separating the high voltage and signal cables with grounded aluminum foil was not sufficient to prevent the pickup.

3.4.3.3 Studies of shielded HV cables

After the HV cables were properly shielded to prevent crosstalk from micro-discharge the level of noise dropped dramatically, enabling useful data to be taken. However, not all problems noted above disappeared. Most noticeably, correlated events such as in Figure 3.21b continued to be a problem, adding confusion as to where and how the signals are picked up. This section highlights the most noticeable features.

High voltage veto Tests by J. Dawson at Sussex found that micro-discharge events could be observed on the HV cable when connected to an oscilloscope via a high voltage safe capacitor that allows high frequency signals through. This led to the development of the HV-veto (described in Section 2.2.9.1), which effectively joins the signals from the high voltage lines of the eight left-hand detectors and separately the eight right-hand detectors and feeds the signals into two ADC ports. Figure 3.22 shows the resulting waterfall plots of the energy of the high voltage signals

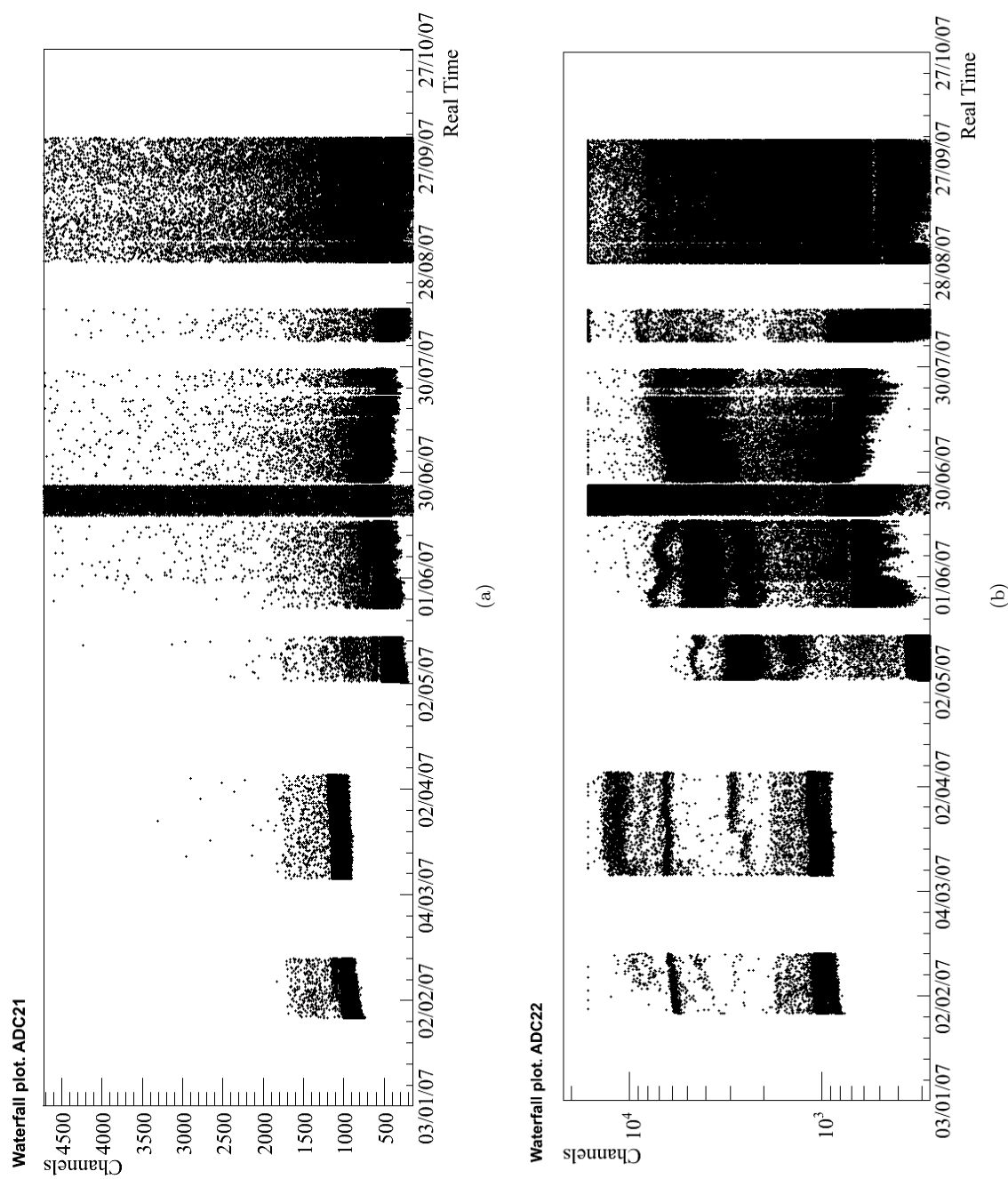


Figure 3.22: Waterfall plots of the HV-veto with coincident detector signals. The time axis is in the format day/month/year. (a) HV signals of left-hand detectors. (b) HV signals of right-hand detectors.

(HV events) against time, where (a) is from the left-hand detectors and (b) from the right-hand detectors. The data covers datasets L1a-c.

Only HV events that were coincident with an anode signal are shown. The remaining HV events are discarded by the DAQ with an algorithm implemented by J. Wilson.

After May 2007 two things happened. Firstly, the experiment was moved from the back tunnel underground to its current location between Halls A and B (these locations were marked in Figure 2.1b). Secondly, electronics were used to add the HV-veto signals together as there was concern that the initial method could cause crosstalk. The electronics also served as an extra amplifier. No reduction of crosstalk between the detectors was observed.

The dark band of events at about 1000 channels are below the trigger threshold and are just a sample of the noise levels on the HV-veto. The events between 1000–2000 channels are discussed in Chapter 4, where they are shown to be related to alpha decays. Most of the events above 2000 channels (before the move) on Figure 3.22b are believed to be discharge-related events. The fact that most discharge events form narrow bands could mean that the discharges occur at a specific locations. It is likely that these discharges occur at the end of the HV cables close to the detectors where both the copper shielding of the cable and the internal voltage lines are exposed. Audible breakdown occurred here at installation until pieces of Kapton insulation tape were used to cover any exposed parts of the (grounded) HV cable shield, so it is possible that minor breakdown still occurs.

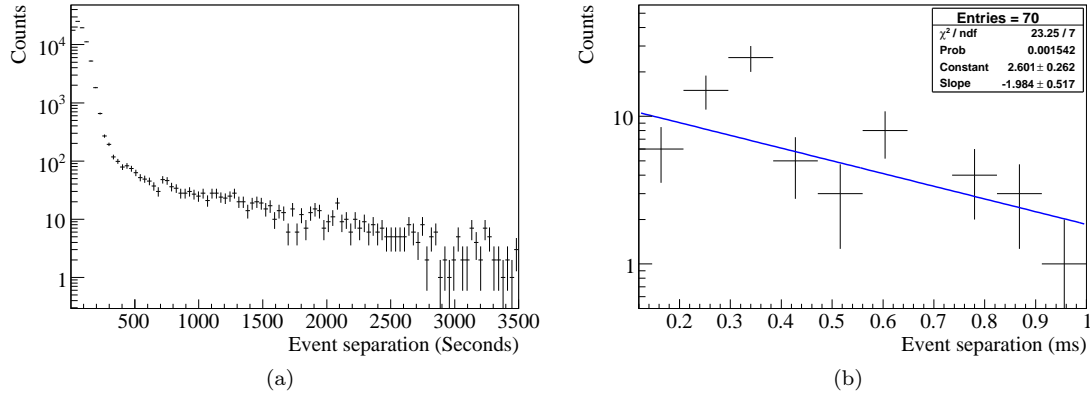


Figure 3.23: Distribution of event separations with shielded HV cable.

Event time distributions Figure 3.23 investigates the distribution of event time separations for the energy 2000–10 000 channels in Figure 3.22b, and serves as a consistency check to what was observed in Figure 3.19 with unshielded HV cables. The results are quite different. Figure 3.23a, which does not form an exponential, demonstrates the events are no longer randomly distributed in time. Figure 3.23b also fails to fit an exponential equation and the decay constant of the attempted fit corresponds to a half-life of $350 \pm 90 \mu\text{s}$ which is also no longer in agreement with

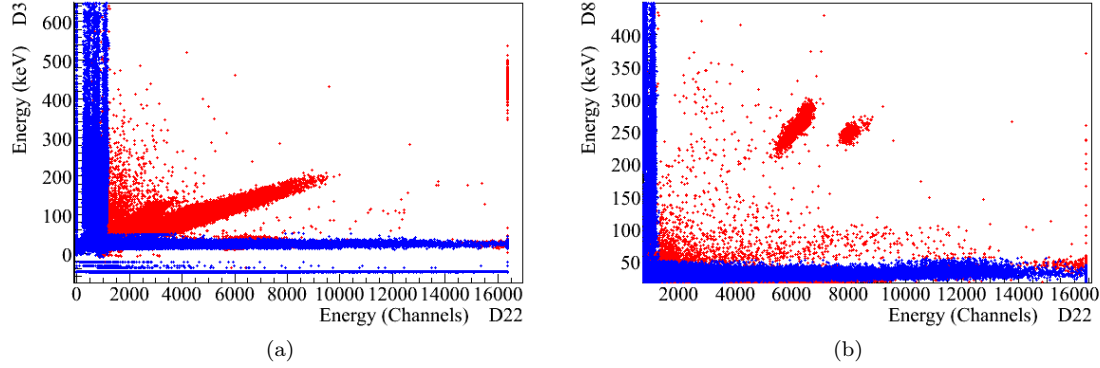


Figure 3.24: Most noticeable correlations between the HV-veto and detector signals.

the half-life of the decay of ^{214}Po . This suggests that the bands of events in Figure 3.22b are separate to the problem of micro-discharge.

HV-veto correlation with detectors Figure 3.24 shows the main correlations observed between detectors 3 and 8 and the HV-veto (D22). The clusters of events seen in Figure 3.24b could be mistaken for photopeaks in an energy spectrum but are clearly an electronic background and probably HV breakdown again. It is possible that the more scattered events are caused by micro-discharges.

Further correlations between detectors The HV-veto is not effective at observing all false events. Many correlations are observed between detectors that are not observed by the HV-veto. The number of combinations, N , of detectors that can be correlated, scales with the *Sequence of Triangular Numbers*,

$$N = \frac{1}{2}n(n - 1) \quad n = 2, 3, 4, \dots \quad (3.12)$$

where n is the number of detectors.

The number of working detectors from dataset L1a-c is 12 and corresponds to 66 combinations. For the 64-array this corresponds to 2016 combinations to test! Identifying which detectors might be correlated can be done by counting the number of coincident events for each combination. This is made easy by graphically displaying the results as in Figure 3.25.

In Figure 3.25, the number of coincident events between all combinations of detectors are colour-coded and laid out in the positions matching the detector configuration of the experiment (Figure A.1 on page 151). The markers, \blacklozenge , again indicate the detector being tested within each sub-figure. The detectors with the most number of coincident events with the marked detector are coloured red and detectors with cooler colours represent fewer counts. The largest number of counts observed is normalised to the measuring time of each detector and displayed in counts/year, just above each sub-figure. A coincidence event is counted in this example when more than 200 keV is observed in more than one detector. Detectors 10 and 13 are not included

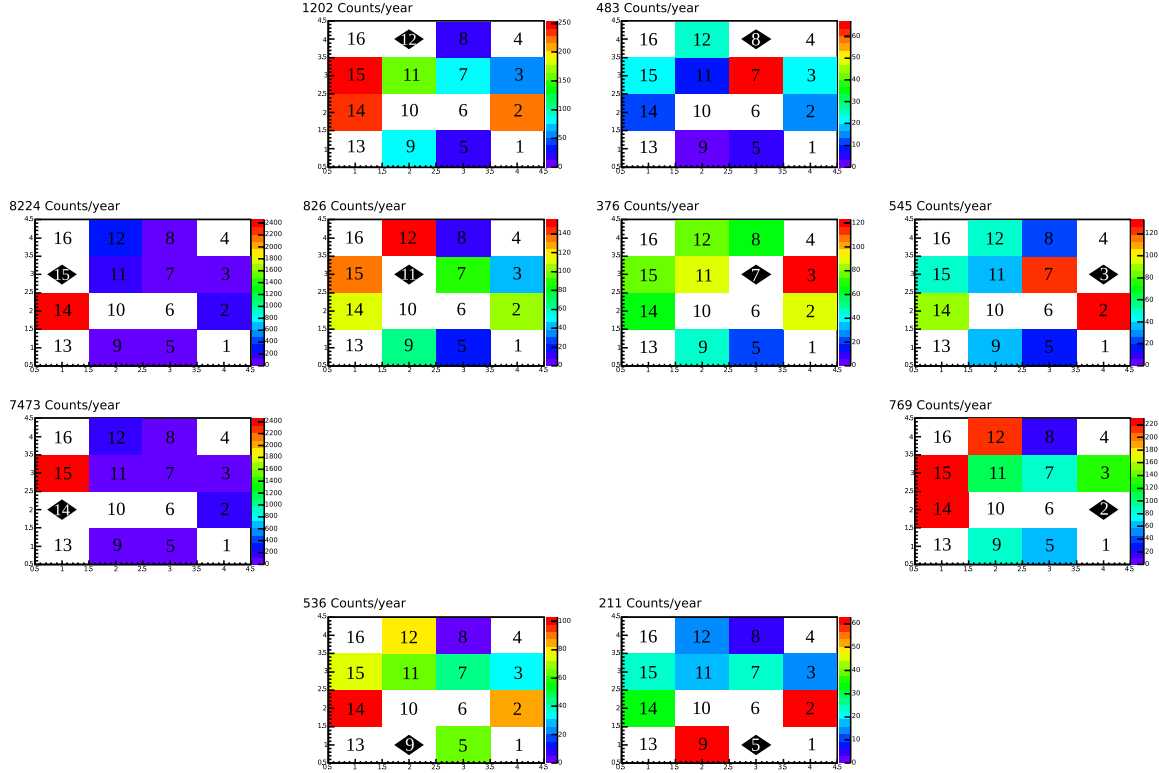


Figure 3.25: Technique for highlighting ‘talking’ detectors. The colour of each square represents the number of coincident events with the marked detector. The uncoloured squares correspond to detectors not used in this study.

in the example because they have very limited or no data available at this energy. Detectors 1, 4, 6 and 16 are also not used because they do not work.

We would expect the largest number of coincident events to be with the closest detectors, however detector 2, which is located second from the bottom on the right, sees the largest number of coincident events with the opposite detectors, 14 and 15. In addition, detectors 14 and 15 have 7000 and 8000 coincidences per year respectively, compared to just 200 counts/year seen by detector 5. Detector 13 also shows a large rate of coincidence events, at 1000 counts/year. These detectors all show a large number of events that do not have the expected properties of nuclear decays. Figure 3.26 shows examples of the correlations between detectors 2, 14 and 15.

The correlation plot of detector 14 versus 2 (Figure 3.26a) was used to select events that show an energy deposition on the detectors greater than the detectors’ noise thresholds. The same highlighted events are shown in the correlation plot of detector 15 versus 14 (Figure 3.26b), where one branch of correlated events is seen to be highlighted by the selection of Figure 3.26a. The other branch is also correlated with detector 13 (not shown).

It is not clear if these features are caused in the same way as Figure 3.24, which showed clear correlations between the HV-veto but not between detectors. Similarities are more akin to

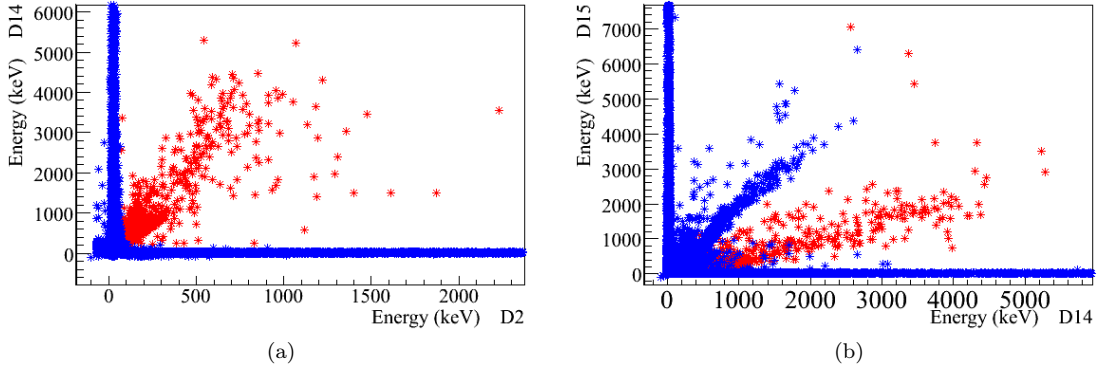


Figure 3.26: Correlation plots between detectors 2, 14 and 15.

Figure 3.21 on page 76 before the HV cable shielding was used.

The difficulty that this problem poses is that it makes searches for coincidences of deposits from radiation complicated, as detector pairs that show this effect must first be identified and used to discard such events. Moreover, there is also the possibility that only one detector observes the false events, in which case there would be no way of discarding them. Based on the good agreement of the simulations made in Chapter 4, this number is expected to be small compared to the number of real events. However, with detectors 14 and 15, which seem to be particularly susceptible to the problem, it is not always possible to reject the events below ~ 200 keV on detector 15 because the noise threshold of detector 14 that is used to reject the events often has a too large noise threshold: as can be appreciated from Figure 3.26, in order to reject the correlated events, low trigger thresholds are required on both detectors.

3.5 Data Cleaning Technique

The process of ‘data cleaning’ is to provide a dataset where noisy parts of the data are either removed or identified so that anyone analysing the data for physics may do so with some confidence that the data they are analysing is not electronic noise. The technique used to prepare the data analysed in this thesis is now given and ties together many studies made earlier in this chapter.

The general approach can be summarised with the three following steps.

1. The most noisy *runs* are rejected, discarding the largest data files.
2. All coincident events with the HV-veto and between detectors are flagged¹⁰.
3. The number of events per *run* are counted for various energy selections and according to the Poisson distribution they form, *runs* are either rejected (flagged) or the thresholds are increased.

¹⁰A flag refers to when an event or run is labelled so as not to be included in the analysis.

Steps 1. and 3. are described in more detail below. Step 2. is straightforward but must be performed before step 3. in order to avoid rejecting unnecessary amounts of data with step 3. If necessary, step 2. can later be undone.

3.5.1 File size cut and dead time

Rejecting the largest data files not only speeds up the analysis but also limits the dead time of each run.

The number of bytes recorded per event per active ADC port is about 75, as was mentioned in Section 2.2.11.2 and demonstrated how file sizes can vary dramatically if the noise threshold crosses the trigger threshold. ADC ports connected to detectors that do not work were often kept active to monitor noise levels on the signal lines. Including the ADC ports used by the HV-veto the number of active ports are at most 19. Using a dead time per event of $120\ \mu\text{s}$ (see Figure 2.10 on page 35) the maximum fractional dead time would normally be described by the following equation,

$$\text{fractional dead time} = \frac{\text{run file size [bytes]}}{\text{bytes per event}} \times \frac{\text{dead time per event [s]}}{\text{length of run [s]}} \quad (3.13)$$

A maximum file size of 5 Mb was chosen as being manageable. The resulting maximum dead time would then be just 0.01%.

For datasets L1a-c however, a further complication arises from the temporary modification to the DAQ that only records HV-veto events that are also observed on an active ADC port. Unrecorded HV-veto events also contribute to the dead time. To account for this, the number of HV triggers that occur between recorded events are saved for datasets L1a-c and enables the actual number to be calculated. Any *runs* with a particularly large dead time when the true number of ADC triggers have been counted can later be discarded. This has not been necessary since the largest dead time in any run in datasets L1a-c with a file size of $\leq 5\ \text{Mb}$ was found not to exceed 1.2%. This assumes a dead time of $120\ \mu\text{s}$ per event.

The average dead time for the datasets L1a-c can also be calculated with the total number of ADC triggers and the total live-time and is 0.1%. The dead time varies slightly for each selection of data so is calculated separately and subtracted whenever the data is normalised by time with the ACID function `SSgetusedtimeR`.

3.5.2 Threshold cut

The main part of the cleaning process is to redefine the lower thresholds that specify above what energy the data should be analysed. This section motivates and describes the method used by the ACID tool, `SSclean_data`.

3.5.2.1 Motivation for a new approach

Early approaches to preparing the data involved counting the number of events within a large energy range, for example, between 0.2–10 MeV. Then a Poisson function would be fitted to the

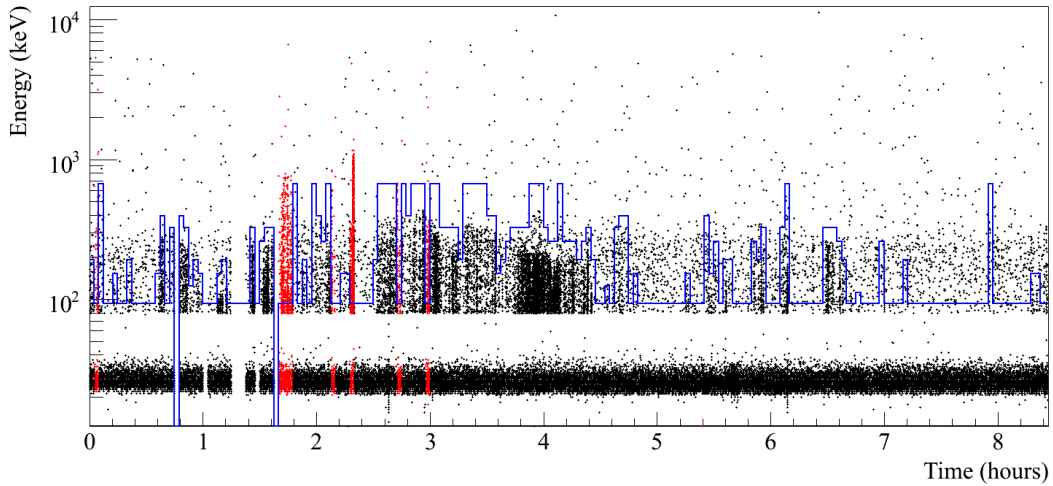


Figure 3.27: Example waterfall plot from group sfa20_20070425 - D8, to demonstrate how the cleaning tool works. A noisy detector is chosen as an example.

distribution of events, as previously demonstrated in Figure 3.10a on page 63, allowing the most noisy *runs* to be rejected. However, if the data must be analysed as close to the noise threshold as possible then a decision must be made as to where to set the lower threshold. The choice of threshold is balanced between how much data is available to analyse above a given threshold and how low levels of energy the data are actually required to reach. Thus it is essential to know in advance where the noise thresholds are and how the live-time varies with energy.

To achieve this, the automated tool, `SSclean_data`, was developed essentially to map the profile of the noise, as opposed to rejecting whole *runs*. This enables the live-time of the data to be easily calculated as a function of energy, as was demonstrated in Figure 3.9b on page 62. This in turn allows energy spectra to be produced either for the full energy range where each bin of the histogram has its unique live-time, or analysis can still be made with a traditional user-specified threshold that rejects periods of data with larger thresholds.

3.5.2.2 Human involvement and general comments

Figure 3.27 shows a waterfall plot of a period of data with noise thresholds that jump up and down, or bursts, as they are referred to. The blue line in the plot demonstrate how the `SSclean_data` tool attempts to follow the noise level of the data. Above the blue line the data should be good for analysis with the exception of the highlighted events where the data is rejected for all energies.

The human eye is very good at spotting patterns in the data and anyone armed with a coloured pen could easily mark the regions of noise. Indeed, the tool can only be as effective as it is ‘trained’ to be. But such a tool has a number of advantages. In addition to saving time, it uses judgments based on statistical fits, which are both repeatable and un-biased towards different datasets. Human involvement cannot be avoided in the development of the tool, however, and involvement falls into the following categories.

Statistical Deciding what value of χ^2 corresponds to a good fit and how many standard deviations from the mean should an event rate be discarded.

Granularity Determining how large energy and time windows should be compared, taking care to find an acceptable balance of using sufficient statistics on which to base a test and not rejecting unnecessary amounts of data.

Overshoot If a noisy period of data is identified a decision must be made how far forwards and backwards in time, or greater in energy should neighbouring regions (if any) be also rejected.

The specific decisions will be made clear in the following section, but the general ideas can be appreciated when considering Figure 3.27. Someone looking at the data might suggest rejecting all events with less energy than 500 keV. This might be a valid suggestion, but must be applied consistently to all data. Most detectors observe the occasional electronic disturbance and rejecting data may not be done too carelessly because the low energies are required by many studies, including that of the ^{113}Cd four-fold forbidden beta decay in Chapter 5. So the data in the region of, for example, 200–400 keV and 5 hours, cannot be discarded if it passes the same statistical tests applied to datasets that appear noise free. The point is, because no data can be guaranteed to be noise free, the best available data from the noisy detectors must be kept until a sample of data can be provided proving that the event rate is actually lower. A motto for the philosophy of the tool is thus: *Innocent until proven guilty*.

If evidence is found to suggest that when a detector that has been *bursting* within the last minute (or hour or so) it will provide poorer quality data than a detector that has not shown a burst for a day or a week, then this should be incorporated into the cleaning technique by adjusting *overshoot* settings. To date, no such evidence has been found.

If someone analysing the data would like to be biased towards only using the ‘best’ detectors, this could be possible in a number of ways.

- ▷ General comments in the data log book can be referred to. This in the future could be a true/false option stored with the data specifying whether bursts have ever been observed on the detector.
- ▷ Leakage current measurements could be used to decide which are the best detectors to analyse.
- ▷ The frequency with which thresholds have been increased and the average threshold may also be used.

3.5.2.3 Method

The noise threshold is mapped as follows. The number of events for different energy ranges are counted per *run* and fitted with a Poisson function as previously demonstrated in Figure 3.10 on page 63. The energy ranges are based on the numbers in Table 3.3 and are chosen according to the normal event rate for the detectors so that the number of counts lie somewhere in the region

No.	Range (keV)	No.	Range (keV)
1	500–10 000	9	80–90
2	300–500	10	70–80
3	250–300	11	60–70
4	200–250	12	50–60
5	150–200	13	40–50
6	120–150	14	30–50
7	100–120	15	20–30
8	90–100	16	0–20

Table 3.3: Template for energy cuts.

of about 1–3 counts/hour. Keeping the mean rate of events low increases the sensitivity of the Poisson fit to reject noisy runs.

The precise energy ranges are actually slightly larger (an example of *overshooting*) and this is explained shortly, but the general steps involved are straightforward and listed below.

1. A Poisson distribution is created from data from a *group of runs* for a detector, where events are counted within the energy range 500–10 000 keV.
 - (a) Any *runs* with a number of events that fall outside 99% of the distribution are rejected.
 - (b) Any *runs* with thresholds above 500 keV and thus could not be included in the fit are also rejected.
2. A Poisson distribution is created from the data within the energy range 300–500 keV. *Runs* with thresholds greater than 300 keV are ignored.
 - (a) Any *runs* outside the event rate that fall outside 99% of the distribution have their thresholds pushed to 500 keV.
 - (b) Any *runs* with thresholds between 300–500 keV, which could not be included in the fit, have their thresholds pushed to 500 keV.
 - (c) A Poisson function is re-fitted. If the fit returns a value of $\text{Prob}(\chi^2)$ less than 0.1% all of the *runs* have their thresholds pushed to 500 keV.
3. Step 2. is repeated for the decreasing energy windows (Table 3.3) until all thresholds are between the energy window, at which point step 2(b) is called and the function is ended.

The above steps are sufficient to reject nearly all noise. However, careful observation has revealed that one or two counts from the burst ‘tips’ occasionally slipped through the cleaning process. To avoid this, various overshooting techniques were tested. The current method is not a final solution but has been found to be effective for datasets L1a-c. The method samples 10 keV below the lower energy window and additionally increases the energy to which the thresholds

are set according to the equation, $1.35 \times \text{Threshold} - 15\text{ keV}$. This equation was based on observations that the occasional event with energies larger than the bulk of events from a burst reaching 500 keV, did not reach 600 keV. In addition, because low energy events are important for the analysis of the ^{113}Cd beta spectrum, overshooting was limited for the lowest threshold energies by subtracting the 15 keV.

It is important to note that these measures do not bias the results, but can lead to an unnecessary loss of useful data. It is anticipated that the level of overshooting on the energy will have to be reviewed for future datasets. Particularly if data with a lower noise threshold is to be analysed. In addition, the energy ranges given in Table 3.3 should be reviewed for lower background data.

The value of $\text{Prob}(\chi^2)$ of 0.1% was also chosen based on what was found to work on a sample of data. It should be noted that the distribution of the reported $\text{Prob}(\chi^2)$ by the fit is not flat (Section 3.3.1.4), so for truly randomly distributed data much less than 0.1% is rejected. However, because of changing radon levels and the occasional fast decays, the distribution of events was found not always precisely to fit a Poisson distribution. The choice of $\text{Prob}(\chi^2)$ was thus a fine balance between needing to reject continuous periods of noise and not wanting to reject data with a slightly changing radon level. The choice of 0.1% was balanced towards rejecting good data and consequently it was noted with some datasets the thresholds were occasionally set higher than necessary. With future tighter control on the radon levels this is expected to be less of a problem.

3.5.2.4 Suggested improvements

In addition to the above anticipated amendments, a couple of refinements can be suggested. A minor improvement might be to overshoot the thresholds forwards and backgrounds in time by one *run*. That is, if the threshold is increased on a *run*, the thresholds of the neighbouring *runs* should also be increased. This is likely to have little impact on the overall loss of data, but does help reduce the chance of the occasional false event being included when a burst occurs at a *run* boundary. That is, when a burst occurs at the end and beginning of two data files.

When discussing (in Section 3.3.1.4) the implications of rejecting the most noisy *runs* from a Poisson distribution on the mean event rate, it was noted that repeating the cut for different time windows would lead to a significant shift in the mean. However, there would be a definite advantage to additionally counting the event rate for shorter periods, such as a second. Occasionally a burst may produce too few events that are not rejected by the method described above. Such events are more likely to be rejected, statistically, by sampling shorter periods. Because the average event rate will be much lower than a single count, it is highly unlikely to observe more than one count at a time, except, if decays from short-lived isotopes are observed. If such decays are of interest then a decision can be made to reject any events with a greater event rate than are likely from even fast decays. Then, either the whole *run* could be rejected if the number of rejected *runs* is small, or the events can be flagged and the dead time imposed by the cut should be calculated. This can become complicated if more than one such cut is performed, for example, over different energy ranges. Code was developed in ACID for keeping track of such small cuts,

but still requires testing; the method was not used in the analysis of the data for this thesis.

This chapter has explored various electronic disturbances observed in the data and provided methods for selecting only the best data. This work has also demonstrated that electronic noise can never completely be rejected and that it will be necessary to use more stable detectors in a full scale detector array.

3.6 Summary of Usable Data

A summary of the live-time of the detectors (in hours) for datasets L1a-c is presented in Table 3.4 together with the crystal and paint masses. The live-time (in kg days) as a function of energy is given in Figure 3.28, which includes the accumulated running time of all detectors.

No.	ID	Live-time				Dead-time				x-tal mass g	paint mass mg
		Total hrs	File cut hrs	>600 keV (%)	>100 keV hrs (%)	>600 keV %	>100 keV %				
1	631869_04	0	0	0	-	-	-	-	-	6.505	17
2	631937_02	3738	3515	3469.8 (93)	1567.0 (42)	0.12	0.19	0.09	0.09	6.454	18
3	631969_08	3738	3515	3377.8 (90)	1385.7 (37)	0.12	0.19	0.09	0.09	6.454	18
4	631959_01	0	0	0	-	0	-	-	-	6.544	20
5	631969_04	4022	3797	3747.7 (93)	2560.0 (64)	0.11	0.16	0.11	0.11	6.512	20
6	631937_03	0	0	0	-	0	-	-	-	6.487	28
7	631960_03	4022	3797	3747.8 (93)	1185.5 (29)	0.11	0.04	0.04	0.04	6.526	20
8	631972_02	4022	3797	2733.4 (68)	761.9 (19)	0.13	0.02	0.02	0.02	6.465	17
9	631969_09	2928	2715	2689.5 (92)	1634.8 (56)	0.13	0.20	0.20	0.20	6.469	21
10	631938_06	4022	3797	3651.8 (91)	788.5 (20)	0.12	0.32	0.32	0.32	6.461	19
11	631959_06	2094	1907	1883.6 (90)	1199.0 (57)	0.18	0.25	0.25	0.25	6.468	21
12	631969_10	2928	2715	2689.6 (92)	1076.4 (37)	0.13	0.06	0.06	0.06	6.492	20
13	632083_02	4022	3797	3439.2 (86)	0 (0)	0.11	-	-	-	6.529	21
14	631969_01	4022	3797	3764.8 (94)	2602.2 (65)	0.11	0.15	0.15	0.15	6.548	21
15	631969_03	4022	3797	3732.8 (93)	2371.4 (59)	0.11	0.15	0.15	0.15	6.520	20
16	631869_06	0	0	0	-	0	-	-	-	6.527	18

Table 3.4: Summary for datasets L1a-c. The total live-time displayed for each detector is the number of hours that a detector is taking data. The number of hours of data after the most noisy files with greater than 5 Mb is also shown. The live-time above the specified energies is calculated after all cleaning cuts have been made, as described in Section 3.5. The estimated dead-time based on the dead-time of 120 μ s per event is also subtracted. The percentage dead-time as a fraction of the measuring time above each specified energy is also shown. The detector ID is the detector manufacture number and detectors are located according to the scheme given in Figure A.1 on page 151. The crystal and paint masses are also shown.

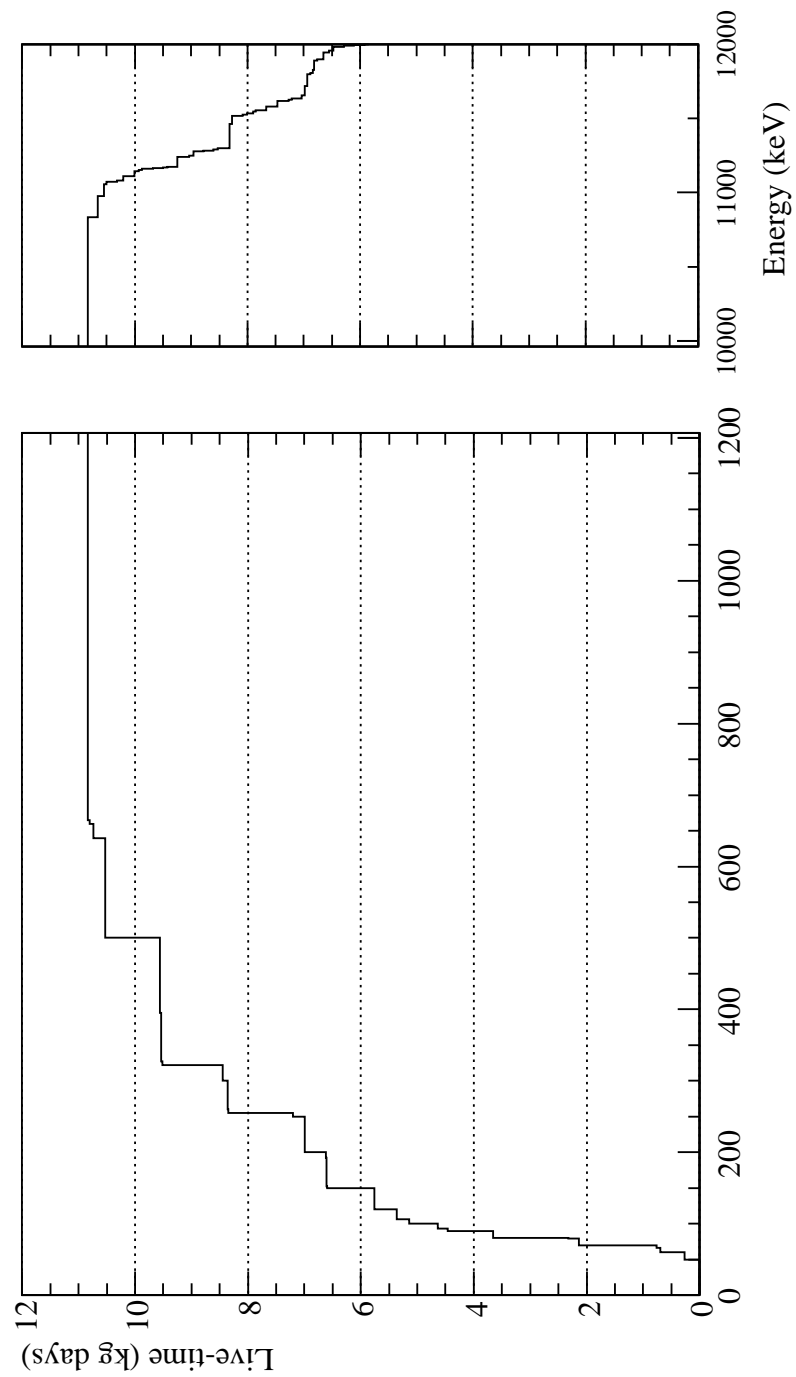


Figure 3.28: Total live-time for datasets L1a-c as a function of energy with a maximum of 10.8 kg days.

Chapter 4

Radioactive Background Study

Identifying radioactive backgrounds and their source, so that measures can be taken to reduce them, is key to the success of the COBRA experiment. This task is made difficult, however, when there are a number of backgrounds in different locations and many unknown factors, such as the width of the dead layer. It is possible that more than one combination of contaminants and detector properties can produce very similar energy spectra. For example, gamma radiation has a large range and it is difficult to identify whether it originated inside a detector, in the paint or in the supporting structures. Beta radiation and alpha radiation can provide more clues to where a radiation source is because they have much shorter ranges. However, beta spectra are not easy to identify because the Q-value is also shared with a neutrino and it is also difficult to predict what an alpha spectrum would look like from an external source as this would require extensive knowledge about intricate details such as the passivation paint smoothness. These problems are investigated in this chapter and some solutions are found. These include the identification of the main dominant background and some minor backgrounds in Section 4.1, and new limits on the possible contamination of the naturally abundant radioactive chains of ^{238}U and ^{232}Th inside the detectors are made in Section 4.2.

The results in Table 4.1, which show radiation measurements performed on samples of cadmium, zinc, tellurium, a sample naked CZT detector and paint samples, will be referred to throughout this chapter. Measurements were performed with an ultra-pure germanium detector at the LNGS facility.

4.1 External Backgrounds

External backgrounds are here defined as any background source (not DBDs) that are outside the CZT crystal. Surface treatments and contacts are considered external because alternative materials can often be found, whereas this is not true for the detector material as it is also the DBD source. As shown in Table 4.1, the red paint used to protect the detectors from oxidization (these are the main detectors used in this analysis) has been measured to have a significant concentration of uranium, thorium and potassium, with a combined activity greater than 10 Bq/kg. This was

Chain	Decay	Cd	Zn	Te	CdZnTe	Red paint	Clear paint
^{232}Th	^{228}Ra	< 4	< 8	< 7	< 12	1100 ± 100	< 180
	^{228}Th	< 4	< 8	< 7	< 9	730 ± 70	< 190
^{238}U	^{226}Ra	< 4	< 8	< 7	< 10	2100 ± 100	< 140
	^{234}Th	< 200	< 150	< 240	< 250	1100 ± 300	< 1500
	$^{234\text{m}}\text{Pa}$	< 70	< 150	< 140	< 220	1600 ± 100	< 4300
^{235}U	^{235}U	< 4	< 5	< 5	< 7	170 ± 30	< 15
	^{40}K	< 24	< 55	< 51	< 91	6900 ± 800	< 1000
	^{60}Co	< 2	< 3	< 4	< 5	< 20	< 72
	^{137}Cs	< 1	< 2	< 2	< 4	< 15	< 56

Table 4.1: Radioactive contamination measurements of detector and passivation materials in mBq/kg [Mue07]. Measurements were taken by M. Laubenstein with an ultra clean germanium counter at LNGS.

expected to be the dominant background in the energy spectra, however, the analysis in this section reveals that radon gas surrounding the detectors is the dominant source, and emphasises the requirement for nitrogen flushing.

4.1.1 Paint contribution

Using *Venom*, events were simulated for ^{40}K decays and the isotopes in the natural decay chains of ^{238}U and ^{232}Th . The simulation modelled the set-up at LNGS used for datasets L1a-c. This involved an array of 16 detectors located in their Delrin holder on the bottom of the copper nest. In the simulation, the detectors included a $260\ \mu\text{m}$ paint layer on 5 surfaces¹, the bottom of the detectors was left bare (the cathode contact was not included) and initially no dead layer was used. One million decays were simulated uniformly in the paint and a sum spectrum was created which was then scaled (in counts/keV/day per kg of CZT) so that it could be compared to the data. The scaling factor, f , was calculated from

$$f = \frac{A}{n} \cdot \frac{m_p}{m_c}, \quad (4.1)$$

where A is the activity in counts/day per kg of paint taken from Table 4.1, n is the number of decays simulated² and m_p/m_c is the ratio of the paint to crystal mass. The scaled energy spectra of the simulated radioactive paint components were smeared³ with an energy resolution according to Equation (3.1) (page 55) and are shown together with a sum spectrum in Figure 4.1.

¹This corresponds to 20 mg of paint per detector.

²Note, the requested number of simulated events are distributed in *Venom* amongst the number of isotopes in the decay chain, thus the number of simulated decays of a particular isotope n is obtained by dividing the requested number of events by the number of isotopes.

³Smearing is done by replacing each bin of an energy spectrum with a correctly normalised Gaussian and adding each overlapping Gaussian together. Each Gaussian is given a standard deviation according to the energy resolution provided. This method smooths the data for easier comparison by eye.

The figure shows that if the simulation and radiation measurements are correct, then the paint contributes at most 28% of the number of events seen at 600 keV.

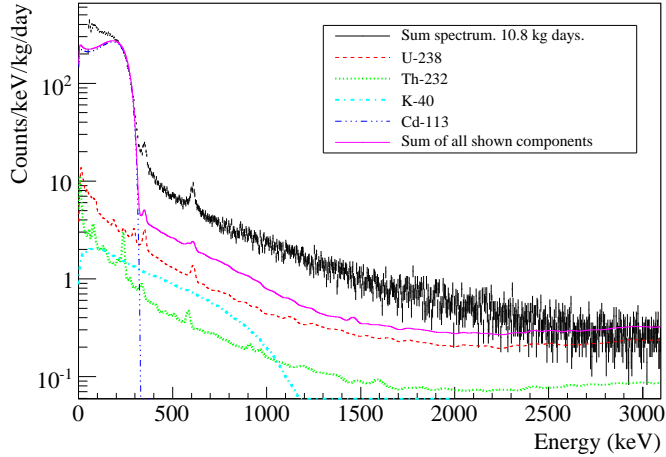


Figure 4.1: Comparison of simulated paint contaminants with the data. A prediction of the four-fold forbidden non-unique beta decay of ^{113}Cd is also included.

The two main peaks that are seen in both the data and the simulation are the 351.9 keV and 609.3 keV gammas that are released after the isotopes ^{214}Pb and ^{214}Bi (from the ^{238}U chain) decay through beta emission to excited states. As gammas, they are not much affected by a dead layer or paint thickness, but the betas also involved in the decays are. In fact, the gamma peaks are only visible when the beta radiation is not detected.

The blue curve in Figure 4.1 is a theoretical prediction [Mus06] of the ^{113}Cd four-fold forbidden non-unique beta decay shape, which is the dominant feature in the data below 350 keV and is investigated in more detail in Chapter 5 where it is found to inaccurately represent the data. It is included here only for demonstration purposes and is scaled by eye.

A closer look at Figure 4.1 reveals that the 609 keV peak of the simulated sum spectrum not only looks smaller compared to the background but is also distorted by the 583 keV gamma from the decay of ^{208}Tl in the ^{232}Th chain. This distortion is not so evident in the data. One possible explanation of these discrepancies could be that there is a larger uranium contamination in the paint, or on the surface, of the detectors than is given in Table 4.1. This idea is investigated in Figure 4.2 by rescaling the ^{238}U spectrum to compare the signal to background ratios of the 609 keV gamma peak. Even if no other backgrounds are included, the best the simulation can achieve is about 60% of the true signal height relative to the background. As the dotted curve demonstrates, the existence of uranium inside the detector would only make the fit worse because then most of the beta radiation would also be detected. Clearly there exists a more distant source of 352 keV and 609 keV gammas. This gamma source is most likely radon.

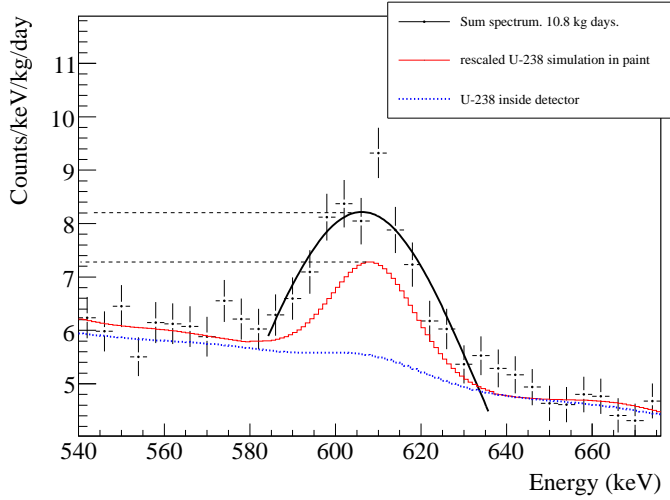


Figure 4.2: Comparison of simulated 609 keV gamma peak heights to background demonstrates that both internal uranium contamination and contamination of the paint would produce smaller 609 keV photopeaks and points to the existence of an external gamma source.

4.1.2 Radon evidence

Radon (^{222}Rn) is produced in the eighth step the ^{238}U chain, before the isotopes ^{214}Pb and ^{214}Bi which give rise to the observed gamma peaks. As a noble gas, radon is chemically stable, so within its 3.8 day half-life it is able to leach out of rock, soil or concrete where concentrations of naturally occurring uranium are often higher. In fact, many materials such as electronic components are also known to release radon [Nac07]. Thoron (^{220}Rn from the ^{232}Th chain) can also be released from materials containing thorium, but with a half-life of just 55.6 s is less likely to escape into the air in this time and the levels are normally below 1% of the levels of ^{222}Rn [Heu95]. A recent radon measurement in the COBRA cabin suggests levels at about 40 Bq/m³ [Zub08].

Figures 4.3a-b include a radon simulation where all isotopes below ^{222}Rn in the ^{238}U decay chain are studied. Events are simulated this time in the air surrounding the detectors and the radon spectrum is scaled so that the sum spectrum best fits the data. The sum of the paint and radon events can be seen to be in much better agreement with the 609 keV peak in the data because fewer betas deposit energy in the crystals. However, the region around the 352 keV peak is still not in perfect agreement for reasons that are not clear. Scaling the radon spectrum was performed by eye for simplicity. In Figure 4.3b, alpha radiation peaks are clearly visible in the data and the radon simulation, but are not evident in the paint simulation. This is because the alphas produced in the paint lose energy as they travel through the paint towards the detector, so very few alpha events produced in the paint deposit their full energy in the detector. Alpha particles produced close to the bottom (cathode) of the detector, which is unpainted, are able to deposit almost their full energy. Remaining differences between the simulation and the data are discussed later in this chapter. First, confirmation is sought that the main peaks observed in Figure 4.3b are indeed alpha radiation due to radon contamination.

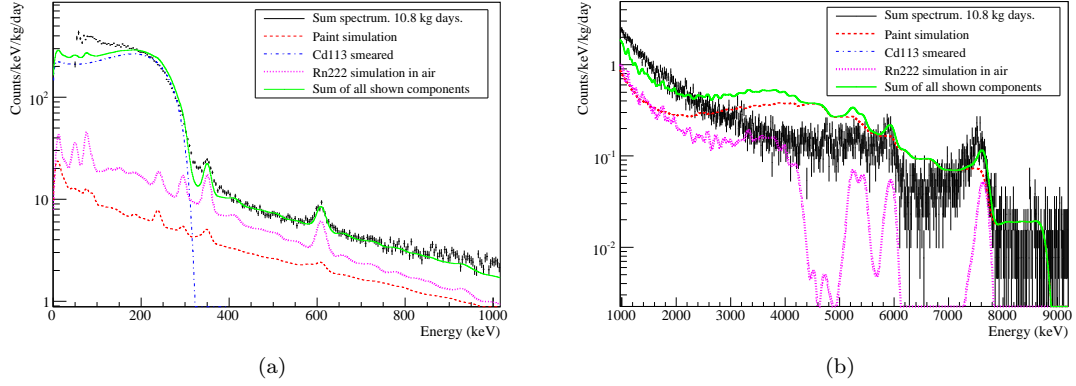


Figure 4.3: Comparison of simulated radon and paint background with the data. (a) The 609 keV gamma peak height to background ratio can be seen to be in much better agreement than in Figure 4.2. (b) The high energy part of the spectrum clearly shows alpha peaks from radon on the cathode surface.

4.1.2.1 Cathode signals

Previous examples of the energy spectra in this thesis have not shown the alpha peaks that are clearly visible at 5.8 MeV and 7.6 MeV (Figure 4.3b). This is because they were only recently identified, having previously been rejected because they are coincident with the high-voltage (HV) veto. Features such as these, which had been observed before at lower energies, have been confirmed in test set-ups to be high-voltage related. For example, a high-voltage cable that was not connected to a detector has produced similar effects, so it is not surprising that it went unnoticed. Because of the similarities of high voltage discharge events (or micro-discharge), there is even greater motivation to find solid evidence that the peaks in the data show real physics.

Alpha peak positions Figure 4.4 shows (a) the sum energy spectrum for datasets L1a-c with and without the HV-veto cut, and (b) only the HV-veto tagged events together with the radon simulation (blue) as plotted earlier in Figure 4.3. The true energies of the main alphas released in the radon chain are also marked and labelled. Both the simulation peaks and the peaks from the data are shown to be significantly below their true energies, which are given later in Table 4.2 on page 101. Also shown in the table are the Q-values of the decays that are between 100–150 keV larger, with the extra energy going to x-rays and nuclear recoil. Despite this additional energy, the energy loss, presumably in the air (there is no cathode contact in the simulation), is enough to reduce the energy of the alphas in the simulation to 5.94 MeV and 7.64 MeV for the ²¹⁸Po and ²¹⁴Po decays respectively. The Gaussian fits to the peaks in the data show a further reduced energy of 5869 ± 10 keV and 7526 ± 13 keV respectively. This suggests the alphas lose between 70 keV and 120 keV when they pass through the cathode contact plate of the detector. According

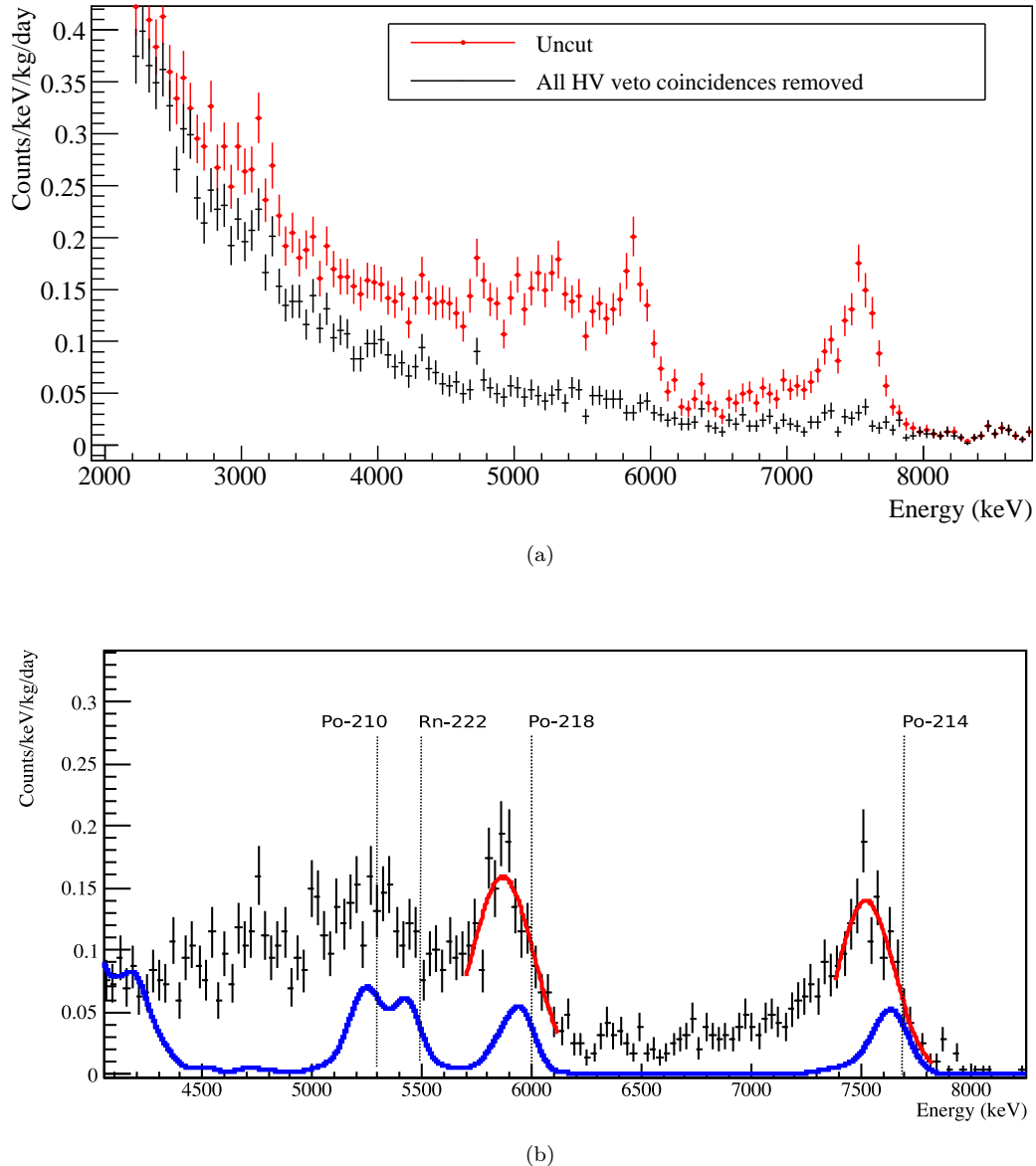


Figure 4.4: Difference between spectra with and without the HV-veto. (a) Alpha radiation peaks are only visible when the HV-veto cut is not made. (b) Only events coincident with the veto are plotted, effectively showing the difference between the spectra in (a). The blue curve is a radon simulation and the vertical lines mark the true alpha energies.

to SRIM⁴, an energy loss of 70–120 keV for alphas passing through gold corresponds to a thickness of 160–260 nm. The manufacturer reports a cathode contact thickness⁵ of approximately 180 nm, which is consistent with the observed energy shift.

Reduced ^{210}Po signals The ^{210}Po and ^{222}Rn peaks in Figure 4.4 partially overlap, so one might expect them to produce a combined peak larger than the ^{218}Po and ^{214}Po peaks. This is not the case because the radon chain is not in equilibrium. The lack of ^{210}Po events can be easily explained when considering the half-lives of the radon chain also given in Table 4.2. The fairly long half-life of 22.3 years of the ^{210}Pb decay suppresses the number of ^{210}Po isotopes that are created. In fact, at the current radon levels it would take many years for the level of ^{210}Pb isotopes to build up to bring the rest of the radon chain into equilibrium. The fraction of ^{210}Pb to ^{214}Po decays that are expected for the current age of the detectors can be estimated with a ‘back-of-the-envelope’ calculation. In the calculation, we make the following (conservative) assumptions:

1. The detectors are exposed for five years (the approximate age of the detectors) at the current radon levels.
2. That all radon daughter products attach themselves to the surfaces of the detectors.
3. That none of the ^{210}Pb isotopes decay in the first five years.

Then, if we take the production rate of 0.2 counts/keV/kg/day, which is the approximate peak height of the ^{218}Po and ^{214}Po peaks in Figure 4.4, then the number of isotopes we expect to be created in five years is $(0.2 \times 5 \times 365) = 365$. The decay rate of this number of ^{210}Pb isotopes is

$$\frac{\ln 2 \times 365 \text{ [atoms]}}{22.3 \text{ [years]} \times 365 \text{ [days/year]}} \simeq 3 \times 10^{-2} \text{ Counts/keV/kg/day.}$$

That is roughly a factor of 10 lower than the alpha peaks of the ^{218}Po and ^{214}Po decays, so we would not expect the ^{210}Po peak to be visible in the energy spectrum. The ^{222}Rn peak is also suppressed, but for different reasons, and is discussed in Section 4.1.3 on page 108.

High voltage veto The HV-veto, also described in Sections 2.2.9.1 and 3.4.3.3, consists of high voltage capacitors connected to the high voltage line on each detector. The other ends of the capacitors are joined together in sets of eight with the left-hand eight lines being fed into a spare ADC channel (ADC21) via a shaper designed for the cathode signals. The right-hand eight detectors were fed into a separate ADC channel (ADC22). It is useful to refer back to Figure 3.22 on page 77, which shows waterfall plots of the HV-veto events. Between the data taking period 22 January and 8 April 2007 the only amplification made to the cathode signals was with the shaper and the ADCs; the examples shown in this section are for this period only.

⁴Scientific software, “The Stopping and Range of Ions in Matter”, that can be downloaded from <http://www.srim.org/>

⁵Note the cathode contact actually contains a layer of platinum as well as gold (see page 118), however for this argument it is assumed the attenuation properties of platinum and gold are similar.

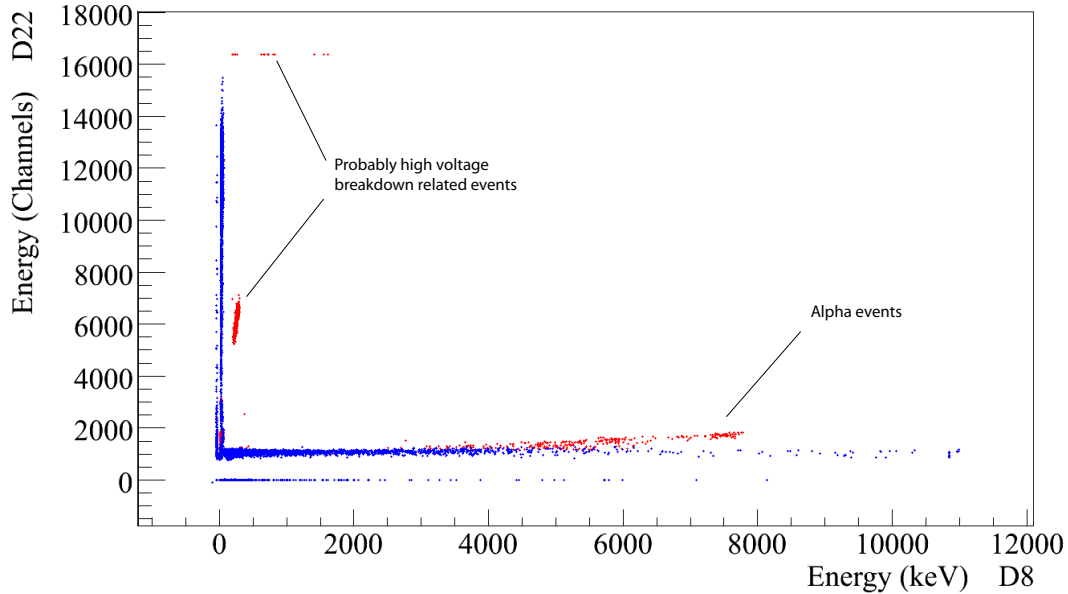


Figure 4.5: Correlation plot of the right-hand HV-veto and detector 8 which effectively shows the cathode signal height against the anode differential signal height in the same instance.

Most of the highlighted events above 2000 channels in Figure 3.22 are believed to be related to high voltage discharge in the cables. The events highlighted below 2000 channels are those believed to be alpha decays passing through the cathode contact plate. The narrow band of events at about 5500 channels in Figure 3.22b are correlated with detector 8, and for this reason this detector is used as an example to demonstrate the difference between high voltage related events and alpha events.

Anode and cathode signal correlations Figure 4.5 shows the energy seen by detector 8 and the right hand veto in the same instant. Those events that are probably high voltage related are marked and fall below 2 MeV on detector 8. The highlighted events below 2000 channels that extend between 2–8 MeV on detector 8 are the alpha events and are shown again in a close up in Figure 4.6. A number of observations can be made from Figure 4.6. Firstly, the linear correlation that is seen between the energy on the detector 8 (anode signal) and the HV side (cathode signal), at least on the upper edge of the protruding ‘finger’, demonstrates that a linear calibration of the HV-veto can be made. This was attempted and provided the following equation relating detector 8 energy, E , to the cathode signal:

$$E = 8.18 \times \text{Channel} - 6620 \text{ (keV)}. \quad (4.2)$$

This relationship is, however, only true for events being created on the cathode surface. Cathode signals on CZT detectors result from an induced signal from electrons travelling towards

the detector anode. The signals have been long studied [HBGN03] as a way to gain depth information from the size of the cathode signal. The pulse height of the cathode events have been shown to be roughly inversely proportional to the depth inside the detector from the cathode. This is demonstrated in Figure 4.7, which shows a similar correlation plot of anode and cathode signals in a pixellated detector by [Blo07]. The anode calibration in this plot has been corrected (but not to scale) to account for hole trapping that reduces the size of the anode signal for events close to the anode and should represent what is seen by our coplanar-grid detectors. A ^{60}Co and ^{137}Cs calibration source was placed close to the pixellated detector. Events from the 1332 keV gamma from ^{60}Co are marked and form a vertical band at the 175 x-axis value. Events at the top of the band occurred at the cathode side of the detector and events with reduced cathode energy occurred closer to the anode side of the detector.

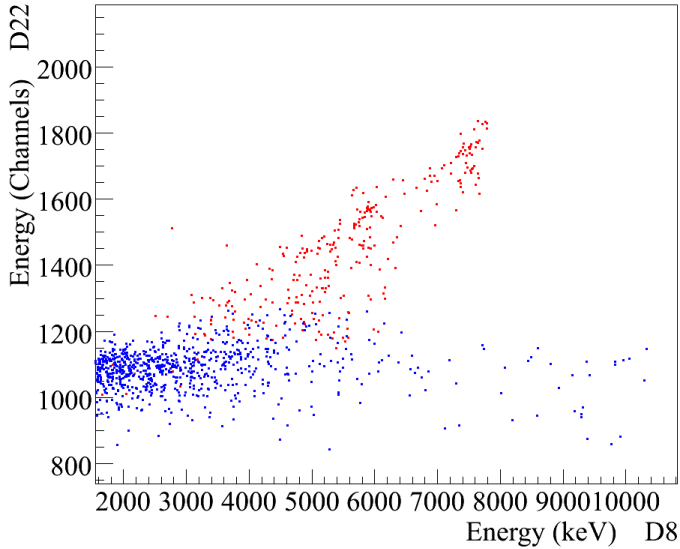


Figure 4.6: A zoom in on the alpha correlation in Figure 4.5. This demonstrates that the alpha events occur on the cathode surface and hints at the size of the dead layer.

Taking a closer look again at Figure 4.6 one sees that no such vertical band exists. This is because all of the 7.7 MeV alpha sources are at the cathode surface and not inside the detector. In fact, a careful study of all correlation plots for each detector did not reveal any event of reduced cathode signal amplitude for the 7.7 MeV region. In other words, no evidence supporting the existence of the isotope ^{214}Po from the ^{238}U chain inside the detector was seen. This unfortunately does not prove they do not exist. An internal ^{214}Po decay may be observed with a longer measuring time. In addition, it is unlikely that the HV-veto is able to detect ^{214}Po decays when they occur close to the detector anode. We can estimate roughly what fraction we might expect to see, if we assume that the cathode signal strength decreases linearly from a maximum at the cathode side to zero at the anode side: with the ~ 3 MeV noise threshold of the veto (see

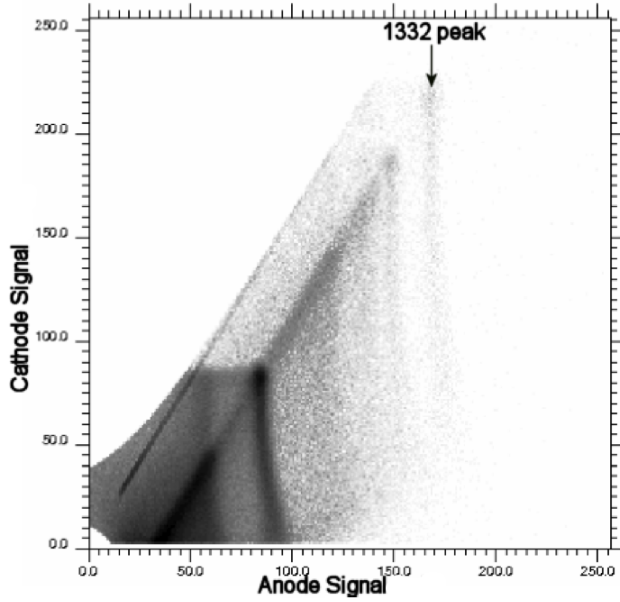


Figure 4.7: Anode and cathode signals of a pixellated CZT detector. A ^{60}Co and ^{137}Cs source was placed next to the detector. The vertical bands represent different interaction depths inside the detector. Taken from [Blo07, p150].

Figure 4.6) we can expect to see $(1 - 3/7.7) \approx 60\%$ of the 7.7 MeV events above the threshold. This efficiency is something that can obviously be improved, as well as a direct calibration of the ratio of cathode and anode signals to the depth of an event. But if a 60% efficiency for detecting an internal 7.7 MeV alpha is true, already low limits for internal ^{214}Po alphas, or indeed any larger energy alphas such as the 8.8 MeV alpha from ^{212}Po in the ^{232}Th chain, can be made. Such limits are calculated in Section 4.2.

It should also be noted that a 7.7 MeV alpha entering through the sides of the detectors would likewise be expected to show a signal at the cathode of the detector and be reduced in size according to where between the anode and cathode it entered. The lack of such events coming from isotopes in the uranium and thorium chains in the paint supports the idea that a dead layer exists on the surface of the detectors. A dead layer need not be thick, which again is what Figure 4.6 suggests: Unlike the 7.7 MeV region where no vertical band of events is seen, the 6 MeV alpha does appear to have a band of events trailing below it. Being so close to the noise threshold the evidence is subtle but it is something that is observed on many, but not all detectors. The 6 MeV events that, as it was suggested, are alphas from ^{218}Po should not show such a band of events because the 7.7 MeV events from ^{214}Po does not. The obvious solution is that the surplus events in this region are in fact ^{214}Po alphas showing also a reduced energy on the anode side having lost energy from passing through a dead layer.

Finally in this section, to remove any doubt as to whether the cathode signals seen by the HV-veto are unique for each detector, Figure 4.8 shows that the events at 3–8 MeV are not correlated between detectors. Where simultaneous energy depositions are seen on two detectors it is likely

to be either γ - γ or β - γ coincidences. If this is not enough evidence for radon, the following section certainly confirms the identity of the HV-veto tagged events.

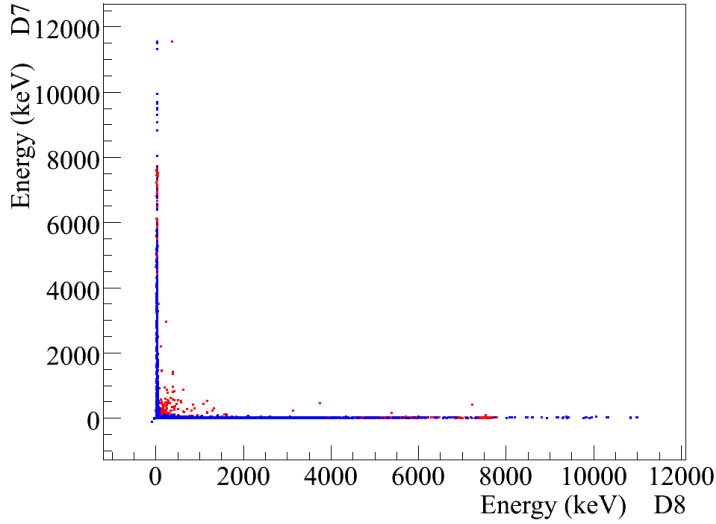


Figure 4.8: The lack of correlations between detectors 7 and 8 demonstrates that HV-veto (cathode) signals are only seen on the detector in which they occur.

4.1.2.2 Alpha-alpha timing coincidences

A timing coincidence is when two or more events are observed closely together in time and are likely caused by the successive decays of short lived mother and daughter isotopes. The half-lives of the isotopes in the radon chain are given in Table 4.2. The fastest decays that the ADC can resolve provide the best chance to observe a timing coincidence above the random background of uncorrelated events. If we select only those events that were tagged by the HV-veto that have been identified as occurring only on the detector surface and thus must be alpha events, then it is only timing coincidences between alpha events that we need to consider. As can be seen in Table 4.2, of the four alphas in the radon chain the first three are expected to occur in a reasonably short time frame. That is, relative to the average time between events in the energy range 1–10 MeV, which is 2.14 hours.

First, let us consider the decay of $^{222}\text{Rn} \rightarrow ^{218}\text{Po} \rightarrow ^{214}\text{Pb}$ (abbreviated $^{222}\text{Rn} \curvearrowright ^{214}\text{Pb}$) where ^{222}Rn first decays emitting a 5.5 MeV alpha shortly followed by the decay of ^{218}Po with a half-life of 3.05 min and emitting a 6.0 MeV alpha. By selecting only pairs⁶ of events that are separated by ≤ 12 minutes, which corresponds to four ^{218}Po half-lives, the energy of the first event of the pair can then be plotted against the second event. This is demonstrated in Figure 4.9, where events more closely spaced than 10 ms have been rejected to help avoid including faster decays. The efficiency for detecting the fast alpha decays where both alphas enter the detector

⁶In this analysis three closely spaced events in time would be considered as two pairs.

is 81% as can be calculated using Equation (4.7). Figure 4.9 clearly shows an accumulation of events in the expected region. This confirms the existence of the alphas from ^{222}Rn although the alpha peak is not clearly evident in an energy spectrum (Figure 4.4).

By selecting only the cluster of events in Figure 4.9 with an energy cut of 5.1–5.6 MeV on the first event and 5.6–6.1 MeV on the second event, a histogram of the time between the events was made and shown in Figure 4.10. The decay constant of the fitted exponential provides a half-life of 5 ± 3 minutes, which is consistent with the 3 minute half-life of the ^{218}Po decay.

The next alpha decay in the chain is from ^{214}Po with an energy of 7.7 MeV, which occurs only after ^{214}Pb and ^{214}Bi have decayed via beta radiation. The sequence is now $^{218}\text{Po} \rightarrow ^{214}\text{Pb} \rightarrow ^{214}\text{Bi} \rightarrow ^{214}\text{Po} \rightarrow ^{210}\text{Pb}$ ($^{218}\text{Po} \curvearrowright ^{210}\text{Pb}$) and the alphas are separated with a combined half-life of 46.7 minutes. Figure 4.11 shows the timing coincidence plot for the period 10 ms–4 hr which corresponds to 5.2 times the combined half-life and an efficiency (if both alphas are detected) of 95%. Again, a larger number of events are seen in the expected region of the plot, about 6.0 MeV and 7.7 MeV for the first and second events respectively, compared to the region opposite region 7.7 MeV and 6.0 MeV for the first event and second events respectively⁷. Note, this figure also includes the events of the $^{222}\text{Rn} \curvearrowright ^{214}\text{Pb}$ decay sequence.

The thorium chain also provides a fast α - α decay ($^{220}\text{Rn} \rightarrow ^{216}\text{Po} \rightarrow ^{212}\text{Pb}$) that can be searched, but no evidence for the decays were seen on the cathode surface (Figure 4.6).

Half-life $T_{1/2}$	Parent isotope	Decay mode	Energy keV	Q-value keV
	(branch, %)	(branch, %)		
3.8235 d	^{222}Rn (100)	α (99.9)	5489	5590
3.05 min	^{218}Po (99.98)	α (100)	6002	6115
26.8 min	^{214}Pb (100)	β		
19.9 min	^{214}Bi (99.979)	β		
164.3 μs	^{214}Po (100)	α (100)	7687	7833
22.3 y	^{210}Pb (\sim 100)	β		
5.013 d	^{210}Bi (\sim 100)	β		
138.4 d	^{210}Po (100)	α (\sim 100)	5304	5407
stable	^{206}Pb			

Table 4.2: Alpha emitters in the radon-220 chain (part of U-238 chain) [Lun, Wah96].

⁷Note, we also expect to see an accumulation of uncorrelated events in the opposite region due to the higher frequency of events at 6.0 MeV and 7.7 MeV.

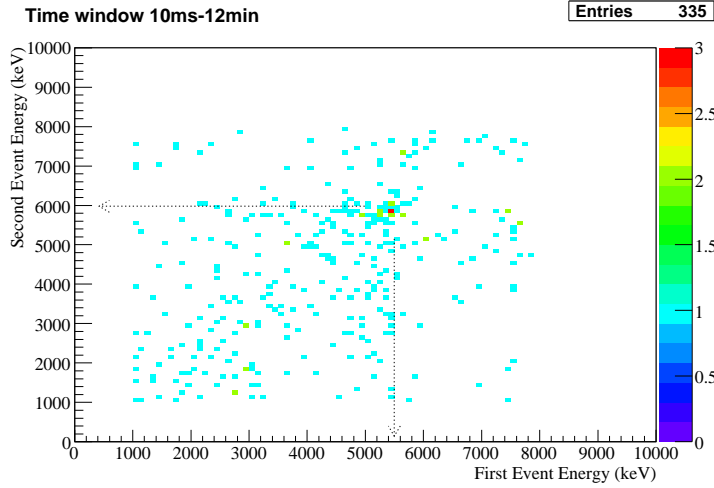


Figure 4.9: Timing coincidence correlation plot for the $^{222}\text{Rn} \sim ^{214}\text{Pb}$ decays. The first and second event energies for events separated in time within the specified window are plotted against each other with the number of events in a 100×100 keV pixel represented by its colour. The plot is a sum over all detectors with a combined live-time of 377 days.

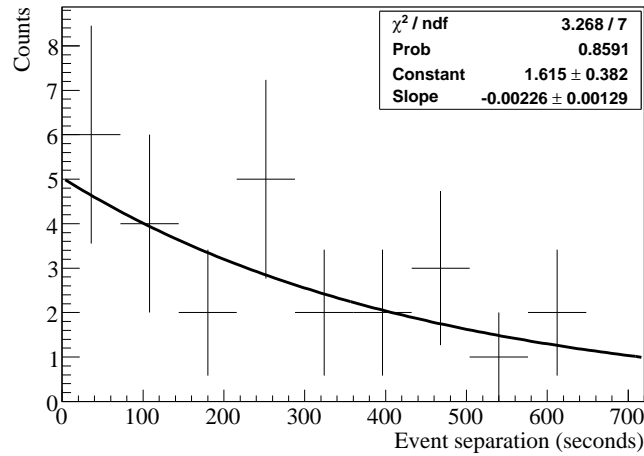


Figure 4.10: Histogram of event separation for the $^{222}\text{Rn} \sim ^{214}\text{Pb}$ decay cut.

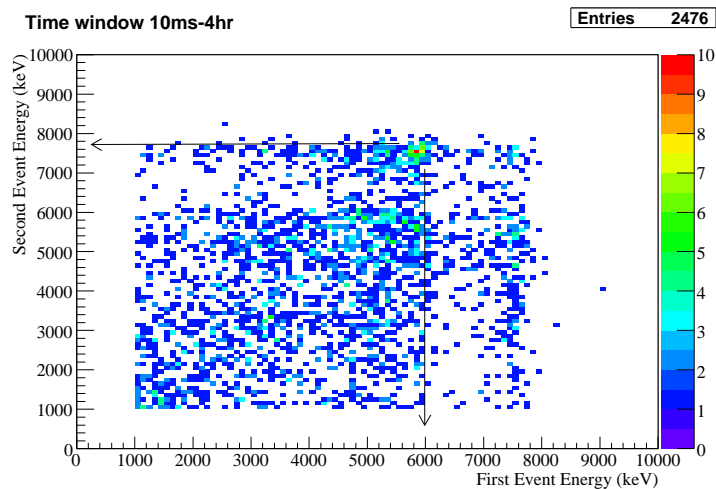
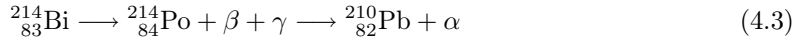


Figure 4.11: Timing coincidence correlation plot for the $^{218}\text{Po} \sim 210\text{Pb}$ decays. Like Figure 4.9 the plot has a combined live-time of 377 days.

4.1.3 Beta-alpha timing coincidence

While the previous studies only looked at the first three months of data from datasets L1a-c and only events tagged by the HV-veto, the following study uses the full dataset to search for the fast β - α decay in the radon/uranium chain. Events that were identified as alphas on the cathode surface are included. However, a selective cut was made on all correlation plots to manually remove any high voltage discharge related events, such as identified in Figure 4.5 on page 97. This was achieved using the techniques described in Appendix B.4.2.3.

The decay of interest,



also listed in Table 4.2, first releases a beta particle that is quickly followed by the release of a 7.7 MeV alpha particle with a half-life of $164.3\ \mu\text{s}$. The beta radiation is released at various energies because the Q-value is not only shared with an antineutrino but also the ^{214}Po atom, that can be created in various excited states from which it instantly decays, emitting gamma radiation. The most likely end points for the beta radiation and the most likely gamma energies are listed in Table 4.3. The Q-value for the decay is 3.275 MeV.

Beta endpoint, MeV (branch, %)	Gamma energy, keV (branch, %)
3.275 (19.9)	609.32 (44.6)
1.88 (7.18)	768.36 (4.76)
1507.5 (17.0)	1120.29 (14.7)
1424.57 (8.18)	1238.11 (5.78)
1.51 (16.9)	1764.49 (15.1)
1.02 (16.9)	2204.21 (4.98)

Table 4.3: Most likely beta spectrum end points and de-excitation gammas from the ^{214}Bi decay [Lun, Wah96].

Correlations As in the previous section, a timing correlation plot is made and shown in Figure 4.12 with a timing cut of $120\text{--}800\ \mu\text{s}$ ⁸. The lower timing cut is set to be above the timing resolution of the ADC (Figure 2.10 on page 35) and the upper timing cut is about five half-lives and together should encompass 70.4% of the events. As one would expect, nearly all of the first events have energies less than the Q-value of the ^{214}Bi decay. The few events that have a greater energy are probably from another yet unidentified fast decay. The energies of the second events, however, are spread right across the scale. Most of the second events have energies less than 6 MeV. These events are likely to be a combination of ^{210}Pb alphas from the paint and radon and show a reduced energy due to the likely dead layer effects noted earlier, as well as the thickness of the paint when alphas from radon are seen. Most of the events between 7 and 8 MeV are likely to be ^{210}Pb alphas on the cathode surface. Above 8 MeV, it is not clear what the events are caused

⁸In the unlikely chance that three (or more) events occur in a row they are counted as two (or more) pairs.

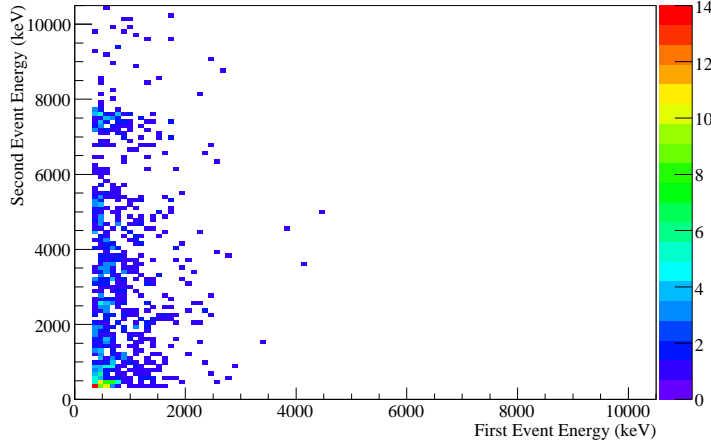


Figure 4.12: Timing coincidence correlation plot for the $^{214}\text{Bi} \rightsquigarrow ^{210}\text{Pb}$ decays. A timing window of 120–800 μs was used.

by, but the fact that none of the first events have this energy provides confidence that they are real. This is not the signature of bursts or HV-discharge. Disturbances in the data have been noted to sometimes show high energy events closely followed by lower energy events, but not the other way around. Such disturbances would also be separated in time by the very limit of the timing resolution of the ADC which is just below the 120 μs cut.

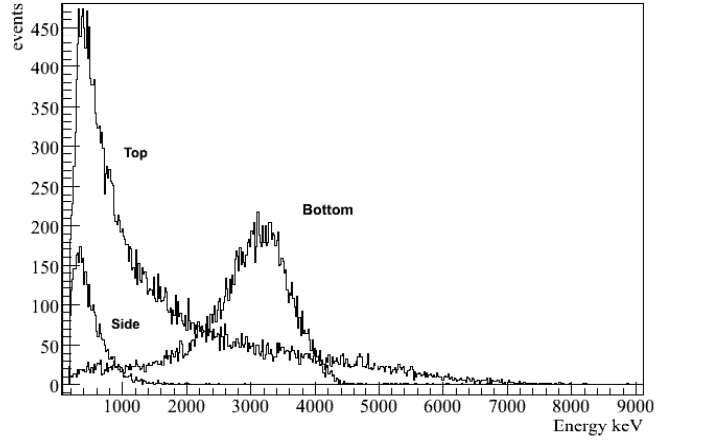


Figure 4.13: Alpha measurements of an ^{241}Am source placed at different positions relative to a CZT detector.

Anode signals A likely explanation of the events above 8 MeV is provided by a test made by J. Dawson using similar painted crystals in the lab at Sussex, which found that alpha radiation entering from the top (anode side) of the detectors was poorly calibrated with many of the event

energies being overestimated. The plot demonstrating this is shown in Figure 4.13 and shows energy spectra taken using an ^{241}Am source placed near the top, bottom and side of the detector. The alphas are produced with a Q-value of 5.6 MeV but are attenuated as they escape from the source and enter the detector. The bottom of the detector, which has been shown previously to not reduce the energy of the alphas by more than 150 keV, provides the best estimate of the actual energy of the alphas as they reach the detector. The peak energy is about 3.2 MeV and almost no events are observed above 4.5 MeV.

The side of the detector shows a large energy loss, as expected, because the alphas travel through both the paint and the dead layer. The peak of the spectrum is shifted towards \sim 100 keV, which is used in Section 4.1.5.1 to estimate the maximum possible dead layer. As one might expect the alpha spectrum taken from the top, anode side, of the detector looks similar to that taken from the sides, because the top of the detector is also painted. There is one major difference though and that is that a significant fraction of the events observed by the anode side of the detector are measured with energies greater than the Q-value, 5.6 MeV, of the decay. This miscalibration of alpha energies is probably due to a limitation in the way that the co-planar grids work. The energy of an alpha particle is probably recorded differently depending on whether the interaction occurs on or in between the two anode grids.

The largest energies of alphas entering through the top of the detectors is between 7 and 8 MeV. This is a factor of between 1.3 and 1.5 times larger than the peak energy, 3.2 MeV, observed by the cathode. Applying the same factor of increase to the 7.7 MeV alpha from the ^{210}Po decays means we can expect the energy from these decays to be sometimes overestimated to as much as 12 MeV. Unfortunately, there is not sufficient data above 12 MeV to reveal if the event rate drops above this energy. However, these observations demonstrate that future prototypes of the experiment will need to look at ways of identifying and rejecting interactions on the anode surface.

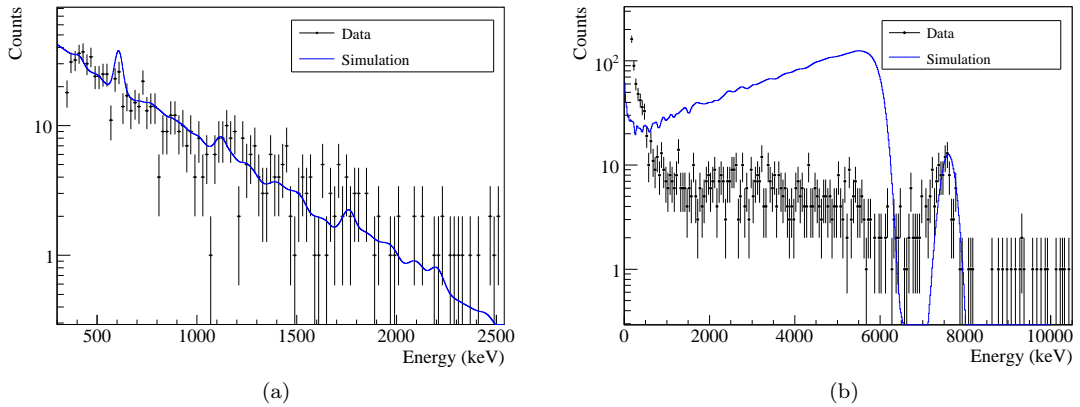


Figure 4.14: Energy spectra of the first beta decay (a) and second alpha decay (b) of ^{214}Bi and ^{214}Po . 200 keV bins are used in both spectra. The simulation in (b) does not match the data well because the dead layer and variable paint width was not included in the simulation.

Energy spectra Because the half-life of ^{214}Po is so short, no uncorrelated⁹ events are expected in the $800\ \mu\text{s}$ time window and no other fast decays are expected to compete with the event rate of ^{214}Po decays. For this reason, plotting the energy spectra of the first and second events in the search of Figure 4.12 is very useful as they should accurately show the energy spectra of the ^{214}Bi and ^{214}Po decays as seen by the detectors. This is demonstrated in Figure 4.14, where (a) shows the energy spectrum of the first event (^{214}Bi decay). A simulation of the ^{214}Bi decay in the air surrounding the detectors is compared and can be seen to be in reasonable agreement. Figure 4.14b, which shows the spectrum of the second event (^{214}Po α -decay), differs greatly from the simulation because the alphas are more sensitive to the detector surface properties. The prominent peak at 7.7 MeV is from the alphas entering the detector through the cathode. All the events below this energy must be alphas that have entered the detectors from the top or sides, since by passing through both paint and a dead layer much of their energy will be lost. Most of the events have an energy below 500 keV yet a significant number fall between 500–6000 keV. It seems likely that the events in this energy region are more dominated by ^{214}Bi contamination in the paint, because they will not have to travel so far into the detector and should lose less energy. No evidence, however, has been found yet to support this theory.

Modelling the alpha spectrum accurately is still very much a ‘work in progress’ and the simulation is mainly shown for demonstration purposes. The simulation does not take into account the dead layer or that the paint is known to not be smooth and so has a variable width. The simulation actually uses half the average paint mass that corresponds to a width of $13\ \mu\text{m}$. Apart from the signals that occur on the detector anodes that are not yet well understood, the rest of the events should be theoretically possible to accurately simulate. The only variables that need to be changed are listed below.

- ▷ Alpha source locations
 - ▷ In the paint
 - ▷ On the paint surface
 - ▷ In the air
- ▷ Alpha source strengths
- ▷ Paint width
- ▷ Paint smoothness
- ▷ Dead layers

Note that the dead layer could vary across surfaces and different sides of the detectors.

Finding the best parameters is a trial and error process unless other ways can be found to exactly characterise the detectors. Due to the length of time required to run one simulation under one set of parameters, this task has not been performed. However, it should be possible, given enough time to reproduce the spectrum with the above parameters.

⁹Events from separate radionuclides that occur closely together in time. This is calculated in Section 4.2.

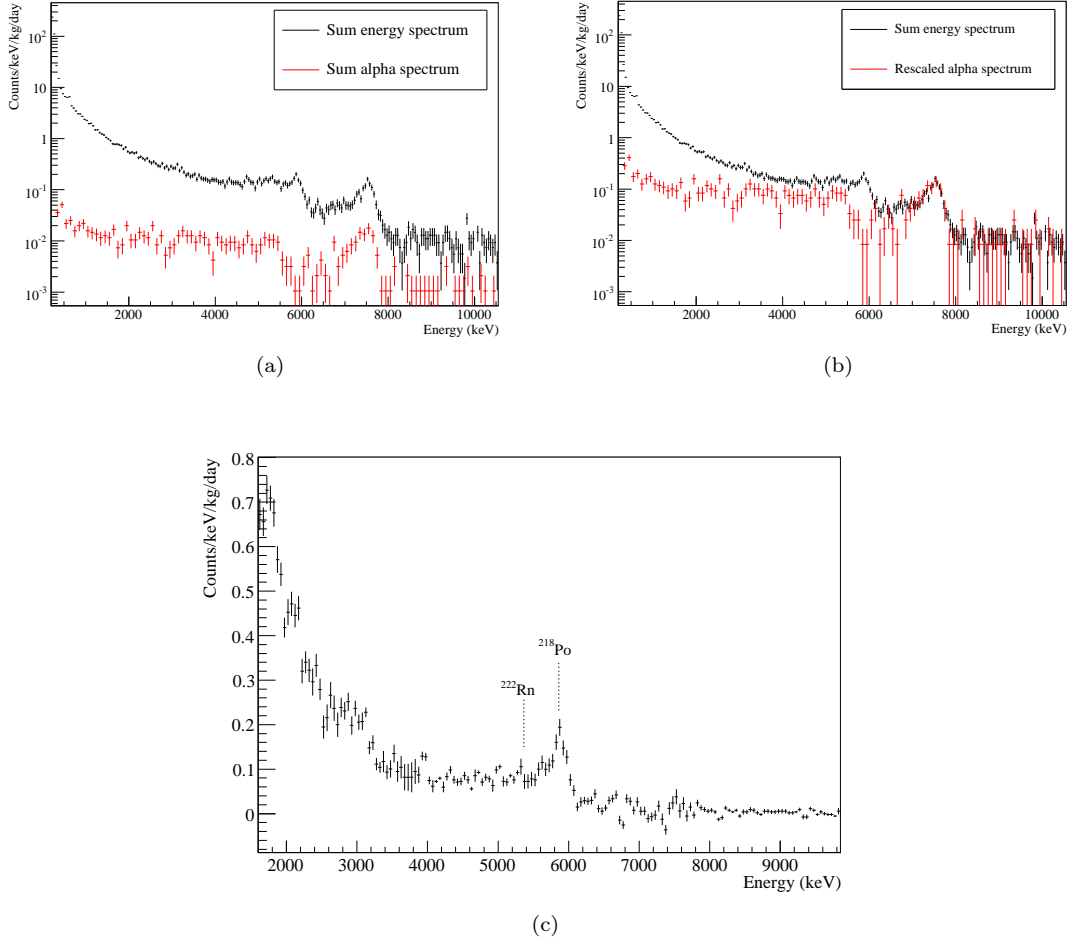


Figure 4.15: Comparison of the sum spectrum with the ^{214}Po alpha spectrum. (a) compares the two spectra. (b) shows the alpha spectrum rescaled to fit the ^{214}Po alpha peak. (c) shows the sum spectrum with the alpha spectrum subtracted and shows the expected location of the ^{222}Rn peak, assuming the same loss of energy as the ^{218}Po peak.

Reduced ^{222}Rn peak It is interesting to see what remains when the ^{214}Po alpha spectrum is subtracted from the general energy spectrum summed over all detectors. This is demonstrated in Figure 4.15. (a) demonstrates the correct scale of the number of tagged ^{214}Po decays. The alpha spectrum is then rescaled in (b) so that the ^{214}Po alpha peak overlaps the peak observed in the data. The scaled alpha spectrum is then subtracted and the remainder is shown in (c). The result emphasises the alpha peak from ^{218}Po but fails to reveal the 5.5 MeV alpha peak from ^{222}Rn that was previously shown to exist in Figure 4.9 on page 102. This apparent contradiction can be explained by considering the difference between the radon and polonium atoms. As previously mentioned, radon is a noble gas and will distribute itself randomly throughout the nest. Polonium, on the other hand, is a metal and will adhere to most surfaces it touches. Consequently, in the three minute half-life that the ^{218}Po isotopes exist, many are able to attach themselves to the

detector surfaces. This enables a larger fraction of alphas from ^{218}Po and the remaining isotopes in the radon chain, to be observed by the detectors. Furthermore, the ability to observe ^{222}Rn decays will be reduced by the fact that the alphas lose energy in the gas and have an obstructed line of sight to the cathode contact because of the glue and Kapton cables used to deliver the high voltage.

Estimating the radon levels from the alpha peaks will also be made difficult for the same reasons. For the polonium peaks, one would have to calculate or simulate the number of ^{218}Po atoms that could theoretically attach themselves within the time limit to the exposed parts of the cathode contact and inner side of the Kapton foil. For the ^{222}Rn isotopes, again a precise simulation including Kapton foils would be required. For this reason an estimate on the radon level is best achieved by the gamma peaks previously mentioned.

Decay curves Creating a histogram of the time between events for the selected energy cuts enables one to test how ‘clean’ the cuts are by comparing the decay constant to the half-life of ^{214}Po decay. Figure 4.16a on the next page shows the decay curve for the large energy range 350 keV to 10.5 MeV with a fitted half-life ($T_{1/2} = \ln 2/\lambda$) of $163.5 \pm 8.5 \mu\text{s}$, which agrees with the value $164.3 \pm 2.0 \mu\text{s}$ reported by [Lun].

Figures 4.16b-e show the decay curves for when the alpha energy is restricted to (b) 350–500 keV, (c) 0.5–6 MeV, (d) 6–8 MeV and (e) 8–10.5 MeV. The fit for the alpha peak region (d) gives a reasonable $\text{Prob}(\chi^2)$ of 0.44. However, the low $\text{Prob}(\chi^2)$ s for (b) and (c) indicate other parts of the alpha spectrum are not entirely clean. It is not known whether the low probabilities for the fit are caused by another fast decay or electronic noise. The trough-shaped spectrum of (e) might indicate a possible electronic problem, but the statistics are too low to be certain.

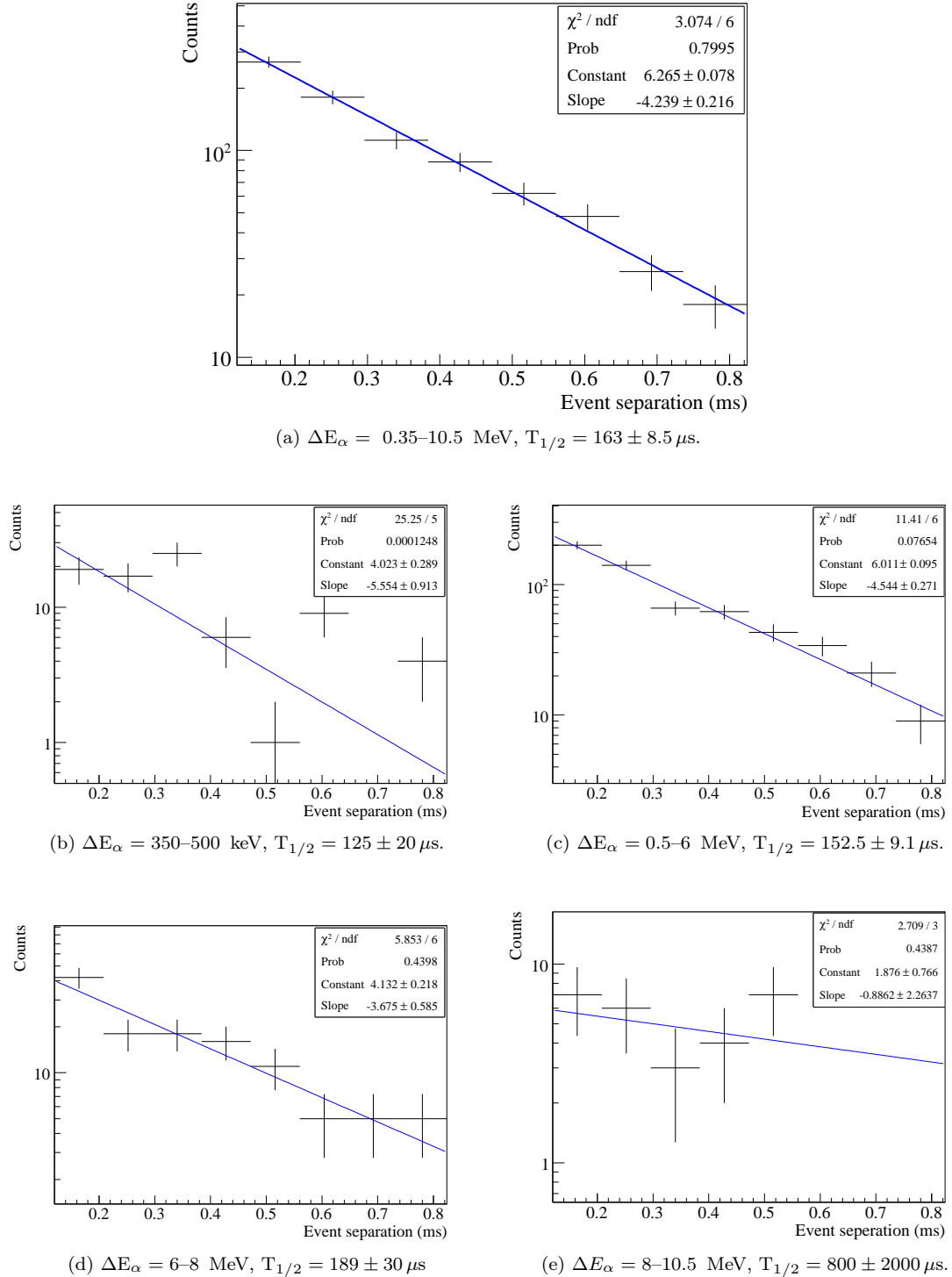


Figure 4.16: Decay curves for the $^{214}\text{Bi} \sim 210\text{Bi}$ search. The spectra show the distribution of times between events where the energy of the second (alpha) event is restricted to the specified energy ranges.

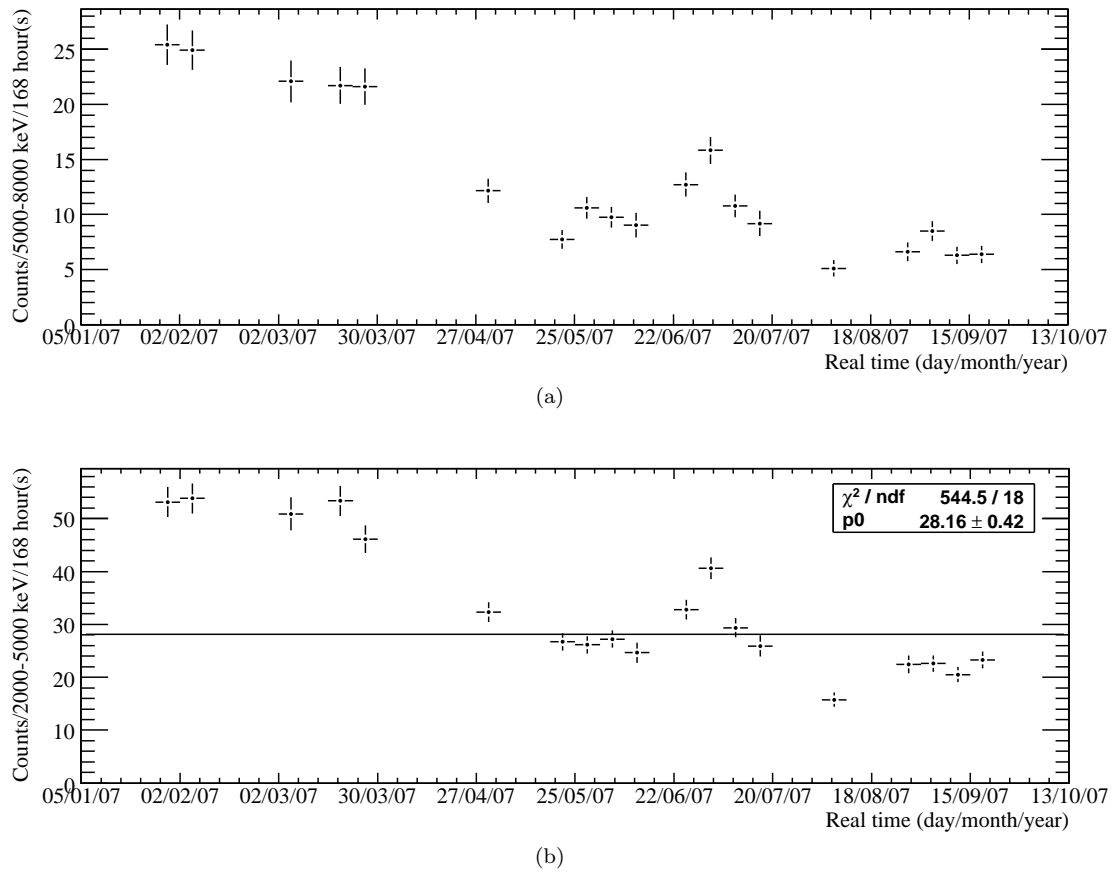


Figure 4.17: Count rates per week for selected energy windows summed over all detectors. (a) Looks at the rate between 5–8 MeV which is the signal region of alphas from radon entering through the cathode of the detectors. (b) Looks at the rate between 2–5 MeV, which likely the signal region of alphas entering the side of the detectors. Both (a) and (b) show variations in rate as radon levels in the nest change.

4.1.4 Count rate consistency checks

Based on evidence such as Figures 4.14 and 4.3b it was suggested that alphas from the paint must play a significant part in the spectrum in the 2–5 MeV region. The aim of this section is to further investigate the contributions of radiation from paint and radon by looking at the variation of count rates in time and between detectors.

Radiation in the paint that was measured to be predominantly from long lived isotopes in the natural decay chains (Table 4.1) should show no measurable changes in activity in the eight months of data taking for datasets L1a-c. However, depending on the location of the experiment and how well the detectors are sealed against drafts, the levels of radon can change significantly. This is demonstrated in Figure 4.17 on the preceding page where plot (a) shows the counts per week over all detectors within 5–8 MeV. In this energy window the majority of the counts were shown to be alphas from the ^{218}Po and ^{214}Po isotopes from radon, and so should heavily reflect the radon levels in the nest. The highest count rates can be seen between January and April. During this period the apparatus was located in the back tunnel at LNGS (Figure 2.1b on page 19) where the radon levels were reported to be high. After this date the apparatus was moved to its current location between halls A and B. The cause of the sudden rise in event rate at the beginning of July is not known but could have something to do with work being carried out at the LNGS facility that produced a lot of dust, or changes to the main air conditioning system for the lab that was being upgraded. The event rate drop seen in the beginning of August coincides with the installation date of the nitrogen flushing system. At this point, the heater used to evaporate liquid nitrogen quickly could not be operated, so the initial low is when the warm dewar provided enough gas pressure to expel the radon. After this, the natural boil-off rate was very small, which allowed the radon to find its way back close to the detectors. The gaps in the data are when the experiment was offline.

Figure 4.17b uses the energy window of 2–5 MeV, which is just below the alpha energies from radon and above most beta and gamma energies. This shows a similar pattern to Figure 4.17a, demonstrating that radon must also play a part at these energies. A zeroth order polynomial is fitted to show the average count rate is 28.16 ± 0.42 counts/week. The lowest rate in this figure is 15.8 ± 1.3 counts/week, thus we know that at least $(28.16 - 15.8)/28.16 = 44\%$ of the sum energy spectrum in the 2–5 MeV region also comes from radon entering the detector through the painted sides of the detectors.

Next, variations in count rates between detectors are investigated. In particular, β - α coincidence spectra are compared. The same cuts as in Section 4.1.3 are made by selecting only events separated between 120–800 μs , and an additional cut to reject all events tagged by the HV-veto is made. The results are demonstrated in Figure 4.18. The number of β - α events seen by each detector can be seen to vary significantly, which is thought to be due to a combination of different dead layer and paint thicknesses.

A closer study of the counts seen by each detector is made. Figure 4.19 compares the event rate of β - α pairs per detector. The count rate of a colourless detector from dataset CL1 is also shown at the position of detector 19. The zeroth order polynomial fit gives an average count rate of 0.43 ± 0.03 counts/day, but shows a $\text{Prob}(\chi^2)$ of close to zero demonstrating that the count

rates are not statistically the same.

Using the measured paint masses (Table 3.4), a plot of paint mass against the number of counts below 6 MeV is shown in Figure 4.20a. A linear correlation here would suggest the count rate is dependent on the paint mass, where the greater the paint mass would mean more paint contaminants close to the detectors. No obvious correlation can be seen. However, there could be an indication that they are inversely correlated, which may be a result of thinner regions of paint that would allow more alphas through. It is possible that these two influences (alpha radiation from the paint and from radon) are in competition. No correlation is seen with the detector mass either, as is demonstrated in Figure 4.20b.

If there were a correlation with paint mass it would have provided a clue as to what level the paint activity contributes to the energy spectrum. This is, in turn, important for setting a lower limit on the dead layer of the crystals. In fact, it is also possible the dead layers are preventing one from demonstrating a correlation, since each detector will probably have a different dead layer thickness.

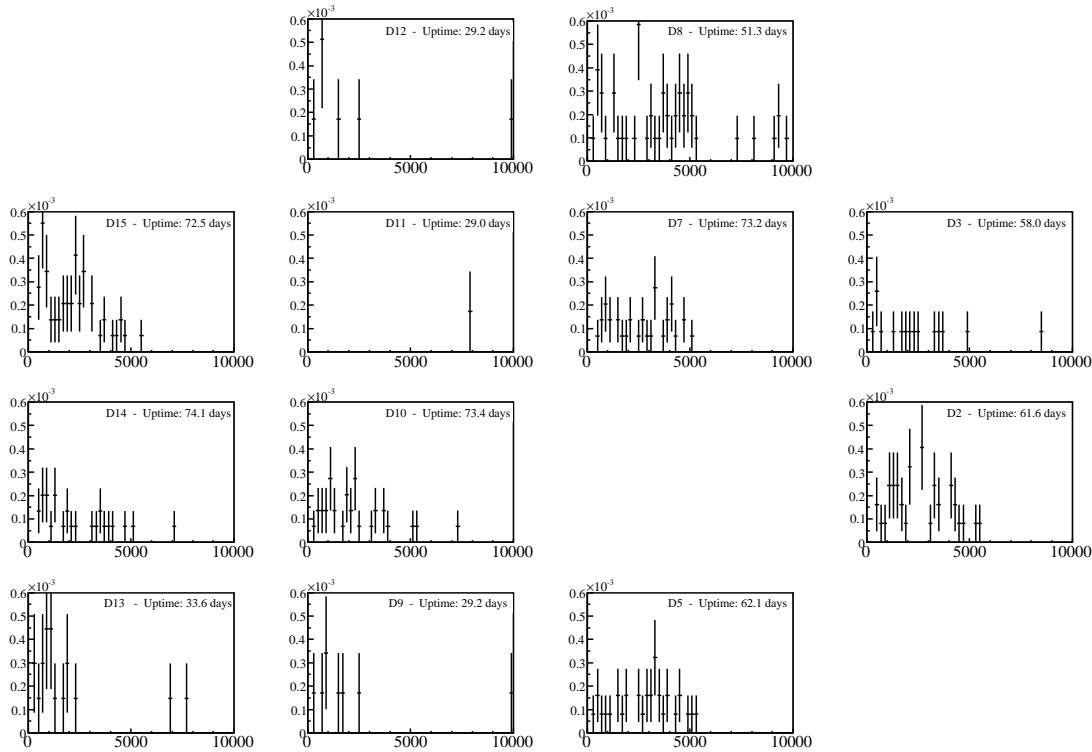


Figure 4.18: Alpha energy spectra from the ^{214}Po decay for each detector. Events were counted when the time between events was 0.12–1 ms and the first event was allowed an energy between 350 and 3500 keV. All events correlated with the HV-veto were removed. Spectra are arranged according to the detector positions (see page 151). The x-axes varies between 0 and 10 000 keV and the y-axes vary between 0 and 6×10^{-4} counts/day.

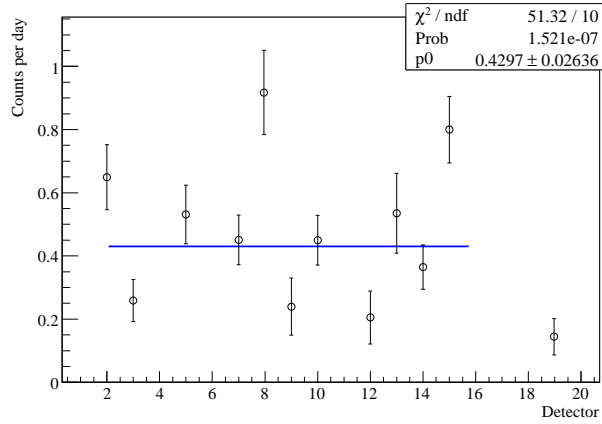


Figure 4.19: A comparison of the total number of events per day observed in Figure 4.18. The average rate is 0.43 ± 0.03 counts/day with effectively no probability that they are in statistical agreement. Detector 11, which for some reason had only one count, is not included in the fit. Also shown, but not included in the fit is the colourless detector (19) from the dataset CL1.

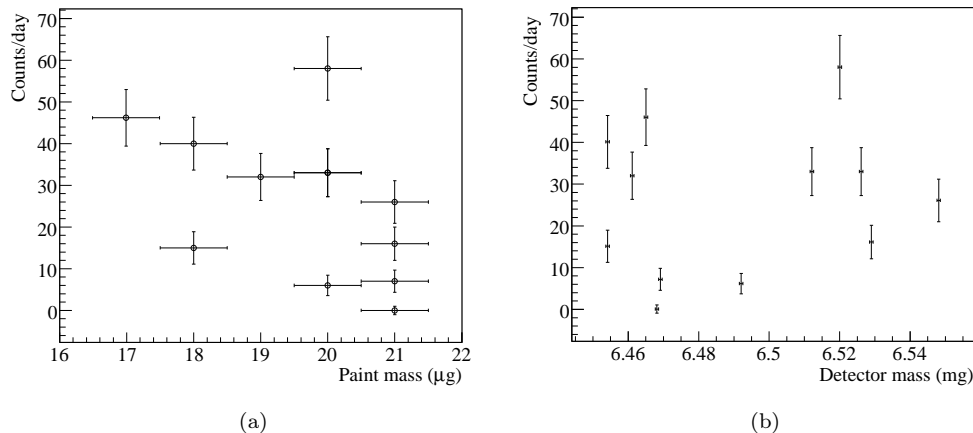


Figure 4.20: The count rate below 6 MeV in Figure 4.18 is compared with (a) the paint mass and (b) the detector mass.

4.1.5 Completing the spectrum

The purpose of this section was, by modelling the background, to identify any remaining backgrounds and put constraints on the dead layer of the detectors. Any early measurements of other contaminants will be useful when designing the next experiment. An active volume measurement is essential for calculating accurate limits on internal decay rates. Unfortunately, due to the high level of radon, both tasks are made very difficult. The main findings are, however, brought together to demonstrate what might still be achieved if new radon free data were collected.

4.1.5.1 Dead layer constraints

We have seen earlier how the paint simulations predict the existence of a dead layer because the count rate from the simulated alphas was greater than observed in the data (this is also seen in Figure 4.22). We were then able to confirm from Figure 4.6 on page 98, which shows a plot of cathode signals against anode signals, that if the measurements of the paint sample is correct, then a dead layer must exist in order to explain the lack of alphas from the paint seen at their full energies. Alphas from the paint would be distributed vertically at 7.7 MeV. It was suggested that the small number of events distributed vertically at 6 MeV could be 7.7 MeV alphas from the ^{214}Po decay having travelled through a dead layer from the passivation paint. It is possible that these events provide an actual measurement of the minimum dead layer for detector 8 shown. A similar lack of events at 7.7 MeV was observed on all detectors, but not all detectors showed events at 6 MeV. Note that in Figure 4.22, which shows a simulation of ^{238}U in the paint, a dead layer of 5 μm is sufficient to reduce the 7.7 MeV alphas to 6 MeV. Thus a 5 μm minimum dead layer is probably a reasonable estimate.

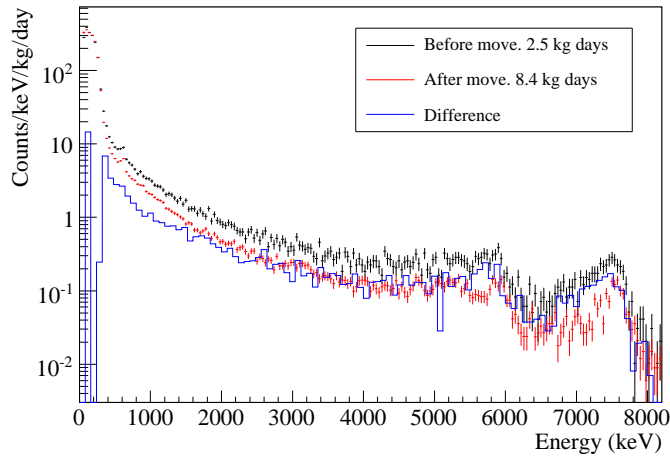


Figure 4.21: Comparison of energy spectrum before and after the move. The spectrum is a sum over all detectors where (black) dataset L1a is compared with (red) datasets L1b-d. The difference in spectra results from reduced radon levels after the experiment was moved from the back tunnel to between Halls A and B at LNGS. Blue shows the difference of the spectra.

Figure 4.21 again attempts to reveal evidence of alphas from the paint. The figure shows a sum spectrum for periods before and after the move. However, the whole spectrum is seen to drop by the same factor of 2 from 1.5 MeV upwards and does not reveal any underlying features. The reduction factor is less in the range 350–1500 keV, indicating another background (possibly from the paint) is in greater competition. Below 350 keV the ^{113}Cd beta spectrum, of course, dominates. Ideally what we require is data from the painted red detectors in a completely radon free environment. The resulting energy spectra could then be compared to simulations with various dead layers to obtain the best fit.

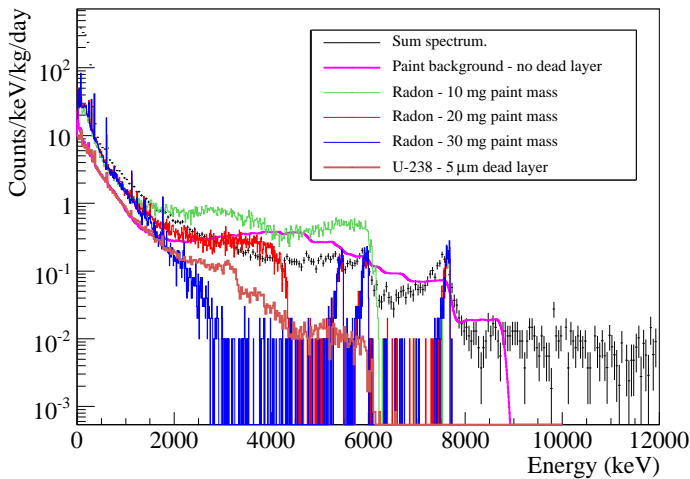


Figure 4.22: Comparison of various simulations with the data. Note, the radon simulations have not been smeared and are scaled so that the ^{214}Po alpha peak only roughly fits the spectrum. Events for the radon simulations were generated uniformly in the air of the detector nest, before it was realised that it is necessary to also simulate ^{218}Po and its daughter nuclei separately on the paint surface. No dead layer was used in the radon simulations.

To a lesser extent this can also be done with the current data that includes the strong radon background. It should, theoretically, be possible to simulate the known backgrounds and vary all of the free parameters until the simulation is in full agreement with the observed spectrum. These parameters were listed on page 107, where it was noted that the paint smoothness will affect the results. We know the mass of the paint, so any grooves or thinner areas of paint must be compensated by thicker areas. Thus, an approximation could be made by simulating a few different thicknesses of paint with an average that represents the paint mass of 20 mg.

This is briefly investigated in Figure 4.22, which looks at three radon simulations for different paint masses and no dead layer. It can be seen that half the paint width already produces about the same attenuation as a 5 μm dead layer. The findings of the correlation plots of cathode to anode signals (Figure 4.6) suggest dead layers of at least 5 μm , but this poses a problem as it suggests that there must be regions of the detectors that are unpainted. Otherwise, how else do the alphas contribute to the 6 MeV region? If this question can be answered then it should be possible to use the simulations to impose limits on the width of the dead layer.

An upper limit on the dead layer is probably currently best made from the ^{241}Am spectrum previously shown in Figure 4.13 on page 105. Alphas from the 5.6 MeV source were only just able to enter the sides of the detector, producing a peak at about 300 keV. At the time the spectrum was created, the real energy of the alphas entering the detector was not known, because, it was also not known how much energy was lost in the source casing. However, this analysis (Section 4.1.2.1) has shown that the energy lost by the alphas from radon as it passes through the cathode contact is just ~ 100 keV, which means the spectrum taken through the cathode in Figure 4.13 provides the calibration: most alphas from the source have a reduced energy of about 3.3 MeV. According to a SRIM simulation (see results in Figure A.2 on page 152) the range of a 3.3 MeV alpha in CZT is about 11 μm . Because the paint further reduces the energy of the alphas by an unknown quantity, 11 μm serves as an upper limit. Thus, this analysis provides the result that the dead layers are likely between 5–11 μm . Given that the upper limit is only provided from the analysis of one detector, a conservative estimate of 15 μm is sometimes used.

4.1.5.2 Single detector studies

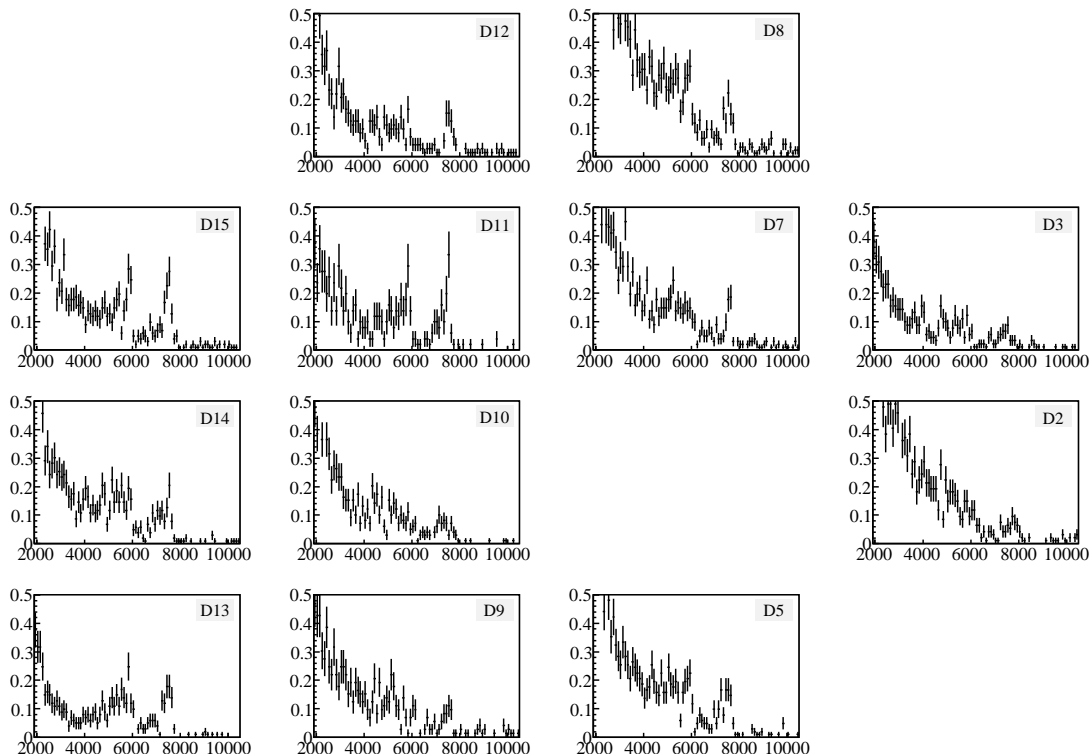


Figure 4.23: Energy spectra showing the high energy events measured by each working detector. The spectra are arranged in the positions that the detectors are in the nest, with the bottom detectors closest to the nest entrance. The x-axis on each plot extends between 2 and 10.5 MeV and the y-axis is between 0 and 0.5 counts/keV/kg/day.

Due to limited time and statistics, this thesis has mainly focused on spectra summed over all detectors. Figure 4.23 demonstrates that the energy spectra of each detector vary significantly, providing further challenges/constraints for the simulations. Some detectors show more prominent polonium peaks than others. This is probably because these detectors' cathodes are less protected by the cathode contact and glue. The larger number of events towards higher energies on particularly detectors 2 and 8 are expected to be due to either thinner dead layers or greater areas of very thin paint.

4.1.5.3 Indications of remaining backgrounds

This section takes a closer look at the spectral features in Figure 4.24. The dotted arrows indicate the locations of already identified alpha peaks. The solid arrows mark possible peaks that have not yet been identified. The peaks are less visible when events with coincident cathode signals are rejected indicating that they are also likely to be alpha emitters at the cathode. The peaks were fitted with Gaussian functions and their energies are given in the figure caption. The most prominent of these peaks at 3.1 and 6.4 MeV are discussed in further detail.

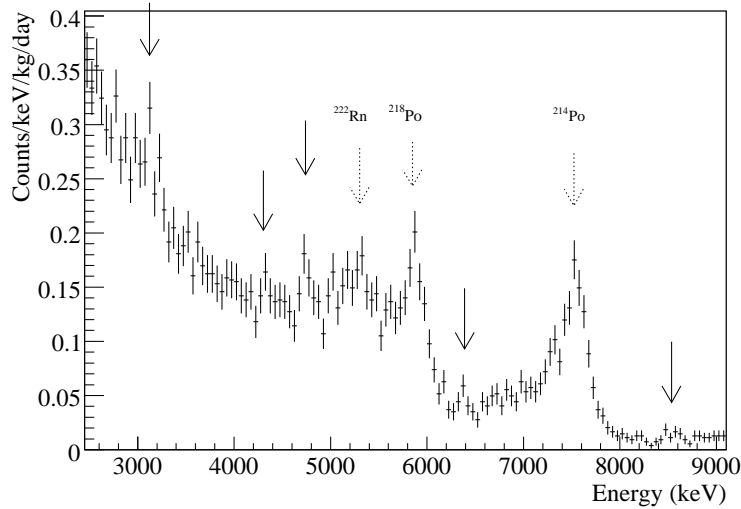


Figure 4.24: Energy spectrum showing smaller peaks at high energy. Arrows indicate possible radiation peaks. The dotted arrows are peaks that have already been identified. The bin width in this plot is 50 keV. The peaks marked with solid arrows were fitted with Gaussian functions that returned the following energies: 3126 ± 40 , 4306 ± 14 , 4740 ± 20 , 6369 ± 10 and 8544 ± 23 keV.

Platinum The number of gammas with energies within the uncertainty of the 3126 ± 40 keV peak position are too many to investigate for this thesis, but 3.1 MeV is already above the energy of all gammas from the natural decay chains of uranium and thorium. If, however, the events are from alpha decays then this greatly reduces the number of possible radioactive sources. For radionuclides on the cathode surface we can expect between 120–140 keV to be lost in transition

through the cathode, as with the identified polonium peaks. If the source is internal then we can expect to see the full Q-value released from the decay. Taking a conservative uncertainty on the peak positions as 150 keV, to allow for an uncertainty in the calibration and location of the source, a search in the Lund/LBNL¹⁰ database for external alpha radiation with an energy 3260 ± 150 keV yields the results highlighted in blue in Table 4.4. For an internal source, Q-values of alpha decays between 3130 ± 100 keV are marked in green.

Of the isotopes listed, only ^{190}Pt , ^{148}Gd and ^{108}Te have reasonable branching ratios and ^{190}Pt (platinum), which has a Q-value of 3249 ± 6 keV, is the only isotope that occurs naturally, making it the favourite candidate.

Alpha Energy (keV)	Q-value (keV)	Alpha branch (%)	Decay mode branch (%)	Half-life $T_{1/2}$	Isotope
	3087 44		$< 7 \times 10^{-7}$	17.5 h 1	^{152}Tb
	3095 50		~ 0.011	2.74 s 8	^{113}Xe
3016 4	3100 3	100	4.3×10^{-4} 1	9.28 d 10	^{149}Gd
3080 15	3226 50	100	3.9 13	4.6 s 3	^{109}Te
3152 10	3282 50	100	~ 0.1	2.5 s 2	^{111}I
3180 6	3249 6	100	100	6.5×10^{11} y 3	$^{190}\text{Pt}^*$
3182.787 24	3271.21 3	100	100	74.6 y 30	^{148}Gd
3183 5	3497 4	~ 0.1	9.5×10^{-3}	17.609 h 1	^{151}Tb
3409 5	"	~ 100	"	"	"
3211 7	3330 6	100	0.8	2.7 s 8	^{112}Xe
3239 30	3357 50	100	0.018	0.57 s 2	^{114}Cs
3305 5	3559 4	0.02	0.0094	6.4 h 1	^{153}Dy
3318 4	3445 4	100	49	2.1 s 1	^{108}Te

Table 4.4: Possible alpha emitters for the 3170 keV peak for (blue) an external and (green) internal source. Uncertainties on the last digits are shown in italics. *Indicates the only isotope that was found to be naturally abundant and is also the favourite candidate.

Armed with this lead, it was then confirmed that platinum is used when making gold plated contacts and that the manufacturer estimates that the cathode contacts consist of an inner layer of about 1000 Å of platinum followed by 800 Å of gold. That platinum is the inner layer can explain why less energy is lost before entering the detector compared to the polonium isotopes.

Using the manufacturer's estimate for the thickness of platinum it is then possible to predict the count rate we expect to see from ^{190}Pt . The number of platinum source atoms is calculated with the equation

$$N = a\rho V \frac{N_A}{m}, \quad (4.4)$$

where the natural abundance, a , of ^{190}Pt is 0.01%, the density of platinum, ρ , is 21.5 g/cm³, the volume of platinum, V , is 10^{-5} cm³ (for cathode surface area of 1 cm²), the molar mass, m ,

¹⁰<http://nucleardata.nuclear.lu.se>

is 195 g/mol and N_A is Avogadro's number. The number of source atoms, N , in this volume is $\sim 6.6 \times 10^{13}$. If we assume only 20% of the alphas are seen directly by the detector (the precise number could be found through simulation), the number of observable source atoms is $\sim 1.3 \times 10^{13}$. The rate of the decays, R , can be calculated with

$$R = \frac{N \cdot \ln 2}{T_{1/2}}, \quad (4.5)$$

where the half-life $T_{1/2}$ is 6.5×10^{11} years. The rate comes to $\sim 4 \times 10^{-2}$ events/day, which, for an average detector mass of 6.5 g, corresponds to ~ 6 counts/kgCZT/day.

We can compare this rate to the area under the peak in the data. This was achieved by fitting a Gaussian function on top of an exponential background. Due to the low statistics, the resolution had to be fixed in order for the fit to minimise and it was assumed to be 200 keV (FWHM). The resolution was estimated by adjusting the offset of the average resolution equation (Equation 3.1) so that it is consistent with the resolution of the polonium alpha peaks. The fit (Figure 4.25) returned a $\text{Prob}(\chi^2)$ of 0.62 and the area under the fitted Gaussian was calculated as 6.3 ± 2.7 counts/kg/day. The numbers are in remarkable agreement.

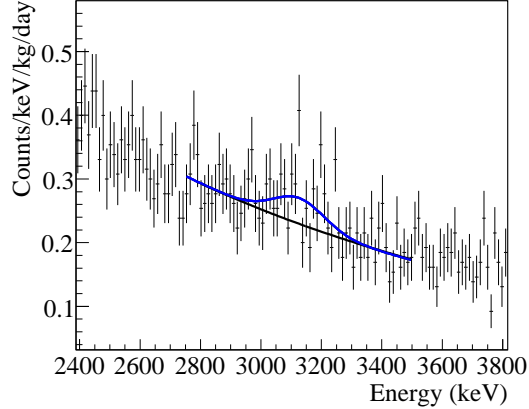


Figure 4.25: Gaussian fit on an exponential background for the ^{190}Pt alpha peak.

This has important implications to the COBRA experiment because it is just above one of the main DBD signal regions from ^{116}Cd that has a Q-value of 2805 keV. If the paint and radon background is removed, alphas from the tail of this peak will likely be the next dominant background in this region. In addition, ^{190}Pt decays to another unstable isotope ^{186}Os , which decays via alpha radiation to the stable isotope ^{180}W . The energy of the alpha from ^{186}Os is 2822 keV, effectively on the ^{116}Cd signal region. The half-life of ^{186}Os is, however, even longer at 2.0×10^{15} years, thus with the small number of ^{186}Os isotopes that are created it is unlikely to ever be an observable background. However, it does add weight to the necessity that an alternative to using platinum for the contacts of the detectors must be found.

Other candidate backgrounds It is not clear what could be contributing to the other possible peaks in Figure 4.24. A number of candidate backgrounds are now presented and reasons for discounting many of them are given. Special attention is paid to the feature at 6370 keV because it is particularly apparent. Again, this energy is above the gamma energies of naturally occurring isotopes.

Eight isotopes, ^{52}Ti , ^{134}Sb , ^{133}Sn , ^{15}C , ^{40}Cl , ^{94}Rb , ^{136}I , and ^{29}S , decay through beta radiation and can produce gammas within 6370 ± 100 keV. However, the isotopes can be dismissed on the basis that the branching probabilities for the gammas are less than 0.2% and no more prominent peaks are seen from the more dominant branches or from daughter radionuclides.

The alpha emitters in this energy region are more numerous. Foremost, the potential alpha backgrounds that occur naturally in nature and are external to the detectors are investigated. Assuming a similar loss of energy that was observed with the polonium peaks, 130 keV is added to 6370 keV, and naturally occurring alphas with 6500 ± 100 keV are presented in the top block of Table 4.5. These isotopes can also be discredited on the basis that we would expect to see peaks from the other alphas (not shown) with greater branches. For example, ^{219}Rn , which is part of the ^{235}U chain, decays by producing an alpha of 6420 keV with a branch of 7.5%, where 81% of the time a 6820 keV alpha is produced. Furthermore, the daughter isotope, ^{215}Po , emits an alpha of 7390 keV with a branch of 99%. No larger peaks from the alphas are observed in the data.

There are too many alphas that do *not* occur naturally in nature to be investigated here within the above energy region. To limit the search to the most likely candidates, only alphas within the range 6500 ± 50 keV were sought, with a further condition set that the product of the branching ratios of both the alpha, I_α , and the decay mode, I_D , are greater than 25% ($I_\alpha \times I_D > 0.25$). This was achieved by downloading the Lund/LBNL database [TOR] and writing a macro to search for the isotopes of interest. The results are printed in the middle block of Table 4.5. No likely candidates within this list were identified.

Finally, a list of potential internal alpha emitters is presented in the lower block of Table 4.5, where a selection is made that the Q-values of the decays are between 6450–6550 keV and the decay branch, I_D , is greater than 10%. The only naturally occurring isotopes in this selection are ^{219}At and ^{220}Rn . ^{219}At can be discredited on the basis that it is created as part of a minor branch of the ^{235}U chain in which no obvious peaks are discernible. The isotope ^{220}Rn , which has a Q-value of 6400 keV, forms a central part of the decay chain of the naturally abundant radionuclide ^{232}U , so other alpha peaks from the chain would have a similar (small) size and most will be masked by the more prominent radon-related backgrounds. There is one alpha decay in the chain (see Table A.2 on page 154), that is of ^{212}Po , which has a Q-value of 8954 ± 11 keV. This is in a low background region of the energy spectrum. There is no indication of a peak at this energy, only at the slightly lower energy of 8.6 MeV. No evidence of an internal thorium source was found in Section 4.2.

A complete list of Q-values of the naturally occurring alpha emitters recorded in the Lund/LBNL database is given in Appendix A, Table A.3. A list of alpha energies from naturally occurring radionuclides with $I_\alpha \times I_D > 0.1$ is given in Table A.4.

It was noted that many of the tests to reject unlikely candidates could be automated without

great difficulty and it is suggested that a peak-identifying algorithm could be developed that can deal specifically with the particulars of the COBRA experiment. For example, to have the ability to take into account the energy lost due to the anode thickness or dead layer, and the time between decays, to match the information recorded in the database.

Alpha Energy (keV)	Alpha branch I_α (%)	Q-value (keV)	Decay mode branch I_D (%)	Half-life $T_{1/2}$	Parent isotope
6425.0 10	7.5 6	6946.1 3	100	3.96 s 1	$^{219}\text{Rn}^*$
6529.0	0.12	"	"	"	"
6552.6 10	12.9 6	"	"	"	"
6483.5	0.02 1	7201.9 14	99.988 4	32.3 ms 4	$^{217}\text{At}^*$
6531.2 21	0.127 10	7263.0 19	100	35 ms 5	$^{218}\text{Rn}^*$
6568.3 9	0.544 19	7594.5 5	100	0.516 s 3	$^{211}\text{Po}^*$
6450.3	100	6607.50	~99	25 ms 9	^{171}Pt
6456.5	96.9	6862.5	70 9	6.2 s 1	$^{190\text{m}}\text{Bi}$
6464.4 14	100	6596.4 14	57 6	43 s 1	^{200}At
6465.8 3	85 2	6580.0 21	50.2	38.3 m 3	^{227}Pa
6475.5	100	6305.5	90 +10-20	3.2 s 6	$^{193\text{m}}\text{Bi}$
6478.3	43 2	6921.4 21	~90	8.72 m 4	^{225}Th
6499.2 25	97	6629.9 23	66 9	45 s 3	^{203}Rn
6520.2	93.7 7	6863.8 14	99.790 5	100.5 d 2	^{257}Fm
6520.3	99.978 13	6657.3	~98	5.8 s 2	^{196}Po
6534.5	>80	6660.5	100	3.10 m 2	^{211}Fr
6537.4	100	6660.4	>95	<10 s	^{217}Po
6543.5	~100	6703.47	60 30	3.18 m 6	^{210}Fr
6545.8	100	6704.6	100	6 ms +5-2	^{170}Pt
6549.0 25	100	6629.9 23	80	28 s 2	$^{203\text{m}}\text{Rn}$
		6353.50	84 6	342 ms 18	^{173}Pt
		6353.7 14	18 3	184 s 1	^{202}At
		6361.5	99.9971 3	333.5 d 28	^{248}Cf
		6376.5	18 9	37 s 3	^{192}Bi
		6382.50	96.6 12	10.1 ms 4	^{157}Ta
		6383.8 16	63 6	5.67 m 17	^{206}Rn
		6385.3	100	23.9 m 12	^{212}Rn
		6386.50	23 4	2.8 m 1	^{205}Rn
		6391.51	~97	56 s 3	$^{219}\text{At}^*$
		6397.2 6	>99.5	27 d 1	^{240}Cm
		6404.67 10	100	55.6 s 1	$^{220}\text{Rn}^*$
		6412.50	44 7	53.6 s 10	^{197}Po

Table 4.5: Possible alpha emitters for the 6370 keV peak. The first six isotopes (upper block) are naturally occurring external candidates. The central block are candidates with combined branching ratios greater than 25% ($I_\alpha \times I_D > 0.25$). The lower block are internal candidates with $I_\alpha \times I_D > 0.1$. *Indicates isotopes that occur naturally in nature.

4.2 Internal Backgrounds

Internal backgrounds are any nuclear decays that occur inside the crystal itself that are not neutrinoless DBDs. It is important to use only pure materials for neutrinoless DBD searches. If we need to modify the production process, we must know as soon as possible. Identifying internal backgrounds can be done by finding unique signatures in the data that can only be produced by a known decay inside the detector. The easiest decays to search for are those that have the most striking signatures, because they are least likely to be mimicked by another background or random processes.

For isotopes in the natural radioactive decay chains, the best chance of tagging them is made with the alpha radiation they produce. Because the range of alphas in CZT is very short ($\sim 11\mu\text{m}$) one can be certain that they do not escape outside the detectors and that their full energy is measured. The only exception to this would be for events that occur within microns of the sides of a detector or if an internal defect exists that reduces the efficiency of a detector. Alpha decays produced by short-lived isotopes can be easily singled out because the probability of two random events to occur in quick succession at the Q-values of the decays is small.

No cosmogenically activated isotopes that decay via alpha emission are expected in the crystals. This is because the heaviest component of the detectors, tellurium, has a maximum of only 130 nucleons. The isotopes of CZT could be broken up through spallation from cosmic rays to unstable lighter nuclei, but there are only 16 alpha emitters from lower mass isotopes¹¹ and all have half-lives of less than 7 seconds. Furthermore, these radionuclides are all located on the table of isotopes where the imbalance of neutron to proton number gives rise to short half-lives of less than a minute, so any daughter alpha emitters have long decayed by the time data taking started underground. Searches for cosmogenics must be made by looking for coincidences of beta and gamma radiation, which is difficult because betas share their energy with a neutrino, and gammas have only a small probability of depositing their full energy in an array of detectors.

The isotopes ^{40}K , ^{60}Co and ^{137}Cs , listed in Table 4.1 on page 91, do not form part of the uranium and thorium chains and it cannot be easily tested whether they are internal or external because they decay via beta radiation or electron capture to stable isotopes. Consequently, the main focus of this section is on the achievable goal of setting a limit on the activity of uranium and thorium backgrounds inside the detectors of the 64 array.

4.2.1 Search for Bismuth-214

To search for evidence of the ^{238}U decay chain inside the detectors, the short $164.3\mu\text{s}$ half-life of the ^{214}Po isotope, which forms part of the chain, offers a good chance for its identification. The speed of the decay after being created by its mother nucleus, ^{214}Bi , results in two successive energy (β - α) depositions that are unlikely to be mimicked by random events. This was demonstrated in Section 4.1.3, where the timing coincidence search successfully identified the decays from surface contamination from the daughter nuclei of radon. This search is essentially identical, except now any coincident signals seen on the cathode by the HV-veto are rejected, since all ^{214}Po alpha

¹¹ According to a search in the Lund/LBNL database [Lun].

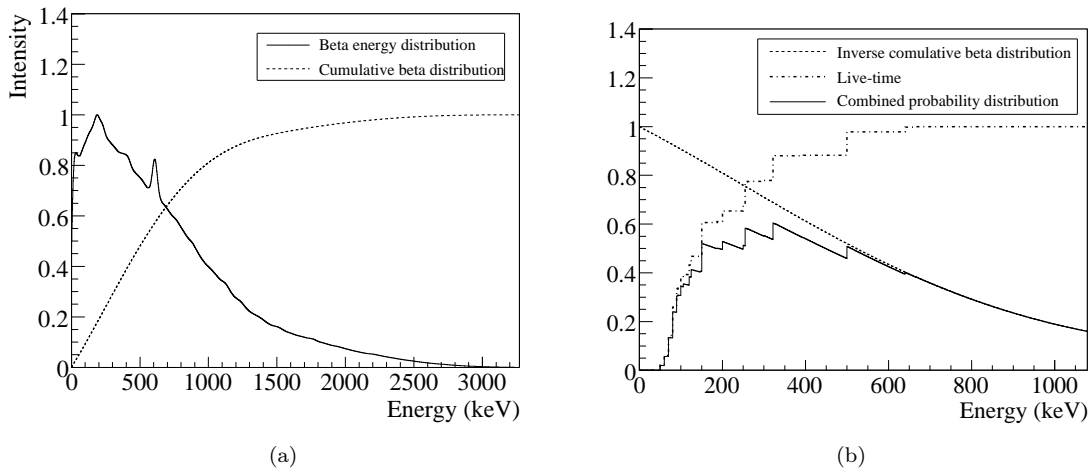


Figure 4.26: Bismuth-214 beta spectrum in comparison to detector lower energy thresholds. (a) The beta energy spectrum (solid line) simulated with *Venom*, is shown together with its cumulative distribution (dashes). It shows that that more than 80% of the beta spectrum falls below 1000 keV. (b) The inverse cumulative beta distribution (dashes) is plotted against the live-time (dot-dash) of the sum spectrum for all active detectors for datasets L1a-c. The two distributions are multiplied together to form a combined probability distribution for observing the beta radiation. The most beta observations should be made with the bismuth search lower energy cut made between 150–500 keV, with the very best at 325 keV.

signals observed by the veto were found to be on the cathode surface. In addition, where the cathode events were observed to be shifted to the left of the peak, for internal decays the full Q-value of the ^{214}Po decay which is 7833 keV is expected.

A simulation of the beta spectrum of ^{214}Bi , which also includes the de-excitation gammas released in the decay, is shown in Figure 4.26a on the current page. Note that because the cumulative beta distribution nears its maximum very quickly, it is important to include the lowest energy possible in the search in order to maximise the detection efficiency. To check that this will not lead to a noticeable random background in the search from uncorrelated events, the expected random background must first be calculated.

4.2.1.1 Expected random background and choice of lower threshold

Of particular interest is whether it is necessary to avoid the four-fold forbidden beta spectrum¹² of the ^{113}Cd decay that, below 320 keV, increases the background level by two orders of magnitude. It should be tested whether the high rate of events from ^{113}Cd leads to a significant background in the search for fast $\beta\text{-}\alpha$ decay. This can be answered by measuring the rate of events in the energy windows that we expect to observe the beta and alpha decays, and substituting these rates into Equation (3.9) on page 57.

The event rates can be found by integrating over the energy spectrum, such as in Figure 3.9 on page 62. It was found that the count rate in the beta decay energy region of 100–3500 keV

¹²The four-fold forbidden non-unique beta spectrum is discussed in Chapter 5.

is 63 000 counts/(kg day). The lower energy threshold of 100 keV is chosen so that it is close to the lowest energy data available, and the higher energy cut of 3500 keV is sufficiently above the Q-value of the ^{214}Bi decay. The count rate in the expected alpha energy window, which is approximately 7.3–8.3 MeV, is a much lower 21 counts/(kg day). The energy range of the alpha is chosen to be ± 500 keV about the Q-value, which is slightly greater than the width of the observed radon peaks and will thus serve as a conservative limit in this search.

When searching for the $\beta\text{-}\alpha$ decays, events are selected from the specified energy windows and the time window of 120–800 μs . The lower timing cut is made in order to be above the ADC resolving time (Figure 2.10 on page 35). The upper cut is set to about five half-lives in order to avoid including any fast decays from other decay chains. Within 800 μs of the ^{214}Bi decay, 96% of the ^{214}Po decays will also have occurred.

Assuming a detector mass of 6.5 g and scaling the rates given above accordingly, substituting the numbers into Equation (3.9) reveals an expected random background of just $\sim 2 \times 10^{-4}$ counts/year per detector ($\sim 7 \times 10^{-5}$ counts/kg/day). This shall be seen to be sufficiently low. Thus, the coincident event rate from uncorrelated events is not a limiting factor for the choice of threshold.

In fact, the limiting factor is the quantity of low energy data. If the noise or trigger threshold for a *run* is above the required energy, the whole *run* must be rejected. The consequence of this is demonstrated with the solid line PDF in Figure 4.26b, which shows the probability of observing beta radiation from the ^{214}Bi decay for different lower energy thresholds. The PDF is created by multiplying the total live-time of the data as a function of energy (dot-dash) by the inverse cumulative function of the beta spectrum (dashes) of ^{214}Bi . The live-time distribution is scaled so that the maximum live-time gives a scaling factor of 1. The inverse cumulative function is scaled so that for a threshold of 0 keV, 100% of the beta distribution is observed. The resulting PDF shows that the best chance of observing the electron from the bismuth decay is roughly between 150–500 keV and that only, at most, 40% of the actual number of events would be seen.

In conclusion, the current rate of events does not produce a significant background of chance event pairs for the fast $\beta\text{-}\alpha$ search of ^{214}Bi , but the optimum lower energy threshold for the search is limited by the reduced live-time with lower energy. For this analysis a lower threshold of 350 keV is used. Greater efficiencies would be made in observing ^{214}Bi contamination by reducing the noise threshold to allow more low energy data to be collected.

4.2.1.2 Bismuth contamination limit

Before analysis, the data was cleaned by the methods described in Section 3.5 and, in addition, all coincident events between detectors and HV-veto were removed. As suggested in the previous section, event pairs are tagged by selecting first an event energy of 350–3500 keV followed by a second event within 120–800 μs . The energy of the second event was only restricted between 350–10 500 keV, since widening the window (and thus coincidence rate) does not affect the efficiency of the search in the signal region because the chance event rate is negligible.

A histogram showing the energies of the second events is shown in Figure 4.27, which mainly

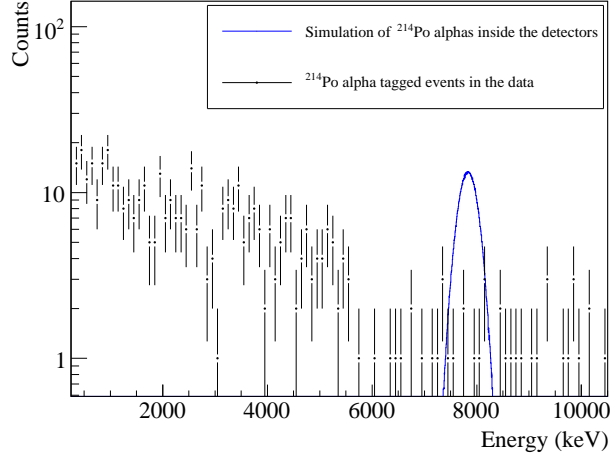


Figure 4.27: Energy spectrum of the tagged ^{214}Po events compared to a simulation of internal decays.

shows the alpha spectrum from ^{214}Po events from radon and the ^{238}Th in the paint. As suggested earlier, the events above 6 MeV are expected to be mis-calibrated ^{214}Po events from the anode side of the detector so the events in the signal region $\sim 7.3\text{--}8.3$ MeV can only be used as an upper limit for the internal contamination. There is, however, a slightly greater density of events in the signal region than to the right of it, so a better estimate for the true internal contamination can be made by assuming a flat background between 7.3–10.3 MeV and subtracting the background sample from between 8.3 and 10.3 MeV.

The number of events in Figure 4.27 in the signal region, 7.3–8.3 MeV is 12, which, using Equation (3.10) for the uncertainty, amounts to 12.0 ± 4.6 counts/MeV. In the region 8.3–10.3 MeV there are 19 counts, which amounts to 9.5 ± 2.7 counts/MeV. Subtracting this from the signal region leaves just 2.5 ± 5.3 counts.

With these numbers, upper limits for the activity of ^{214}Bi inside the detectors can be found. The activity in Becquerel per kilogram of CZT is calculated with the following relation:

$$A = \frac{n}{\epsilon \cdot M_T} \quad (4.6)$$

where n is the number of event pairs, M_T is the quantity of analysed data in kg seconds and ϵ is the efficiency for observing the decays and is 45.5%. The efficiency is a product of a number of factors ($\epsilon_\alpha \epsilon_\beta \epsilon_{m\alpha} \epsilon_{m\beta} \epsilon_{\Delta t}$) that reduce the detection efficiency of the decay. These are,

- ▷ ϵ_β and ϵ_α , which are the probabilities of observing the beta and alpha radiation in the specified ranges. They are calculated by simulating the ^{214}Bi and ^{214}Po decays independently with *Venom*. The simulations involved generating a million decays using the **bkggen** particle gun, and randomly distributing them throughout an array of 16 detectors. An energy spectrum for each simulation was summed over all detectors that were used in this

analysis¹³, and coincident events between detectors where an energy of more than 350 keV¹⁴ was observed, were rejected. The spectra were then normalised by the number of events simulated and the efficiency found by integrating over the spectra between the specified energy windows. The efficiencies were found to be 0.81 and 0.99 respectively.

- ▷ $\epsilon_{m\beta}$ and $\epsilon_{m\alpha}$ are the branching ratios for the modes of the decays. In this case 99.979% of ^{214}Bi decays via beta radiation and 100% of ^{214}Po decays via alpha radiation.
- ▷ $\epsilon_{\Delta t}$, the efficiency of detecting the decays within the time window 120–800 μs . An efficiency of 56.8% is calculated with Equation (4.7) below, where the probability P_λ for observing an event is determined by the decay constant λ , and the start and stop times t_1 and t_2 after the ^{214}Bi event has occurred.

$$P_\lambda = \lambda \int_{t_1}^{t_2} e^{-\lambda t} dt = e^{-\lambda t_1} - e^{-\lambda t_2} \quad (4.7)$$

The quantity of data available for analysis is calculated by counting the number of hourly *runs* available for analysis in the energy range 350–10 500 keV, separately for each detector. The total for each detector is multiplied by each detector mass (without paint) before summing together. The total comes to 9.54 kg days, which corresponds to 88% of the maximum available data.

With the above numbers and Equation (4.6) the activity of ^{214}Bi inside the detector comes to $32 \pm 12 \mu\text{Bq}/\text{kg}$ using all of the counts, or $7 \pm 14 \mu\text{Bq}/\text{kg}$ when the estimated background is subtracted. These numbers are factors of 300 and 1500 lower respectively, than the best measurements made with the germanium counter for ^{226}Ra (also part of the ^{238}U chain) which was given in Table 4.1. Because 32 μBq , which is calculated from 12 counts in the region of interest, is dominated by a background rate of radon events, it is useful to present the result as an upper confidence limit. The 90% upper confidence limit for 12 counts is 17.8 counts. This corresponds to the mean of a Poisson PDF of which 10% of the distribution falls below 13 counts. 17.8 counts corresponds to an upper confidence limit of 47 $\mu\text{Bq}/\text{kg}$.

4.2.2 Alpha-alpha limits

The search for ^{214}Bi was hindered in two key areas. Firstly the half-life of the second decay, ^{214}Po , at just 164.3 μs leads to at least a 40% loss in detection efficiency due to the current resolving time of the ADC, which is 120 μs . The second and most crucial issue is that the search is heavily affected by ^{214}Bi contamination on and in the paint. This second issue becomes a problem because, as it was suggested, most of the events above 6 MeV on the alpha spectrum are likely to be mis-calibrated alphas on the anodes of the detectors. The fraction of detected external alphas in the ^{214}Bi search is magnified due to the longer range of the preceding beta particle that allows very little filtering between internal and external events. Searching for α - α coincidences greatly increases the efficiency for discrimination between internal and external alphas.

¹³Detectors 2, 3, 5, 7, 8, 9, 10, 11, 12, 13, 14 and 15.

¹⁴Coincident events were rejected in the simulation because they were rejected in the data.

Uranium-238 Ideal candidates to search for are those with the fastest half-life that the ADC resolving power allows so that uncorrelated chance events are avoided. Also from the ^{238}U chain, the 3.05 min half-life of the ^{218}Po decay is just fast enough to avoid chance events. The details of the decay are listed in Table A.1 on page 153. The decay sequence involves the release of an alpha with a Q-value of 5590 keV from ^{222}Rn followed by a 99.98% chance of an alpha from ^{218}Po to ^{216}Pb releasing 6115 keV ($^{222}\text{Rn} \sim 214\text{Pb}$). The chance coincidence rate for this decay in a 6.5 g detector, an energy window of ± 500 keV about the Q-values and a time window of three half-lives is 0.13/year. This corresponds to a background of $0.6 \mu\text{Bq}/\text{kg}$ or about 0.6 counts.

The timing coincidence correlation of the first and second event energies of the decays is shown in Figure 4.28 on the next page, where the box indicates the signal region. A lower time cut of 1 s is used in attempt to reduce the chance of coincidences with other fast decays and an upper cut of three half-lives (9.15 min) is used. The plot demonstrates through the high number of counts outside the box that the number of counts in the signal region is still predominantly determined by the background of other fast decays that are not inside the detector. The precise number of counts within the signal region must actually be determined by making the energy cuts before the timing cut, because unlike with the ^{214}Bi search, the probability for an uncorrelated event to occur outside the energy window is not negligible and reduces the efficiency of the search. The true number is 2 counts and the event separation for these events is given in Figure 4.30a. The 90% confidence limit on 2 counts is 5.3 counts.

To reduce the number of accidental coincidence events from other fast decays the time window was restricted to within 1 s and three half-lives (9.15 min). The overall efficiency of detecting the decays is 85.3%, which includes losses due to the time cut of 1s–9.15 min, the minor efficiency losses for the branches listed in Table A.1 and a 1% loss for each alpha to potentially escape the detectors. The full 10.8 kg days is used for the search and the number of internal decays is calculated at $< 5.2 \mu\text{Bq}/\text{kg}$ (90% C. L.).

Thorium-232 From the ^{232}Th chain there are a couple of α - α decays that are separated by short yet workable half-lives. Namely ^{220}Rn and ^{216}Po which follow each other with half-lives of 55.6 s and 0.145 s respectively. The full ^{232}Th chain is provided in Table A.2 where the isotopes of interest are $^{224}\text{Ra} \rightarrow 220\text{Rn} \rightarrow 216\text{Po} \rightarrow 212\text{Pb}$. With the progressively shorter half-lives of ^{220}Rn and ^{216}Po , the background from external decays is likewise reduced in the searches as is demonstrated in the timing coincidence correlation plots in Figures 4.29 and 4.31. The number of events that fall in ± 500 keV of the Q-values is 1 for the first search and none in the second. This null result corresponds to an internal limit of $< 2.6 \mu\text{Bq}/\text{kg}$ (90% C.L.). The results are summarised in Table 4.6.

Further techniques Because the final search returned no counts resulting in the limit on ^{232}Th contamination being dependent on the live-time of the data, there was no need to further develop techniques to improve the cuts to identify the decays. But with the likely chance of observing an event from the $^{220}\text{Rn} \sim 212\text{Pb}$ search with greater statistics, external events could be further rejected by imposing the condition that the preceding decay must also have occurred within three or four half-lives. To a lesser extent, this technique might also be applied to the ^{238}U chain.

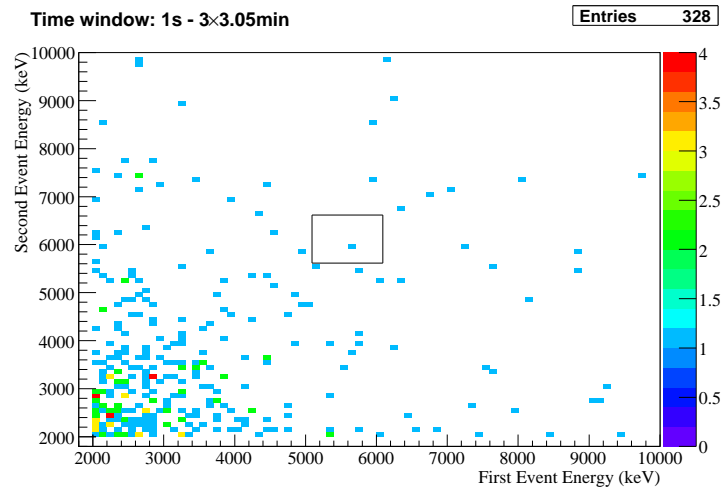


Figure 4.28: Timing coincidence correlation for the $^{222}\text{Rn} \rightsquigarrow ^{214}\text{Pb}$ search.

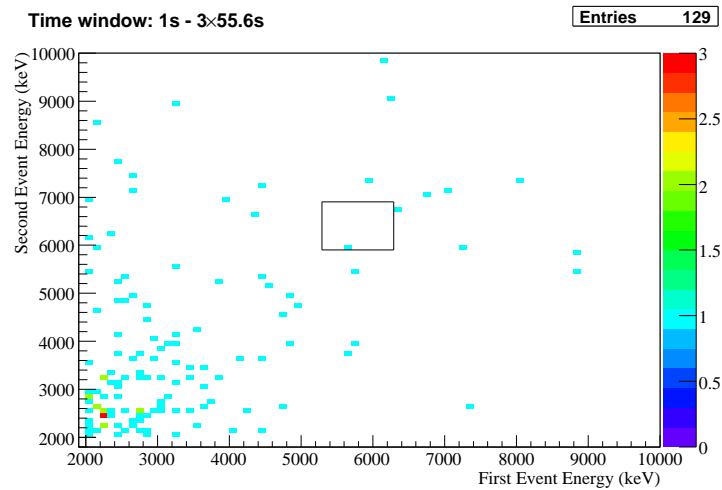


Figure 4.29: Timing coincidence correlation for the $^{224}\text{Ra} \rightsquigarrow ^{216}\text{Po}$ search.

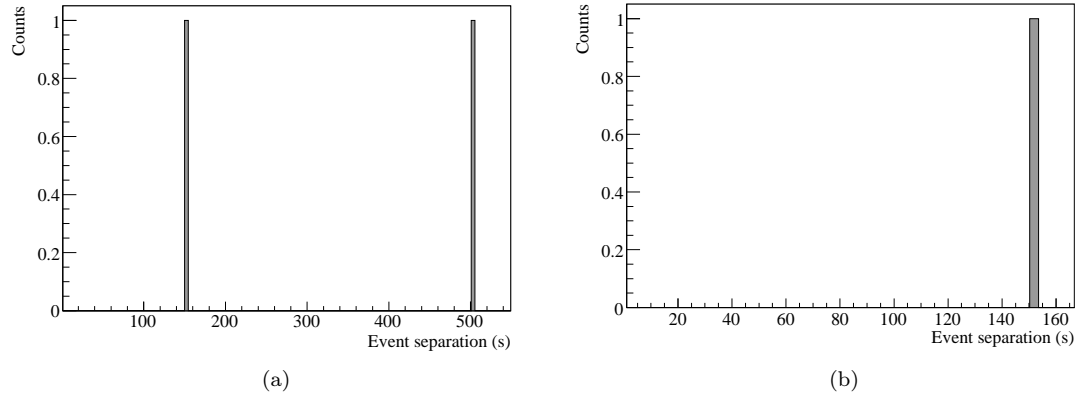


Figure 4.30: Event separation distribution plots for (a) the $^{222}\text{Rn} \sim ^{214}\text{Pb}$ and (b) $^{224}\text{Ra} \sim ^{216}\text{Po}$ search.

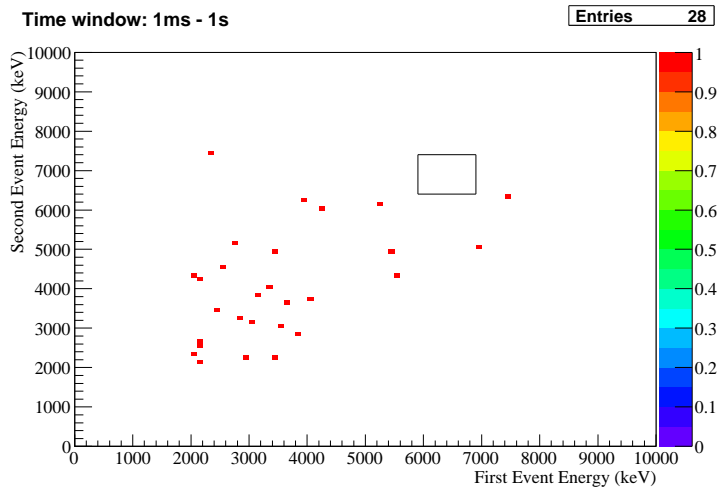


Figure 4.31: Timing coincidence correlation for the $^{220}\text{Rn} \sim ^{212}\text{Pb}$ search.

No.	Event energy (MeV) First	Second Second	Second isotope half-life	Time cut	Efficiency	Counts ($\mu\text{Bq}/\text{kg}$)	Chance rate ($\mu\text{Bq}/\text{kg}$)	Activity ($\mu\text{Bq}/\text{kg}$)	90% C.L. ($\mu\text{Bq}/\text{kg}$)
1	5.59	6.12	3.05 min	1 s–9.15 min	0.853	2	0.6	2.5	6.6
2	0.35–3.5	7.8	164.3 μs	120–800 μs	0.455	12, 2.5 \pm 5.3*	8×10^{-4}	32, 7 \pm 14*	47
3	5.79	6.40	55.6 s	1–167 s	0.798	1	0.1	1.3	5.2
4	6.40	6.90	0.145 s	1 ms–1 s	0.966	0	5×10^{-4}	0	2.6

No.	Decay	Mode	Chain
1	$^{222}\text{Rn} \rightarrow ^{218}\text{Po} \rightarrow ^{214}\text{Pb}$	$\alpha\text{-}\alpha$	^{238}U
2	$^{214}\text{Bi} \rightarrow ^{214}\text{Po} \rightarrow ^{210}\text{Bi}$	$\beta\text{-}\alpha$	"
3	$^{224}\text{Ra} \rightarrow ^{220}\text{Rn} \rightarrow ^{216}\text{Po}$	$\alpha\text{-}\alpha$	^{232}Th
4	$^{220}\text{Rn} \rightarrow ^{216}\text{Po} \rightarrow ^{212}\text{Pb}$	$\alpha\text{-}\alpha$	"

Table 4.6: Summary of internal contamination results of the CZT crystals of datasets L1a-c. The activity marked with an asterisk is a prediction of the real number of internal events after the level of background events above the signal region is subtracted. It appears likely, however, that all uranium contamination measurements are dominated by the radon or paint backgrounds.

Chapter 5

General Analysis

This chapter consists of a brief analysis of some of the key physics contained in the data, namely, studies are made of the ^{113}Cd spectrum and half-life limits are calculated for neutrinoless DBDs. Section 5.1 is adapted from a recently submitted paper [DRW⁺09] on the analysis of the ^{113}Cd beta spectrum, and is a joint analysis by J. Dawson and myself. Section 5.2 demonstrates the calculation of DBD half-lives for the first layer of the 64-array.

5.1 Investigation of the ^{113}Cd Shoulder

5.1.1 Introduction

The majority of beta emitters are characterised as *allowed* or *singly forbidden*, which effectively describes how likely an isotope will decay. The level of suppression largely depends on the change in spin and parity ($\Delta I^{\Delta\pi}$) during the decay. A few beta emitters are even more heavily suppressed and the decay, $^{113}\text{Cd}(1/2^+) \rightarrow ^{113}\text{In}(9/2^+)$, is classified as a four-fold forbidden non-unique decay with estimates of its half-life at about 10^{16} years. Measuring the precise half-life is mainly hampered by the fact that the spectral shape of the emitted beta radiation is difficult to calculate and that the full beta spectrum has never been observed at very low energies due to noise threshold problems. Although the COBRA experiment is not currently able to break records for the lowest energy measurement, it is the first experiment to perform 11 independent measurements (from different detectors) in a similar environment. This enables us to test our understanding of our systematics as well as to test the efficiency and reliability of our detectors.

There have been five previous attempts to measure the half-life of ^{113}Cd . The first using a CdTe device resulted in $(4\text{--}12)\times 10^{15}$ years [Mit88]. Measurements using CdWO₄ as a scintillator found $7.5 \pm 0.3 \times 10^{15}$ years [DGK⁺96] as a cryogenic bolometer obtained $9.0 \pm 0.5(\text{stat.}) \pm 1(\text{sys.}) \times 10^{15}$ years [A⁺94]. Previously the COBRA collaboration obtained $8.2 \pm 0.2(\text{stat.})^{+0.2}_{-0.1}(\text{sys.}) \times 10^{15}$ years [G⁺05] using room temperature CdZnTe semiconductor detectors. A very recent result using a CdWO₄ scintillator measured $8.04 \pm 0.05 \times 10^{15}$ years [BBB⁺07].

This analysis uses data from datasets L1a-b. From this data 11 of 12 working detectors

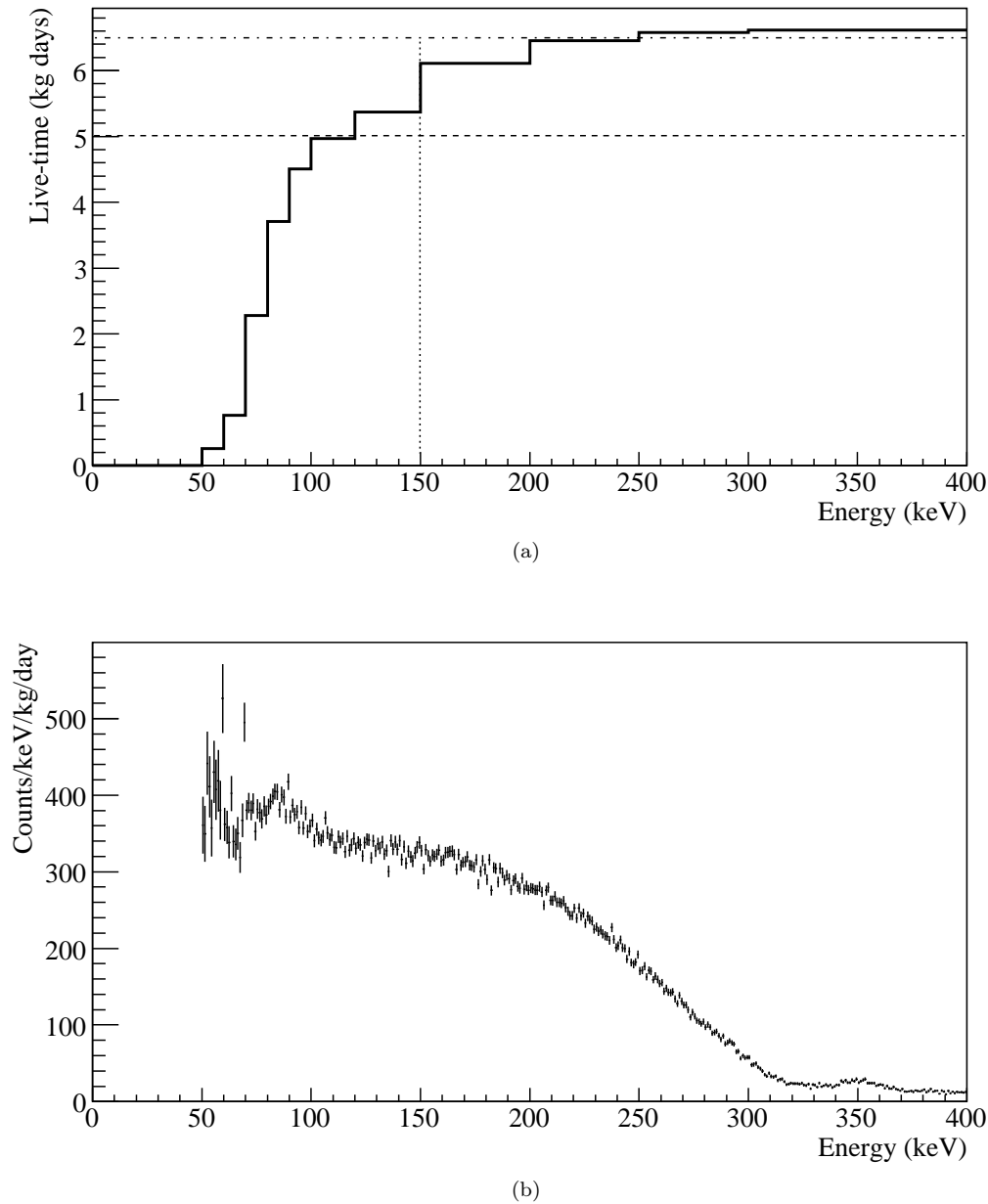


Figure 5.1: Summed live-time (a) and summed energy plot (b) of datasets L1a-b. (a) The live-time decreases as the energy decreases due to varying detector noise thresholds. The average threshold between 0–400 keV (dashes) is 5.0 kg days. The average live-time between 150–500 keV (dot-dash) is 6.5 kg days. (b) Most of the counts below 300 keV are from the beta decay of ^{113}Cd .

(2, 3, 5, 7, 8, 9, 10, 11, 14, and 15) are used, with detector 13 not used because of its particularly high noise threshold. Figure 5.1a shows the total live-time (solid line) for these detectors. Due to varying noise thresholds the live-time decreases from 7.1 kg days above 500 keV to nothing below 50 keV. The average live-time between 0–400 keV (dashes) is 5.0 kg days. The average live-time between 150–400 keV (dot-dash), which is the energy range that the fit in this analysis is performed, is 6.5 kg days.

Figure 5.1b shows the sum spectrum for the same detectors and period of data. The ^{113}Cd four-fold forbidden beta spectrum is responsible for the majority of events below 300 keV. Below 100 keV the features are mostly due to two effects. Firstly, the reduced statistics due to shorter measuring times in this region increases the uncertainty of each bin. Secondly, each detector can have slightly different noise levels affecting the lowest energies. Because the noise is statistically random it can't be rejected on a run-to-run basis. A consequence of combining spectra with different event rates are steps in the combined energy spectrum, which is visible at both 60 keV and 70 keV. A method to remove this effect in the a sum spectrum could be to use only the low energy data from detectors with the lowest event rates. Alternatively, only data with no intermediate thresholds could be used, however, this would discard most of the data if a low threshold is required.

In order to avoid these questions at low energies the ^{113}Cd beta spectrum is only studied above 150 keV. Above 350 keV a good understanding of the major radioactive backgrounds has been demonstrated. In the following subsection the backgrounds are extrapolated to energies below 350 keV and subtracted from the spectra of each detector before fitting with a theoretical ^{113}Cd spectral shape.

5.1.2 Background model

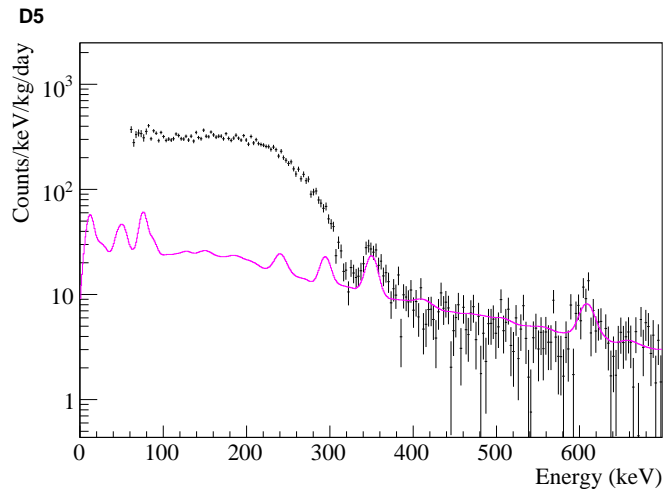


Figure 5.2: The ^{222}Rn simulation (magenta) is scaled to the energy spectra (crosses) of the detectors (detector 5 in this example) before it is subtracted.

The background for this analysis is assumed to be predominantly from the measured contaminants uranium, thorium and potassium in the red passivation paint (Table 4.1 on page 91), as well as from radon that was identified in Chapter 4. Simulations of the paint contaminants were produced as described in Section 4.1.1 and demonstrated in Figure 4.1. The simulations were smeared separately for each detector according to the resolutions shown in Table 3.2 on page 53 and scaled according to the paint masses (Table 3.4), and were then subtracted from the sum spectra of each detector.

Radon was simulated in the air surrounding the detectors and also smeared according to the resolutions of the detectors. The radon simulation was then scaled using the method of least-squares between the range 350–700 keV. An example of a fit of the radon simulation (solid line) for detector 5 is given in Figure 5.2. The fitted radon spectra were also then subtracted from the energy spectra of each detector.

Det	Background			Cd-113		Frac. of background to total counts (%)	Contribution to systematic (%)
	Counts	Error	Frac. (%)	Counts	Error		
D2	1537.4	86	5.6	12630	92	10.9	0.47
D3	1257.8	77	6.1	12167	100	9.4	0.61
D5	1718.8	69	4.0	13440	94	11.3	0.44
D7	1446	72	5.0	12497	86	10.4	0.42
D8	2122.8	113	5.3	12777	139	14.2	1.01
D9	1392	63	4.5	13158	112	9.6	0.65
D10	1269.3	100	7.9	12019	92	9.6	0.53
D11	1102.5	50	4.5	11679	109	8.6	0.79
D12	1478.9	64	4.3	12671	116	10.5	0.75
D14	1463.6	73	5.0	12381	85	10.6	0.42
D15	1636.9	66	4.0	12980	91	11.2	0.59

Table 5.1: Table of background counts subtracted and the number of ^{113}Cd counts counts in counts/kg/day. Also shown is the fraction of the background counts to the total number of counts (^{113}Cd and background), as well as the contribution of the error on the background to the systematic uncertainty. This is taken as the product of the fraction of background to total counts and the fraction of the error on the background. The average of the contribution to the systematic uncertainty is 0.54%.

The uncertainty on the background level is taken as the uncertainty on the background model fit to each spectrum. Table 5.1 shows the number of counts subtracted from each spectrum (typically of the order of 10% of the total observed counts between 120–320 keV) and their uncertainty. The fraction of background to the total number of counts (^{113}Cd and background) times the fractional uncertainty on the background fit is taken as systematic uncertainty for each detector. The average systematic due to the background subtraction for all detectors is calculated to be 0.54%.

5.1.3 Sources of systematic errors

The following subsections describe the main sources of systematic errors. Table 5.2 shows the comparison between the differing effects. The dominant sources of systematic error are the cadmium content and energy resolution.

In the collaboration's previous attempt to measure the ^{113}Cd half-life [G+05], the largest source of error came from the uncertainty in the dead layer. This has now been improved and it can be shown that this systematic was previously heavily over-estimated.

Origin	Contribution to $T_{1/2}$
Cd content	$\pm 2\%$
Dead layer	-0.7%
Crystal masses	$\pm 0.015\%$
Efficiency error	$\pm 0.02\%$
Background Subtraction	$\pm 0.54\%$
Energy resolution	$\pm 2\%$
Total (quadratic)	$+2.9\% , -3.0\%$

Table 5.2: Table of systematics

5.1.3.1 Cadmium content and crystal mass

CdTe semiconductors are well known to suffer from polarisation problems. This issue was addressed with the addition of a small quantity of zinc in replacement of some of the cadmium: $\text{Cd}_{1-x}\text{Zn}_x\text{Te}$, where the proportion of zinc, x , is typically around 0.1. Due to the production method the zinc content gradually decreases as the boule of CZT is grown and depending on where the detector is cut the zinc content proportion can vary, according to the manufacturer, between 0.7 and 1.1. This corresponds to change in cadmium content proportion between 0.89 and 0.93. Since all the detectors are different and could have come from different locations in the boule we therefore assume an average value of 0.91 to calculate the half-life for each crystal, and include a systematic uncertainty of 2% in the half-life.

The mass measurements per crystal as given by the manufacturers are shown in Table 3.4 and are assumed to have an error of 0.001 g, or 0.015%.

5.1.3.2 Crystal dead layer

As has been discussed in earlier chapters, it is possible that the crystals possess an inactive layer of CZT. Tests performed by J. Dawson (Figure 4.13) indicate the dead layer on the sides of the detectors is less than $11\ \mu\text{m}$ and analysis of the cathode (high voltage) signals suggested that the dead layer on the sides is greater than $5\ \mu\text{m}$ (Section 4.1.5.1). The bottom (cathode) of the detector has been demonstrated not to have a dead layer but events close to the anode were observed at poor resolution. The dead layer reduces the effective mass of the detector and thus the quantity of ^{113}Cd . The presence of a dead layer of the order of $15\ \mu\text{m}$ on five sides would reduce the amount of active mass of the detectors by 0.7%.

5.1.3.3 Efficiency

As the detectors are small (1 cm^3) it will sometimes be the case that some proportion of the ^{113}Cd betas will escape the detector without fully depositing their energy, slightly distorting the observed spectrum. Complete escapes are also possible. Using *Venom*, ^{113}Cd betas were simulated uniformly throughout a crystal volume. The energy spectrum of the betas was generated from the results of the fitting. For a threshold of 120 keV , the probability of observing a ^{113}Cd beta is found to be 0.9932 . This must be factored into the total half-life estimate. The uncertainty on this quantity is assumed to be 0.0002 .

5.1.3.4 Energy calibration

The estimation of the systematic uncertainty based on the energy calibration was made using the summed spectrum of all 10 detectors. The observed 351.9 keV line from the ^{238}U chain was fitted with a Gaussian function, which returned the mean energy of $351.2 \pm 0.9\text{ keV}$. This line was used as it is the closest photo-peak to the falling edge of the ^{113}Cd spectrum. The falling edge of the beat spectrum highly constrains the fit, so the energy calibration of this feature is the most important. We assume, therefore, that the energy calibration is good to at least 0.9 keV . The fit procedure described in the following section was repeated with the spectra shifted (both in the positive and the negative senses) by 0.9 keV . The normalisation and hence the half-life changed by $\pm 2\%$.

5.1.4 Fit method

The shape of the beta spectrum is theoretically described as,

$$N(E) = F(Z, E) \cdot p \cdot (E + m_e)(Q - E)^2 \cdot S(E), \quad (5.1)$$

where the Fermi function,

$$F(Z, E) \sim \frac{2\pi\eta}{1 - \exp(2\pi\eta)}, \quad (5.2)$$

with $\eta = Z\alpha/\beta$ and $\beta(E) = p(E)/(E + m_E)$. Following the approach of [DGK⁺96] the correction factor for the spectral shape of a four-fold forbidden beta decay, $S(E)$, is assumed to be [BJ69],

$$S(E) = p(E)^6 + 7c_1 \cdot p(E)^4 + 7c_2 \cdot p(E)^2 \cdot q(E)^4 + c_3 \cdot q(E)^6. \quad (5.3)$$

The energy resolution of the detectors smears the spectrum, but as the detector resolution changes with energy, it was necessary to Monte Carlo test spectra and perform chi-squared fits to the data. The resolutions and functions were described in Section 3.2.2.

A *Minuit* routine was devised with the following free parameters,

- ▷ Q – the Q-value of the beta transition.
- ▷ The spectral shape $S(E)$ parameters: c_1 , c_2 and c_3 .
- ▷ The amplitude of the spectrum that is related to the half-life.

To determine the half-life of each crystal the output fit parameters were used to determine the integral number of counts between 0 and the determined Q-value. As each parameter has an error associated, including the Q-value, Gaussian random deviates were drawn to give estimates of each parameter and the resulting beta spectrum integrated. This procedure was repeated for each detector 1000 times, and the determined integral counts averaged. The standard deviation of this distribution represents the uncertainty on the integral due to the errors on the fit.

The half-life was calculated according to, $T_{1/2} = \ln 2 \cdot \epsilon Nt/S$, where ϵ is the efficiency of detecting a beta decay, N is the number of ^{113}Cd source atoms, t is the measuring time and S is the total number of counts in the beta spectrum. The efficiency ϵ was taken as 0.9932 (as discussed in Section 5.1.3.3). The number of ^{113}Cd source atoms is calculated for each detector and assumes a natural abundance of the ^{113}Cd isotope of 12.22(12)% [TOR] and the overall proportion of cadmium with respect to zinc to be 0.91 (as discussed in Section 5.1.3.1).

5.1.5 Results

Each spectrum was fitted individually with a theoretical ^{113}Cd spectrum over the fit range 150–400 keV. This fit range, which passes the expected endpoint of the spectrum, is necessary to establish that the residual background is consistent with 0. Above 150 keV we are confident that the background model accurately describes the data¹ and therefore the background subtraction is valid.

The Q-value and spectral parameters (c_1 , and c_2 and c_3) should be the same for each detector since they describe the shape of the beta spectrum. Previous estimates of the spectral shape parameters have been measured by other authors and are given in Table 5.3.

Author	c_1	c_2	c_3
[DGK ⁺ 96]	1.01 ± 0.01	1.48 ± 0.05	0.68 ± 0.21
[A ⁺ 94]	0.765 ± 0.095	0.589 ± 0.177	2.04 ± 0.74
[B ⁺ 07]	1.016 ± 0.005	1.499 ± 0.016	3.034 ± 0.045

Table 5.3: Measurements by other authors of spectral shape parameters for Equation (5.3).

A first attempt at fitting all the spectra resulted with a best estimate of Q as 323 ± 0.4 keV. with $c_1 = 0.97 \pm 0.03$, $c_3 = 3.14 \pm 0.04$ and $c_3 = -0.33 \pm 0.02$. Only the value of c_1 measured here is consistent with the previous measurements, the reason being that c_2 and c_3 are mainly dependent on the behaviour at low beta energies. The threshold in this work is too high to constrain these parameters.

A recent publication by [B⁺07] (Table 5.3) gives a well measured beta spectrum of ^{113}Cd down to 30 keV with the best errors on the spectral parameters. The 11 spectra were re-fitted using these spectral shape values as inputs rather than free-floating parameters with a fit range of

¹Differences between the data and simulations at large energies ($\gtrsim 2$ MeV) are due to the dead layer and paint thickness and will not affect the ^{113}Cd analysis.

150 to 400 keV. The errors on each spectral parameter were used to ascertain the error on the half-life in the procedure described in Section 5.1.4. The fits are shown in Figure 5.3.

Table 5.4 shows the output fit parameters and their errors and the resulting half-lives determined from this fit. In this scenario the weighted mean Q-value is 320.45 ± 0.28 keV. Weighted means of these half-lives give a new estimate of ^{113}Cd half-life as $[8.232 \pm 0.29(\text{stat})] \times 10^{15}$ years.

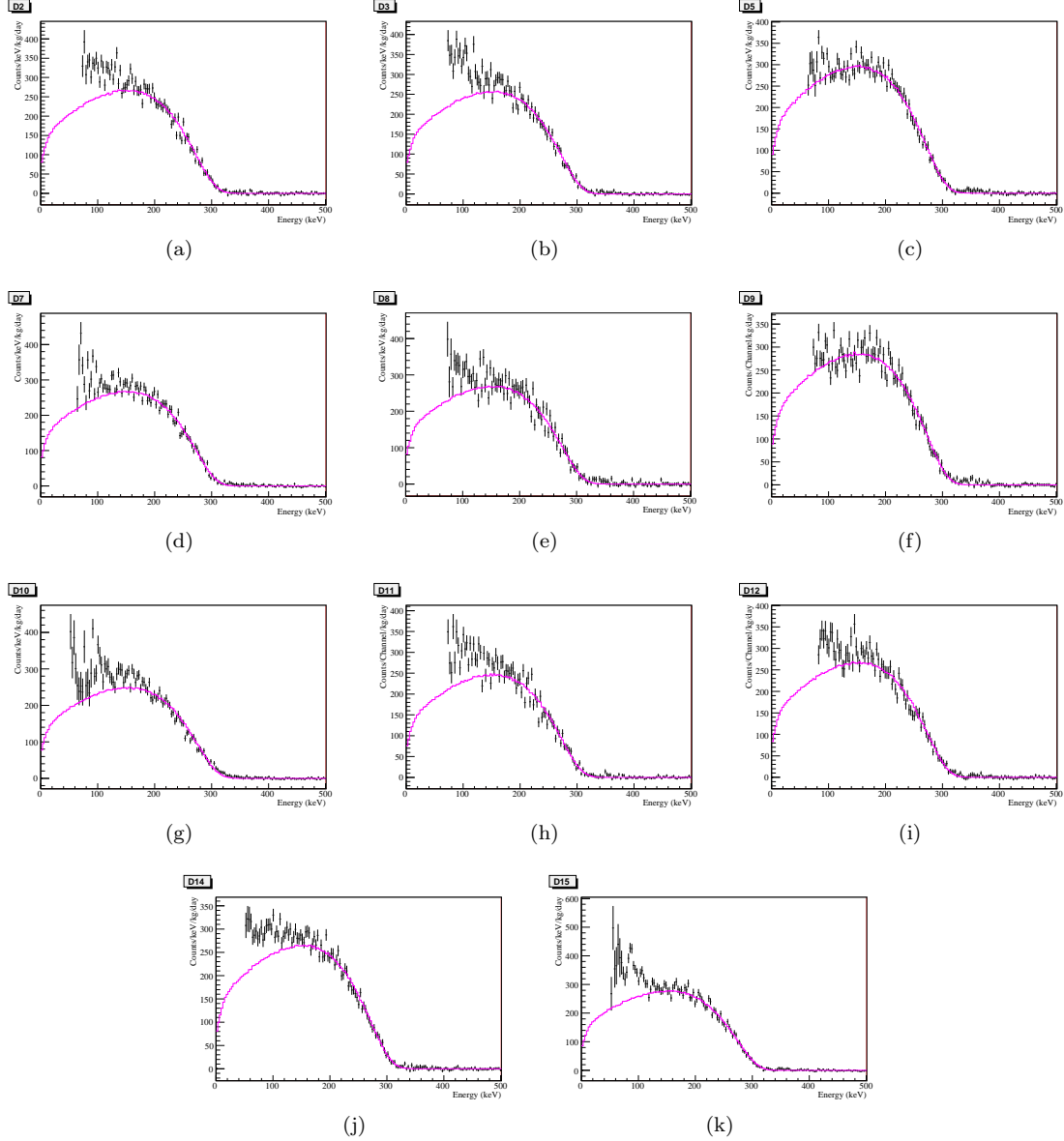


Figure 5.3: ^{113}Cd spectra and fit with c_1 , c_2 and c_3 fixed.

Detector	Q (keV)	Error keV	Normalisation	Error	χ^2	Dof	half-life (yr)	Error
D2	319.60	0.90	6.99×10^{-25}	1.8×10^{-26}	137.6	83	8.34×10^{15}	2.9×10^{14}
D3	319.79	0.91	6.71×10^{-25}	1.74×10^{-26}	119.7	83	8.64×10^{15}	2.9×10^{14}
D5	318.46	0.84	7.94×10^{-25}	1.87×10^{-26}	96.4	83	7.54×10^{15}	2.3×10^{14}
D7	319.95	0.81	6.95×10^{-25}	1.57×10^{-26}	127.2	83	8.30×10^{15}	2.5×10^{14}
D8	322.9	1.28	6.59×10^{-25}	2.34×10^{-26}	110.8	83	8.18×10^{15}	3.9×10^{14}
D9	320.6	0.99	7.34×10^{-25}	2.07×10^{-26}	145.7	83	7.77×10^{15}	2.9×10^{14}
D10	322.86	0.91	6.11×10^{-25}	1.55×10^{-26}	181.8	83	8.84×10^{15}	3.0×10^{14}
D11	319.88	1.01	6.43×10^{-25}	1.91×10^{-26}	147.2	83	8.84×10^{15}	3.4×10^{14}
D12	321.73	1.04	$6.71e \times 10^{-25}$	1.95×10^{-26}	108.14	83	8.25×10^{15}	3.2×10^{14}
D14	319.51	0.84	6.96×10^{-25}	1.63×10^{-26}	101.2	83	8.40×10^{15}	2.6×10^{14}
D15	321.50	0.80	7.00×10^{-25}	1.57×10^{-26}	88.2	83	7.96×10^{15}	2.4×10^{14}

Table 5.4: Table of ^{113}Cd fit results.

5.1.6 Discussion

We have made the most numerous measurements of four-fold forbidden beta decays, in this case for ^{113}Cd , using 11 independent CdZnTe detectors. Each can have a unique (and independent) set of detector parameters such as energy resolution, mass and ^{113}Cd content *etc.* This gives a clear cross-check on our estimate of total systematic uncertainty. Figure 5.4 shows a histogram of the half-lives determined for each detector. The spread in these results must be consistent with (or at least smaller than) the combination of the estimated total systematic uncertainty and the determined statistical errors. The total systematic uncertainty was estimated earlier in Section 5.1.3 to be $\sim 3\%$. The statistical uncertainties on each half-life are derived from the fit and are shown in Table 5.4. The mean uncertainty is 2.9×10^{14} years, which is 3.5% of the mean of the half-life distribution. Assuming the systematic and statistical uncertainties are independent, they can be combined ($\sqrt{3.0^2 + 3.5^2}$) and provide an estimate of the spread of the determined half-lives of 4.6%.

The percentage spread of the determined half-lives is calculated as the standard deviation divided by the mean of the distribution, and is found to be 5%, which is slightly larger than our estimates. This indicates that we have under-estimated the systematic uncertainty and that the real systematic is 3.6%.

This is a valuable independent procedure to find the true systematic error and 3.6% will therefore be quoted in the results. One clear possibility to explain this discrepancy could be the assumed spread in cadmium content since we have as yet no independent measurements of the content of these detectors.

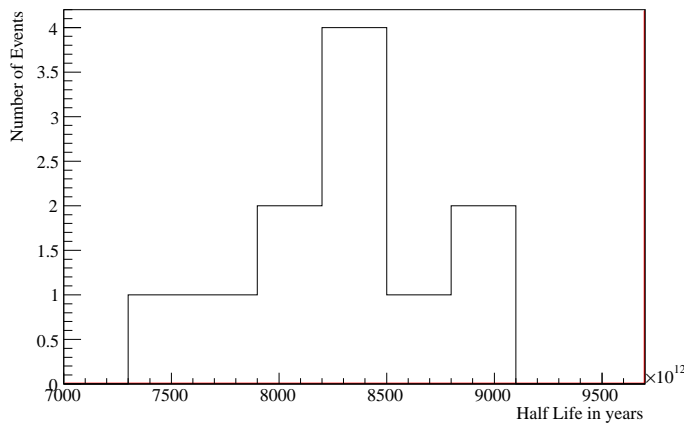


Figure 5.4: Histogram of the determined half-lives for all 11 detectors.

The estimation of the Q-value of the distribution is not affected by the systematic errors like the half-life. The estimate of the Q-value is dependent on the fitted function, and assuming the used functional form to be correct is found to be 320.45 ± 0.28 (stat) keV. Interestingly, the work of [B⁺07] fails to fit a feasible Q-value, one that is consistent with the Table of Isotopes value of 320 ± 3 keV [Aud03]. For the fits to our data, the Q-value appears to be constrained more by the

range 150 keV and 300 keV, rather than the endpoint of the spectrum.

Encouraged by the results of [G⁺05], for the first time microscopic models were explored to predict the half-life and spectral shapes of four-fold forbidden non-unique beta decays [Mus06]. The measured spectrum of one of the detectors is shown together with the fitted spectrum and the one based on the calculation in Figure 5.5. The spectral shape we measure does not match well with the theoretical spectrum and instead agrees with the four-fold forbidden unique spectrum as shown by [B⁺07]. This is an interesting result and will hopefully motivate some further investigation as to why the fit for a unique transition, normally only linked to one nuclear matrix element, fits better than the actual non-unique calculation.

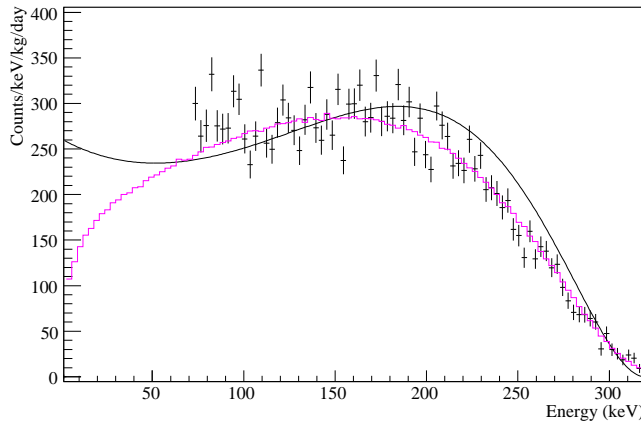


Figure 5.5: ^{113}Cd spectrum (crosses) from Detector 9 showing fit (magenta), and microscopic calculation of [Mus06] (bold line). The calculated spectrum does not agree with the data. This is true in all measured spectra.

5.2 Neutrinoless DBD Limits

Searching for evidence of neutrinoless DBD peaks is of course central to the aim of the COBRA experiment. If no peaks are evident then a limit on the half-life of the decays can be calculated. Using the data (datasets L1a-c) prepared for this thesis, limits are calculated² for various decay processes, with some results outperforming some of the worlds best published results. Results from a smaller dataset (VME1) of 4.34 kg days using four CZT detectors have already been published [BBB⁺07]. This analysis is thus heavily based on that performed for the published paper and also on the description given in [Wil07].

5.2.1 Background parameterisation

The first step in the fitting procedure is to characterise the background. This was achieved by approximating the spectrum with the following 8 parameter ($p[]$) equation,

$$\begin{aligned} y(E) &= p[7] \times (f_A + f_B + f_C) \\ f_A &= p[0] + p[1] \times \exp(-p[2] \cdot E) \\ f_B &= p[3] \times \exp(p[4] \cdot E) \\ f_C &= \frac{p[5]}{p[6]\sqrt{2\pi}} \times \exp\left(-\frac{(E - 609 \text{ keV})^2}{2p[6]^2}\right) \end{aligned} \quad (5.4)$$

where the sub-functions f_A and f_B describe the general background form and f_C describes the 609 keV gamma peak from ^{214}Bi . The equation is only valid above 500 keV. The function is fitted separately for each detector, allowing for fact that the background could vary between detectors. It is assumed that the background shape does not change with time so the same function is held valid for all *groups* of data.

5.2.2 Calculating the half-life

Fits are performed using the Maximum Likelihood method, which is one of the most powerful statistical techniques. The likelihood function, \mathcal{L} , takes a maximum value for the parameters that are most likely to describe the data (see [Cow98] for details). The minimisation fitting program, `Minuit`, is used in this analysis so in fact $-\mathcal{L}$ is used. The function \mathcal{L} can be constructed so that it makes the best use of available data, such as dealing with the complexity of varying thresholds, and allows for the fact that the following quantities can be different for each detector.

- ▷ Background parametrisation and amplitude.
- ▷ Crystal mass.
- ▷ Paint mass (although this is not used in the likelihood).

The following quantities can vary between each data *group*, for each crystal.

- ▷ Energy resolution.

²DBD half-life limits are calculated using a *likelihood* fitting algorithm developed by J. Wilson.

- ▷ Thresholds for analysis (both low and high).
- ▷ Live-time.

Each detector is fitted separately with the combined background and signal function $F(E) = y(E) + g(E)$. The signal is represented by one of two methods. For the $\beta^- \beta^-$ modes the signal is represented by the Gaussian function

$$g(E) = \frac{\theta_s \epsilon}{\sigma \sqrt{2\pi}} \exp\left(\frac{(E - Q)^2}{2\sigma^2}\right), \quad (5.5)$$

with a mean, Q , at the Q-value of the fitted signal and a standard deviation, σ , that is taken from the resolution equation stored with the data files for each *group*. The scaling factor, θ_s , represents the number of signal events. The detection efficiency of the signals, ϵ , is calculated with Venom through the simulation of the decays with the current 16-array setup. For the $\beta^+ \beta^+$ /EC modes the whole simulated signal spectrum is used and fitted such that θ_s also represents the number of signal events.

The log-likelihood function for a given detector is

$$\mathcal{L}_d = \sum_{\text{allgroups}} \left(\sum_{b=\min}^{\max} D_b \times \log(F_b) - F_b \right), \quad (5.6)$$

where D_b is the number of data events observed in bin b and F_b is the calculated number of events determined at the corresponding energy of bin b , according to the fitted function, $F(E)$. The likelihood is summed over all bins in the selected energy range of the fit and over all *groups* of the data. The total likelihood function for the data is calculated by summing the likelihoods over all detectors,

$$\mathcal{L} = \sum_{d=1}^{N_{\text{det}}} \mathcal{L}_d. \quad (5.7)$$

To maximise \mathcal{L} , the parameters that are allowed to vary are the number of signal events, θ_s , and a normalisation factor for the background in each detector, $p[7]$, from Equation (5.4).

Finally, the half-life limits are calculated at the 90% confidence level (C.L.) with,

$$T_{1/2} < \frac{N_{\text{iso}} t_{\text{live}} \epsilon \ln 2}{\theta_s + 1.28\sigma_s} \quad (5.8)$$

where N_{iso} is the number of candidate nuclei per crystal for the given decay, t_{live} is the total duration of the data collection in crystal-years, and ϵ is an efficiency factor of the DBD signal determined from simulations. σ_s is the standard deviation on θ_s , so by adding $1.28\sigma_s$ provides a one-sided limit with 90% certainty that the number of counts from a DBD isotope is less than θ_s , and hence the true half-life, T_{half} , is less than the calculated number with 90% confidence.

5.2.3 Results

Analysis was performed to datasets L1a-c, which corresponds to 10.8 kg days. An example of a combined fit of the ^{116}Cd and ^{130}Te fits to their ground states is given in Figure 5.6. The resulting

90% C.L. half-lives of various $\beta^- \beta^-$ decay modes are presented in Table 5.5 and β^+/EC results given in Table 5.6. The fits of ^{116}Cd and ^{130}Te as well as ^{70}Zn and ^{128}Te to their ground states were performed together due to the proximity of their peaks. Due to the as yet small size of the prototype and the known paint and radon backgrounds, most limits from this work are not competitive with the current best limits, also shown in the tables. However, the limits shown in boldface in Table 5.6 are already world leading.

Uncertainties in the energy resolution and live-time and possible biases in the fit procedure were all found to have negligible effect on the analysis [BBD⁺07]. In fact, as was found in the ^{113}Cd analysis (Section 5.1.3), estimates of the dead layer and zinc content led to the greatest uncertainties. A dead layer of $15\ \mu\text{m}$, for example, would reduce the active volume by 0.6% and the fraction of zinc to cadmium content is only known within the range 7–11%. For this analysis a dead layer is not included, however a conservative estimate of the zinc content is taken so that 7% is used when calculating a limit on a zinc isotope and 11% when calculating a limit on a cadmium isotope.

As shown in Table 5.5, the half-life limit calculated for ^{116}Cd is approximately 10^{20} years. This is six or seven orders of magnitude below the expected value. Thus, with the same setup, the background must be reduced by a similar order of magnitude from the current level, which is ~ 0.3 counts/kg/keV/day at 2805 keV. Because all identified backgrounds in this thesis have been shown to be outside the detector crystals, no evidence has yet been found to suggest that this reduction in background can not be achieved. Furthermore, if the ^{116}Cd content were enriched to 90% this would increase the signal strength by a factor of 12. In addition, with higher quality detectors the resolution is expected to improve from the current average of 2.6% to 1% FWHM, which, according to Equation 1.9 on page 6, should improve the half-life limit by a factor of 1.6.

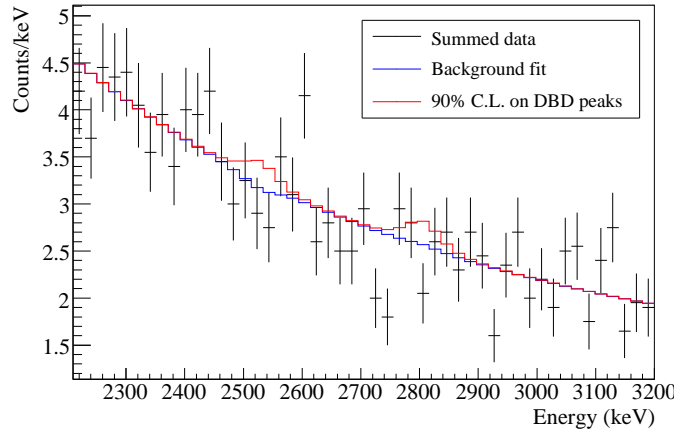


Figure 5.6: Combined spectrum DBD half-life fit for ^{116}Cd and ^{130}Te to ground state.

Isotope and decay	E_{peak} (MeV)	Mass (mg)	ϵ (%)	T _{1/2} limit (years, 90% C.L.)	
				This work	World's best
¹¹⁶ Cd to g.s.	2.805	440	61.0	9.00×10^{19}	1.7×10^{23} [DGK ⁺ 03]
¹³⁰ Te to g.s.	2.529	2210	65.4	6.98×10^{20}	3.0×10^{24} [AAA08]
¹³⁰ Te to 536 keV	1.993	2210	58.2	4.37×10^{20}	9.7×10^{22} [ABC ⁺ 00]
¹¹⁶ Cd to 1294 keV	1.511	440	71.4	2.10×10^{20}	2.9×10^{22} [DGK ⁺ 03]
¹¹⁶ Cd to 1757 keV	1.048	440	60.5	1.91×10^{20}	1.4×10^{22} [DGK ⁺ 03]
⁷⁰ Zn to g.s.	1.001	3.92	90.2	1.87×10^{17}	9.0×10^{17} [DKN ⁺ 05]
¹²⁸ Te to g.s.	0.868	2070	92.1	1.28×10^{20}	1.1×10^{23} [ABB ⁺ 03]
¹¹⁶ Cd to 2027 keV	0.778	440	68.2	4.88×10^{19}	2.1×10^{21} [PBB ⁺ 94]
¹¹⁶ Cd to 2112 keV	0.693	440	77.2	4.29×10^{19}	6.0×10^{21} [DGK ⁺ 03]
¹¹⁶ Cd to 2225 keV	0.580	440	77.1	1.15×10^{19}	$1.0 \times 10^{20}\dagger$ [Bar90]
¹³⁰ Te to 1794 keV	0.735	2210	63.1	2.61×10^{20}	-
¹³⁰ Te to 1122 keV	1.407	2210	55.8	1.00×10^{20}	-
¹¹⁴ Cd to g.s.	0.536	1690	96.5	3.84×10^{20}	-

Table 5.5: Summary of fits for $\beta^- \beta^-$ decays. The measured 90% confidence limits on the half-lives are shown together with the best results from other experiments. [†]A 68% confidence limit, not 90%, was used for this value. Also provided are the fitted peak energies, the average mass of the isotopes in each detector and the efficiency, ϵ , of detecting the signal.

Isotope and decay	Mass (mg)	Fit range (MeV)	T _{1/2} limit (years, 90% C.L.)	
			This work	World best
⁶⁴ Zn $0\nu\beta^+EC$ to g.s.	317	0.5–1.3	1.45×10^{18}	2.4×10^{18} [DKN ⁺ 05]
⁶⁴ Zn $0\nu2EC$ to g.s.	317	0.7–1.3	2.08×10^{17}	7.0×10^{16} [DKN ⁺ 05]
¹²⁰ Te $0\nu\beta^+EC$ to g.s.	6.26	0.5–2.0	3.57×10^{17}	2.2×10^{16} [KMZ03]
¹²⁰ Te $0\nu2EC$ to g.s.	6.26	1.2–2.0	1.87×10^{16}	-
¹²⁰ Te $0\nu2EC$ to 1171 keV	6.26	0.5–2.0	9.39×10^{17}	-
¹⁰⁶ Cd $0\nu\beta^+\beta^+$ to g.s.	73.4	0.5–2.0	2.85×10^{18}	2.4×10^{20} [BBI ⁺ 99]
¹⁰⁶ Cd $0\nu\beta^+EC$ to g.s.	73.4	1.4–3.0	3.23×10^{18}	3.7×10^{20} [BBI ⁺ 99]
¹⁰⁶ Cd $0\nu2EC$ to g.s.	73.4	1.4–3.0	1.00×10^{17}	1.5×10^{17} [BNAD84]
¹⁰⁶ Cd $0\nu\beta^+\beta^+$ to 512 keV	73.4	0.5–2.0	1.18×10^{18}	1.6×10^{20} [BBI ⁺ 99]
¹⁰⁶ Cd $0\nu\beta^+EC$ to 512 keV	73.4	0.8–2.0	5.88×10^{18}	2.6×10^{20} [BBI ⁺ 99]

Table 5.6: Summary of fits for $\beta^+ \beta^+$ decays. The measured 90% confidence limits on the half-lives are shown together with the best results from other experiments. Also shown is the average mass of the isotopes in a detector and the range over which the fits were performed.

Summary and Suggestions

Neutrino oscillation experiments have proven that neutrinos must have finite masses, yet they can only provide lower limits on their masses. Neutrinoless double-beta decay will likely offer a unique opportunity to measure the effective electron neutrino mass because it is directly linked to the rate of the decay. The COBRA experiment proposes searching for neutrinoless double-beta decay with an array of at least 64 000 CdZnTe detectors. This thesis looked at data from the first 16 detectors of a 64 array prototype, and identified problems that are essential to resolve before the ultimate experiment. In addition, the latest double-beta decay limits were calculated and an analysis of the ^{113}Cd shoulder performed. Work carried out for this thesis also included setting up and optimising the apparatus in the laboratory at LNGS, Italy, and the development of tools to monitor, calibrate and analyse data as it was collected.

Hardware

Chapters 1 and 2 introduced and described the COBRA experiment. Through setting up the apparatus and the analysis performed on the data a number of hardware improvements are suggested. These include:

- ▷ Improvements to the Faraday cage and grounding to reduce the electronic noise threshold. The separate parts of the Faraday cage should be welded and feed-throughs should be used where possible when passing cables in and out of the cage. The calibration guide tubes should be passed through a tunnel to help prevent electromagnetic pulses from entering the cage. The pre-amp boxes need bolting firmly to ground.
- ▷ The vibration sensor requires further testing and possibly replacing with a microphone that is sensitive to higher frequencies, as these were more easily picked up by the detectors in lab tests.
- ▷ The mains spike detector also requires further testing.
- ▷ More thermometers (with greater sensitivity) are required to monitor temperature variations of the electronics, such as the pre-amps, shapers and the ADCs.
- ▷ Improve the sensitivity of the HV-veto to allow better rejection of external alpha events. Replacing the HV Kapton cables with cables of lower capacitance and that are less susceptible to breakdown might significantly increase the signal to background ratio.

▷ ADC improvements

- ▷ Allow finer adjustment of trigger thresholds at low energies. A non-linear scale would be useful.
- ▷ A faster resolving time would improve the study of fast successive decays.
- ▷ It would be useful if the ADCs could sample the noise levels below the trigger threshold without adding to the dead-time. This would allow the triggers to be automatically adjusted when the noise levels change.

Software

Also introduced in Chapter 2 were the contributions of software developed for this thesis. The collection of tools, ACID, allows the data to be easily converted from ASCII into a compressed binary format. The binary file is structured in a user-friendly manner to allow functions to be easily developed to loop through only the best data. A novel method was devised to map the profile of the noise threshold and to calculate the live-time as a function of energy. Many diagnostic tools were created to monitor the quality of the data and to search for the signatures of physics processes.

Some improvements that could be made to the software include:

- ▷ Currently flag and threshold settings are saved with the data. The option to save these settings separately would allow the data to be prepared for multiple analysis purposes without duplicating the dataset.
- ▷ A database could be created to include properties such as the detector and paint masses, as well as the measured leakage currents, and be easily accessible to ACID.
- ▷ It is anticipated that the tool `SSclean_data` will require testing on samples of future lower background datasets to ensure that it performs at optimum efficiency—rejecting all significant noisy data while limiting the loss of useful data.
- ▷ To further automate the preparation of the data, a method for identifying correlated features between detectors that cannot be accounted by real decays should be developed, since checking all combinations by eye will be a time-consuming process even for the 64-array.

Electronic effects

A number of electronic backgrounds were investigated and identified mostly to fall into the following categories.

Leakage current. Leakage current between the detector grids and between the anodes and cathode had the effect of increasing the noise thresholds. The leakage current between the anodes and cathode led to unpredictable changes in the noise levels in some detectors that required careful removal. Leakage current between the grids could be reduced by lowering the grid bias to as low as a few volts but reducing the high voltage had

limited effect, as at least 500 V was required to obtain a reasonable calibration. This form of electronic noise was not picked up by neighboring detectors.

Micro-discharge. Small electrical discharges inside the insulating material or trapped air in the high voltage cables were found to be a major background in the experiment until the cables were encased in a grounded copper shield. Evidence found in this analysis suggests that the discharges might be stimulated by nuclear radiation and should be further investigated.

Electrical breakdown. Other electrical breakdown, possibly between the high voltage lines and ground. This form of breakdown was mostly distinguishable by the fact that it was observed by many detectors.

RF pickup. Radio frequency pickup was sometimes observed in energy spectra below 100 keV. This could be eliminated by more thorough grounding and shielding of the apparatus.

General results

With careful study of the COBRA data the following results were found.

- ▷ Radiation from radon (^{222}Rn) and its daughter decay products were found to be the dominant background above 320 keV. The uranium and thorium contaminants in the paint were the next most significant backgrounds.
- ▷ The most prominent peaks in the data were identified as being from radon, and alpha peaks were shown to be entering through the thin cathode contact. The shift in energy of the alpha peaks confirmed the thickness of the contacts to be between 160–260 nm, which is consistent with the manufacturers estimate of 180 nm.
- ▷ The radon alpha peaks were also found to be observable by the high voltage veto, which demonstrated that the cathode signals could be used as a depth gauge of energy depositions within the detectors.
- ▷ A peak observed at 3.2 MeV was identified as being from platinum used in the cathode contact plate and a number of candidate isotopes were found for other observable peaks.
- ▷ A method of using timing coincidences between successive alpha decays was devised that was able to place the very low limit on the internal contamination limits, at 90% confidence, of ^{235}U at less than $6.6 \mu\text{Bq}/\text{kg}$ and ^{232}Th less than $2.6 \mu\text{Bq}/\text{kg}$. These results are 3–4 orders of magnitude lower than the limits previously measured using a high purity germanium counter.
- ▷ Studies of the alphas from radon and an ^{241}Am source revealed that the dead layers of the detectors are likely between 5–11 μm .
- ▷ Using a model for the background based on a combination of radon and the main paint contaminants, a prediction of the background below 320 keV was subtracted from the energy

spectra for each detector and an analysis of the ^{113}Cd spectrum was performed. Half-life estimates of the four-fold forbidden non-unique beta decay were calculated as $[8.232 \pm 0.30(\text{sys}) \pm 0.29(\text{stat})] \times 10^{15}$ years and a Q-value of 320.45 ± 0.28 keV, which are consistent with the latest best measurements.

- ▷ With the lowest background and the most data ever collected using CZT detectors, the main neutrinoless DBD 90% C.L. limits were calculated for various transitions and are given in Tables 5.5 and 5.5. Limits were calculated for ^{116}Cd to ground state at $< 9.00 \times 10^{19}$ years and ^{130}Te to ground state at $< 6.98 \times 10^{20}$ years. Some limits on the ^{64}Zn and ^{120}Te isotopes are world leading.

Conclusion

The COBRA experiment is uses semiconducting CdZnTe detectors to search for the extremely rare process of neutrinoless double-beta decay that offers a unique chance of providing a measurement of the electron neutrino mass, and is the ‘gold plated channel’ to show that the neutrino and antineutrino are the same. COBRA’s approach has many advantages. These include the large Q-value, 2.8 MeV, of the isotope ^{116}Cd , which is above all naturally occurring gamma-lines of the natural decay chains that are one of the dominant backgrounds of most other double-beta decay experiments. CdZnTe has a radio-pure production process and excellent energy resolution. Because the source is equal to the detector this greatly enhances the efficiency for detecting a signal. The modular design of the experiment provides the ability to track background radiation so that it can be discarded. The detector material, CdZnTe, contains five $\beta^- \beta^-$ and four $\beta^+ \beta^+$ /EC decaying isotopes; some of these decay to produce signatures that are distinct from any random process.

The COBRA prototype described in this thesis is the largest array of CdZnTe detectors ever to be used in an ultra low background environment and the research described here is the first to tackle major issues associated with operating this array, which include the development of data handling, monitoring data taking and defining criteria for profiling the noise threshold. An efficient, scalable, storage system was developed as well as a set of analysis tools that automate complex tasks, such as, identifying unwanted backgrounds and performing searches for rare decays. The analysis tools were designed with new users in mind, and are already invaluable to the latest research students. This research also describes significant advances in the understanding of backgrounds specific to operating CdZnTe detectors. These include positively identifying alpha decays on the cathode surface that are shown to be from a dominant radon background. A formerly unknown background from platinum was identified that will need to be excluded from the final COBRA experiment. The work performed in this thesis is a major contribution to bring COBRA to its current status. This is indispensable research for a successful neutrinoless double beta-decay measurement.

Appendix A

Additional Figures and Tables

16 4	12 8	8 12	4 16
15 3	11 7	7 11	3 15
14 2	10 6	6 10	2 14
13 1	9 5	5 9	1 13

Figure A.1: Detector number schemes. **Top left:** Datasets L1a-c. **Bottom right:** Dataset L1d.

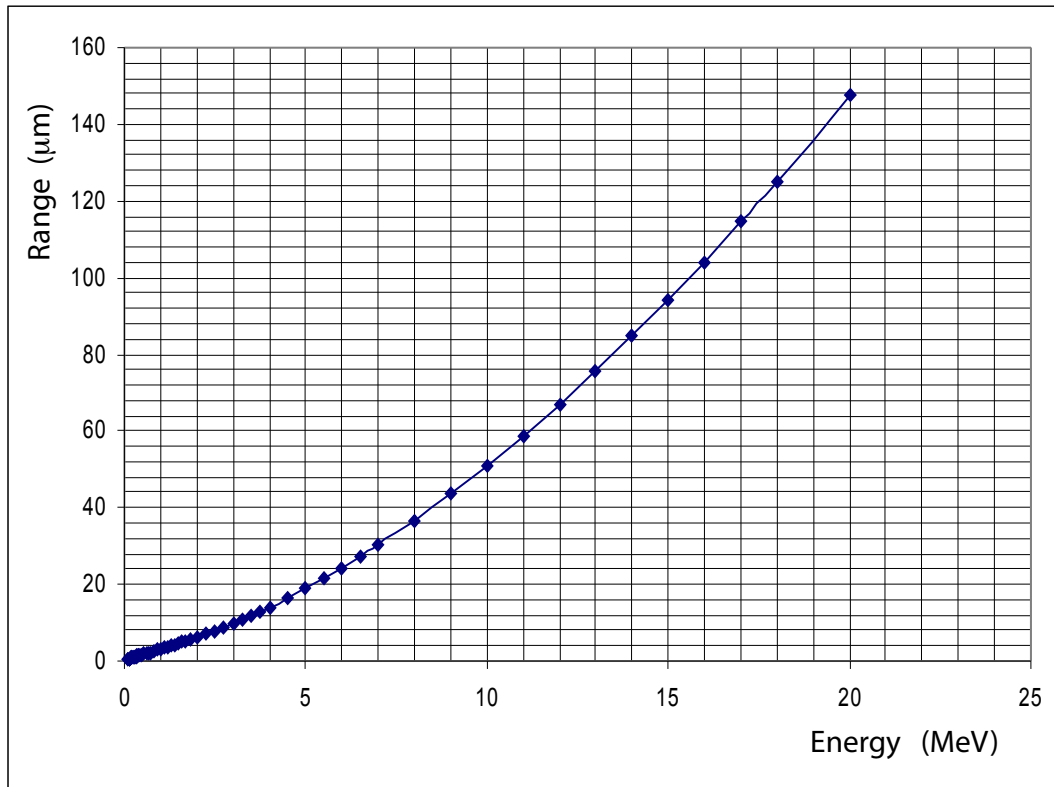


Figure A.2: SRIM simulation of alpha ranges in CZT. From [Daw06].

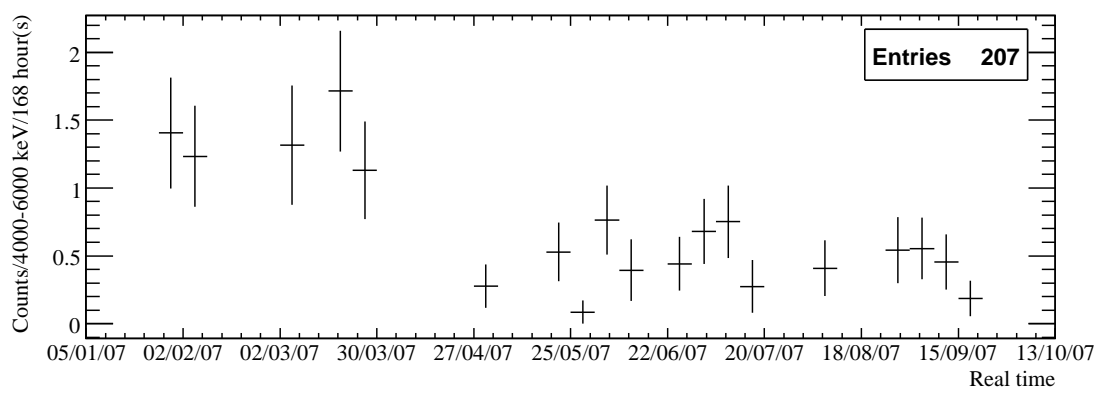


Figure A.3: Event rate of a selection of ^{214}Po decays. ^{214}Po alphas (see Figure 4.14 on page 106) are first tagged in the dataset L1a-d and the weekly event rate between 4-6 MeV over all detectors is shown with time. A drop in event rate is seen in the beginning of April after the experiment was moved. This demonstrates that events from the selection are heavily influenced by radon levels.

isotope	half-life	Q-value	α -decay	branch	β -decay	branch	γ -decay	emiss.
decay mode			energy		energy		energy	prob.
(%)	$T_{1/2}$	keV	MeV	(%)	MeV	(%)	keV	(%)
^{238}U	$4.468 \times 10^9 \text{ y}$	4270 3	4.197	(77)				
$\alpha \downarrow (100)$			4.147	(23)			49.55	(0.062)
^{234}Th	24.1 d	273 3			0.199	72.5	92.37	(2.42)
$\beta \downarrow (100)$					0.104	17.8	63.28	(4.1)
					0.060	7.1	92.79	(2.39)
$^{234\text{m}}\text{Pa}$	1.175 m	2195 5			2.29	98.4		
$\beta \downarrow (100)$					1.53	0.62	766.37	(0.316)
					1.25	0.74	1001.03	(0.839)
^{234}U	$2.45 \times 10^5 \text{ y}$	4858.5 7	4.775	(72.5)				
$\alpha \downarrow (100)$			4.723	(27.5)			53.20	(0.38)
^{230}Th	$7.538 \times 10^4 \text{ y}$	4770.0 15	4.688	(76.3)				
$\alpha \downarrow (100)$			4.621	(23.4)			67.67	(0.123)
^{226}Ra	1600 y	4870.63 25	4.784	(94.5)				
$\alpha \downarrow (100)$			4.601	(5.55)			186.10	(3.51)
^{222}Rn	3.8235 d	5590.3 3	5.490	(99.9)				
$\alpha \downarrow (100)$			4.987	(0.08)				
^{218}Po	3.05 m	6114.68 9	6.002	(100)				
$\alpha \downarrow (99.98)$								
^{214}Pb	26.8 m				0.73	(40.5)	295.21	(18.15)
$\beta \downarrow (100)$							241.98	(7.12)
					0.67	(46)	351.92	(35.1)
^{214}Bi	19.9 m	3272 11			3.275	(19.9)	609.32	(44.6)
$\beta \downarrow (99.979)$					1.88	(7.18)	768.36	(4.76)
						(17.5)	1120.29	(14.7)
						(8.26)	1238.11	(5.78)
					1.51	(16.9)	1764.49	(15.1)
					1.02	(16.9)	2204.21	(4.98)
^{214}Po	$164.3 \mu\text{s}$	7833.46 6	7.687	(100)				
$\alpha \downarrow (100)$								
^{210}Pb	22.3 y	63.5 5			0.063	(19)		
$\beta \downarrow (\sim 100)$					0.017	(81)	46.54	(4.24)
^{210}Bi	5.013 d	1162.1 8			1.161	(99)		
$\beta \downarrow (\sim 100)$								
^{210}Po	138.4 d	5407.46 7	5.305	(99)				
$\alpha \downarrow (100)$								
^{206}Pb	stable							

Table A.1: Uranium-238 Decay Chain [Lun, Wah96].

isotope	half-life	Q-value	α -decay	branch	β -decay	branch	γ -decay	emiss.
decay mode			energy		energy		energy	prob.
(%)	$T_{1/2}$	keV	MeV	(%)	MeV	(%)	keV	(%)
^{232}Th	$1.40 \times 10^{10} \text{ y}$	4082.8 14	4.012	(77.9)				
$\alpha \downarrow$ (100)			3.954	(22.1)			63.81	(0.27)
^{228}Ra	5.75 y	45.9 9			0.039	(60)		
$\beta \downarrow$ (100)					0.015	(40)		
^{228}Ac	6.15 h	2127 3			2.18	(10)	338.32	(11.3)
$\beta \downarrow$ (100)					1.70	(11.6)	968.97	(16.2)
					1.11	(31.0)	911.21	(26.6)
^{228}Th	1.9131 y	5520.12 22	5.423	(71.1)				
$\alpha \downarrow$ (100)			5.340	(28.2)			84.37	(1.22)
			5.221	(0.44)			215.99	(0.28)
^{224}Ra	3.644 d	5788.87 15	5.685	(94.9)				
$\alpha \downarrow$ (100)			5.449	(5.1)			240.99	(4.1)
^{220}Rn	55.6 s	6404.67 10	6.288	(99.9)				
$\alpha \downarrow$ (100)			5.747	(0.11)			549.73	(0.11)
^{216}Po	0.145 s	6906.5 5	6.778	(100)				
$\alpha \downarrow$ (100)								
^{212}Pb	10.64 h				0.569	(12)	300.09	(3.25)
$\beta \downarrow$ (100)					0.331	(83)	238.63	(43.5)
					0.159	(5)		
^{212}Bi	60.55 m	α : 6207.14 4	6.089	(27.1)				
(35.94) (64.06)		β : 2254.0 17	6.050	(69.9)	2.248	(86.6)	1620.74	(1.5)
$\alpha \swarrow \searrow \beta$					1.521	(6.8)	727.33	(6.7)
^{208}Tl	^{212}Po	α : 3.053 m	8954.13 11	8.785	(100)			
(100)	(100)	β : 0.298 μs	5001.0 17			1.80	(51)	583.19 (30.6)
						1.52	(21.7)	860.56 (4.5)
						1.29	(22.8)	510.77 (8.2)
						1.52	(3.1)	2614.53 (35.8)
^{208}Pb	stable							

Table A.2: Thorium-232 Decay Chain [Lun, Wah96].

Q-value (keV)	I_D (%)	Isotope	Q-value (keV)	I_D (%)	Isotope
1652.8	10^{-4}	^{187}Re	5520.1	100	^{228}Th
1905.2	100	^{144}Nd	5590.3	100	^{222}Rn
1986	100	^{148}Sm	5616.8	10^{-2}	^{214}Bi
2204.6	100	^{152}Gd	5788.9	100	^{224}Ra
2310.5	100	^{147}Sm	5935.2	100	^{225}Ac
2494.8	100	^{174}Hf	5979.3	100	^{223}Ra
2822	100	^{186}Os	5982	2.1	^{213}Bi
3249	100	^{190}Pt	6146.4	100	^{227}Th
3792	10^{-6}	^{210}Pb	6207.1	36	^{212}Bi
4082.8	100	^{232}Th	6391	97	^{219}At
4213.3	10^{-8}	^{231}Th	6404.7	100	^{220}Rn
4270	100	^{238}U	6457.9	100	^{221}Fr
4678.7	100	^{235}U	6750.5	100	^{211}Bi
4770	100	^{230}Th	6874	100	^{218}At
4858.5	100	^{234}U	6946.1	100	^{219}Rn
4870.6	100	^{226}Ra	7201.9	100	^{217}At
5042.2	1.4	^{227}Ac	7263	100	^{218}Rn
5149.9	100	^{231}Pa	7594.5	100	^{211}Po
5167.6	100	^{229}Th	7833.5	100	^{214}Po
5407.5	100	^{210}Po	8178	100	^{215}At
5432	10^{-3}	^{223}Fr			

Table A.3: Q-values of naturally occurring alpha emitters. I_D is the fraction of decays via alpha emission. Results from a custom search in the Lund/LBNL database [TOR].

E_α (keV)	I_α (%)	I_D (%)	Isotope	E_α (keV)	I_α (%)	I_D (%)	Isotope
1830	100	100	^{144}Nd	5423.1	72	100	^{228}Th
1960	100	100	^{148}Sm	5489.5	100	100	^{222}Rn
2140	100	100	^{152}Gd	5606.7	26	100	^{223}Ra
2233	100	100	^{147}Sm	5685.4	95	100	^{224}Ra
2500	100	100	^{174}Hf	5716.2	53	100	^{223}Ra
2757.7	100	100	^{186}Os	5756.9	20	100	^{227}Th
3180	100	100	^{190}Pt	5792.5	18	100	^{225}Ac
3947.2	22	100	^{232}Th	5830	51	100	^{225}Ac
4012.3	78	100	^{232}Th	5977.7	24	100	^{227}Th
4151	21	100	^{238}U	6038	24	100	^{227}Th
4198	79	100	^{238}U	6050.8	70	36	^{212}Bi
4366.1	17	100	^{235}U	6126.3	15	100	^{221}Fr
4397.8	55	100	^{235}U	6275	100	97	^{219}At
4620.5	23	100	^{230}Th	6278.2	16	100	^{211}Bi
4687	76	100	^{230}Th	6288.1	100	100	^{220}Rn
4722.4	28	100	^{234}U	6341	83	100	^{221}Fr
4774.6	71	100	^{234}U	6552.6	13	100	^{219}Rn
4784.3	94	100	^{226}Ra	6622.9	84	100	^{211}Bi
4845.3	56	100	^{229}Th	6693	90	100	^{218}At
4901	10	100	^{229}Th	6819.1	79	100	^{219}Rn
4951.3	23	100	^{231}Pa	7066.9	100	100	^{217}At
5013.8	25	100	^{231}Pa	7129.2	100	100	^{218}Rn
5028.4	20	100	^{231}Pa	7450.3	99	100	^{211}Po
5058.6	11	100	^{231}Pa	7686.8	100	100	^{214}Po
5304.4	100	100	^{210}Po	8026	100	100	^{215}At
5340.4	27	100	^{228}Th				

Table A.4: Alpha energies from naturally occurring isotopes with a combined branching ratio ($I_\alpha \times I_D$) greater than 10%. I_α is the fraction of alphas produced at the given energy and I_D is the fraction of decays via alpha emission. Results from a custom search in the Lund/LBNL database [TOR].

Alpha Energy (keV)	Q-value (keV)	Alpha energy branch (%)	Decay mode branch (%)	Half-life $T_{1/2}$	Parent isotope
4824.2 <i>12</i>	4908.6 <i>12</i>	84.4 <i>5</i>	100	1.592E+5 y <i>2</i>	²³³ U
4845.3 <i>12</i>	5167.6 <i>10</i>	56.2 <i>2</i>	100	7340 y <i>160</i>	²²⁹ Th
5830 <i>2</i>	5935.2 <i>14</i>	50.7 <i>15</i>	100	10.0 d <i>1</i>	²²⁵ Ac
6341.0 <i>13</i>	6457.9 <i>14</i>	83.4 <i>8</i>	100	4.9 m <i>2</i>	²²¹ Fr
7066.9 <i>15</i>	7201.9 <i>14</i>	99.9 <i>1</i>	99.988 <i>4</i>	32.3 ms <i>4</i>	²¹⁷ At
8375.9 <i>25</i>	8537 <i>3</i>	~100	100	4.2 μ s <i>8</i>	²¹³ Po

Table A.5: Alpha emitters in the ²³³U chain. Uncertainties on the last digits are shown in italics [Lun]. ²³³U can be created in minute quantities through the capture of thermal neutrons by ²³³Th. It has also been produced for nuclear weapons research and cancer treatment.

Property	CdZnTe (CZT)	CdTe
Atomic numbers	48, 30, 52	48, 52
Average atomic number	49.1	50
Average nucleon number	117.6	120.0
Band gap E_g (eV)	1.572	1.5
Mean e^- -hole pair energy E_{ch} (eV)	4.64	4.43
Density ρ (g/cm ³)	5.78	5.85
Electron mobility μ_e (cm ² /Vs)	1000	1100
Hole mobility μ_h (cm ² /Vs)	50–80	100
Resistivity R_s (Ω /cm)	3×10^{10}	10^9

Table A.6: Physical properties of CdZnTe and CdTe [Kie05].

Appendix B

Users Guide for ACID1.7

—*Analyser for COBRA’s Interesting Data*

B.1 Introduction

The COBRA experiment uses an array of CdZnTe semi-conducting detectors to search for the predicted, extremely rare, decay of neutrinoless double beta decay ($0\nu\text{DBD}$). The current prototype of the experiment is to monitor signals from an array of 64 detectors arranged in four layers of 4×4 . Data collected from each detector is unique. Some detectors might have a high noise threshold, others might have very little noise. Then there are detectors where the noise level can jump very quickly between low and high. It is also possible that the signal lines can act like antennas that pick up the electromagnetic pulses from electrical discharges. Consequently, data from each detector must be analysed carefully to separate, as far as possible, electronic backgrounds from real detector events. For 64 detectors this is by no means a simple task, in particular, when testing all combinations of possible cross-talk between detectors.

This analysis code, written mostly from scratch for this thesis, was developed with the purpose of reducing the labour of the analysis, with the ultimate goal of automating the analysis procedure. Automation, or artificial intelligence, will be key to the success of preparing data if the experiment is to be upgraded to a 64 000 detector array. Furthermore, a number of analysis tools were developed for the purpose of gaining a better understanding of the data. An introduction to preparing the data and a tutorial for using the main functions is provided in this guide.

B.2 sfalist2root

—*an ASCII to binary converter*

`sfalib2root.cxx` is a major expansion of H. Kiel’s program `list2root.cxx` and is used to load the data ASCII data files into a binary ROOT format. It also imports calibration and resolution information of the detectors.

B.2.1 Compiling

`sfalist2root.cxx` can be compiled with `g++` by adding the following lines to a Makefile:

```
% : %.cxx
    g++ $< 'root-config --cflags --libs' -o $@ -O2 -Wall -g
    #strip $@
```

Note that the ROOT libraries must be in your path when compiling. Running the command,

```
]$ make sfalist2root
```

will create the binary file `sfalista2root`.

Before compiling it is necessary to modify the first line of code of `sfalista2root.cxx` to specify the number of detectors/ADC ports,

```
#define NDETS 24 // define the number of detectors
```

This number can be set higher than the true number if more convenient. Doing so can be useful if more detectors will later be added as joining since joining datasets with a different number of detectors is not currently possible.

B.2.2 Required files

Two files must be first created before compiling.

B.2.2.1 list_group_name

This is a text file containing the paths to all the data files to be compiled to ROOT format. The actual name of the list must have the prefix, “`list_`”. To generate this list you can type the following command in your bash window

```
]$ ls /DataDirectory/daq_2006*.dat > list_group_name
```

Use wild-cards to select the period of data required.

B.2.2.2 group_stats.dat

This file provides information about which detectors are active, the calibration and resolution equations and a user threshold. If this file does not exist an option to create a default template is offered. The `group_stats.dat` file takes the form,

cal	res
1 1 0 0 0	1 0 0 0 0
1 1 0 0 0 1 0 0 0 0	
1 1 0 0 0 1 0 0 0 0	
...	

where each line represents a detector. The first number of each line specifies if the data from the detector should be used, where 1 is true and 0 is false. The **cal** region is the calibration for the detector with the first two parameters being the slope and uncertainty and the second two the intercept and uncertainty and relates the ADC channel numbers to keV. The **res** region is the resolution function and uncertainties and relates the FWHM in keV from the energy in keV. The last number of the line is the *user threshold* in keV. Events with an energy below the threshold are only used if another detector has an energy above its threshold.

B.2.3 Executing

B.2.3.1 example

The following command

```
]$ ./sfalist2root -s 5e6 group_name
```

will compile a ROOT file `group_name.root` from the list, `list_group_name`. The option `-s 5e6` ensures files with greater than 5 Mb are not used in the analysis.

B.2.3.2 options

Run the tool with no arguments to report the list of arguments

```
]$ ./sfalist2root
NAME          ./lmt/sfalista2root - import COBRA data to ROOT file
SYNOPSIS      ./lmt/sfalista2root [OPTION]... [run_name]
DESCRIPTION
-n [NAME]     sum name: new data is added to this file
-s [SIZE]      maximum daq file size
-r            do not reject short runs
-i            ignore calibrations
-d            print debug information
-c            use hv trigger counter
```

The most used option is `-s`, which ensures the most noisy data files are not included. This not only speeds up the analysis but also limits the dead time per *run*. The option `-n` can be used to add the data to another dataset. If the dataset is called `sum.root` the option is `-s sum`. The `-r` option ensures *runs* that are not an hour long *are* included. This is useful for debugging purposes. The option `-i` allows the data to be imported in uncalibrated form, that is in channels.

The option `-d` forces the data being read from the data files to be printed to screen. The option should be used after `sfalist2root.cxx` has been modified to check that the data is still correctly being read from file. It is helpful to print the output to a temporary file to compare the output with the data files.

```
]$ ./sfalist2root -d group_name > test.txt
```

Terminating the program with [Ctrl]–[c] after a second will allow enough data to be processed for inspection. Finally, the `-c` option is used when the DAQ is operating in the mode to reject uncorrelated triggers from the ADC recording high voltage discharge events. Using the option ensures the trigger counts (see Figure 2.11 on page 37) are read correctly.

B.3 joingroups

—add root files together

`joingroups.cxx` is used to add different ROOT files (or *groups*) together so that they can be analysed in one ROOT file. The tool uses as its input a file containing a list of the paths to each *group*'s ROOT root file. The list should have the prefix “`list_`” as in Section B.2.2.1. An example of a bash command used to create the list is

```
]$ ls /datadir/*/*SFA*.root > list_sumname
```

It is therefore useful to name all the ROOT files to be compiled to start with the same prefix, *e.g.* SFA in this example.

`joingroups.cxx` should also be compiled with the Makefile used to compile `sfalist2root.cxx` and the number of detectors must also be set at the beginning of the file. Note, it is not currently possible to combine groups with a different detector number.

B.4 sfaplot

—analysis software for ACID data-files

`sfaplot.C` is the main analysis tool and contains numerous functions for preparing and plotting the data. This section describes the basics for using the tool and gives many examples of how to use the main functions.

B.4.1 Getting started

This subsection describes how to load and plot a basic energy spectrum. A ROOT session is first started, `sfaplot` is loaded and then the data is loaded.

```
]$ root
root [0] .L toolfolderlink/sfaplot.C+
root [1] SSload("dataset.root")
```

Note the “`+`” sign, which tells ROOT to pre-compile the program before it is loaded. This creates the binary file `sfaplot_C.so` that is only re-created if `sfaplot.C` is modified. Note, if `sfaplot_C.so` was created on another computer it is necessary to modify `sfaplot.C` (`]$ touch toolfolderlink/sfaplot.C`) before loading the tool (step [0]) as this will ensure that the tool will function correctly on the current computer.

During step [1] some feedback is printed to screen and the word `done` is reported when the data is loaded. Check that the number of detectors, groupname(s) and the number of *runs* that are also printed to screen look sensible. The most likely cause if the data does not load correctly is that the number of detectors, `NDETS`, specified at the top of `sfaplot.C`, does not match the number of detectors used to compile the ROOT file. If this is so, correct `NDETS` and repeat steps [0] and [1].

To plot the energy spectrum of detector 1 simply enter

```
root [2] SSplot_spec2(1)
```

This will produce a spectrum covering the full energy range of available data. A number of options can be set before specifying how the spectrum should be displayed and what cuts should be applied. The options can be displayed by entering

```
root [3] SSplot_spec2(
```

and pressing the [Tab] key. The following lines are printed to screen

```
void SSplot_spec2(char help = 'H')
void SSplot_spec2(Int_t detn, Int_t rebin = 1, Char_t* use_flags = "000",
                  Int_t use_sumw2 = 0, Int_t rawdata = 0, Double_t undercut = 10.)
```

which shows that there are actually two functions with that name. A help function and the main function. The help function is called by just entering

```
root [3] SSplot_spec2()
```

Most functions are over ridden with a help function which can either be called by not specifying any inputs or otherwise entering 'H' as the first input. The main function can be modified to use a 10 keV bins, not include flags events and runs, and to display the uncertainty on each bin with

```
root [4] SSplot_spec2(1,10,"000",1)
```

A list of available ACID functions can be obtained by typing

```
root [5] SS[Tab]
```

and, for example, the list of plotting functions can be viewed by typing

```
root [6] SSplot_[Tab]
```

Other useful functions start with SSsearch..., SScut..., SSclean..., SSfit..., SSget..., and SSdump... NB, "SS" is not an acronym, it is just the sound a snake makes.

B.4.2 Tutorial

This tutorial describes how to use the most commonly used tools in the context of steps involved in preparing a dataset for analysis. The tutorial can be taken as a guide to how to prepare the data, but not as a recipe because each dataset is unique and can have different problems.

B.4.2.1 A first look at the data

When new data is first collected from freshly installed detectors the immediate question is whether the data rates are consistent with previous measurements. This can take many weeks to answer fully because the rate of events at high energies is very low. However, the ^{113}Cd shoulder below 320 keV provides a sufficient count rate to be recognisable within hours.

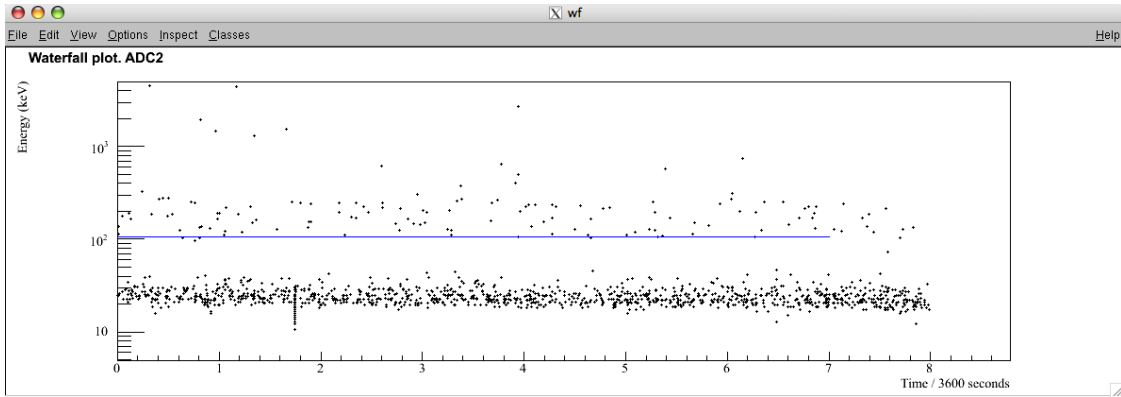


Figure B.1: Waterfall plot shows first eight hours of data. This function is created with `SSplot_waterfall(2)`.

The first step is to plot a waterfall-plot as in Figure B.1. The blue line marks the trigger threshold. The events above this line can be seen to be spread fairly evenly in time, with most of the events below 320 keV, which are predominantly the beta decays of ^{113}Cd . The events below the trigger threshold are recorded whenever an event on another detector has a larger energy than it's trigger threshold. The sub-threshold events indicate where the noise threshold is. The gap between the noise threshold suggests that the trigger threshold can probably be reduced slightly.

To more clearly, and quickly, see how the event rates compare to previous measurements it is handy to make a comparison to a numerical approximation. This is demonstrated in Figure B.2, where the green curve represents a typical spectrum and the crosses the new data. It is easy to see that the new data roughly overlaps the line, which adds reassurance that even if the event rates have changed slightly, that at least some sensible data is being taken.

The figure was created with the function `SSbeta_getTriggerThresh`, which is being developed, mainly for the purpose of suggesting a better trigger threshold. In this example it suggests a threshold setting of 4, which corresponds to an energy of 46 keV. This would probably have been about right, but without testing the new threshold there is no real way of knowing. Sometimes the noise thresholds of some detectors can be too unpredictable that the trigger thresholds have to be set higher for safety to avoid the risk of filling the hard-disk up with noise. Ideally a more intelligent trigger is required by the DAQ that can vary itself according to the state of the detector.

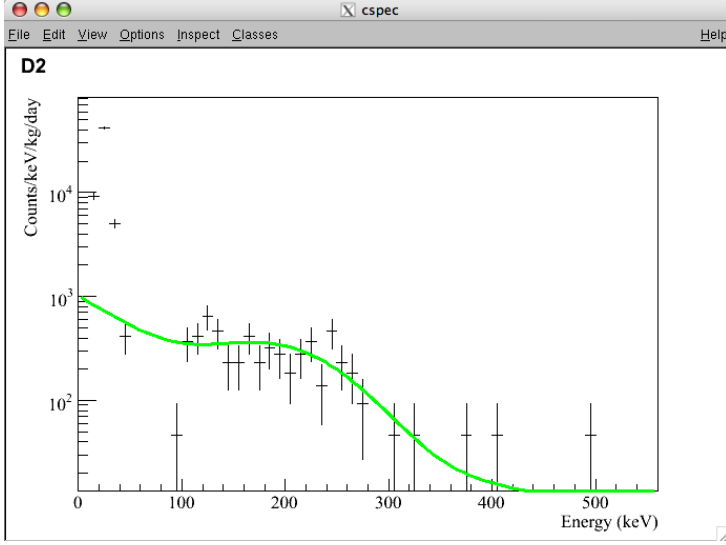


Figure B.2: Numerical approximation of previous spectra (green line) compared to new data (crosses). Plot produced with `SSbeta_getTriggerThresh(2)`.

B.4.2.2 Identifying talking detectors

In Figure 3.25 on page 80 it was demonstrated how “talking detectors” can be highlighted by counting the number of coincident events between detectors. Each sub-figure was created with `SScut_plot_coincidences(dets,0,"000",dets[i],1,200)`, where `dets` is an array of integers representing all detectors being analysed and is defined as `int dets[]={1,2,3,...,16,0}`. The code that plots each sub-plot on one canvas is located in in the ACID directory in

```
macros/macro.plotCoincidenceArray.C
```

and can be adapted for each specific task without the need for re-compiling the main program.

B.4.2.3 Investigating and removing correlated events

Having identified which detectors are likely to be talking, a correlation plot can be created with `SSplot_correlations` to investigate the correlation. The function `SSplot_highlightcorrelations` uses `SSplot_correlations` to create a correlation plot with flagged events highlighted in red.

Figure B.3 demonstrates how events seen both by the left HV-veto (D22) and detector 8 is investigated. Figure B.3a was created by running `SSplot_highlightcorrelations(8,22)`, zooming into the relevant area and using the tool to draw a quadrilateral around one of the observed features.

To perform the selection click on and then single-click on three corners of the quadrilateral starting from the top left and working clockwise. On the forth corner double click. This saves the four coordinates into a `TCutG` object called `CUTG`. To flag the events contained within the coordinates run the function `SScut_graphical_eVSe()`. To confirm that the selection worked

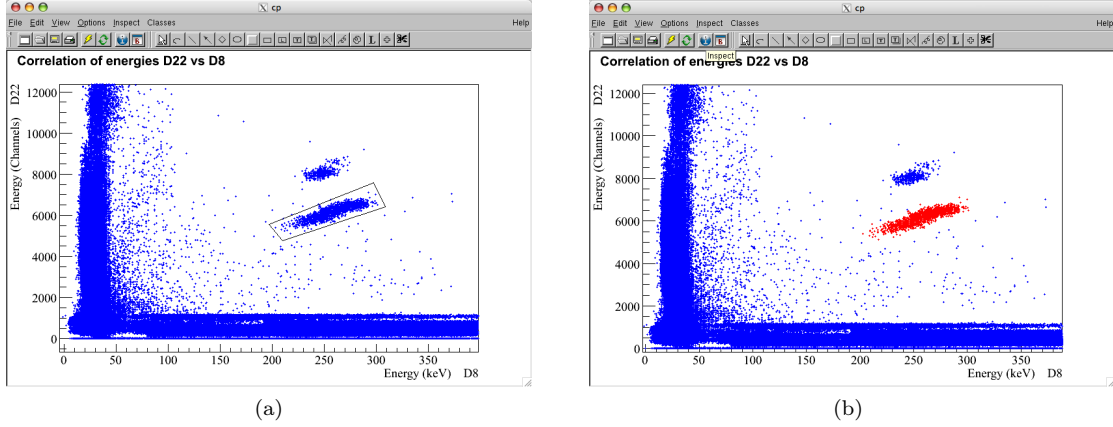


Figure B.3: Correlation plots used to investigate features in the data. (a) Demonstrates how the tool can be used to select events of interest and (b) shows how the events are successfully tagged.

correctly run `SSplot_highlightcorrelations` again and the events should now be highlighted as in Figure B.3b.

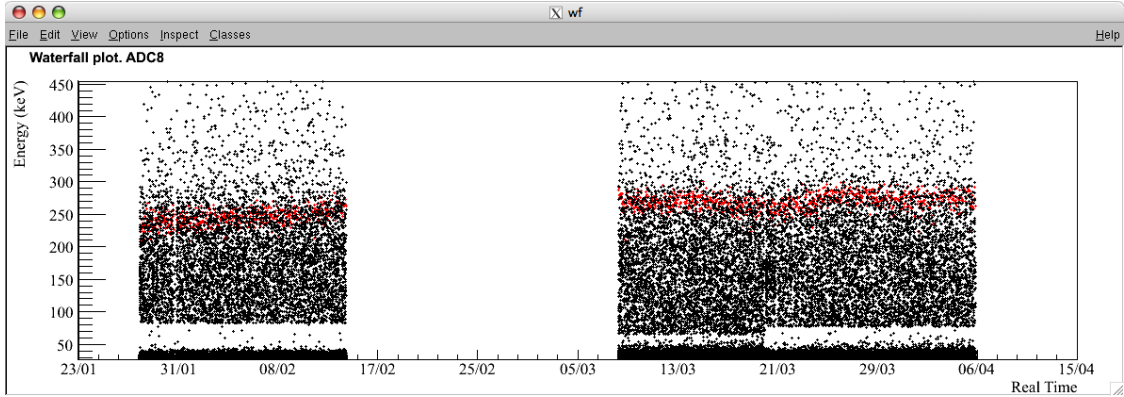


Figure B.4: A waterfall plot shows how the tagged events are distributed in time.

To observe how the events are distributed in time, flagged events can be highlighted on a waterfall plot with the automatic overlay option “A”. This is demonstrated in Figure B.4 and was created with `SSplot_waterfall(8,6,0,’A’)`. Use with the character option “1_” to only plot the tagged events and with “0_” to only plot non-flagged events. Event flags are usually set as either 1 or 0, where 1 means the data should not be used (or is flagged) and 0 is for normal data. Flags however can also be set to any number except character number for ‘_’, ‘0’ or ‘1’. If for example the flags of interest are set to 97, which corresponds to `int('a')`, then these events can be plotted on a waterfall plot with the character option “a_”. For further information on this function call the help option with `SSplot_waterfall('H')`.

The tool can also be used to select events from a waterfall plot. The procedure is identical

as just described except that the function `SScut_graphical_eVSt()` is used to flag the selected events.

To manually reject periods of data by time the function `SScut_runsbytime()` can be used.

To reject all events that have an energy above the trigger threshold on more than one detector enter

```
root [0] int dets[] = {1,2,3,...16,0}
root [1] SScut_plot_coincidences(dets,1,"__",0,0,0,01)
```

where step [0] selects the detectors that should be used and step [1] rejects all coincident events.

B.4.2.4 Investigating count rates

Investigating how the count rate of the highlighted events in Figure B.4 are distributed in time can also be achieved with very few commands. Only the first three *groups* were used in Figure B.4 (group transitions can be marked on a waterfall plot with `SSaddgroupmarkers`) so only the first three groups are also selected for this analysis.

```
root [0] SSgroups_set("+1:3") // select groups
root [1] SSplot_eph(8,24,"1__",100,150,350,1) // create plots for tagged events
root [2] SSfit_poisson() // fit Poisson distribution
```

The result is shown in Figure B.5. For the limited statistics the distribution of events is consistent with a Poisson distribution (top plot) as the $\text{Prob}(\chi^2)$ of 0.90 for the fit suggests. The fit on the bottom plot was performed with the ROOT FitPanel and demonstrates that even though the eye can clearly see two downward trends in the data, within the error bars the events are consistent with each other. To confirm what the eye can already see, the *run test*¹ is more effective because it looks at the number of groups of counts above or below the mean count rate and so is more sensitive to non-statistical variations in the event rate. Once the command `SSplot_eph` (or `SSplot_eppt`) has been run the following command `SSdoruntest()` can be used, which reports there is just a 0.13% chance that the counts are distributed randomly in time.

`SSplot_eph` is of course also used to investigate the event rate of ordinary events and is the main function used for cleaning the data. As an example, the function options to plot the distribution of the number of non-flagged events per hour for detector 2 over the energy range 150–8000 keV is `SSplot_eph(2,1,"000",50,150,8000)`, where 50 keV is the upper range of the plot. The option to draw the event rate against time (the *time line*) is not set in this example and is actually better to draw with the function `SSplot_eppt`.

`SSplot_eppt` has a small but important difference in the way it produces the time line that is noticeable when choosing a counting period greater than an hour. In `SSplot_eph`, if some *runs* are flagged or a *group* ends before a counting period is complete, *runs* from the next period are used and the starting point of the next period is moved forward. This is necessary to produce a sensible distribution of event counts (Figure B.5 top) but does not accurately match

¹Also known as the *Wald-Wolfowitz Test*.

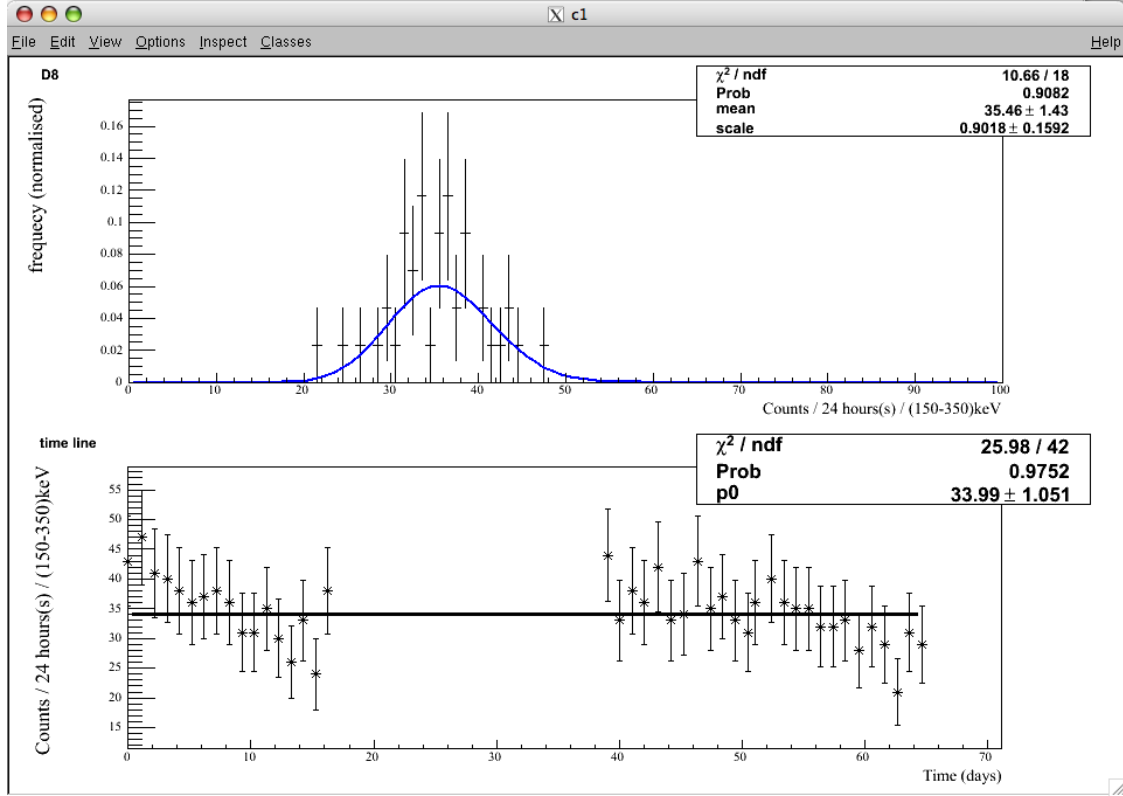


Figure B.5: Event rate distribution of flagged events. (top) The distribution fits a Poisson distribution, which is also a Gaussian distribution at the event rate of 35.5 ± 1.4 Counts/day. (bottom) The number of counts per day are shown as they occur in time and can be seen to vary.

the event times. `SSplot_eppt` on the other hand sticks faithfully to the actual times and if a counting period is short of data this is taken care of by scaling the counts by the live-time of each period. Consequently periods with missing data simply have a larger statistical uncertainty, and is represented by the error bars.

`SSplot_epp` is similar to `SSplot_eph` but is more suitable for looking at the count rates over shorter periods. Where `SSplot_eph` uses counting periods quantised in hours, the unit of time used by `SSplot_epp` is a second. It is best to choose a period by which an hour is exactly divisible to again avoid having to borrow counts from neighbouring *runs*.

B.4.2.5 Locating the noise thresholds

Having first flagged correlated events as described in the Section B.4.2.3 the data is ready for locating the noise thresholds. Flagging correlated events should be done first in order to avoid rejecting an unnecessary quantity of data. The function to locate the noise thresholds and remove the most noisy runs is `SSclean_data` and should be applied to each detector in turn.

The methods used to locate the thresholds were described in Section 3.5 and an example waterfall plot (Figure 3.27) with thresholds set is shown on page 83.

B.4.2.6 Plotting and combining energy spectra

Energy spectra can be produced with both SSplot_spec and SSplot_spec2. SSplot_spec was developed first and compiles an energy spectrum for a specified detector over a defined energy range and rejects data with a noise threshold above the specified energy. SSplot_spec2 uses all available data by keeping track of the live-time of each keV bin. An example of a spectrum produced with SSplot_spec2 was given in Figure 3.9 on page 62.

A quick way to compare an energy spectrum of one detector with another is

```
root [0] SSplot_spec2(1,10,"000",1)
root [1] h1 = h_handle; h1->SetLineColor(kRed)
root [2] SSplot_spec2(2,10,"000",1)
root [3] h1->Draw("same")
```

The live-time of the spectrum, which by default is not drawn, is saved to `h_handle2`. To combine two energy spectra they must first be multiplied by their live-time spectra. The following code demonstrates how this can be done.

```
root [4] SSplot_spec2(1,1,"000",1); // plot 1
root [5] h1 = (TH1D*)h_handle->Clone("h1"); // save plot 1
root [6] t1 = (TH1D*)h_handle2->Clone("t1"); // save live-time 1
root [7] SSplot_spec2(2,1,"000",1); // plot 2
root [8] h2 = (TH1D*)h_handle->Clone("h2"); // save plot 2
root [9] t2 = (TH1D*)h_handle2->Clone("t2"); // save live-time 2
root [10] hsum = (TH1D*)h_handle->Clone("hsum"); // create a template
root [11] tsum = (TH1D*)h_handle2->Clone("tsum"); //
root [12] h1->Multiply(t1); // scale plot 1
root [13] h2->Multiply(t2); // scale plot 2
root [14] hsum->Add(h1,h2); // add plots
root [15] tsum->Add(t1,t2); // add live-times
root [16] hsum->Divide(tsum); // rescale sum plot
root [17] hsum->Draw(); // draw sum plot
```

The macro `macro.addspectra.C` can be used as template to produce a sum spectrum for a selection of detectors. Because the detectors' masses are not currently stored in the ROOT file the SSplot_spec functions use an average detector mass of 6.5 g. The above macro is thus also useful for rescaling the spectra with the correct detector masses.

When saving a sum spectrum it is important to also save its respective live-time spectrum scaled in units of kg days. This will enable the sum spectrum to be added to a sum spectrum of a different dataset later, if necessary.

B.4.2.7 Suggested organisation

The suggested organisation of the analysed data is to create a matching folder name for each data group. For example,

```
DATA_DIR/GROUP_NAME1
    GROUP_NAME2
    ...
ANALYSIS_DIR/GROUP_NAME1
    GROUP_NAME2
    ...
    ...
```

Each analysis group folder will contain the following files and directories,

- lmt This is a soft link to the acid directory.
- pics This directory contains the graphical results from the *group* data.
- README A text file containing any comments about observations of the data or compilation of settings that could be useful in case of future re-analysis.
- opt.dat This test file is used to store compilation settings, particularly the number of detectors used in the analysis.
- CleanData.C A macro with all the functions called to prepare the data. An example is given below.
- list_GROUP_NAME The list containing the paths to all of the data files used to compile the ROOT file, GROUP_NAME.root.
- group_stats.dat A text file with the calibration and resolution equations described in Section B.2.2.2.
- GROUP_NAME.root The ROOT file containing the compiled data of the same calibration.

The following is an example of functions contained in the file `CleanData.C`

```
int i;
int dets[20] = {1,2,3,4,5,6,7,8,9,10,11,12,13,14,15,16,0};
    // load the ACID software
    // this method can be used if opt.dat contains the entry '#define NDETS 20'
gROOT->ProcessLine(".x lmt/acid.C");
    // load the data file
SSload("GROUP_NAME.root");
    // reject first 10 hours of for detector 1
SScut_runsbytime(1,0,10,3600);
```

```
// flag all coincident events
SScut_plot_coincidences(dets,1,"___",0,0,0,01);
// locate thresholds and reject most noisy runs
for(i=0;dets[i];++i) SSclean_data(dets[i]);
SSsavechanges(0,"TAG_GROUP_NAME_cleaned.root");


---


```

Appendix C

Data-taking Log

Explanation of Files and Folders: cobra2:/data/COBRA/

VME DATA

```
-----  
LLR = Low Level Run, PreC/PosC = pre/post-Calibration  
vme20050429: PreC. LLR with threshold of 10.  
vme20050501: PosC. LLR for D1 only, continued last run with lower threshold, although the daq also was  
reading from D2 although it was not plugged (check for crosstalk)  
vme20050509: --Tests for detector resolution optimization, ADC spikes, D2 & D4 turned on  
vme20050513: PreC. LLR for D1, 2 & 4.  
vme20050514: -- LLR continued after tests on cause of band noise. No calibration file. D2 not plugged in.  
vme20050516a: -- PosC.D2 reconnected. GB varied midway for testing noise bands.  
vme20050516b: PreC. PosC. LLR started with settings unchanged except 2x9V batteries used for GB.  
vme20050518a: --Continuation of vme20050516b; used for testing noise bursts.  
vme20050518b: --Tests if turning OFF/ON GB affects the calibrations.  
vme20050519a: --Tests to optimise the GB voltage. Range from 5V to 60V.  
vme20050519b: PreC. PosC. LLR. D1,2,4 on. Maximum range (28MeV). Thresholds at 0, but D4 later increased to 2.  
vme20050601: PreC. LLR. Grid Bias turned down from 30V to 20V. +25min rest. Other settings unchanged.  
vme20050620: --Tests to optimise the Pre-Amp potentiometer settings  
vme20050621: LLR. PreC. for 1st half, PosC for 2nd half. D1,2,4 on. D2 turned off for 1 week. D1 good.  
vme20050729: LLR. PreC/PosC ADC1 amp increased for low energy study but noise threshold is over 50keV.  
vme20050902: LLR. PreC/PosC  
vme20050930: --Noisy data. detectors turned off and on. did not help.  
vme20051012: LLR continues from last group. Low threshold=2. Deadtime?  
vme20051019: LLR continues from last group with Thr=3  
vme20051020: LLR PosC clearcap set to 50. autoclearcap=10.  
vme20051128: -- testing crosstalk  
vme20051207: LLR. PreC After cjr shift. start has feature at about 600keV  
vme20060107: LLR PosC Grid Bias reset somehow  
vme20050120: LLR PreC/PosC Peak at 600keV reappears.  
vme20050209: LLR PreC/PosC Peaks at 600keV continues with blip  
vme20060222: -- record of noise threshold with GB and HV switched off. Noise equiv to 90keV
```

SFA DATA

```
-----  
sfa16_20060304: -- First test Low Level Run. Detectors mislabeled. Not confident that conversion map is  
correct.. Interesting x-talk due to saturating bursts.  
sfa16_20060308: -- As above above but bursting detectors activated.  
sfa16_20060312: -- As above (almost)  
sfa16_20060313: -- As above (almost)  
sfa16_20060314: -- As above (almost)  
afa16_20060317: -- (Back at LNGS) Shows 1.3% x-talk between adc channels 2 and 6.
```

```

asf16_20050318: -- Sc137 spectra before any optimisation. ADC2 pulsed and I'm not sure what we are seeing
                  in other detectors.
asf16_20060320: -- Poor Co/Cs spectra. db9's not optimised. ev preamps on dets 7 and 16
asf16_20060321: -- * HV and DB9 optimisation test
asf16_20060322a: -- * GB optimisation test
asf16_20060322b: -- Test LLR with rough calibration. Castle open. Lots of x-talk. Lead to turning off det1.
asf16_20060323a: -- * DB9 optimisation tests at 1000V. Fills in remaining points previous sweep did not cover.
asf16_20060323b: ** PreCalib. Attempted LLR but stopped to read just thresholds.
asf16_20060324a: -- Attempted LLR but had to increase thresholds
asf16_20060324b: -- Attempted LLR but had to increase thresholds
asf16_20060325: -- (Leave LNGS) Det 10 breakdown and strange peaks appear in all dets. Increase thresholds.
asf16_20060326: -- Try increasing thresholds and deactivating dets 2 and 10 on ADC but strange peaks
                  still there.
asf16_20060328: LLR Restart cobra 2 to get web-cam working and turn off HV1. Peaks go. Only 5 calibrated
                  dets running.
asf20_20060717a: -- Optimisation of colourless layer
asf20_20060717b: -- testing high energy events
asf20_20060718: -- testing high energy events
sfa20_20060727: LLR loads of data but more noise than real events
sfa20_20060810b: LLR loads of data. D19 and D20 only detectors on.
sfa20_20060912: -- over night test to check that new HV gives same data rates. it does.
sfa20_20060913: -- PreC. Test to see x-talk with all dets on with aluminium foil in between: still no good
sfa20_20060913b: -- Test to see that 19 and 20 still have good signals. Spectra look good.
sfa20_20060914: -- Overnight test to see how we do with 19 and 20 on and all the decent looking crystals
                  on layer1. Unfortunately had HV mapping wrong so this is nonsense
sfa20_20060915: -- Scanning each channel in turn, putting HV to 1500V, all others HV and GB to 0 in
                  effort to see what causes disruptions. Series of 5 minute runs
sfa20_20060916: LLR PreCalib. Active dets: 2, 7, 15, 19, 20. 2 has problems and will probably be turned off.
sfa20_20060922: LLR PostCalib. Active dets: 7, 15, 19, 20. 20 started bursting (GB breakdown?)
sfa20_20061002: -- Test to see background rates with HV and GB off.
sfa20_20061003: -- Test to see background rates with HV lines 21 and 22 at 2kV. See events layers 1 and 2.
sfa20_20061003b: -- Test to see background rates in D19 when D20 is at HV1kV and GB30V which is the
                  settings it was at for the last runs. Aim: extrapolate background to 2-3MeV region.
sfa20_20061004: -- Same as above but increased thresholds.
sfa20_20061007: -- HV test: Scanning through voltages on D1 to observe the crosstalk effect as a
                  function of voltage.
sfa20_20061010: -- HV test: As above but applied voltage to D22 (ie no crystal not D1)
sfa20_20063010: -- HV test: Scan through detectors, turning one more to 1500V each hour (start at 1, till
                  all channels 1-22 are at HV1500V)
sfa20_20063110: -- HV test: As above but start with 16 and turn on HV for detectors 15, 14, 13,...1.
                  Some mess due to disk full - second half repeated (see README in folder)
sfa20_20061101: -- GB test: As sfa20_20063010 but working GB (to 50V) not HV on layer 1, 1-16
sfa20_20061116: -- GB test: To ensure the GB doesn't cause pickup, choose channel 15 and run for ~5hours.
                  See no events.
sfa20_20061120: -- PreCalib
sfa20_20061120: LLR PostCalib with 7, 15 and 19. (Not able to locate calibration file)

*** trip to LNGS to install HV-veto ***
sfa20_20061208: -- Test as below but with the resistors still attached after the capacitor?
sfa20_20061209: -- Testing Jaime's adding box veto. See readme.
sfa20_20061210: -- Testing +ve signals on detectors 2, 3, 5, 7, and 8. 2+3 added and recorded in ADC17,
                  5*7+8 added and recorded to ADC18. Some successful vetos, lower voltage bands on 3, 7,
                  and 8 unrelated.
sfa20_20061211: -- Testing burn in test. At first higher rate at lower voltage and then a return to normal
sfa20_20061213: -- Over lunch test to test HV-veto. dets 12-16 on ADC's 17-20. HVline2 ground broken.
sfa20_20061213b: -- Over night test to test HV-veto. Amplification on shaper increased to improve SNR on
                  veto. Rough optimizing of detector voltages. Ground wire on HV line2 fixed.
sfa20_20061214: -- Over lunch test to test HV-veto WITH SUMMING BOX. Looking at oscilloscope was more
                  conclusive that the SN ratio looked better with it than with the wire-up together
                  method.
sfa20_20061214b: -- Over night test to test summing box veto. Last Night at LNGS.
sfa20_20061215: -- OPTIMISATION calibration run.

```

```

*** end of shift ***

// The next 3 groups the HV-veto was plugged into an adc with deactivated triggers so the veto could can
not be used effectively. Otherwise the data would be good.
sfa20_20061218: -- LLR PreCalib. HV-veto installed and hopefully working. Merry Christmas and Happy New Year.
sfa20_20061222: -- LLR cont of sfa20_20061218 without 10.
sfa20_20070110: -- LLR PostCalib cont with clearcap set to 1. HV rates dropped.
sfa20_20070115: -- PreCalib HV-veto moved to module 6. probs with daq so aborted run
sfa20_20070117: -- PreCalib probs with daq so it had to be restarted after calib. Veto data looking good.
sfa20_20070122: LLR PreCalib Poor calib for D2 and D14, See README. ADC mod 1 failure on 08/02/2007 NB on
python I have split this into 2 groups with the second called sfa20_20070208
sfa20_20070227: -- LLR cont of sfa20_20070122 after resending trigger propagation command. Prob with too
low threshold on veto to ADC21. stopped run
sfa20_20070302: LLR PostCalib cont of sfa20_20070122. Re-adjusted thresholds by eye. Should have some
good low threshold data.

*** Jeanne goes to LNGS to arrange move and does post calibration ***
*** end of shift ***

sfa20_20070314: LLR PreCalib PostCalib The Na22 pre calib is the post calib of sfa20_20070302

*** start of shift to move experiment
sfa20_20070417: -- LLR first test after move to see if everything works. Electronic noise.
sfa20_20070418: -- LLR second test after move after Jaime improved grounding and added HV-veto. Much
better.
sfa20_20070421: --
sfa20_20070422: --
sfa20_20070423: --
sfa20_20070424: --
*** end of shift ***

sfa20_20070425: LLR PostCalib. a shift in calibration occurred at 26/05/07 so PreCalib not valid
sfa20_20070514: -- Stability test to see if calibrations drift over night. Only a small drift is seen on
some detectors at 51keV
sfa20_20070515: -- Optimisation of potentiometers. Improvements gained
sfa20_20070515: -- PreCalib valid. LLR but trigger linking was not activated so restarting
sfa20_20070516: LLR PostCalib take pre calib from above run. Calibration jump at end?
sfa20_20070621: LLR PostCalib, for pre calib use post calib of last run

*** start of shift to install CREMATs and nitrogen filter ***
sfa20_20070725: -- test LLR after CREMATs installed. look ok
sfa20_20070725b: -- optimization of potentiometers
sfa20_20070726: -- optimisation of voltages
sfa20_20070727: -- test LLR after potentiometer optimization
sfa20_20070728: -- test LLR after voltage optimization with good detectors set to 1400V. Break down
observed again.
sfa20_20070729: -- test LLR after re-jigging voltages. 1400V dropped to usually 1250V and a couple of GB
dropped on problem detectors. Data mostly back to normal.
*** end of shift ***

sfa20_20070730: LLR PreCalib. Successful low level run until a power cut...
sfa20_20070813: LLR PreCalib. Matthias/Jeanne restarted daq and calibrated. Another power cut.
sfa20_20070822: LLR PostCalib. Oleg restarted crate but we have no pre-calib. Detector 11 failed.
sfa20_20070926: LLR PreCalib. Detector 11 turned off. Active dets=2,3,5,7,8,9,10,12,13,14,15 (11detectors)

*** start of shift to install remaining of 64 array ***
64_installation_testing
sfa64_20071014: -- First calibrations

```

```
sfa64_20071015: -- first data with 64 array
sfa64_20071016: -- more data
sfa64_20071017:
sfa64_20071017b:
sfa20_20071019: -- calibration
*** end of shift ***

sfa20_20071021: LLR PreCalib,PostCalib. HV-veto not activated.
sfa20_20071108: LLR PreCalib. New air conditioner installed.
sfa20_20080121: LLR PreCal/PostCal

*** start of shift to install colourless detectors (Oli) ***
sfaCL_20080320: LLR PreCalib and Testrun
sfaCL_20080321: LLR PreCalib and Run
```

Collaboration Members

Collaborators mentioned in this thesis

Thomas Bloxham	PhD student at the University of Birmingham. Graduated.
Jaime Dawson	Postdoctoral researcher at the University of Sussex 2005–2008.
Henning Kiel	PhD student at the University of Dortmund. Graduated.
Tobias Köttig	PhD student at the University of Dortmund.
Ben Morgan	Postdoctoral researcher at the University of Warwick.
Daniel Müenstermann	PhD student at the University of Dortmund. Graduated.
Sandra Oehl	Diploma student at the University of Dortmund. Graduated.
Oliver Schultz	PhD student at the University of Dortmund.
Jeanne Wilson	Postdoctoral researcher at the University of Sussex 2004–2008.
Kai Zuber	Lecturer and then Reader at the University of Sussex between 2003–2008. Main supervisor for this thesis. zuber@physik.tu-dresden.de

All collaborators

Thomas Bloxham	University of Birmingham
Andrew Boston	University of Liverpool
Osvaldo Civitarese	University of La Plata
Jaime Dawson	University of Sussex
Simon Fox	University of York
Martin Freer	University of Birmingham
Brian Fulton	University of York
Claus Gößling	University of Dortmund

Matthias Junker	LNGS / INFN
Tobias Köttig	University of Dortmund
Henric Krawczynski	Washington University in St Louis
John McGrath	University of York
Ben Morgan	University of Warwick
Daniel Müenstermann	University of Dortmund
Christopher Reeve	University of Sussex
Oliver Schulz	University of Dortmund
Fedor Simkovic	University of Bratislava
Danielle Stewart	University of Warwick
Jouni Suhonen	University of Jyväskylä
Robert Wadsworth	University of York
Jeanne Wilson	University of Sussex
Kai Zuber	University of Sussex / Dresden University of Technology

Nomenclature

0ν	Nuetrinoless.
2ν	Two-neutrino.
ADC	Analogue to Digital Converter.
C.L.	Confidence limit.
COBRA	CdTe 0 neutrino double Beta decay Research Apparatus.
cobra2	Control computer for cobra3.
cobra3	Crate mounted VME computer to which the data acquisition software is installed.
CPG	co-planar grid.
Cut	A method of removing events from a dataset with criteria such as correlations or restricting energy ranges.
CZT	CdZnTe - Cadmium Zink Telluride.
DAQ	Data acquisition - referring in this thesis to the software responsible for controlling the ADCs and writing the data to disk.
DBD	Double-beta decay.
Event	An interaction with a detector that produces a charge pulse on the signal lines. The energy and time of an event is recorded whenever the voltage goes beyond a critical threshold, the <i>trigger threshold</i> .
g.s.	Ground state.
GB	Grid bias. This is the voltage applied across the detector grids.
Group	A collection of runs which usually share common calibrations.
HV	High voltage. This typically refers to the voltage supplied to the cathodes.
INFN	Istituto Nazionale di Fisica Nucleare (the National Institute of Nuclear Physics).
LNGS	Laboratorio Nazionale del Gran Sasso

m.w.e. Meters water equivalent. The equivalent radiation protection from a depth of water in meters.

nat. ab. Natural abundance.

Q-value The energy released in a nuclear decay.

Run An hour long period of data which always directly corresponds to the data recorded in a complete data file, sometimes referred to as a daq-file.

STFC Science and Technology Facilities Council or Swindon Town Football Club.

Veto A system for tagging events that occur at the same time, so they can be rejected.

Waterfall plot 2D scatter plot showing the energy versus the time of events.

Publications

A list of publications co-authored during work for this thesis

- [BBD⁺07] First results on double-beta decay modes of Cd, Te and Zn Isotopes. *Physical Reviews of Modern Physics C*, 2007.
- [DMR⁺08] An Investigation on Cooling of CZT Co-Planar Grid Detectors. *Nuclear Instruments and Methods in Physics Research A*, 2007.
- [DRR⁺08] A search for double beta decays of tin isotopes with enhanced sensitivity. *Physical Review C*, 2008.
- [DDK⁺08] A search for various double beta decay modes of tin isotopes. *Nuclear Physics A*, 2008.
- [DRW⁺09] An Investigation into the ^{113}Cd Beta Decay Spectrum using a CdZnTe Array. *Nuclear Physics A*, 2009.

Bibliography

- [A⁺94] A. Alessandrello et al. *Nucl. Phys. B Proc. Suppl.*, 35:394, 1994.
- [AAA⁺01] Q. Ahmad, R. Allen, T. Andersen, et al. Measurement of the rate of $\mu_e + d \rightarrow p + p + e^+$ interactions produced by ${}^8\text{B}$ solar neutrinos at the Sudbury Neutrino Observatory. *Phys. Rev. Lett.*, 87:071301, 2001.
- [AAA08] A. Arnaboldi, D. Artusa, and F. and others Avignone. Results from a search for the $2\nu\beta\beta$ -decay of ${}^{130}\text{Te}$. *Physical Review, C*:78, 2008.
- [AAAI⁺05] C. Arnaboldi, DR Artusa, FT Avignone III, et al. A New Limit on the Neutrinoless DBD of ${}^{130}\text{Te}$. *Arxiv preprint hep-ex/0501034*, 2005. CUORICINO.
- [AAB⁺05] R. Arnold, C. Augier, AM Bakalyarov, et al. Technical design and performance of the NEMO 3 detector. *Nuclear Inst. and Methods in Physics Research, A*, 536(1-2):79–122, 2005.
- [ABB⁺03] C. Arnaboldi, C. Brofferio, C. Bucci, et al. A calorimetric search on double beta decay of ${}^{130}\text{Te}$. *Physics Letters B*, 557(3-4):167–175, 2003.
- [ABC⁺00] A. Alessandrello, C. Brofferio, O. Cremonesi, et al. New experimental results on double beta decay of ${}^{130}\text{Te}$. *Physics Letters B*, 486(1-2):13–21, 2000.
- [ACD⁺96] R. André, J. Cibert, Le Si Dang, J. Zeman, and M. Zigone. Nonlinear piezoelectricity: The effect of pressure on CdTe. *Phys. Rev. B*, 53(11):6951–6954, Mar 1996.
- [ACK⁺07] I. Abt, A. Caldwell, K. Kröninger, J. Liu, X. Liu, and B. Majorovits. Identification of photons in double beta-decay experiments using segmented germanium detectors—Studies with a GERDA phase II prototype detector. *Nuclear Inst. and Methods in Physics Research, A*, 583(2-3):332–340, 2007.
- [Aud03] A. H. & Thibault C. Audi, G & Wapstra. *Nucl. Phys., A* 729:337, 2003.
- [AW05] D. Akers and J. Wenzinger. Induced Positron Annihilation Investigation of Cadmium Zinc Telluride Crystal Microstructures. *Idaho National Laboratory Idaho Falls, Idaho 83415*, June 2005. <http://www.osti.gov/bridge/servlets/purl/911691-I05np2/911691.PDF>.

- [AZG06] ZB Alfassi, T. Zlatin, and U. German. Simultaneous measurement of gamma-rays and neutron fluences using a HPGE detector. *Journal of Radioanalytical and Nuclear Chemistry*, 268(2):237–241, 2006.
- [B⁺07] Belli et al. *Physical Review C*, 76:064603, 2007.
- [Bar89] Roger Barlow. *Statistics: a guide to the use of statistical methods in the physical sciences*. John Wiley, 1989.
- [Bar90] A. & Cherehovsky V. Barabash, A. & Koplov. Search for the double beta-decay of ^{100}Mo and ^{116}Cd to the excited states of ^{100}Ru and ^{116}Sn . *Phys. Lett. B*, 249:115, 1990.
- [BBB⁺07] P. Belli, R. Bernabei, N. Bukilic, F. Cappella, et al. Investigation of β decay of ^{113}Cd . *Physical Review C*, 76(6):64603, 2007.
- [BBd⁺89] P. Belli, R. Bernabei, d'Angelo, et al. Deep underground neutron flux measurement with large BF 3 counters. *Il Nuovo Cimento A (1971-1996)*, 101(6):959–966, 1989.
- [BBD⁺07] T. Bloxham, J. Boston, J. Dawson, C. Reeve, et al. First results on double-beta decay modes of Cd, Te and Zn Isotopes. *Physical Reviews of Modern Physics*, C:76, 2007.
- [BBI⁺99] P. Belli, R. Bernabei, A. Incicchitti, et al. New limits on $2\beta+$ decay processes in ^{106}Cd . *Astroparticle Physics*, 10(1):115–120, 1999.
- [BJ69] H. Behrens and J. Janecke. *Numerical Tables for Beta Decay and Electron Capture*. Springer Publ., Berlin, 1969.
- [Blo07] T. Bloxham. *The simulation and use of Cadmium Zinc Telluride detectors as part of the search for neutrinoless double beta decay*. PhD thesis, The University of Birmingham, 2007.
- [BNAD84] E. B. Norman and M. A. DeFaccio. Serches for double $\beta+$, $\beta+/\text{EC}$ and double electron-capture decays. *Physics Letters B*, 148(1-3):31–34, 1984.
- [Bon06] J. Bonn. Status of the KATRIN Experiment. *Acta Physica Polonica B*, 37(7):2039, 2006.
- [CDD⁺98] B.T. Cleveland, T. Daily, R. Davis, Jr, et al. Measurement of the Solar Electron Neutrino Flux with the Homestake Chlorine Detector. *The Astrophysical Journal*, 496(1):505–526, 1998.
- [Cow98] G. Cowan. *Statistical Data Analysis*. Oxford science publications, 1998.
- [Daw] J. Dawson. *Calibration Tool Manual*. University of Sussex, 2006. http://cobra.physik.uni-dortmund.de/internal/src/spectrum_analysis.

- [Daw05] J. Dawson. Energy Calibration and Resolution Function of CZT Detectors. <http://cobra.physik.uni-dortmund.de/internal/memo/2005-11.pdf> COBRA memo, November 2005.
- [Daw06] J. Dawson. Personal communication. 2006.
- [DDK⁺08] J. Dawson, D. Degering, M. Köhler, R. Ramaswamy, C. J. Reeve, J. R. Wilson, and K. Zuber. A search for various double beta decay modes of tin isotopes. *Nuclear Physics A*, 2008.
- [DGK⁺96] FA Danevich, A.S. Georgadze, VV Kobychev, et al. Beta decay of ^{113}Cd . *Physics of Atomic Nuclei*, 59(1):1–5, 1996. The main reference, have a paper copy and is also on the COBRA website.
- [DGK⁺03] FA Danevich, A.S. Georgadze, VV Kobychev, et al. Search for 2β decay of cadmium and tungsten isotopes: Final results of the Solotvina experiment. *Physical Review C*, 68(3):35501, 2003.
- [DKN⁺05] FA Danevich, VV Kobychev, SS Nagorny, et al. ZnWO₄ crystals as detectors for 2β decay and dark matter experiments. *Nuclear Inst. and Methods in Physics Research, A*, 544(3):553–564, 2005.
- [DMR⁺08] J. V. Dawson, C. Montag, C. J. Reeve, J. R. Wilson, and K. Zuber. An Investigation on Cooling of CZT Co-Planar Grid Detectors. *Nuclear Inst. and Methods in Physics Research, A*, 2008.
- [DRR⁺08] J. Dawson, R. Ramaswamy, C. J. Reeve, J. R. Wilson, and K. Zuber. A search for double beta decays of tin isotopes with enhanced sensitivity. *Physical Review C*, 2008.
- [DRW⁺09] J. Dawson, C. Reeve, J. Wilson, K. Zuber, et al. An Investigation into the ^{113}Cd Beta Decay Spectrum using a CdZnTe Array. *Nuclear Physics A*, 2009.
- [DV05] Michael G. Danikas and Nikolaos Vrakotsolis. Experimental results with small air gaps: further thoughts and comments on the discharge (or charging phenomena) below the so-called inception voltage. *Journal of Electrical Engineering*, 56:246–251, 2005. http://iris.elf.stuba.sk/JEEEC/data/pdf/09-10_105-3.pdf.
- [Ein05] Albert Einstein. Ist die Trägheit eines Körpers von seinem Energiegehalt abhängig? *Annalen der Physik*, 18:639, 1905. http://www.physik.uni-augsburg.de/annalen/history/papers/1905_18_639-641.pdf - original. http://www.fourmilab.ch/etexts/einstein/E_mc2/www/ - translation.
- [EL06] O. Elgaroy and O. Lahav. Sub-eV upper limits on neutrino masses from cosmology. *PHYS. SCRIPTA T*, 127:105, 2006.

- [EMNV91] SR Elliott, MK Moe, MA Nelson, and MA Vient. The double beta decay spectrum of ^{100}Mo as measured with a TPC. *Journal of Physics G: Nuclear and Particle Physics*, 17:S145–S153, 1991.
- [EV02] Steven R. Elliott and Petr Vogel. Double Beta Decay. *Annual Review of Nuclear and Particle Science*, 52(1):115–151, 2002.
- [FHI⁺98] Y. Fukuda, T. Hayakawa, E. Ichihara, et al. Evidence for Oscillation of Atmospheric Neutrinos. *Phys. Rev. Lett.*, 81(8):1562–1567, Aug 1998.
- [FP00] A. Fassò and J. Poirier. Spatial and energy distribution of muons in γ -induced air showers. *Phys. Rev. D*, 63(3):036002, Dec 2000.
- [G⁺05] C. Gössling et al. *Physical Review C*, 72:064328, 2005.
- [Geh86] N Gehrels. Confidence Limits for Small Numbers of Events in Astrophysical Data. *ApJ*, 303:336, 1986.
- [GM35] M. Goeppert-Mayer. Double Beta-Disintegration. *Phys. Rev.*, 48(6):512–516, Sep 1935.
- [H⁺00] K. M. Heeger et al. High-voltage microdischarge in ultra-low background He-3 proportional counters. *IEEE Trans. Nucl. Sci.*, 47:1829–1833, 2000. <http://ieeexplore.ieee.org/iel5/23/19744/00914454.pdf?arnumber=914454>.
- [Har06] Philip Harris. *Data Analysis Techniques*. University of Sussex, 2006. Course notes based partly on *Statistics* by R. Barlow.
- [HBGN03] J. Hong, E. C. Bellm, J. E. Grindlay, and T. Narita. Cathode depth sensing in CZT detectors. 2003.
- [Heu95] G Heusser. Low-Radioactivity Background Techniques. *Annual Review of Nuclear and Particle Science*, 45(1):543–590, 1995.
- [HO02] E. Harry and OCEI Orton. Partial Discharge Testing of In-Situ Power Cable Accessories - An Overview. *Electric Energy T&D magazine*, 2002. <http://www.electricenergyonline.com/article.asp?m=9&mag=6&article=44>.
- [Jul05] S. Jullian. Experimental status on neutrinoless double beta decay searches. *Comptes Rendus Physique*, 6:778–788, September 2005.
- [Kie05] H. Kiel. *Determination of the Half Lives of Rare Decays of Cd, Te and Zn Isotopes for the COBRA Experiment*. PhD thesis, University of Dortmund, Germany, 2005.
- [KK03] H. V. Klapdor-Kleingrothaus. First Evidence for Neutrinoless Double Beta Decay. *FOUND.PHYS.*, 33:813, 2003.
- [KK05] H.V. Klapdor-Kleingrothaus. First Evidence for Lepton Number Violation and of the Majorana Character of Neutrinos. *Nuclear Physics B - Proceedings Supplements*, 145:219–224, August 2005.

- [KKS95] H.V. Klapdor-Kleingrothaus and A Staudt. *Non-accelerator Particle Physics*. Institute of Physics Publishing Bristol and Philadelphia, 1995.
- [KMZ03] H. Kiel, D. Munstermann, and K. Zuber. A Search for various Double Beta Decay Modes of Cd, Te and Zn Isotopes. *Nuclear Physics A*, 723:499, 2003.
- [Kno79a] Glenn F. Knoll. *Radiation Detection and Measurement*. John Wiley & Sons, New York, third edition, 1979.
- [Kno79b] Glenn F. Knoll. *Radiation Detection and Measurement*. John Wiley & Sons, New York, second edition, 1979.
- [LAL03] P.N. Luke, M. Amman, and J.S. Lee. Factors affecting energy resolution of coplanar-grid CdZnTe detectors. *Nuclear Science Symposium Conference Record, 2003 IEEE*, 5:3295–3299 Vol.5, Oct. 2003.
- [Lee04] Paul N. Luke & Mark Amman & Julie S. Lee. Factors Affecting Energy Resolution of Coplanar-Grid CdZnTe Detectors. *IEEE*, page 3295, 2004.
- [Leo87] R. W. Leo. *Techniques for Nuclear and Particle Physics Experiments*. Springer, 1987.
- [LNG] <http://www.mpi-hd.mpg.de/nuastro/Viewphotos/map.pdf>.
- [Lub98] James G Lubenau, Joel O. & Yusko. Radioactive Materials in Recycled Metals-An Update. *Health Physics*, 74(3):293–299, 1998.
- [Lun] The Lund/LBNL Nuclear Data Search. <http://nucleardata.nuclear.lu.se/nucleardata/toi/index.asp>. Accessed 2008.
- [Maj37] Ettore Majorana. Teoria simmetrica dell’eletron e del positrone. *Nuovo Cimento*, 14:171–184, 1937.
- [MHS⁺98] D. McGregor, Z. He, H. Seifert, R. Rojeski, and D. Wehe. CdZnTe semiconductor parallel strip Frisch grid radiation detectors. *IEEE Transactions on Nuclear Science*, 45(3 Part 1):443–449, 1998.
- [Mit88] P. Mitchell, L. & Fisher. *Phys. Rev.*, D 38:895, 1988.
- [Mue01] D. Muenstermann. Untersuchung seltener Kernzerfälle mit Cadmium-Tellurid-Detektoren. Diploma thesis, University of Dortmund, Germany, 2001.
- [Mue07] D. Muenstermann. *Construction of a Low Background Facility for the COBRA Experiment and its Performance*. PhD thesis, University of Dortmund, Germany, 2007.
- [Mun03] Alan Munter. Neutron scattering lengths and cross sections, 2003. <http://www.ncnr.nist.gov/resources/n-lengths/>.
- [Mus06] M. & Suhonen J. Mustonen, M. T. & Aunola. *Physical Review C*, 76:054301, 2006.

- [Nac07] A. Nachab. Radon reduction and radon monitoring in the NEMO experiment. *AIP Conf. Proc.*, 897:35–38, 2007.
- [Oeh04] S. Oehl. A Shielding System against Neutrons for the COBRA-Experiment and Characterisation of CdZnTe detectors with the Transient Current Techniques. Master’s thesis, Univeristät Dortmund, DE., 2004.
- [PBB⁺94] A. Piepke, M. Beck, J. Bockholt, et al. Investigation of the $\beta\beta$ decay of ^{116}Cd into excited states of ^{116}Sn . *Nuclear Physics, Section A*, 577(3-4):493–510, 1994.
- [PCP⁺96] E. Porras, T. Carter, J. M. Pérez, et al. Production of radionuclides by 1.7 GeV proton-induced reactions on CdTe crystals. *Nuclear Instruments and Methods in Physics Research Section B: Beam Interactions with Materials and Atoms*, 111(3-4):315–320, May 1996.
- [Pov] E. Caurier & F. Nowacki & A. Poves. Nuclear Structure Aspects of the Neutrinoless Double Beta Decay. *arXiv:0709.0277v2 [nucl-th]*.
- [PP04] S. Pascoli and S. T. Petcov. The SNO solar neutrino data, neutrinoless double beta-decay and neutrino mass spectrum. *Physics Letters B*, 580:280–289, February 2004.
- [PRO] PROS helpfile. PROS is developed, distributed, and maintained by the Smithsonian Astrophysical Observatory, under partial support from NASA contract NAS5-30934. *Description of PROS error computations for low count/bin data*. http://stsdas.stsci.edu/cgi-bin/gethelp.cgi?explain_errors (accessed January 04, 2008).
- [PTZ00] O. Ponkratenko, V. Tretyak, and Y. Zdesenko. Event Generator DECAY4 for Simulating Double-Beta Processes and Decays of Radioactive Nuclei. *Physics of Atomic Nuclei*, 63:1282, 2000.
- [Rac37] G. Racah. *Nuovo Cim*, 14:322, 1937.
- [RC53] F. Reines and C. L. Cowan. Detection of the Free Neutrino. *Phys. Rev.*, 92(3):830–831, Nov 1953.
- [Ree04] C. Reeve. Simulating backgrounds of the COBRA experiment. Master’s thesis, Univeristy of Sussex, 2004.
- [Ree06a] C. Reeve. Summary of CAMAC-Delrin Data. Internal memo. <http://cobra.physik.uni-dortmund.de/internal/memo/2006-06.pdf>, 2006.
- [Ree06b] C. Reeve. Summary of the VME data. Internal memo., 2006.
- [ROO] *ROOT Users Guide 5.16*. ftp://root.cern.ch/root/doc/Users_Guide_5_16.pdf.
- [Rot96] W. Rothenstein. Neutron scattering kernels in pronounced resonances for stochastic Doppler effect calculations. *Annals of Nuclear Energy*, 23(4-5):441–458, March 1996.

- [RS07] Y. Ramachers and D. Stewart. Energy resolution improvement in room-temperature CZT detectors. *Journal of Instrumentation*, 2(12):P12003, 2007.
- [Sch08] O. Schultz. Personal communication. Dortmund University., 2008.
- [SCNC02] C. Szeles, S.E. Cameron, J.O. Ndap, and W.C. Chalmers. Advances in the crystal growth of semi-insulating CdZnTe for radiation detector applications. *Nuclear Science, IEEE Transactions on*, 49(5 Part 2):2535–2540, 2002.
- [SD98] C. Szeles and M.C. Driver. Growth and properties of semi-insulating CdZnTe for radiation detector applications. *Proc. SPIE*, 3446(1), 1998.
- [SDH97] M. Stoneking and D Den Hartog. Maximum-likelihood fitting of data dominated by Poisson statistical uncertainties. *Review of Scientific Instruments*, 68.1:11, 1997. <http://plasma.physics.wisc.edu/uploadedfiles/journal/Stoneking300.pdf>.
- [Sie80] R.W. Siegel. Poistion Annihilation Spectroscopy. *Ann. Rev. Mater. Sci.*, 10:393–425, 1980.
- [Sim83] J.A. Simpson. Elemental and Isotopic Composition of the Galactic Cosmic Rays. *Annual Review of Nuclear and Particle Science*, 33(1):323–382, 1983.
- [SR08] S Snöldner-Rembold. Search for Neutrinoless Double Beta Decay with NEMO 3 and SuperNEMO. *Journal of Physics, Conference Series* 110, 2008. doi:10.1088/1742-6596/110/8/082019.
- [SSM06] U. Seljak, A. Slosar, and P. McDonald. Cosmological parameters from combining the Lyman-alpha forest with CMB, galaxy clustering and SN constraints. *JCAP*, 0610:014, 2006.
- [Teg05] M. Tegmark. Cosmological Neutrino Bounds for Non-Cosmologists. *Physica Scripta*, 121:153–155, 2005.
- [TOR] TORI - Table of Radioactive Isotopes. http://ie.lbl.gov/toi/tori2_2.mdb Database last updated Feb. 1999. Accessed Dec. 2008.
- [TY95] V. Tretyak and Zdesenko Y. Tables of double beta decay data. *Atomic Data and Nuclear Data Tables*, 61:43–90, 1995.
- [Vas] Vladimir Vasiliev. Double beta decay parameters calculator. <http://www.hep.ucl.ac.uk/~vv/2bcalc.html>.
- [Wah96] W. Wahl. First α -, β -, γ - and x-ray Radionuclide Table Prepared for Applications in Spectrometry and Radiation Protection. *Strahlenschutz Praxis*, 1996.
- [Wik] <http://en.wikipedia.org/>. Retrieved Feb 2008.
- [Wil05] J. Wilson. A Preliminary Simulation of Backgrounds due to Paint on the Crystals. COBRA memo, <http://cobra.physik.uni-dortmund.de/internal/memo/2005-01.pdf>, 2005.

- [Wil06] J. Wilson. *Documentation for the COBRA Data Acquisition (DAQ) code*, 2006.
<http://cobra.physik.uni-dortmund.de/internal/memo/2006-03.pdf>.
- [Wil07] J. Wilson. Analysis method for COBRA SFA data. <http://cobra.physik.uni-dortmund.de/internal/src/likelihood/results/results.pdf>, September 2007.
- [Wol30] Pauli Wolfgang. Brief an die Radioaktiviten. 1930.
- [Zub06] Kai Zuber. Neutrinoless Double Beta Decay Experiments. *Acta Physica Polonica B*, 37:1905–1921, 2006.
- [Zub08] Kai Zuber. Personal communication. University of Sussex, Brighton, UK, 2008.